

MECHANOCHEMICAL SYNTHESIS OF FUNCTIONAL LAYERED MATERIALS

by

Samuel Vladimir Pedersen



A dissertation

submitted in partial fulfillment

of the requirements for the degree of

Doctor of Philosophy in Materials Science and Engineering

Boise State University

May 2022

© 2022

Samuel Vladimir Pedersen

ALL RIGHTS RESERVED

BOISE STATE UNIVERSITY GRADUATE COLLEGE

**DEFENSE COMMITTEE AND FINAL READING APPROVALS**

of the dissertation submitted by

Samuel Vladimir Pedersen

Dissertation Title: Mechanochemical Synthesis of Functional Layered Materials

Date of Final Oral Examination: 8 March 2022

The following individuals read and discussed the dissertation submitted by student Samuel Vladimir Pedersen, and they evaluated the student's presentation and response to questions during the final oral examination. They found that the student passed the final oral examination.

Brian J. Jaques, Ph.D.	Chair, Supervisory Committee
David Estrada, Ph.D.	Member, Supervisory Committee
Dmitri Tenne, Ph.D.	Member, Supervisory Committee
Joshua Wood, Ph.D.	Member, Supervisory Committee

The final reading approval of the dissertation was granted by Brian J. Jaques, Ph.D., Chair of the Supervisory Committee. The dissertation was approved by the Graduate College.

## DEDICATION

This dissertation is dedicated to my parents who have always encouraged me to pursue scientific inquiry and to strive towards understanding this world of ours. Your words of support, grounded in the faith we share in Jesus Christ and to whom all glory is truly given, helped to remind me of the true aim of our lives. Thank you for your guidance and support, always.

## ACKNOWLEDGMENTS

In life, there are moments of inspiration and inquiry that come about through interactions with untold number of people. While many have cheered me on in my endeavor towards this dissertation, a few individuals challenged me seek out answers unknown and guided me on the path towards discovery.

To begin, I wish to express my gratitude to my Dr. Brian Jaques, my committee chair, advisor, and mentor. He gave me an incredible opportunity to explore materials science while guiding me along this journey. His patient support across multiple projects spanning thermoelectrics, molten aluminum, and black phosphorus afforded numerous opportunities to conduct scientific research while encouraging a healthy balance between academics, science, and life, both in the laboratory and outside in the community. Lastly, he gave me a chance to pursue a life-long goal, and for that I am forever grateful.

I would like to thank my committee members, Dr. David Estrada, Dr. Joshua Wood, and Dr. Dmitri Tenne for their advice, time, and energy towards shaping my research and mentoring me, helping me to become a better scientist and engineer. Your challenges and suggestions constantly pushed me towards deeper understanding and stretched my perspective of science and graduate studies.

Much of the research presented in this dissertation grew out of a collaborative project between the Advanced Materials Laboratory, the Advanced Nanomaterials and Manufacturing Laboratory, and Iris Light Technologies, funded in part by the Boise State University College of Engineering Seed Funding Program and IGEM Commerce (grant

number 003786), the Center for Advanced Energy Studies and AFWERX STTR award #FA8649-20-P-0986 and the Center for Nanoscale Materials, an Office of Science user facility which is supported by the U.S. Department of Energy, Office of Science, Office of Basic Energy Sciences, under Contract No. DE-AC02-06CH11357 as well as by the U.S. Department of Energy's Energy Efficiency & Renewable Energy (EERE) Advance Manufacturing Office (AMO) through the Argonne Chain Reaction Innovations Program through CRADA No. A18169 with Iris Light Technologies, Inc. Instrumental to this dissertation work was Dr. Chad Husko (Iris Light Technologies) whose excitement towards merging research and industry goals and collaborative spirit pushed me to strive for scientific and engineering success. Support from the MSE department at BSU was greatly appreciated in helping me transition from industry back into an academic environment and aided me in pursuing my education while working behind the scenes to support research.

While those directly involved in the research are acknowledged at the end of each chapter, many others deserve acknowledgements for their support. I would like to thank everyone in the Advanced Materials Laboratory for their assistance and constructive conversations: Allyssa Bateman, Jennifer Watkins, Jordan Vandegrift, Yaiza Rodriguez-Ortego, Adrianna Lupercio, Kaelee Novich, Scott Riley, Timothy Phero, Cade Greseth, Taylor Nowling, Sandeep Dhakal, and Cayden Doyle. From the Advanced Nanomaterials and Manufacturing Laboratory, I wish to acknowledge Florent Muramutsa, Dr. Joshua Eixenberger, and Ariel Weltner. Additionally, I would like to thank Bryan Forsmann at CAES. Within the college of engineering, many individuals helped in a variety of ways to

enable the research to proceed smoothly, including: Arvin Cunningham, Griff Allen, Phil Boysen, Jessica Economy, Karthik Chinnathambi and Nick Bulloss.

Finally, I must thank my family and friends for supporting me through this journey. To my parents, Roger and Patti, who have sacrificed so much, adopting me into their family, loving me unconditionally, encouraging me to explore science, and enjoy the journey. To my uncle, Dale Scott, you have always encouraged me to seek out answers and to never stop learning. To my friend Evan, thanks for all those lunch time conversations and racquetball matches. Lastly, to my friend Kyle Sieck. Your friendship over the years has changed my life for the better and made this journey enjoyable and rewarding. To my family and friends, thank you for your support and encouragement.

## ABSTRACT

As society continues to create new digital content, the telecommunications industry is seeking new technologies to enable higher bandwidth and lower costs to keep pace with the growing demand. Two-dimensional black phosphorus is proposed as a replacement for III-V compound semiconductors as the optically active material in next-generation silicon photonics as it can enable device scaling with lower power consumption. Therefore, the primary motivation of this dissertation was to investigate BP synthesis and chemical doping using an industrially scalable process, high energy ball milling.

Initially, the work focused on understanding the ball mill conversion kinetics of red to black phosphorus, hitherto unknown, and is detailed in Chapter 2. The process follows a nucleation and growth dominated mechanism whose rate is controlled by the collision energy and milling intensity. Photoluminescence on mechanochemically synthesized BP showed visible and infrared emissions at the few-layer limit, indicating this process route provides optically viable BP suitable for silicon photonics.

To address feasibility of doping, arsenic alloys with phosphorus were subsequently produced by ball milling in order to better understand how the crystal structure changes with substitutional doping; this work is described in Chapter 3. A similar conversion kinetics study was also performed showing a two-step mechanism. First, within a few minutes of milling, the trigonal PAs structure forms followed by a much slower phase transformation to the orthorhombic structure. This work provided a

solid benchmark for how substitutional atoms affects the crystal structure, vibrational modes, binding energies, and photoluminescence.

Candidate dopants for BP beyond arsenic included germanium, sulfur, selenium, and tellurium. Milling results for germanium phosphides are presented in Chapter 4 and results for phosphorus with sulfur, selenium, and tellurium are presented in Chapter 5. Germanium appears to dope BP (<1 at% Ge) as do sulfur (<10 at%) and selenium (<10 at%). Tellurium does not appear to form a stable dopant with black phosphorus via ball milling. Higher concentrations produced layered trigonal and monoclinic Ge-P crystals, while several crystalline and amorphous phosphorus sulfides and selenides are synthesized by this novel route. Together, Chapters 3-5 indicated that mechanochemical doping of BP with arsenic, germanium, sulfur and selenium is feasible with future work to explore electrical measurements.

Finally, within the appendix, a discussion is presented challenges for ball mill doping of BP including milling material, red phosphorus purity, and candidate dopants; limited structural characterization of BP doped with germanium and selenium are included. Less comprehensive work on ball mill reactions of phosphorus with boron, tin, antimony, and bismuth are also reported in the appendix. These results confirmed inability to form phosphorus antimonides while several of the known tin phosphides were successfully synthesized. Independent of the black phosphorus work, a separate study on the synthesis of several intermetallic half-Heuslers for thermoelectric applications is also included in the Appendix. The half-Heusler work shows the versatility of ball milling to synthesize a wide range of intermetallic compounds and revealed nuances regarding challenges of milling together high temperature refractory metals, transition metals, and

soft metalloids, in terms of particle size reduction, single phase synthesis, and milling media contamination.

## TABLE OF CONTENTS

DEDICATION .....	iv
ACKNOWLEDGMENTS .....	v
ABSTRACT .....	viii
LIST OF TABLES .....	xv
LIST OF FIGURES .....	xvi
LIST OF ABBREVIATIONS .....	xxii
CHAPTER ONE: INTRODUCTION .....	1
References .....	7
CHAPTER TWO: MECHANOCHEMICAL CONVERSION KINETICS OF RED TO BLACK PHOSPHORUS AND SCALING PARAMETERS FOR HIGH VOLUME SYNTHESIS .....	12
Abstract .....	14
2.1 Introduction.....	14
2.2 Results .....	16
2.2.1 Black Phosphorus Characterization.....	16
2.2.2 Conversion Kinetics.....	18
2.3 Discussion.....	22
2.4 Methods .....	28
Acknowledgements.....	33
Author Contributions .....	33

Competing Interests.....	33
References.....	34
Figures .....	39
Tables.....	54
<b>CHAPTER THREE: MECHANOCHEMISTRY OF PHOSPHORUS-ARSENIC ALLOYS FOR VISIBLE AND INFRARED PHOTONICS .....</b>	<b>56</b>
Abstract.....	58
3.1 Introduction.....	58
3.2 Results and Discussion .....	61
3.3 Conclusion.....	72
3.4 Methods.....	73
Acknowledgements .....	76
Author Contributions.....	76
Competing Interests.....	77
References.....	78
Figures .....	83
Tables .....	100
<b>CHAPTER FOUR: MECHANOCHEMISTRY OF THE PHOSPHORUS-GERMANIUM COMPOUNDS .....</b>	<b>102</b>
Abstract.....	104
4.1 Introduction.....	104
4.2 Results.....	106
4.3 Discussion .....	108
4.4 Methods.....	115

Acknowledgements .....	116
Author Contributions .....	116
Competing Interests .....	116
References .....	117
Figures.....	122
Tables .....	126
<b>CHAPTER FIVE: MECHANOCHEMISTRY OF THE PHOSPHORUS- CHALCOGENIDE COMPOUNDS.....</b>	<b>128</b>
5.1 Introduction.....	130
5.2 Results .....	132
Results: Mechanical alloying of P-S compounds.....	132
Results: Mechanical alloying of P-Se compounds.....	135
Results: Mechanical alloying of P-Te compounds.....	136
5.3 Discussion.....	137
Discussion: Mechanical alloying of P-S compounds .....	137
Discussion: Mechanical alloying of P-Se compounds .....	139
Discussion: Mechanical alloying of P-Te compounds .....	140
5.4 Methods .....	144
Acknowledgements.....	145
Author Contributions .....	145
Competing Interests .....	145
References .....	146
Figures.....	151
Tables .....	162

CHAPTER SIX: CONCLUSIONS.....	163
References.....	170
APPENDIX A.....	171
APPENDIX B.....	202

## LIST OF TABLES

Table 2.1	Solid state reaction models considered for the master-plot method <sup>73</sup> .....54
Table 2.2	PM 100 planetary ball mill parameters used for kinematic modeling.....54
Table 2.3	Comparison of kinetic models and calculated ball milling energies.....55
Table 3.1	Crystallographic details of phosphorus and arsenic structure..... 100
Table 3.2	EDS compositions of ball mill synthesized PAs powders. .... 101
Table 4.1	Crystallographic details of phosphorus-germanium compounds..... 126
Table 4.2	P-Ge phases produced by high energy ball milling..... 126
Table 4.3	Raman modes of P-Ge phases..... 127
Table 4.4	High pressure synthesis conditions of P-Ge phases and black phosphorus. ..... 127
Table 4.5	Comparison of P, As, Ge atoms for solid solution formation..... 127
Table 5.1	XRD phases within mechanochemically synthesized P-S, P-Se, P-Te powders ..... 162
Table 5.2	Structural units within mechanochemically synthesized P-S powders ... 162
Table 5.3	Structural units within mechanochemically synthesized P-Se amorphous glasses ..... 162
Table A.1.1	Target dopant concentrations of the Ge- and Se- doped phosphorus ball milling runs along with the impurities from milling as determined by ICPMS. The samples were milled with WC balls and vessel in order to reduce contamination introduced during milling. .... 185
Table B.1	Synthesis and ZT comparison for select half-Heuslers. ....240
Table B.2	Thermoelectric performance of select half-Heuslers produced by mechanical alloying, arc-melting, and ball mill refined arc-melting synthesis routes as compared to literature. ....241

## LIST OF FIGURES

Figure 2.1	Characterization of the mechanochemical conversion of RP to BP. ....	39
Figure 2.2	XRD curves for BP conversion at 500 rpm with reference BP (vertical black bars) and Si standard (stars) showing increased phase fraction of BP with increased milling time. ....	40
Figure 2.3	XRD curves for BP conversion at 400 rpm with reference BP (vertical black bars) and Si standard (stars) showing increased phase fraction of BP with increased milling time. ....	41
Figure 2.4	XRD curves for BP conversion at 300 rpm with reference BP (vertical black bars) and Si standard (stars) showing increased phase fraction of BP with increased milling time. Note that the peak at 17 degrees for BP at 300 rpm is less prominent than at higher rpm values; indicating smaller crystallites and lower degree of conversion. ....	42
Figure 2.5	XRD curves for BP conversion at 200 rpm with reference BP (vertical black bars) and Si standard (stars); at 200 rpm, a large induction period of 200+ hours to generate sufficient nuclei of BP is evident.....	43
Figure 2.6	XRD calibration curves using integrated area % of BP peaks (040 and 111) for determining black phosphorus weight fractions; error bars are one standard deviation obtained from three samples for each weight fraction. ....	44
Figure 2.7	Electron microscopy shows particle size reduction through BP synthesis and exfoliation while retaining polycrystallinity.....	45
Figure 2.8	Characterization of mechanochemically synthesized and exfoliated few-layer BP.....	46
Figure 2.9	Master plot method using $f(\alpha)/f(\alpha)_{\alpha=0.5}$ ratios overlaid with experimental phase fractions; the A2 (JMAK), B1 (auto-catalytic) models best match the data while the F1 model (DC) loosely fits the data above 50%. The 300 rpm phase fraction deviates substantially above 50% which may indicate a mechanism change. ....	47
Figure 2.10	Mechanochemically induced phase transformation kinetics of RP to BP using the JMAK and DC models. ....	48

Figure 2.11	DC model including the 200 rpm dataset; the induction time obscures the trend of steeper slopes (larger rate constants) at higher rpms.....	49
Figure 2.12	Extent of conversion for RP to BP as a function of specific milling dose.	50
Figure 2.13	TEM of BP flakes showing multiple crystalline domains with different orientations surrounded by an amorphous matrix (scale bars from left to right are 20 nm and 10 nm while the diffraction pattern scale bar is 2 nm <sup>-1</sup> , respectively).....	51
Figure 2.14	TEM images of BP flakes showing multiple crystalline domains with different orientations surrounded by an amorphous matrix (scale bars from left to right and top to bottom are 100 nm, 50 nm, 5 nm, and 10 nm, respectively).....	52
Figure 2.15	In situ pressure and temperature cycle for a 600 rpm run with 5 grams of RP converted to BP. ....	53
Figure 3.1	Structural characterization of mechanochemically synthesized P-As powders.....	83
Figure 3.2	Powder X-ray diffraction Rietveld refinement on ball mill synthesized P-As 10-90 at% arsenic composition.....	85
Figure 3.3	Vegard behavior of lattice parameters and unit cell volume of o-PAs alloys.....	86
Figure 3.4	Structural characterization of mechanochemically synthesized PAs powders at low arsenic content (0-10 at%).....	87
Figure 3.5	Raman characterization of the P-As alloys from 0-30 at% arsenic.....	88
Figure 3.6	Kinetics of orthorhombic PAs 50 at% synthesis.....	89
Figure 3.7	Scanning electron microscopy of PAs alloyed powders. ....	90
Figure 3.8	X-ray photoelectron spectra (XPS) for P-As alloys generated by mechanochemical alloying.....	91
Figure 3.9	Transmission electron microscopy on exfoliated flakes of an o-PAs 20 at% alloy. ....	92
Figure 3.10	Transmission electron microscopy on P-As 60 at % ( <i>Cmca</i> ) flakes. ....	93
Figure 3.11	Transmission electron microscopy on P-As 80 at % ( <i>R3m</i> ) flakes.....	94

Figure 3.12	Laser diffraction particle size analysis on ultrasonic probe tip exfoliated P-As compositions.....	95
Figure 3.13	Photoluminescence of orthorhombic P-As alloys.....	96
Figure 3.14	UV-Visible absorption spectroscopy on ultrasonic probe tip exfoliated P-As compositions.....	97
Figure 3.15	Near Infrared photoluminescence on PMMA encapsulated P-As alloys..	98
Figure 4.1	Structural characterization of mechanochemically synthesized P-Ge powders. ....	122
Figure 4.2	Raman spectra of mechanochemically synthesized P-Ge compounds. ..	123
Figure 4.3	Pressure and temperature phase diagram for elemental phosphorus. ....	124
Figure 4.4	Electron energy and Gibbs free energy stability of o-PAs and t-PAs alloys as function of arsenic concentration.....	125
Figure 5.1	Known phosphorus-sulfur compounds. ....	151
Figure 5.2	Local structural units in P-Se glasses.....	152
Figure 5.3	Structural characterization of mechanochemically synthesized P-S powders. ....	153
Figure 5.4	Raman characterization of mechanochemically synthesized P-S powders produced in 10 at% sulfur increments.....	154
Figure 5.5	Postulated BP structure with sulfur atoms .....	155
Figure 5.6	Structural characterization of mechanochemically synthesized P-S powders. ....	156
Figure 5.7	Raman characterization of mechanochemically synthesized P-S powders. ....	157
Figure 5.8	Structural characterization of mechanochemically synthesized P-Se powders. ....	158
Figure 5.9	Structural characterization of mechanochemically synthesized P-Se powders. ....	159
Figure 5.10	Structural characterization of mechanochemically synthesized P-Te powders. ....	160

Figure 5.11	Structural characterization of mechanochemically synthesized P-Te powders. ....	161
Figure A.1	Phosphorus and its periodic neighbors. ....	178
Figure A.1.1	Structural characterization of mechanochemically synthesized germanium and selenium doped BP powders. ....	184
Figure A.1.2	Optical image of P-Ge 2 at% powders after long term storage. ....	185
Figure A.2.1	Structural characterization of mechanochemically synthesized P-Sn powders. ....	188
Figure A.3.1	Structural characterization of mechanochemically synthesized P-Sb powders. ....	191
Figure A.4.1	Structural characterization of phosphorus milling trials with oxygen, boron, and niobium. ....	195
Figure B.1	Normalized x-ray diffraction patterns of planetary ball milled $\text{Ti}_{0.75}\text{Zr}_{0.25}\text{NiSn}_{0.98}\text{Sb}_{0.02}$ half-Heusler powders showing the effects of time and milling speed on phase conversion. Unalloyed phases are indicated by markers and characteristic half-Heusler peaks are indicated by vertical drop lines (shown for the half-Heusler $\text{TiNiSn}$ ). ....	227
Figure B.2	Normalized x-ray diffraction patterns of mechanochemically synthesized half-Heuslers powders. Characteristic peaks of the half-Heusler structure and impurity peaks are marked. ....	228
Figure B.3	A typical powder x-ray diffraction Rietveld refinement result on the mechanically alloyed $\text{Nb}_{0.75}\text{Ti}_{0.25}\text{FeSb}$ half-Heusler. Black circles are observed data, red lines are the calculated profiles, blue lines are difference curves (obs-calc). Vertical lines indicate Bragg reflection positions (phase indicated in figure).....	229
Figure B.4	(a) Solution-based laser scattering particle size analysis of arc-melted (AM), ball mill refined arc-melted (RAM) and ball mill mechanically alloyed (MA) half-Heusler $\text{Nb}_{0.75}\text{Ti}_{0.25}\text{FeSb}$ powders shows that the arc-melted powder size distribution is much broader while the ball milled samples have a narrower size distribution; SEM images of $\text{Nb}_{0.75}\text{Ti}_{0.25}\text{FeSb}$ arc-melted powders before milling (b) and after refinement (c) by high energy ball milling. ....	230
Figure B.5	Normalized x-ray diffraction patterns of spark plasma sintered half-Heuslers synthesized by mechanically alloying in a planetary ball mill.	

Unalloyed starting elements and minor impurity peaks are marked.  
 Characteristic peaks for a typical half-Heusler (TiNiSn) are indicated.. 231

Figure B.6	Chemical map of the surface of the $Ti_{0.75}Zr_{0.25}NiSn_{0.98}Sb_{0.02}$ monolith (mechanically alloyed and SPS'd) showing the heterogeneous chemical structure of the alloy. .... 232
Figure B.7	SEM micrographs of the microstructures obtained through MA and SPS of half-Heusler materials where (a) and (b) show the fracture surface and polished surface of $NbCoSn_{0.9}Sb_{0.1}$ while (c) shows the polished surface of $NbCoSn_{0.9}Sb_{0.1}$ at lower magnification for comparison to (d) $Nb_{0.75}Ti_{0.25}FeSb$ (e) $Hf_{0.25}Zr_{0.75}NiSn_{0.99}Sb_{0.01}$ (f) $Ti_{0.75}Zr_{0.25}NiSn_{0.98}Sb_{0.02}$ . .... 233
Figure B.8	(a) X-ray diffraction patterns for $Nb_{0.75}Ti_{0.25}FeSb$ synthesized by arc-melting powders (AM), these same arc-melted powders refined through additional planetary ball milling (RAM), and elemental powders that were mechanically alloyed via HEPBM (MA). The top set of patterns are for the monoliths produced by consolidation of the three powder sets via spark plasma sintering (AM-SPS, RAM-SPS, and MA-SPS). Peaks of the ternary NbFeSb half-Heusler compound are indexed and impurity phases are indicated. (b) SEM of monolith of $Nb_{0.75}Ti_{0.25}FeSb$ produced with RAM powder as compared to (c) the SPS monolith produced from MA powder, with both monoliths having similar micron sized grains..... 234
Figure B.9	The thermoelectric performance (ZT) of synthesized half-Heuslers (indicated by symbol shape) made via arc-melting (AM, dashed lines), mechanical alloying (MA, solid lines), and ball mill refined arc-melting method (RAM, dotted lines) along with comparable reference data indicated with open symbols. .... 235
Figure B.10	The absolute Seebeck coefficient of both n- and p-types plotted for synthesized half-Heusler (indicated by symbol shape) made via arc-melting (AM, dashed lines), mechanical alloying (MA, solid lines), and ball mill refined arc-melting method (RAM, dotted lines) along with comparable reference data indicated with open symbols..... 236
Figure B.11	The thermal conductivity of synthesized half-Heuslers (indicated by symbol shape) made via arc-melting (AM, dashed lines), mechanical alloying (MA, solid lines), and ball mill refined arc-melting method (RAM, dotted lines) along with comparable reference data indicated with open symbols. .... 237
Figure B.12	The electrical conductivity of synthesized half-Heuslers (indicated by symbol shape) made via arc-melting (AM, dashed lines), mechanical alloying (MA, solid lines), and ball mill refined arc-melting method

(RAM, dotted lines) along with comparable reference data indicated with open symbols.....238

Figure B.13 The calculated power factor of synthesized half-Heuslers (indicated by symbol shape) made via arc-melting (AM, dashed lines), mechanical alloying (MA, solid lines), and ball mill refined arc-melting method (RAM, dotted lines) along with comparable reference data indicated with open symbols.....239

## LIST OF ABBREVIATIONS

2D	Two dimensional
3D	Three dimensional
$a$	Lattice parameter $a$
$\alpha$	Phase fraction
As	Arsenic
at%	Atomic percent
$b$	Lattice parameter $b$
Bi	Bismuth
BP	Black phosphorus
$c$	Lattice parameter $c$
°C	Degrees Celsius
CCD	Charge coupled device
cm	Centimeter
$\text{cm}^{-1}$	Wavenumber
Cmca	Orthorhombic space group No. 64
CVT	Chemical vapor transport
$R\bar{3}m$	Trigonal space group No. 166
DC	Delogu-Cocco
DAC	Diamond anvil cell
DFT	Density functional theory

EDS	Energy dispersive x-ray spectroscopy
$E_g$	Electronic band gap energy
$E_{opt}$	Optical bandgap energy
eV	Electron volt
FLBP	Few-layer black phosphorus
Ge	Germanium
GPa	Gigapascal
GSAS	General Structure Analysis System
hBN	Hexagonal boron nitride
hBP	Hexagonal boron phosphide
HEBM	High energy ball milling
HEPBM	High energy planetary ball milling
HP	High pressure
ICPMS	Inductively coupled plasma mass spectrometer
ICSD	Inorganic Crystal Structure Database
InGaAs	Indium gallium arsenide
IR	Infrared
J	Joule
JMAK	Johnson-Mehl-Avrami-Kolmogorov
K	Kelvin
$k$	Kinetics rate constant
kbar	Kilobar
kg	Kilogram

kJ	Kilojoule
kPa	Kilopascal
m	Meter
MA	Mechanical alloying
MIR	Middle infrared
mm	Millimeter
MPa	Megapascal
mW	Milliwatt
nm	Nanometer
NIR	Near infrared
<i>P</i>	Pressure
P-As	Phosphorus-Arsenic
PDF	Powder diffraction file
P-Ge	Phosphorus-Germanium
PL	Photoluminescence
PNMR	Phosphorus nuclear magnetic resonance spectroscopy
ppm	Parts per million
PSA	Particle size analysis
O	Oxygen
o-PAs	Orthorhombic phosphorus arsenic
RP	Red phosphorus
rpm	Revolutions per minute
S	Sulfur

SAED	Selected area electron diffraction
Sb	Antimony
Se	Selenium
SEM	Scanning electron microscopy
Si	Silicon
Si <sub>3</sub> N <sub>4</sub>	Silicon nitride
SiO <sub>2</sub>	Silicon dioxide
Sn	Tin
SPS	Spark plasma sintering
STEM	Scanning transmission electron microscopy
<i>T</i>	Temperature
<i>t</i>	Time
Te	Tellurium
TEM	Transmission electron microscopy
TMD	Transition metal dichalcogenide
t-PAs	Trigonal phosphorus arsenic
μm	Micrometer
<i>V</i>	Volume
WC	Tungsten carbide
WP	White phosphorus
wt%	Weight percent
XPS	X-ray photoelectron spectroscopy
XRD	X-ray diffraction



## CHAPTER ONE: INTRODUCTION

As modern society continues to create new digital content and increase the interconnectivity of devices, households and vehicles, the amount of data generated has increased dramatically. A clear example is the number of on-line streaming providers for music, television, movies, pod-casts, and audiobooks. Behind the scenes, the telecommunications industry has deployed fiber optics throughout communities connecting homes to datacenters that host all of the digital information. To keep pace with the growing demand, technoeconomic analysis by the industry has highlighted several bottlenecks that will inhibit future growth. Key components singled out are the opto-electronic devices that convert electrical signals into infrared light (such as a laser) and absorption of infrared light to generate signals (a photodetector). Current devices use group III-V compound semiconductors such as ternary indium gallium arsenide (InGaAs) alloys that are grown in separate foundries. Besides cost, a major limitation of InGaAs devices are their inability to be grown easily onto silicon – lattice mismatch with silicon complicates epitaxial growth and leads to interfacial strain that affects emission performance.<sup>1-3</sup> Instead, large InGaAs wafers are grown separately, diced into smaller chips, and glued onto silicon substrates to form the complete silicon photonic integrated device.<sup>2,3</sup> Research has been focused on finding alternative materials that can be scaled down to continue Moore's law for photonics.<sup>2,3</sup> A relatively new class of materials, known as two-dimensional (2D) layered crystals, may enable the desired nanoscale

structures while providing comparable or better opto-electronic performance that is compatible with the existing silicon ecosystem.<sup>1,2,4,5</sup>

Monolayer graphene was isolated in 2004 and resulted in a wave of research focused on exploring two-dimensional materials.<sup>6</sup> Research into quantum confinement effects grew rapidly in the following years in layered crystals such as MoS<sub>2</sub>,<sup>7,8</sup> Al<sub>2</sub>K<sub>2</sub>O<sub>6</sub>Si,<sup>9,10</sup> Bi<sub>2</sub>Te<sub>3</sub>,<sup>11,12</sup> and layered elemental metals such as tellurium,<sup>13</sup> tin,<sup>14</sup> germanium,<sup>15-23</sup> and arsenic.<sup>24-26</sup>

Other well-known 2D materials such as hexagonal boron nitride (hBN)<sup>27,28</sup> and MXenes<sup>29-32</sup> (isolated from MAX phases) were also reinvestigated at the atomic limit. A major benefit of 2D materials is their ability to scale devices to dimensions smaller than those typically achieved with silicon-based semiconductors while still being electrically, optically, and thermally functional, with performances as good or better than their bulk counterparts.<sup>2</sup> Black phosphorus, a layered crystal first synthesized in 1914 by high pressure techniques stands out amongst the 2D materials due to its layer dependent direct bandgap spanning (0.3-2.0 eV), good carrier mobility (~1000).<sup>33-35</sup> Many of the other 2D materials possess wider bandgaps suitable for visible and UV applications, but few have bandgaps that correspond to infrared wavelengths (<1eV), which can compete with the III-V direct bandgap semiconductors like InGaAs.<sup>36</sup> What makes BP so promising is that its bandgap stays direct from the monolayer to the bulk – most other 2D materials only have direct bandgaps at the monolayer but become indirect bandgaps with increasing layer numbers.<sup>37,38</sup> While monolayer BP emits red light, the other layers emit various near infrared light (~900 nm, 1300 nm, 1450 nm, 1550 nm, and so on up to about 4,100 nm, which corresponds to medium wavelength infrared.

Near infrared fiber optic telecommunications is based on the transmission of 1550 nm light, which just so happens to correspond to the bandgap of 5-layer black phosphorus.<sup>39</sup> Optically pumped emission has been demonstrated from an exfoliated BP flake transferred onto a silicon waveguide.<sup>39</sup> As BP is a van der Waal bonded material, it avoids the lattice mismatch problem. However, the challenge with black phosphorus, is that it is a high-pressure phase of elemental phosphorus – to date, there is no known method for growing BP directly onto silicon wafers that can produce uniform thin films. Either high pressure synthesis using diamond anvils<sup>33,34,40-42</sup> or chemical vapor transport with mineralizers<sup>43-47</sup> are required, but neither of these can produce thin films directly on silicon. An alternative approach is to produce BP separately using a bulk synthesis method, process it into an ink containing few-layer crystals, and deposit it directly onto silicon using an additive approach such as inkjet or aerosol printing.<sup>48-51</sup> While diamond anvils can produce BP single crystals, such a system is impractical for industrial production. Instead, another technique is needed that can produce the high pressure and temperature needed to convert red phosphorus into black phosphorus. Mechanochemistry is a process that uses grinding media (such as stainless steel or ceramic balls) sealed inside a rotating vessel to produce high pressure and high temperatures within powders trapped between collisions.<sup>52</sup> High energy ball mills have been used for decades to produce commodity grade materials.<sup>53-60</sup> It was therefore, the aim of this dissertation to investigate the mechanochemical synthesis of BP, and its chemical doping to produce an optically active material.

Initially, the work focused on understanding the ball mill conversion kinetics of red to black phosphorus, hitherto unknown, and is detailed in Chapter 2. The process

follows a nucleation and growth dominated mechanism whose rate is controlled by the collision energy and milling intensity. In order to facilitate the scale-up of BP synthesis via high energy planetary ball mill (HEPBM), the conversion rate as a function of impact energy (i.e., ball density and size) and the cumulative energy input per gram of product formed were determined. The rate was linearly dependent upon the impact energy and the milling dose near 100 kJ per gram was needed to convert RP into BP efficiently.

Exfoliation of the converted BP into few-layer suspensions enable measurement of the photoluminescence. Visible and infrared emissions were detected in drop-cast samples indicating the ball mill synthesis route provides optically viable BP suitable for silicon photonics.

While intrinsic BP can be optically pumped by a shorter wavelength laser to produce infrared emission, the main goal is an electrically pumped BP laser using a p-n junction between chemically doped BP.<sup>3</sup> To validate possible dopants in how they interact with the 2D lattice of phosphorus, a series of alloys using arsenic were produced via high energy ball milling; this work is described in Chapter 3. A similar conversion kinetics study was performed on the o-PAs 50 at% composition which showed a different mechanism involving two steps. First, within a few minutes of milling, the trigonal PAs structure forms followed by a much slower phase transformation to the orthorhombic structure. Exfoliated few-layer flakes of each composition also showed visible and infrared photoluminescence confirming theoretical predictions. This work provided a solid reference for how substitutional atoms affects the crystal structure, vibrational modes, binding energies, and photoluminescence.

Candidate dopants for BP beyond arsenic include germanium,<sup>61</sup> sulfur,<sup>62-64</sup> selenium,<sup>64-68</sup> and tellurium.<sup>64,67,69-71</sup> Milling results for germanium phosphides are presented in Chapter 4. While germanium may act as a dopant at low concentration (<1 at%), it produces two distinct layered crystals with phosphorus at higher concentrations. Namely, this work reports a solid solution trigonal alloy between 2-30 at% germanium and the synthesis of the monoclinic phase via ball milling. Both of these layered crystals, when isolated into monolayers, may find use in opto-electronics provided their indirect bandgaps can be transformed into direct bandgaps using strain or alloying.<sup>17,20,22,72,73</sup>

In the literature search to determine if sulfur, selenium, or tellurium would be good doping candidates for BP, a large knowledge gap for the synthesis of phosphorus compounds with sulfur, selenium, and tellurium was apparent. Commercially, phosphorous pentasulfide ( $P_2S_5$ ) is used as a component in automotive engine lubricants.<sup>74-76</sup> To the best of the author's knowledge, no report of its synthesis by ball milling exists. While these sulfides and selenides are not layered 2D crystals, it was important to determine the solubilities of sulfur and selenium into BP and if these other polymeric cage-like phases would appear as secondary phases. Therefore, milling trials spanning the phase diagram of both systems are reported in Chapter 5. Sulfur and selenium appear to substitute into BP at less than 10 at% whereas higher concentrations produced several of the sulfides and selenide crystalline and amorphous glasses. Tellurium was also included in this chapter as all three elements (S, Se, Te) are part of the chalcogenide group and should exhibit similar chemical reactivity. Furthermore, tellurium doping with single crystal BP was reported in the literature while one report of ball milling phosphorus with tellurium contradicted the lack of any known binary P-Te

compounds.<sup>70,71,77,78</sup> Hence, work in Chapter Five shows that tellurium is not a substitutional dopant in BP and that no binary compound with phosphorus could be produced by ball milling, at least within the limits of the milling time and energy used. Together, Chapters 3-5 indicated that mechanochemical doping of BP with arsenic, germanium, sulfur and selenium is feasible with future work to explore electrical measurements.

Finally, less comprehensive work on ball mill reactions of phosphorus with boron, tin, antimony, and bismuth are reported in the appendix. These results confirmed inability to form phosphorus antimonides while several of the known tin phosphides were successfully synthesized.<sup>79-81</sup> Independent of the black phosphorus work, a separate study on the ball mill synthesis of several intermetallic half-Heuslers for thermoelectric applications is also included in the Appendix. The half-Heusler work shows the versatility of ball milling to synthesize a wide range of intermetallic compounds and revealed nuances regarding challenges of milling a high temperature refractory metals, transition metals, and soft metalloids, in terms of particle size reduction, single phase synthesis, and milling media interactions. The thermoelectric performance of spark plasma sintered monoliths of  $\text{Nb}_{0.75}\text{Ti}_{0.25}\text{FeSb}$  ( $ZT = 0.72$  at  $600\text{ }^\circ\text{C}$ ) and  $\text{NbCoSn}_{0.9}\text{Sb}_{0.1}$  ( $ZT = 0.53$  at  $600\text{ }^\circ\text{C}$ ) show these are potentially promising thermoelectrics for intermediate service temperatures ( $300\text{-}725\text{ }^\circ\text{C}$ ).

Collectively, these chapters are unified by a central theme of mechanochemistry – use of mechanical energy to induce chemical reactions. Individually, each chapter highlights specific aspects of high energy ball mill synthesis and the diversity of materials that can be produced. Each chapter contains its own introduction that reviews

the motivation, material specific details, objective of each study, and discussion of the results achieved. Overall, the rapid straightforward synthesis of layered 2D crystalline powders of chemically doped black phosphorus, black phosphorus-arsenic alloys, and trigonal and monoclinic germanium phosphides may enable the widespread commercialization of 2D materials in opto-electronics.

### References

- 1 Chang, T.-Y. *et al.* Black Phosphorus Mid-Infrared Light-Emitting Diodes Integrated with Silicon Photonic Waveguides. *Nano Lett.* **20**, 6824-6830 (2020)
- 2 You, J. *et al.* Hybrid/Integrated Silicon Photonics Based on 2D Materials in Optical Communication Nanosystems. *Laser Photonics Rev* 2000239 (2020)
- 3 Zhou, Z., Yin, B. & Michel, J. On-chip light sources for silicon photonics. *Light Sci Appl* **4**, e358 (2015)
- 4 Peyskens, F., Chakraborty, C., Muneeb, M., Van Thourhout, D. & Englund, D. Integration of single photon emitters in 2D layered materials with a silicon nitride photonic chip. *Nat Commun* **10**, 4435 (2019)
- 5 Ren, T. & Loh, K. P. On-chip integrated photonic circuits based on two-dimensional materials and hexagonal boron nitride as the optical confinement layer. *J. Appl. Phys.* **125**, (2019)
- 6 Novoselov, K. S. *et al.* Electric Field Effect in Atomically Thin Carbon Films. *Science* **306**, 666-669 (2004)
- 7 Ye, Y. *et al.* Exciton-dominant electroluminescence from a diode of monolayer MoS<sub>2</sub>. *Appl. Phys. Lett.* **104**, 193508 (2014)
- 8 Lembke, D., Bertolazzi, S. & Kis, A. Single-Layer MoS<sub>2</sub> Electronics. *Acc. Chem. Res.* **48**, 100-110 (2015)
- 9 Kim, S. S. *et al.* Tunable Bandgap Narrowing Induced by Controlled Molecular Thickness in 2D Mica Nanosheets. *Chem. Mater.* **27**, 4222-4228 (2015)
- 10 He, Y. *et al.* Mica, a Potential Two-Dimensional-Crystal Gate Insulator for Organic Field-Effect Transistors. *Adv. Mater.* **23**, 5502-5507 (2011)
- 11 Liu, Y. *et al.* Epitaxial growth of ternary topological insulator Bi<sub>2</sub>Te<sub>2</sub>Se 2D crystals on mica. *Small Methods* **13**, 1603572 (2017)
- 12 Teweldebrhan, D., Goyal, V. & Balandin, A. A. Exfoliation and characterization of bismuth telluride atomic quintuples and quasi-two-dimensional crystals. *Nano Lett.* **10**, 1209-1218 (2010)
- 13 Du, Y. *et al.* One-Dimensional van der Waals Material Tellurium: Raman Spectroscopy under Strain and Magneto-Transport. *Nano Lett.* **17**, 3965-3973 (2017)
- 14 Saxena, S., Chaudhary, R. P. & Shukla, S. Stanene: Atomically Thick Free-standing Layer of 2D Hexagonal Tin. *Sci Rep* **6**, 31073 (2016)

- 15 Acun, A. *et al.* Germanene: the germanium analogue of graphene. *J. Phys.: Condens. Matter* **27**, 443002 (2015)
- 16 Li, W. *et al.* Layered phosphorus-like GeP<sub>5</sub>: a promising anode candidate with high initial coulombic efficiency and large capacity for lithium ion batteries. *Energy Environ. Sci.* **8**, 3629-3636 (2015)
- 17 Jing, Y., Ma, Y., Li, Y. & Heine, T. GeP<sub>3</sub>: A Small Indirect Band Gap 2D Crystal with High Carrier Mobility and Strong Interlayer Quantum Confinement. *Nano Lett.* **17**, 1833-1838 (2017)
- 18 Li, L. *et al.* 2D GeP: An Unexploited Low-Symmetry Semiconductor with Strong In-Plane Anisotropy. *Adv. Mater.* **30**, 1706771 (2018)
- 19 Li, C. *et al.* Facile liquid-phase exfoliated few-layer GeP nanosheets and their optoelectronic device applications. *J. Mater. Chem. C* **8**, 5547-5553 (2020)
- 20 Wang, Z. *et al.* 2D GeP-based photonic device for near-infrared and mid-infrared ultrafast photonics. *Nanophotonics* **9**, 3645-3654 (2020)
- 21 Yu, T. *et al.* Two-Dimensional GeP-Based Broad-Band Optical Switches and Photodetectors. *Adv. Optical Mater.* **8**, 1901490 (2020)
- 22 Dushaq, G. & Rasras, M. Multilayer 2D germanium phosphide (GeP) infrared phototransistor. *Opt. Express* **29**, 9419-9428 (2021)
- 23 Zhao, S. *et al.* Flux Method Growth of Large Size Group IV–V 2D GeP Single Crystals and Photoresponse Application. *Crystals* **11**, 235 (2021)
- 24 Zhang, S., Yan, Z., Li, Y., Chen, Z. & Zeng, H. Atomically Thin Arsenene and Antimonene: Semimetal–Semiconductor and Indirect–Direct Band-Gap Transitions. *Angew. Chem. Int. Ed* **54**, 3112-3115 (2015)
- 25 Zhang, Z. *et al.* Manifestation of unexpected semiconducting properties in few-layer orthorhombic arsenene. *Appl. Phys. Express* **8**, 055201 (2015)
- 26 Pumera, M. & Sofer, Z. 2D Monoelemental Arsenene, Antimonene, and Bismuthene: Beyond Black Phosphorus. *Adv. Mater.* **29**, 1605299 (2017)
- 27 Park, H. J. *et al.* One-dimensional hexagonal boron nitride conducting channel. *Sci. Adv.* **6**, eaay4958 (2020)
- 28 Watanabe, K., Taniguchi, T. & Kanda, H. Direct-bandgap properties and evidence for ultraviolet lasing of hexagonal boron nitride single crystal. *Nat. Mater.* **3**, 404-409 (2004)
- 29 Anasori, B. *et al.* Two-Dimensional, Ordered, Double Transition Metals Carbides (MXenes). *ASC Nano* **9**, 9507-9516 (2015)
- 30 Jhon, Y. I. *et al.* Metallic MXene Saturable Absorber for Femtosecond Mode-Locked Lasers. *Adv. Mater.* **29**, (2017)
- 31 Verger, L., Natu, V., Carey, M. & Barsoum, M. W. MXenes: An Introduction of Their Synthesis, Select Properties, and Applications. *Trends Chem.* (2019)
- 32 Verger, L. *et al.* Overview of the synthesis of MXenes and other ultrathin 2D transition metal carbides and nitrides. *Curr. Opin. Solid State Mater. Sci.* (2019)
- 33 Bridgman, P. W. Two new modifications of phosphorus. *J. Am. Chem. Soc.* **36**, 1344-1363 (1914)
- 34 Bridgman, P. W. Effects of High Shearing Stress Combined with High Hydrostatic Pressure. *Phys Rev* **48**, 825-847 (1935)
- 35 Liu, H. *et al.* Phosphorene: An Unexplored 2D Semiconductor with a High Hole Mobility. *ASC Nano* **8**, 4033-4041 (2014)

- 36 Castellanos-Gomez, A. Why all the fuss about 2D semiconductors? *Nature Photon* **10**, 202-204 (2016)
- 37 Du, Y., Ouyang, C., Shi, S. & Lei, M. Ab initio studies on atomic and electronic structures of black phosphorus. *J. Appl. Phys* **107**, 093718 (2010)
- 38 Tran, V., Soklaski, R., Liang, Y. & Yang, L. Layer-controlled band gap and anisotropic excitons in few-layer black phosphorus. *Phys Rev B* **89**, 235319 (2014)
- 39 Husko, C. *et al.* Silicon-Phosphorene Nanocavity-Enhanced Optical Emission at Telecommunications Wavelengths. *Nano Lett.* **18**, 6515-6520 (2018)
- 40 Bridgman, P. W. Further Note on Black Phosphorus. *J. Am. Chem. Soc* **38**, 609-612 (1916)
- 41 Jacobs, R. B. Phosphorus at High Temperatures and Pressures. *J. Chem. Phys.* **5**, 945-953 (1937)
- 42 Rissi, E. N., Soignard, E., McKiernan, K. A., Benmore, C. J. & Yarger, J. L. Pressure-induced crystallization of amorphous red phosphorus. *Solid State Comm.* **152**, 390-394 (2012)
- 43 Lange, S., Schmidt, P. & Nilges, T. Au<sub>3</sub>SnP<sub>7</sub>@Black Phosphorus: An Easy Access to Black Phosphorus. *Inorg. Chem.* **46**, 4028-4035 (2007)
- 44 Nilges, T., Kersting, M. & Pfeifer, T. A fast low-pressure transport route to large black phosphorus single crystals. *J. Solid State Chem.* **181**, 1707-1711 (2008)
- 45 Osters, O. *et al.* Synthesis and Identification of Metastable Compounds: Black Arsenic—Science or Fiction? *Angew. Chem. Int. Ed* **51**, 2994-2997 (2012)
- 46 Köpf, M. *et al.* Access and in situ growth of phosphorene-precursor black phosphorus. *J. Cryst. Growth* **405**, 6-10 (2014)
- 47 Liu, B. *et al.* Black Arsenic–Phosphorus: Layered Anisotropic Infrared Semiconductors with Highly Tunable Compositions and Properties. *Adv. Mater.* **27**, 4423-4429 (2015)
- 48 Wood, J. D. *et al.* Effective Passivation of Exfoliated Black Phosphorus Transistors against Ambient Degradation. *Nano Lett.* **14**, 6964-6970 (2014)
- 49 Kang, J. *et al.* Solvent Exfoliation of Electronic-Grade, Two-Dimensional Black Phosphorus. *ACS Nano* **9**, 3596-3604 (2015)
- 50 Kang, J. *et al.* Stable aqueous dispersions of optically and electronically active phosphorene. *Proc. Natl. Acad. Sci.* **113**, 11688-11693 (2016)
- 51 Hu, G. *et al.* Functional inks and printing of two-dimensional materials. *Chem. Soc. Rev.* **47**, 3265-3300 (2018)
- 52 Suryanarayana, C. Mechanical alloying and milling. *Prog. Mater. Sci.* **46**, 1-184 (2001)
- 53 Sridhar, C. S., Sankar, P. S. & Prasad, R. K. Grinding kinetics, modeling, and subsieve morphology of ball mill grinding for cement industry ingredients. *Part. Sci. Technol* **34**, 1-8 (2015)
- 54 Deniz, V. A study on the specific rate of breakage of cement materials in a laboratory ball mill. *Cem. Concr. Res* **33**, 439-445 (2003)
- 55 Ghalandari, V. & Iranmanesh, A. Energy and exergy analyses for a cement ball mill of a new generation cement plant and optimizing grinding process: A case study. *Adv. Powder Technol.* **31**, 1796-1810 (2020)

- 56 Austin, L. G. & Bagga, P. An analysis of fine dry grinding in ball mills. *Powder Tech.* **28**, 83-90 (1981)
- 57 Klimpel, R. R. & Austin, L. G. Chemical additives for wet grinding of minerals. *Powder Tech.* **31**, 239-253 (1982)
- 58 Nava, J. V., Llorens, T. & Menéndez-Aguado, J. M. Kinetics of Dry-Batch Grinding in a Laboratory-Scale Ball Mill of Sn-Ta-Nb Minerals from the Penouta Mine (Spain). *Metals* **10**, 1687 (2020)
- 59 Greet, C. J., Small, G. L., Steinier, P. & Grano, S. R. The Magotteaux Mill®: investigating the effect of grinding media on pulp chemistry and flotation performance. *Miner. Eng.* **17**, 891-896 (2004)
- 60 Piras, C. C., Fernández-Prieto, S. & De Borggraeve, W. M. Ball milling: a green technology for the preparation and functionalisation of nanocellulose derivatives. *Nanoscale Adv.* **1**, 937-947 (2019)
- 61 Maruyama, Y., Inabe, T., He, L. & Oshima, K. Electrical conductivity of black phosphorous-germanium compound. *Synth. Met.* **43**, 4067-4070 (1991)
- 62 Chang, Y. *et al.* Liquid-exfoliation of S-doped black phosphorus nanosheets for enhanced oxygen evolution catalysis. *Nanotechnol.* **30**, 035701 (2018)
- 63 Lv, W. *et al.* Sulfur-Doped Black Phosphorus Field-Effect Transistors with Enhanced Stability. *ACS Appl. Mater. Interfaces* **10**, 9663-9668 (2018)
- 64 Antonatos, N. *et al.* In Situ Doping of Black Phosphorus by High-Pressure Synthesis. *Inorg. Chem.* (2019)
- 65 Ge, Y. *et al.* Few-layer selenium-doped black phosphorus: synthesis, nonlinear optical properties and ultrafast photonics applications. *J. Mater. Chem. C* **5**, 6129-6135 (2017)
- 66 Xu, Y. *et al.* Selenium-Doped Black Phosphorus for High-Responsivity 2D Photodetectors. *Small* **12**, 5000-5007 (2016)
- 67 Liu, M. *et al.* High yield growth and doping of black phosphorus with tunable electronic properties. *Mater. Today* **36**, 91-101 (2020)
- 68 Li, M. *et al.* Revealing Dopant Local Structure of Se-Doped Black Phosphorus. *Chem. Mater.* (2021)
- 69 Yang, B. *et al.* Te-Doped Black Phosphorus Field-Effect Transistors. *Adv. Mater.* **28**, 9408-9415 (2016)
- 70 Zhang, Z., Khurram, M., Sun, Z. & Yan, Q. Uniform Tellurium Doping in Black Phosphorus Single Crystals by Chemical Vapor Transport. *Inorg. Chem.* **57**, 4098-4103 (2018)
- 71 Yu, Y. *et al.* N-type doping of black phosphorus single crystal by tellurium. *Nanotechnol.* **31**, 315605 (2020)
- 72 Cheng, A.-Q., He, Z., Zhao, J., Zeng, H. & Chen, R.-S. Monolayered Silicon and Germanium Monopnictide Semiconductors: Excellent Stability, High Absorbance, and Strain Engineering of Electronic Properties. *ACS Appl. Mater. Interfaces* **10**, 5133-5139 (2018)
- 73 Kim, D. *et al.* Thickness-dependent bandgap and electrical properties of GeP nanosheets. *J. Mater. Chem. A* **7**, 16526-16532 (2019)
- 74 Spikes, H. The History and Mechanisms of ZDDP. *Tribol. Lett.* **17**, 469-489 (2004)

- 75 Ozturk, T., Ertas, E. & Mert, O. A Berzelius Reagent, Phosphorus Decasulfide (P<sub>4</sub>S<sub>10</sub>), in Organic Syntheses. *Chem. Rev.* **110**, 3419-3478 (2010)
- 76 Johnson, D. W. & Hils, J. E. Phosphate Esters, Thiophosphate Esters and Metal Thiophosphates as Lubricant Additives. *Lubricants* **1**, 132-148 (2013)
- 77 Itoh, K., Mizuhara, Y. & Otomo, T. Mechanochemical synthesis of binary phosphorus telluride: Short range structure and thermal properties. *J. Solid State Chem.* **267**, 119-123 (2018)
- 78 Okamoto, H. P-Te (Phosphorus-Tellurium). *J. Ph. Equilibria Diffus.* **31**, 405-406 (2010)
- 79 Okamoto, H. P-Sb (Phosphorus-Antimony). *J. Ph. Equilibria Diffus.* **30**, 303-304 (2009)
- 80 Okamoto, H. P-Sn (phosphorus-tin). *J. Ph. Equilibria Diffus.* **14**, 263-264 (1993)
- 81 Donohue, P. C. Synthesis, structure, and superconducting properties of new high-pressure forms of tin phosphide. *Inorg. Chem.* **9**, 335-337 (1970)

CHAPTER TWO: MECHANOCHEMICAL CONVERSION KINETICS OF RED TO  
BLACK PHOSPHORUS AND SCALING PARAMETERS FOR HIGH VOLUME  
SYNTHESIS

This chapter is published by Springer Nature in *NPJ 2D Materials and Applications* and should be referenced appropriately.

Reference:

S. V. Pedersen, F. Muramutsa, J. D. Wood, C. Husko, D. Estrada, B. J. Jaques,  
“Mechanochemical conversion kinetics of red to black phosphorus and scaling  
parameters for high volume synthesis.” *NPJ 2D Materials and Applications*. **4** (1) 36  
(2020)

Reproduced/modified by permission of Springer Nature.

\*This chapter includes formatting modifications from the originally published version.

Mechanochemical conversion kinetics of red to black phosphorus and scaling parameters  
for high volume synthesis

Samuel V. Pedersen<sup>1,2</sup>

Florent Muramutsa<sup>1</sup>

Joshua D. Wood<sup>3</sup>

Chad Husko<sup>4</sup>

David Estrada<sup>1,2,5</sup>

Brian J. Jaques<sup>1,2</sup>

Published in:

NPJ 2D Materials and Applications

October 2020

<sup>1</sup>Micron School of Materials Science and Engineering, Boise State University,

Boise, ID 83725, USA

<sup>2</sup>Center for Advanced Energy Studies, Idaho Falls, ID 83401, USA

<sup>3</sup>Promethean Consulting, LLC, Oak Park, IL 60302, USA

<sup>4</sup>Iris Light Technologies, Inc., Chicago, IL 60622, USA.

<sup>5</sup>Idaho National Laboratory, Idaho Falls, ID 83402, USA

## Abstract

Adopting black phosphorus (BP) as a material in electronic and optoelectronic device manufacturing requires the development and understanding of a large-scale synthesis technique. To that end, high-energy planetary ball milling is demonstrated as a scalable synthesis route and the mechanisms and conversion kinetics of the BP phase transformation are investigated. During the milling process, media collisions rapidly compress amorphous red phosphorus (RP) into crystalline, orthorhombic BP flakes, resulting in a conversion yield of  $\approx 90\%$  for about 5 g of bulk BP powder. Milling conversion kinetics, monitored via ex situ x-ray diffraction, manifest a sigmoidal behavior best described by the Avrami rate model with each impact of sufficient energy ( $>25$  mJ) producing BP nuclei; the process appears to be limited by grain growth. Using a kinematic model for ball trajectories and impact energies, the optimum milling condition is determined to be an impact energy near  $\approx 25$  mJ and a milling dose near  $\approx 100$  kJ/gram. Photoexcitation of exfoliated BP flakes reveals emission in the near-infrared, indicating the formation of few-layer BP, a promising advance for optoelectronic device applications.

## 2.1 Introduction

The surge of research into two-dimensional materials after the discovery of graphene in 2004 has led to the investigating the monolayer limit of layered materials that include transition metal dichalcogenides (TMD), hexagonal boron nitride (hBN), MXenes, layered elemental metals (Te, Sn, Ge, As, Se),<sup>1</sup> black phosphorus (BP), and beyond. Orthorhombic BP, the high pressure and temperature phase of elemental phosphorus, consists of a puckered hexagonal sheet of covalently bonded atoms. In bulk

form, the individual sheets are bound together by van der Waal forces; however, new properties emerge due to quantum size effects when exfoliated into the few-layer regime. A property of note is BP's direct bandgap, which changes from 0.3 eV in the bulk to  $\approx 1.7$  eV in the monolayer limit.<sup>2,3</sup> Additionally, BP shows promise in optoelectronic device applications<sup>4-6</sup> from its direct bandgap where BP emissions are between 700 to  $>4000$  nm, which is the near- to mid-infrared wavelength range.

Nevertheless, a standing challenge for BP is its synthesis. Traditionally, generating BP necessitates either high pressure and elevated temperature as in the diamond anvil method first pioneered by Bridgman<sup>7</sup> to phase transform either white or red phosphorus (RP), or the use of a low-pressure mineralizer assisted chemical vapor transport (CVT).<sup>8</sup> While CVT is the established commercial production process, it suffers from high cost and low volume. In the CVT method, RP, tin iodine, and tin are sealed inside a glass ampule that is evacuated to 10<sup>-3</sup> torr, heated above 825 K, and allowed to cool slowly yielding BP crystals over a 1-3 day period that grow outward from an intermediate Sn-P-I compound.<sup>9</sup>

Alternatively, high-energy planetary ball milling (HEPBM) constrains the pressure induced phase transformation inside a steel vessel under an inert atmosphere, alleviating potential safety hazards associated with the CVT method due to over-pressurization of the glass ampules or incorrect cooling rates. Additionally, no expensive and toxic mineralizers (i.e., tin, iodine) are required. In order to facilitate the scale-up of BP synthesis via HEPBM, details such as the conversion rate as a function of impact energy (i.e., ball density and size) and the cumulative energy input per gram of product formed are required. Several reports<sup>10-13</sup> of HEPBM on BP synthesis have explored the

processing effects on synthesis time such as ball to powder mass ratio and rotation speed of the milling vessel but have not reported the scaling parameters. HEPBM is readily transferred to industrial mills capable of kilogram production capacities, provided that the energetics and kinetics of the phase transformation are well understood.

This study determines the necessary impact energy, the apparent rate constants, and the specific milling dose of the RP to BP phase transformation via HEPBM. By using closed-form analytical models of the kinematic motion inside the mill<sup>14</sup> along with estimates for the phase fraction evolution, an empirical relationship is established showing that higher impact energies leads directly to higher conversion rates while the total energy dose is shown to be an independent constant. Furthermore, the low cost nano-crystalline BP upon exfoliation is shown to be suitable for infrared opto-electronic applications paving the way for commercial scale-up opportunities.

## 2.2 Results

### 2.2.1 Black Phosphorus Characterization

Visually, the powder changes color from a burnt umber red to a dull black with various shades of red/brown/black with increasing BP content, as shown in **Figure 2.1(a)**. The bulk red and black powders exhibit similar morphology and agglomerations. The X-ray diffraction (XRD) patterns for the conversion of micron sized amorphous RP powder into orthorhombic BP are shown in **Figure 2.1(b)** as a function of milling duration at the highest experimental milling intensity evaluated in this study. The as-received RP exhibits three broad peaks, with the first defined diffraction peak at approximately  $17^\circ 2\theta$ . The powder diffraction file (PDF 03-065-2491) from the Inorganic

Crystal Structures Database (ICSD<sup>15</sup>) for BP is also shown, with relative peak intensities and positions indicated with the vertical line markers. A gradual shift to higher angles of the first sharp diffraction peak of RP occurs. By contrast, the broader high angle peaks generally decrease in intensity and width as the crystalline BP peaks emerge. XRD scans versus milling rpm using an internal silicon standard and the associated calibration curve are included in **Figure 2.2**, **Figure 2.3**, **Figure 2.4**, **Figure 2.5**, and **Figure 2.6**.

The scanning electron microscope (SEM) images of **Figure 2.7(a)** show that the RP starting powder exhibits an irregular faceted morphology with particles sizes from approximately 0.1-100  $\mu\text{m}$ . The converted BP exhibits similar faceted morphology but has a smaller particle size distribution below 10  $\mu\text{m}$ ; the powders appear to consist of soft aggregates of BP crystals embedded into amorphous particles which break down into flakes consisting of crystalline domains surrounded by amorphous matrix under mild ultrasonication. To further verify the crystalline BP domains within the amorphous flakes, transmission electron microscopy (TEM) images and selected area electron diffraction (SAED) patterns are taken and presented in **Figure 2.7(b)**, revealing the presence of crystalline BP domains embedded within the amorphous flakes and agglomerated powders. The volumetric particle size distributions obtained from solution-based laser diffraction particle size analysis (PSA) shown in **Figure 2.8(a)** shows non-uniform size distribution for RP. This is an expected result considering the large variation in particle sizes observed in the SEM images (see **Figure 2.7**) and the high sensitivity of volumetric PSA for detection of few but large particles. By contrast, the milling comminution process results in a nearly single mode distribution of the converted BP

material, while exfoliation breaks up soft BP aggregates and produces flakes consisting of embedded crystal domains within an amorphous matrix.

To complement the XRD and TEM results on the converted material and verify the crystallinity of the exfoliated BP, Raman spectra are collected on the as-received RP, synthesized BP powder, and exfoliated BP flakes as shown in **Figure 2.8**. The expected BP vibrational modes<sup>3</sup>  $A_g^1$ ,  $B_{2g}$ , and  $A_g^2$ , respectively, are clearly resolved, while the peak at  $520\text{ cm}^{-1}$  is from the silicon substrate. The slightly raised background between  $350\text{-}475\text{ cm}^{-1}$  is likely attributed to residual RP.<sup>11</sup>

As aforementioned, the direct bandgap of BP that spans  $0.3\text{-}1.7\text{ eV}$  makes BP suitable for near-infrared wavelength applications. Few-layer (ca. 5 layers) BP exhibits optically pumped emission<sup>2,5,16</sup> near  $\approx 1575\text{ nm}$ , whereas tri- and bi-layer BP emit at shorter wavelengths. The photoluminescence (PL) spectra for ball mill converted BP after exfoliation is shown in **Figure 2.8**. The broad emission from  $950\text{-}1600\text{ nm}$  indicates the flakes contain bi-layer, tri-layer, and multi-layer BP crystalline domains; however, further efforts to fully separate the various domains by lateral size or layer thickness by such means as density gradient centrifugation must be demonstrated prior to use in photonic applications.<sup>2,16,17</sup>

### 2.2.2 Conversion Kinetics

Detailed individual reaction steps during mechanical milling processes are challenging to elucidate, although recent progress with synchrotron X-ray and Raman spectroscopy is now capable of providing in situ monitoring of reaction steps.<sup>18</sup>

Nevertheless, empirical models based on ex situ measurements can provide general

insight into the overall kinetics behavior, such as determining if the process accelerates to completion, undergoes deceleration, or progresses at a constant rate.<sup>19-21</sup> For evaluating the kinetics of a process, typically through a series of experiments, the energy input (such as a constant temperature or constant heating rate) are varied systematically and the evolution of the phase fraction,  $\alpha$ , as a function of time is used to extract the rate constant,  $k$ .<sup>19,22</sup>

In mechanochemistry, the two kinetic models often used for solid state phase transformations are the classical Johnson-Mehl-Avrami-Kolmogorov (JMAK),<sup>23-25</sup> and a deterministic collision driven model derived by Delogu and Cocco (DC).<sup>20,26,27</sup> Both models have been used to obtain the rate constants for single-phase systems undergoing transformations or amorphization and have been applied to multiphase systems undergoing mechanical alloying.<sup>23-25</sup> After obtaining the apparent rate constants as a function of milling parameters, the relationship between the milling impact energy,  $E_b$ , and the rate constants can be determined. If a single impact is sufficient to drive the conversion to completion, then a linear dependence of the rate constants and the impact energies is expected.<sup>28</sup>

Simulations and in situ monitoring<sup>27,29-36</sup> of media interactions in high-energy ball mills have shown agreement with the underlying assumptions and estimated impact energies obtained through kinematic models of high-energy planetary ball mills. While existing models differ in determining the media velocity at impact,<sup>14,30,31,34,37</sup> all models assume the kinetic energy imparted to the media through collisions with the vial walls is transferred into the powder during impact, at least to a first order approximation (some losses due to friction, heat generation, and inelasticity are expected). Nonetheless, the

impact energy,  $E_b$ , is simply related to the media mass,  $m_b$ , and the impact velocity,  $v_{in}$ , as in:

$$E_b = \frac{1}{2} m_b v_{in}^2 \quad (1)$$

By extension, the cumulative dose,  $E_{dose}$ , is a function of the number of balls,  $N_b$ , the collision frequency,  $f_b$ , the milling time,  $t$ , and powder mass,  $m_p$ , as:

$$E_{dose} = \frac{E_b f_b N_b t}{m_p} \quad (2)$$

Using the conversion data obtained from XRD, the method described by Galwey *et al.*, was employed to generate a master plot to determine which subset of solid-state reaction models are applicable, as shown in **Figure 2.9** and **Table 2.1**.<sup>19</sup> The JMAK model closely matches the dataset, while the DC model follows the data above 30% conversion. As seen in **Figure 2.10(a)** for 300 rpm, the rate of conversion slows down, and this transition is visually distinct for the 300 rpm run versus the higher intensities of 400 – 600 rpm. Similarly, for 200 rpm, the conversion occurs slowly with an induction time of nearly 100 hours before BP is observed. Transforming the data using the JMAK model, **Figure 2.10(b)**, or the DC model, **Figure 2.10(c)**, shows two or three linear segments. In practice, line segments that show different slopes are treated individually with linear regression lines, as it has been shown that these distinct transitions are often due to changes in growth dimensionality.<sup>38</sup>

As a reminder, the DC model is, mathematically, a restricted form of the JMAK model that fixes the exponent  $n = 1$ , resulting in an apparent S-shape about the linear regression line in the DC linearization plot. Functionally, this restriction prevents making inferences about the nucleation and growth behavior afforded by the JMAK model, but as

shown in **Figure 2.10(d)** the extracted rate constants are still comparable. In all cases, both the JMAK and DC models appear to be valid, and the linear fits model the data up to 90% conversion well with values for the coefficient of determination (a goodness of fit statistic relating the percentage of the predicted response variation that is modeled by the regression line),  $R^2$ , above >95%. Deviations<sup>19</sup> from the model are likely due to the initial estimation of the phase fraction below 10 wt% and above 70 wt%. In these regions, there appears to be a consistent decrease in conversion rate for all milling intensities, implying a mechanistic change that requires higher mechanical impact energy to progress the conversion. **Figure 2.11** (plotted on a log scale) includes the 200 rpm curve; the 200 rpm dataset is not shown in **Figure 2.10(c)**, as the induction time obscures the higher rpm behaviors. **Figure 2.10(d)** shows the linear dependence of the apparent rate constants as a function of the calculated impact energy. The calculated impact energies and milling intensities using the kinematic model as applied to the HEPBM and the ascertained kinetic parameters for both the JMAK and DC models are presented in the **Table 2.2** and **Table 2.3**, respectively.

**Figure 2.12** shows the phase fraction evolution as a function of the total energy imparted to the powder on a mass basis, revealing three distinct behaviors. First, for higher milling intensities (i.e., mechanical work performed) above 300 rpm, the total dose required for complete conversion is the same. Second, below 300 rpm, there is a transition at low phase fractions (about 30 wt%) requiring progressively longer milling times, as well as a plateau near 75 wt%. This plateau indicates a potentially limiting step which cannot be overcome by the impact energy at 300 rpm. Third and finally, at even

lower energy (i.e., 200 rpm), nucleation of BP is evident, but only after a long induction time of 200+ hours.

### 2.3 Discussion

The reduction in particle size of RP as it converts to BP due to comminution is typical of ball milling and is desirable as it increases the surface area available for reactions and promotes a single mode particle size distribution which benefits downstream processes such as exfoliation. The broad BP XRD peaks in **Figure 2.1** indicate a high degree of nano-crystallinity while the broad base of the peak at  $17^\circ 2\theta$  indicates some amorphous material is still present. **Figure 2.13** and **Figure 2.14** show TEM images of randomly orientated lattice planes surrounded by an amorphous matrix within a single exfoliated flake, indicative of the nature of point impacts that have occurred and that presumably each impact will produce a local formation of BP within the bulk RP particle.<sup>10,12</sup> Amorphous RP possesses some degree of short and medium range order; it has been described as being a 3, 4, and 5 sided cage-like structures linked together by phosphorus atoms in a polymer like manner.<sup>39,40</sup> Presumably, the phosphorus cages are collapsed into the buckled planes due to the high localized compressive forces from the media collisions.<sup>39,41,42</sup> The Raman spectra in **Figure 2.8(b)** on HEPBM synthesized powder (exfoliated in IPA) shows only modes that correspond to BP, which indicates no significant RP is present. Together with the TEM data, the lack of features corresponding to RP indicates that amorphous BP is likely present.<sup>43-46</sup> High pressure conversion of RP thin films into BP has also reported the formation of amorphous BP.<sup>44</sup> High-energy ball milling has been used to produce amorphous metals and even cycle between crystalline

and amorphous phases of alloys by controlling the milling intensity and duration.<sup>47</sup> In light of this, the coexistence of both crystalline and amorphous, highly disordered, BP within ball mill synthesized BP flakes is unsurprising and has been observed through nuclear magnetic resonance spectroscopy.<sup>11</sup>

While some fraction of BP is present in the XRD patterns at 200 and 300 rpm, such conversion rates are economically impractical due to the power consumption; namely, mill motors constitute the highest recurring electrical costs. The 200 rpm milling intensity shows an entirely different behavior which may be due to the tendency of media to slide along the walls of the vessel with few high-energy collisions at low vial rotation speeds. As a result of the less energetic impacts and low frequency of collision, a significantly higher milling dose is required to producing meaningful quantities of BP at 200 rpm.

From **Figure 2.10(d)**, the  $x$ -axis intercept for a negligible rate constant,  $k = 0$ , ideally indicates a minimum impact energy,  $E_b$ , near 0.5 mJ, but these values do not reflect the apparent change above 70 wt%. As such, this minimum value most likely represents energy required to form stable nuclei but with no practical grain growth. The utility of **Figure 2.10(d)** is that extrapolation of an expected rate constant due to *higher* impact energies is feasible, up to a limit set by the media size, density, vessel diameter and achievable rpm.

The main scaling parameter for HEPBM is obtained from **Figure 2.12** and this dictates the optimum milling condition. The product of the milling intensity,  $E_b \cdot f_b \cdot N_b$ , and time,  $t$ , is the same for milling at 600, 500, and 400 rpm. That is, above a certain impact energy ( $E_b=25$  mJ), the conversion takes the same total energy input. The trade-off then

is the milling time versus potential media wear and design considerations for the mill motor. An apparent specific milling dose of approximately 100 kJ/gram is required to achieve a BP conversion above 90 wt%. While a higher milling dose may improve the yield, it may also introduce more defects into the crystalline domains, as well as produce more media wear and possible contaminations from the milling vessel and media.

The results presented here show that the conversion of RP to BP follows the characteristic S-shape of sigmoidal processes indicative of nucleation and growth dominated phase transformation. The rate constants obtained by applying the JMAK and DC models in **Figure 2.10** show the expected linear behavior as a function of milling intensity; accordingly, higher impact energies and higher collision frequency should result in more frequent nucleation events and, hence, a faster conversion rate. One benefit of the DC model is that it is less sensitive to induction periods than the JMAK model, such that the extracted rate constants better represent the overall conversion rate. However, the JMAK model allows for inferences into the nucleation and growth behavior.

Using the JMAK model, the values of the exponent can potentially provide insight into the dynamics of nucleation and crystal growth. The calculated exponent value is  $n \approx 2.3 - 2.5$ , suggesting that RP to BP undergoes continuous nucleation and subsequent interfaced controlled transformation in two-dimensions.<sup>48,49</sup> The reduced exponent value below 3 can be attributed to the anisotropic growth and blocking effects, or it could be an outcome of a mixture of 3D and 2D growth with site saturation.<sup>48-51</sup> In theory, polymorphic phase transformations are categorized as either displacive (rapid and diffusion-less) or reconstructive (slow and diffusion limited).<sup>52-54</sup> In practice, assumptions

regarding diffusion, preferred nucleation sites such as defects, grain boundaries, or dislocations, and experimentally determined crystal growth habit (i.e., spherical, disc, or rod growth) are required to make reliable inferences from the JMAK exponent.

However, the unique amorphous to crystalline transformation of RP to BP does not fit cleanly into any phase transformation category.<sup>53</sup> We argue that RP to BP is likely a rapid diffusionless, displacive transformation, provided that RP bonds are broken either through thermal or strain input. Generally, high applied pressure inhibits diffusion due to the increase in repulsive forces upon shortening the interatomic bond distance<sup>52</sup> but can enable rapid short displacements via re-orientation.<sup>52</sup> By contrast, grain growth itself is typically a thermally driven process. High pressure studies on the white phosphorus (1.2 GPa) or RP (8 GPa) to BP transition occurred almost instantly after an incubation time of 10–15 minutes when exceeding a minimum temperature of 200 °C.<sup>7,41,43,55-58</sup> This supports the notion of rapid interface propagation instead of a time-dependent diffusion-controlled grain growth. Comparing our mechanochemical results to Xiang *et al.*<sup>44</sup> and to those obtained by Bridgman<sup>59</sup> using rotating diamond anvils ( $\approx 4$  GPa), we contend that the plastic strain facilitated by the direct compression of RP between colliding media breaks molecular bonds within the RP polymer chains, leading to the rapid formation of the orthorhombic crystalline phase. The TEM results here of flakes show clear nanometer-sized lattice domains randomly orientated surrounded by regions of an amorphous matrix, consistent with random nucleation but limited grain growth. Similar behavior was observed with static anvil experiments at a higher pressure ( $\approx 6.8$  GPa) but a much lower temperature ( $\approx 25$  °C) than typical synthesis conditions. Xiang *et al.*<sup>44</sup> revealed a slow transformation rate of tens of hours in which the rhombohedral (A7)

structure of metallic BP nucleates first from RP and persists indefinitely (up to 71 hours). However, the material rapidly converts to orthorhombic BP upon decompression.<sup>44</sup> Collisions in HEPBM are effectively microforges where the RP is entrapped between the media in a millisecond timescale collision. Upon the media rebounding, the BP crystallizes.<sup>47</sup>

In support of our hypothesis, the fact that the rhombohedral crystal structure of BP forms primarily under the applied hydrostatic pressure without external heating indicates the possibility of bulk nucleation of a two-dimensional highly disordered intermediate.<sup>41</sup> Nonetheless, the absence of heat input or strain will produce sluggish nucleation, as evidenced by the in situ time-resolved Raman spectra of Xiang *et al.*<sup>44</sup> Their high-resolution TEM data on quenched samples held under static loading for ~36 hours revealed numerous nano-crystalline domains of orthorhombic BP surrounded by amorphous phosphorus, similar to the TEM results here obtained on mechanochemically synthesized BP. **Figure 2.15** shows the in situ temperature measurements obtained during mechanochemical conversion; while the global temperature does not exceed 40 °C, it is possible that the local impact energy could heat the powder substantially.<sup>60-63</sup> Still, the temperature rise is also highly dependent upon the material undergoing the treatment (i.e., if the process results in an exothermic heat release such as in the milling of thermite, metal oxide formation, or sulfide reactions).<sup>20,47,64</sup> We exclude the possibility of high localized temperatures at the point of impacts, as we do not observe substantial grain sizes. Furthermore, recent work<sup>65</sup> comparing torsional or rotating diamond anvil methods to mechanochemistry shows striking similarities in that the generated plastic strain can

reduce the pressure/temperature requirements for phase transformations<sup>66</sup> in Si, Ge, boron nitride<sup>67,68</sup>, and zirconium<sup>69</sup> with similar nanostructures.

In practice, knowing the rate constant and specific milling dose enables determination of the mill design (diameter, motor horsepower, media size and quantity) in order to achieve a given production rate. The ascertained specific milling dose of approximately 100 kJ/gram and corresponding minimum impact energy near 25 mJ/impact provide meaningful parameters for scale-up either by number of milling stations (i.e., 100 g capable planetary ball mills) or by switching to larger tumbler mills (i.e., 1 kg capacity) and running for the appropriate milling time derived by considering the rate constant, impact energy, and desired amount of product; the difference between the planetary mill versus the tumbler mill being the rate of energy deposition versus the synthesis time.<sup>70</sup>

In conclusion, we have ascertained the rate dependency on impact energy and the scaling parameter (milling dose near 100 kJ/gram) required to convert low cost RP into BP by the highly scalable high-energy ball milling method. While the mechanical impacts readily form BP nuclei, the overall process is grain growth limited; further efforts should seek to enhance the grain growth. The exfoliated BP flakes containing embedded crystalline domains within an amorphous matrix produces PL spectra with emission in the near-infrared range, thereby revealing the potential use of this synthesis route provided improved exfoliation methods are developed to isolate layer dependent BP nanocrystals. Producing commodity-grade BP is an enabling step to employ the nanomaterial in commercial electronic and optoelectronic devices.

## 2.4 Methods

**In the milling experiment**, elemental red phosphorus (1-5 g) (Alfa Aesar, 97% purity, -60 mesh) and stainless steel media (10 mm diameter, 100 g) were weighed and loaded into 250 mL stainless steel vessels inside an argon atmosphere glovebox ( $PO_2 < 0.1$  ppm) and sealed with internal gas pressures between 90-95 kPa at room temperature. The ball to powder mass ratio was 20:1. All milling experiments were conducted with the PM100 planetary ball mill (Retsch, Germany) with pauses in the milling cycles (30 minutes on, 30 minutes off) to prevent overheating of the unit and to switch the direction of flywheel rotation. Milling conditions (rpm and duration) were varied between 200-600 rpm and 0.15 to 25 hours, depending upon the intent of the studies. For the kinetic study, each run was completed three times except the 200 rpm run which was allowed to run once for 220 hours. The three runs at 300, 400, 500, and 600 rpm were paused periodically to obtain samples for phase fraction analysis. For each sampling interval, the sealed vessel was first transferred into an argon glovebox. An appropriate amount of powder was extracted from the free powder at the bottom of the milling vessel and sealed inside glass vials; no powder was added back into the milling vessel. The vessel was resealed and transferred out of the glovebox to resume the milling run. An initial milling run at 600 rpm for 2 hours with 1 gram of red phosphorus was used to condition the media and vessel surfaces before each milling study. The milling vessel was wiped clean between each study but was not cleaned with isopropyl alcohol, thereby preserving the conditioned state of the vessel.

**To obtain few-layer BP suspensions**, the as converted BP powders (0.25 g) are solvent exfoliated in isopropanol (30 mL) using a low-energy mixer mill (MTI, SFM-2)

with (1 mm) diameter chrome steel ball media sealed inside a 50 mL plastic container for 24 hours at a rotational speed of 150 rpm. The suspension is separated from the media using a sieve (-300 mesh) and stored in glass vials. The suspension is drop cast onto silicon substrates for Raman and PL measurements.

**Powder X-ray diffraction (XRD)** data was obtained in the Bragg-Brentano geometry ( $\text{CuK}\alpha$ , Rigaku MiniFlex 600, Japan) on 0.165 g of powder. The internal standard method using NIST Silicon 640D powder (ICSD PDF 00-027-1402) was used to generate a calibration curve for estimates of the phase fraction obtained.

**Raman spectroscopy (Raman)** data was obtained (Horiba LabRam HR Evolution, Japan) on densely packed powder samples (0.01 grams) prepared inside an argon glovebox that were sealed inside a custom-built enclosure with a sapphire window to prevent oxidation and ignition during measurements (both red and black phosphorus in finely divided powder form can be readily ignited in air even when using neutral density filters and low laser power settings). A 50 mW 532nm laser source (Nd:YAG) was used to generate spectra collected with a Si CCD. Spectra obtained at 20X objective with double acquisitions for 60 s at ten random locations throughout the bulk surface using the 1800 lines/mm grating at room temperature.

**Photoluminescence (PL) measurements** were obtained using a Princeton Aston spectrometer with a NIRvana InGaAs thermoelectrically cooled array and an excitation wavelength of 532 nm at 10 mW at room temperature. Data were collected for 5 s using a 100X near-infrared objective. PL was only obtained on exfoliated few-layer solutions as the emission peak for bulk BP powders is outside the detection range of the InGaAs (~1700 nm) detector.

**Solution based laser diffraction particle size analysis (PSA)** was performed on powders ultrasonically dispersed in isopropanol for 1 minute and cycled through the Horiba LA-950 particle size analyzer and solution flow cell; volumetric distributions were obtained using dual 405 and 650 nm laser and light diodes. The complex indices of refractions for RP<sup>71</sup> and BP<sup>72</sup> were taken from literature.

**Scanning electron microscopy (SEM)** was performed on powders pressed onto carbon tape and imaged at low beam currents (50 pA to 50 nA) and accelerating voltages (5-10 keV) using a FEI Teneo FESEM. Exfoliated BP powders were drop-cast onto cut SiO<sub>2</sub> wafers and imaged under similar conditions using secondary and backscattered electron imaging modes.

**Transmission electron microscopy (TEM)** was performed using a JEOL-JEM-2100, Japan, with Orius SC1000 CCD camera; exfoliated samples were drop-cast onto lacy carbon grids and transferred into the vacuum chamber within 5 min. A low accelerating voltage of 100 keV was used with minimal dwell times roughly 30 s for imaging to prevent the amorphization of the flakes.

### Supplementary Discussion

For a kinetic process, we seek a model  $f(\alpha)$  so that the time derivative of the phase fraction,  $\alpha$ , formed  $\frac{d\alpha}{dt}$  is equal to the product of the rate constant  $k(t)$  and our model:

$$\frac{d\alpha}{dt} = k(t)f(\alpha) \quad (1)$$

With separation of variables, it can be shown:<sup>22</sup>

$$\int_0^\alpha \frac{d\alpha'}{f(\alpha')} \equiv F(\alpha) = K(t) \equiv \int_0^t k(t') dt' \quad (2)$$

What this equality implies is that by experimentally varying conditions so rate constant changes using either isothermal or non-isothermal conditions<sup>22</sup> the time,  $t_\alpha$  required to achieve a specific phase fraction  $\alpha$  can be obtained, assuming the model that describes the phase fraction evolution remains unchanged. Furthermore, if one assumes the rate constant  $k(t)$  only has an Arrhenius temperature dependence where  $R$  is the gas constant and  $A$  is a pre-exponential factor:

$$k(T) = A \exp\left(\frac{-E_a}{RT}\right) \quad (3)$$

The integral of the rate constant  $\int k(t) = kt$  and this leads to  $F(\alpha) = kt$ . Through a series of constant temperature or constant heating rate experiments, the evolution of the phase fraction can be used to obtain the rate constant,  $k$ .<sup>19,22</sup> The activation energy,  $E_a$ , can be obtain by varying the temperature,  $T$ , or heating rate  $\frac{dT}{dt}$  using the Kissinger method.<sup>22</sup>

Graphical plots of phase fraction,  $\alpha$ , vs time,  $t$ , or  $d\alpha/dt$  vs  $\alpha$  produce curves generally described as acceleratory, deceleratory, linear, or sigmoidal.<sup>73,74</sup> Experimentally measured parameters ( $\alpha$ ,  $dT/dt$ , or  $d\alpha/dt$ ) can be compared to theoretical models using the method of master plots.<sup>73</sup> While these plots are conventionally generated for isothermal or non-isothermal measurement techniques for thermally activated processes, herein we produce the same plots to show the validity of a few common models used to describe mechanochemically induced phase transformations.

From the master plot method, the JMAK<sup>22</sup> and the DC<sup>75</sup> models (A2 and F1) are shown to be appropriate models for the RP to BP conversion. The flexibility in the JMAK

model (A2, equation 4) to fit sigmoid curves is due in part to the variable exponent which can give insight into the nucleation and growth process.<sup>76</sup>

$$\alpha = 1 - \exp((-k(t))^n) \quad (4)$$

The B1 auto-catalytic model was considered initially but the  $R^2$  values were no better than JMAK results. Additionally, the underlying theory of the product nuclei catalyzing the reaction seems less applicable for a mechanochemical process.<sup>73</sup> In studying the cobalt allotropic phase transition from hexagonal close packed to face-centered cubic, Delogu *et al.* demonstrated that the phase transformed was adequately described by an alternative model (F1, equation 5) based on the assumption that each particle would be converted under a series of impacts, *i.e.*, from a number of collisions,  $n$ , following an exponential dependency:

$$\alpha = 1 - \left[ 1 + kn + \frac{(kn)^i}{i} + \dots \right] \exp(-kn) \quad (5)$$

To apply the JMAK expression, a plot of  $\ln(-\ln(1-\alpha)) = n \ln(kt)$  will produce a straight line, with the slope equal to exponential,  $n$ , and the intercept term contains the rate constant,  $k$ . Similarly, for the DC model, a plot of  $\ln(1-\alpha) = kt$  will yield the rate constant,  $k$ , with a fixed  $n = 1$  parameter.

### **Data Availability**

The data that support the findings of this study are available from the corresponding author upon reasonable request.

### **Code Availability**

All relevant code is available from the authors on request.

### **Acknowledgements**

This work has been funded, in part, by Boise State University College of Engineering Seed Funding Program and IGEN Commerce (grant number 003786). Materials were synthesized and processed in the Advanced Materials Laboratory (Boise State University, Boise, ID). XRD, SEM, and TEM were performed in the Boise State Center for Materials Characterization (Boise State University, Boise, ID). Raman spectroscopy was performed in the Advanced Nano Materials and Manufacturing Laboratory (Boise State University, Boise, ID). Photoluminescence spectroscopy was performed at the Center for Nanoscale Materials, an Office of Science user facility which is supported by the U.S. Department of Energy, Office of Science, Office of Basic Energy Sciences, under Contract No. DE-AC02-06CH11357 as well as by the U.S. Department of Energy's Energy Efficiency & Renewable Energy (EERE) Advance Manufacturing Office (AMO) through the Argonne Chain Reaction Innovations Program through CRADA No. A18169 with Iris Light Technologies, Inc.

### **Author Contributions**

S.P. conceptualized and executed the milling studies, performed and analyzed the characterization data. C.H. performed PL measurements. F.M. and J.W. discussed the data and provided useful suggestions. S.P. wrote the manuscript with comments and edits from all co-authors. D.E. and B.J. supervised and directed the project.

### **Competing Interests**

The authors declare no competing interests.

## References

- 1 Pumera, M. & Sofer, Z. 2D Monoelemental Arsenene, Antimonene, and Bismuthene: Beyond Black Phosphorus. *Adv. Mater.* **29**, 1605299 (2017)
- 2 Zhang, S. *et al.* Extraordinary photoluminescence and strong temperature /angle-dependent Raman responses in few-layer phosphorene. *ACS Nano* **8**, 9590-9593 (2014)
- 3 Kang, J. *et al.* Solvent Exfoliation of Electronic-Grade, Two-Dimensional Black Phosphorus. *ACS Nano* **9**, 3596-3604 (2015)
- 4 Peng, R. *et al.* Midinfrared Electro-optic Modulation in Few-Layer Black Phosphorus. *Nano Lett.* **17**, 6315-6320 (2017)
- 5 Husko, C. *et al.* Silicon-Phosphorene Nanocavity-Enhanced Optical Emission at Telecommunications Wavelengths. *Nano Lett.* **18**, 6515-6520 (2018)
- 6 Jin, X. *et al.* 102 fs pulse generation from a long-term stable, inkjet-printed black phosphorus-mode-locked fiber laser. *Opt. Express* **26**, 12506-12513 (2018)
- 7 Bridgman, P. W. Two new modifications of phosphorus. *J. Am. Chem. Soc.* **36**, 1344-1363 (1914)
- 8 Lange, S., Schmidt, P. & Nilges, T. Au<sub>3</sub>SnP<sub>7</sub>@Black Phosphorus: An Easy Access to Black Phosphorus. *Inorg. Chem.* **46**, 4028-4035 (2007)
- 9 Wang, D. *et al.* Revisiting the Growth of Black Phosphorus in Sn-I Assisted Reactions. *Front. Chem.* **7**, 21 (2019)
- 10 Zhou, F. *et al.* Growth mechanism of black phosphorus synthesized by different ball milling techniques. *J. Alloys Compd.* **784**, 339-346 (2019)
- 11 Ferrara, C. *et al.* Efficiency and Quality Issues in the Production of Black Phosphorus by Mechanochemical Synthesis: A Multi-Technique Approach. *ACS Appl. Energy Mater.* **2**, 2794-2802 (2019)
- 12 Park, C. M. & Sohn, H. J. Black Phosphorus and its Composite for Lithium Rechargeable Batteries. *Adv. Mater.* **19**, 2465-2468 (2007)
- 13 Sun, C. *et al.* One-pot solventless preparation of PEGylated black phosphorus nanoparticles for photoacoustic imaging and photothermal therapy of cancer. *Biomaterials* **91**, 81-89 (2016)
- 14 Kakuk, G., Zsoldos, I., Csanady, A. & Oldal, I. Contributions to the modelling of the milling process in a planetary ball mill. *Rev. Adv. Mater. Science* **22**, 21-38 (2009)
- 15 Bergerhoff, G. & Brown, I. D. *Crystallographic Databases.* 77-95 (International Union of Crystallography, Chester, 1987).
- 16 Kang, J. *et al.* Stable aqueous dispersions of optically and electronically active phosphorene. *Proc. Natl. Acad. Sci.* **113**, 11688-11693 (2016)
- 17 Kang, J., Sangwan, V. K., Wood, J. D. & Hersam, M. C. Solution-Based Processing of Monodisperse Two-Dimensional Nanomaterials. *Acc. Chem. Res.* **50**, 943-951 (2017)
- 18 Užarević, K., Halasz, I. & Frišćić, T. Real-Time and In Situ Monitoring of Mechanochemical Reactions: A New Playground for All Chemists. *J. Phys. Chem. Lett.* **6**, 4129-4140 (2015)

- 19 Galwey, A. K. & Brown, M. E. Isothermal kinetic analysis of solid-state reactions using plots of rate against derivative function of the rate equation. *Thermochim. Acta* **269-270**, 1-25 (1995)
- 20 Humphry-Baker, S. A., Garroni, S., Delogu, F. & Schuh, C. A. Melt-driven mechanochemical phase transformations in moderately exothermic powder mixtures. *Nat. Mater.* **15**, 1280-1286 (2016)
- 21 Colacino, E. *et al.* Processing and Investigation Methods in Mechanochemical Kinetics. *ACS Omega* **3**, 9196-9209 (2018)
- 22 Avramov, I. & Šesták, J. Generalized kinetics of overall phase transition explicit to crystallization. *J. Therm. Anal. Calorim.* **118**, 1715-1720 (2014)
- 23 Blázquez, J. S., Manchón-Gordón, A. F., Ipus, J. J., Conde, C. F. & Conde, A. On the Use of JMAK Theory to Describe Mechanical Amorphization: A Comparison between Experiments, Numerical Solutions and Simulations. *Metals* **8**, 450 (2018)
- 24 Matsuoka, M., Hirata, J. & Yoshizawa, S. Kinetics of solid-state polymorphic transition of glycine in mechano-chemical processing. *Chem. Eng. Res. Des.* **88**, 1169-1173 (2010)
- 25 Rezaee, M. & Mousavi Khoie, S. M. Mechanically induced polymorphic phase transformation in nanocrystalline TiO<sub>2</sub> powder. *J. Alloys Compd.* **507**, 484-488 (2010)
- 26 Napolitano, E., Mulas, G., Enzo, S. & Delogu, F. Kinetics of mechanically induced anatase-to-rutile phase transformations under inelastic impact conditions. *Acta Mater.* **58**, 3798-3804 (2010)
- 27 Delogu, F., Mulas, G., Schiffini, L. & Cocco, G. Mechanical work and conversion degree in mechanically induced processes. *Mat. Sci. Eng. A* **382**, 280-287 (2004)
- 28 Delogu, F., Orrù, R. & Cao, G. A novel macrokinetic approach for mechanochemical reactions. *Chem. Eng. Sci.* **58**, 815-821 (2003)
- 29 Santhanam, P. R. & Dreizin, E. L. Predicting conditions for scaled-up manufacturing of materials prepared by ball milling. *Powder Technol.* **221**, 403-411 (2012)
- 30 Rosenkranz, S., Breitung-Faes, S. & Kwade, A. Experimental investigations and modelling of the ball motion in planetary ball mills. *Powder Technol.* **212**, 224-230 (2011)
- 31 Mio, H., Kano, J. & Saito, F. Scale-up method of planetary ball mill. *Chem. Eng. Sci.* **59**, 5909-5916 (2004)
- 32 Broseghini, M. *et al.* Modeling of the planetary ball-milling process: The case study of ceramic powders. *J. Eur. Ceram. Soc.* **36**, 2205-2212 (2016)
- 33 Cuadrado-Laborde, C., Damonte, L. C. & Mendoza-Zelis, L. Ball milling sound statistical analysis and its relationship with the mechanical work intensity. *Rev. Sci. Instrum.* **75**, (2004)
- 34 Le Brun, P., Froyen, L. & Delaey, L. The modelling of the mechanical alloying process in a planetary ball mill: comparison between theory and in-situ observations. *Mat. Sci. Eng. A* **161**, 75-82 (1993)
- 35 Gusev, V. G., Sobol'kov, A. V., Aborkin, A. V. & Alymov, M. I. Simulation of the Energy-Force Parameters of Planetary Ball Mill Processing and Estimation of Their Influence on the Particle Size in an AMg2 Alloy/Graphite Composite Powder. *Russ. Metall.* **2019**, 24-30 (2019)

- 36 Rogachev, A. S. *et al.* Experimental investigation of milling regimes in planetary ball mill and their influence on structure and reactivity of gasless powder exothermic mixtures. *Powder Technol.* **274**, 44-52 (2015)
- 37 Schilz, J. Internal Kinematics of Tumbler and Planetary Ball Mills: a mathematical model for the parameter setting. *Mater. Trans.* **39**, 1152-1157 (1998)
- 38 Cahn, J. W. The kinetics of grain boundary nucleated reactions. *Acta Metall.* **4**, 449-459 (1956)
- 39 Zaug, J. M., Soper, A. K. & Clark, S. M. Pressure-dependent structures of amorphous red phosphorus and the origin of the first sharp diffraction peaks. *Nat. Mater.* **7**, 890-899 (2008)
- 40 Ruck, M. *et al.* Fibrous red phosphorus. *Angew Chem Int Ed Engl* **44**, 7616-7619 (2005)
- 41 Rissi, E. N., Soignard, E., McKiernan, K. A., Benmore, C. J. & Yarger, J. L. Pressure-induced crystallization of amorphous red phosphorus. *Solid State Comm.* **152**, 390-394 (2012)
- 42 Boulfelfel, S. E., Seifert, G., Grin, Y. & Leoni, S. Squeezing lone pairs: The A17 to A7 pressure-induced phase transition in black phosphorus. *Phys. Rev. B* **85**, (2012)
- 43 Jacobs, R. B. Phosphorus at High Temperatures and Pressures. *J. Chem. Phys.* **5**, 945-953 (1937)
- 44 Xiang, H. *et al.* The mechanism of structural changes and crystallization kinetics of amorphous red phosphorus to black phosphorus under high pressure. *Chem. Comm.* **55**, 8094-8097 (2019)
- 45 Yang, Z. *et al.* Field-effect transistors based on amorphous black phosphorus ultrathin films by pulsed laser deposition. *Adv. Mater.* **27**, 3748-3754 (2015)
- 46 Smith, J. B., Hagaman, D. & Ji, H. F. Growth of 2D black phosphorus film from chemical vapor deposition. *Nanotechnol.* **27**, 215602 (2016)
- 47 Suryanarayana, C. Mechanical alloying and milling. *Prog. Mater. Sci.* **46**, 1-184 (2001)
- 48 Huberty, J. & Xu, H. Kinetics study on phase transformation from titania polymorph brookite to rutile. *J. Solid State Chem.* **181**, 508-514 (2008)
- 49 Will, G. & Berndt, H. Kinetics of the pressure-induced first-order phase transformation of RbJ. *High Pressure Res.* **21**, 215-225 (2001)
- 50 Ocenasek, J., Novak, P. & Agbo, S. Finite-thickness effect on crystallization kinetics in thin films and its adaptation in the Johnson-Mehl-Avrami-Kolmogorov model. *J. Appl. Phys.* **115**, 5, 043505 (2014)
- 51 Sun, N. X., Liu, X. D. & Lu, K. An explanation to the anomalous avrami exponent. *Scr. Mater.* **34**, 1201-1207 (1996)
- 52 Chandra Shekar, N. V. & Rajan, K. G. Kinetics of pressure induced structural phase transitions—A review. *Bull. Mater. Sci.* **24**, 1-21 (2001)
- 53 Elkin, F. S., Tsiok, O. B., Khvostantsev, L. G. & Brazhkin, V. V. Precise in situ study of the kinetics of pressure-induced phase transition in CaF<sub>2</sub> including initial transformation stages. *J. Exp. Theor. Phys.* **100**, 971-976 (2005)
- 54 Ye, F. & Lu, K. Crystallization kinetics of amorphous solids under pressure. *Phys. Rev. B* **60**, 7018-7024 (1999)

- 55 Li, X. *et al.* Synthesis of thin-film black phosphorus on a flexible substrate. *2D Mater.* **2**, 031002 (2015)
- 56 Bridgman, P. W. Theoretically Interesting Aspects of High Pressure Phenomena. *Rev. Mod. Phys.* **7**, 1-33 (1935)
- 57 Keyes, R. W. The electrical properties of black phosphorus. *Phys. Rev.* **92**, 580-584 (1953)
- 58 Shoichi, E., Yuichi, A., Shin-ichi, T. & Shin-ichiro, N. Growth of Large Single Crystals of Black Phosphorus under High Pressure. *Jpn. J. Appl. Phys.* **21**, L482-L484 (1982)
- 59 Bridgman, P. W. Shearing Phenomena at High Pressures, Particularly in Inorganic Compounds. *Proc. Am. Acad. Arts Sci.* **71**, 387-460 (1937)
- 60 Zadorozhnyy, V. Y., Shelekhov, E. V., Milovzorov, G. S., Strugova, D. V. & Zinnurova, L. K. Analysis of the Background Temperature During the Mechanical Alloying of Metal Powders in the Planetary Ball Mill. *Inorg. Mater. Appl. Res.* **9**, 559-565 (2018)
- 61 Andersen, J. M. & Mack, J. Decoupling the Arrhenius equation via mechanochemistry. *Chem. Sci.* **8**, 5447-5453 (2017)
- 62 Schmidt, R., Martin Scholze, H. & Stolle, A. Temperature progression in a mixer ball mill. *Int. J. Ind. Chem.* **7**, 181-186 (2016)
- 63 Takacs, L. & McHenry, J. S. Temperature of the milling balls in shaker and planetary mills. *J. Mater. Sci.* **41**, 5246-5249 (2006)
- 64 Delogu, F. & Cocco, G. Weakness of the “hot spots” approach to the kinetics of mechanically induced phase transformations. *J. Alloys Compd.* **465**, 540-546 (2008)
- 65 Delogu, F. A few details of the austenite to martensite phase transformation in 304 stainless steel powders under mechanical processing. *Acta Mater.* **59**, 2069-2074 (2011)
- 66 Levitas, V. I. High pressure phase transformations revisited. *J. Phys. Condens. Matter* **30**, 163001 (2018)
- 67 Ji, C. *et al.* Shear-induced phase transition of nanocrystalline hexagonal boron nitride to wurtzitic structure at room temperature and lower pressure. *Proc. Natl. Acad. Sci.* **109**, 19108-19112 (2012)
- 68 Gasgnier, M., Szwarc, H. & Ronez, A. Low-energy ball-milling: Transformations of boron nitride powders. Crystallographic and chemical characterizations. *J. Mater. Sci.* **35**, 3003-3009 (2000)
- 69 Levitas, V. I. & Javanbakht, M. Phase transformations in nanograin materials under high pressure and plastic shear: nanoscale mechanisms. *Nanoscale* **6**, 162-166 (2014)
- 70 Gilman, P. S. & Benjamin, J. S. Mechanical alloying. *Ann. Rev. Mater. Sci.* **13**, 279-300 (1983)
- 71 Roth, W. L., DeWitt, T. W. & Smith, A. J. Polymorphism of Red Phosphorus. *J. Am. Chem. Soc.* **69**, 2881-2885 (1947)
- 72 Jiang, H., Shi, H., Sun, X. & Gao, B. Optical Anisotropy of Few-Layer Black Phosphorus Visualized by Scanning Polarization Modulation Microscopy. *ACS Photonics* **5**, 2509-2515 (2018)

- 73 Khawam, A. & Flanagan, D. R. Solid-state kinetic models: basics and mathematical fundamentals. *J. Phys. Chem. B.* **110**, 17315-17328 (2006)
- 74 Sánchez-Jiménez, P. E., Pérez-Maqueda, L. A., Perejón, A. & Criado, J. M. Generalized master plots as a straightforward approach for determining the kinetic model: The case of cellulose pyrolysis. **552**, 54-59 (2013)
- 75 Delogu, F. A combined experimental and numerical approach to the kinetics of mechanically induced phase transformations. *Acta Mater.* **56**, 905-912 (2008)
- 76 Jacobsen, M. K., Velisavljevic, N. & Sinogeikin, S. V. Pressure-induced kinetics of the  $\alpha$  to  $\omega$  transition in zirconium. *J. Appl. Phys.* **118**, 025902 (2015)
- 77 Cullity, B. D. & Stock, S. R. *Elements of x-ray diffraction*. 3rd ed. edn, (Prentice Hall, Upper Saddle River, NJ, 2001).

## Figures

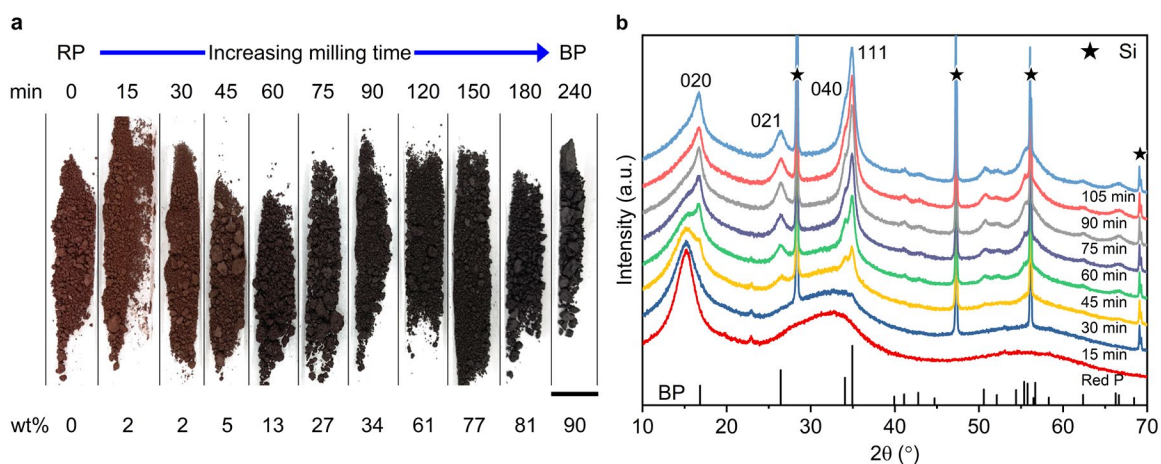


**Figure 2.1 Characterization of the mechanochemical conversion of RP to BP.** (a) Optical image of bulk powders revealing the color progression that occurs during increased milling time via high-energy ball milling; the transition from red to brown to black is a direct result of the mixture of amorphous RP and crystalline BP present (scale bar is 1 cm) (b) Powder x-ray diffraction (XRD) patterns of RP during conversion to BP showing an increase in the intensity of the main BP (040) and (111) peaks with increasing milling time; here, all patterns vertically offset correspond to runs at a constant speed 600 rpm, black bars are BP (PDF 03-065-2491), and silicon standard peaks are marked.

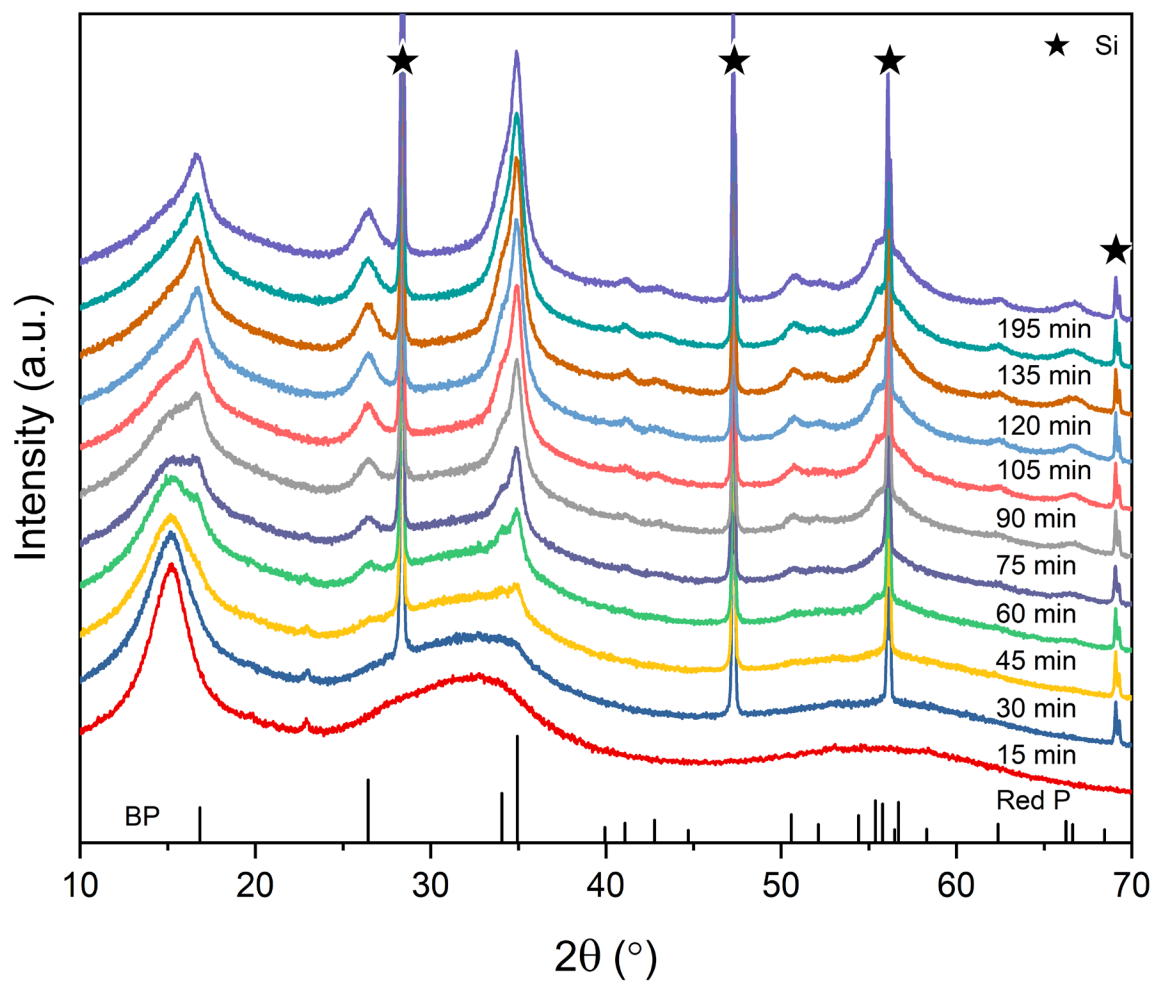


**Figure 2.2** XRD curves for BP conversion at 500 rpm with reference BP (vertical black bars) and Si standard (stars) showing increased phase fraction of BP with increased milling time.

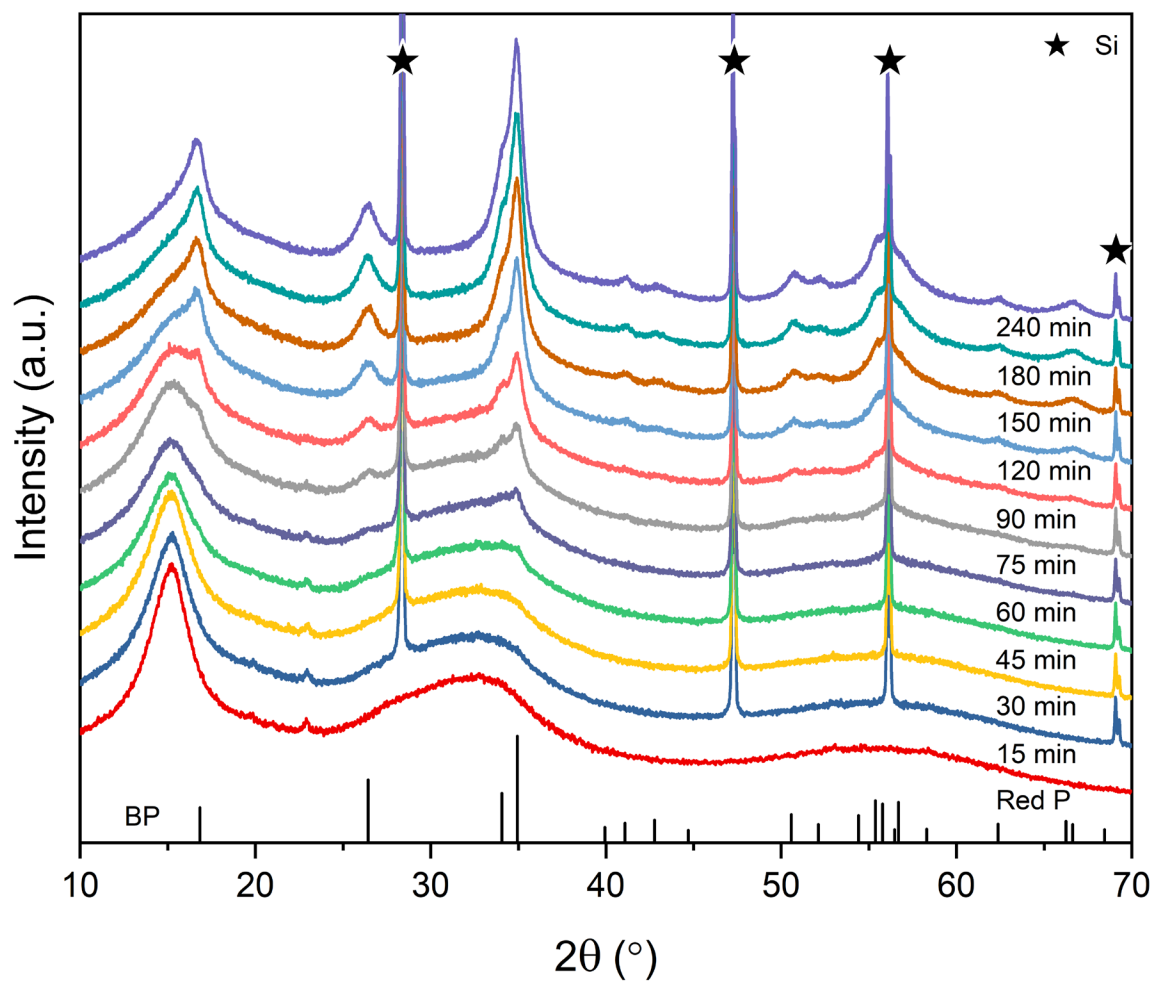


**Figure 2.3** XRD curves for BP conversion at 400 rpm with reference BP (vertical black bars) and Si standard (stars) showing increased phase fraction of BP with increased milling time.

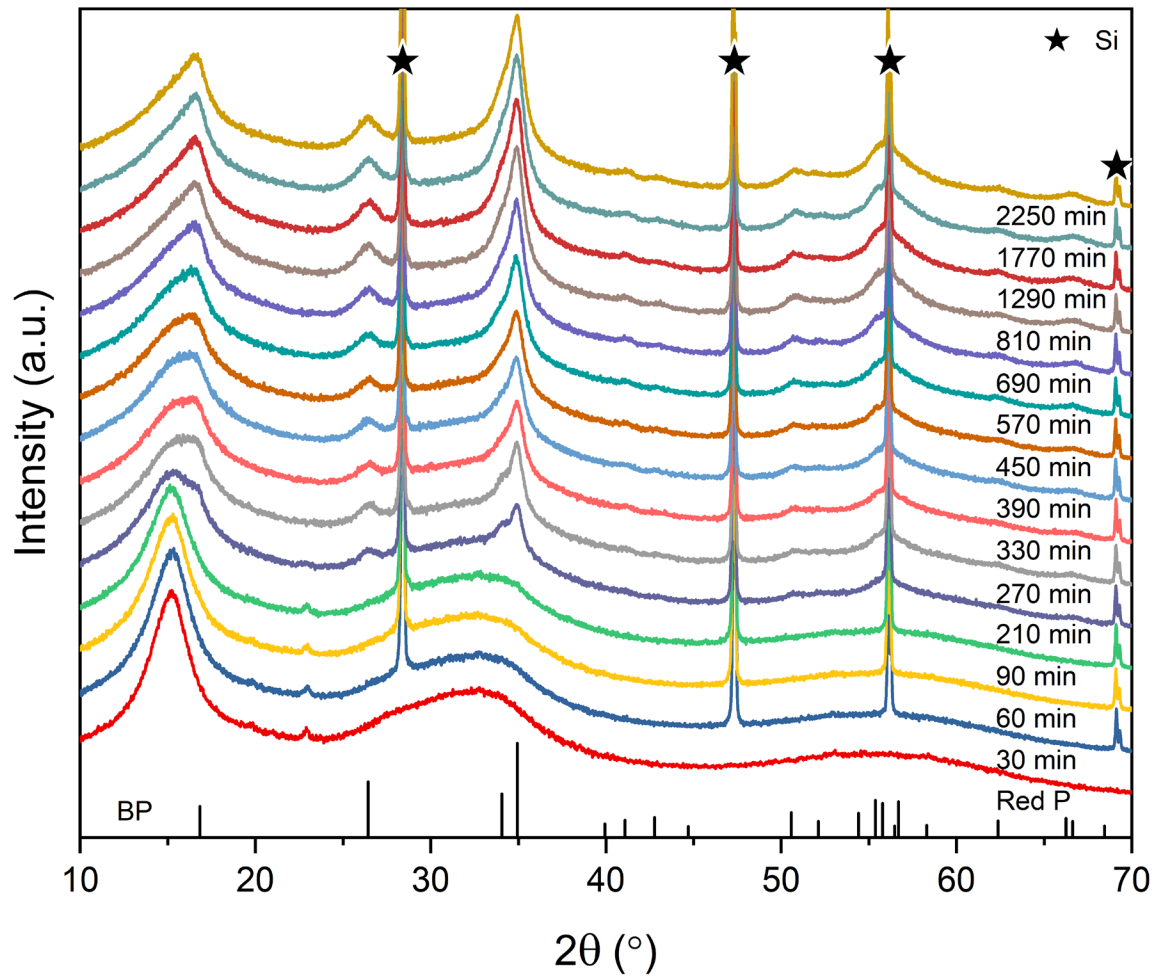


**Figure 2.4** XRD curves for BP conversion at 300 rpm with reference BP (vertical black bars) and Si standard (stars) showing increased phase fraction of BP with increased milling time. Note that the peak at 17 degrees for BP at 300 rpm is less prominent than at higher rpm values; indicating smaller crystallites and lower degree of conversion.

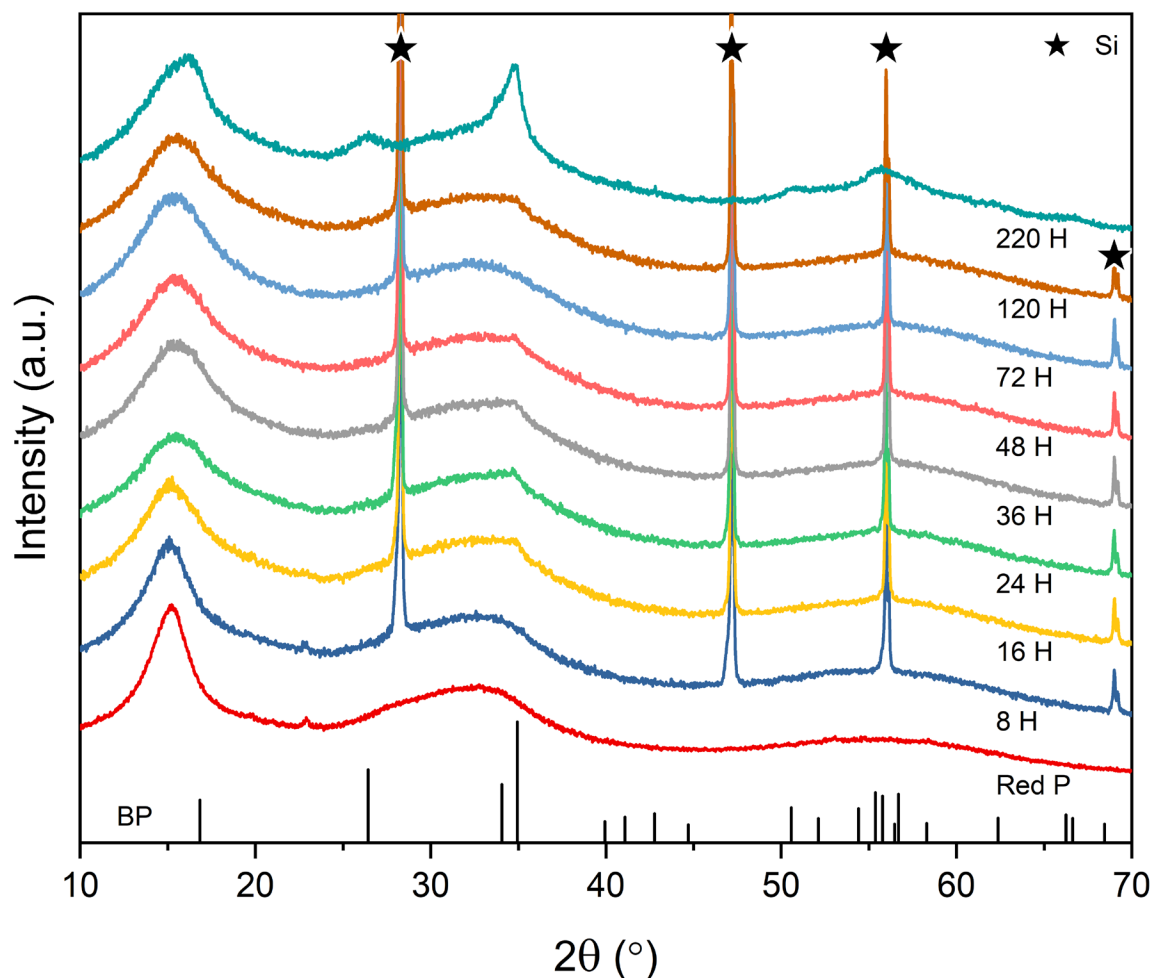


**Figure 2.5** XRD curves for BP conversion at 200 rpm with reference BP (vertical black bars) and Si standard (stars); at 200 rpm, a large induction period of 200+ hours to generate sufficient nuclei of BP is evident.

Between 120 hours and the next sampling period (120 hours later) the BP peaks begin to appear. No Si standard was present in the final 220 hour sample, BP phase fraction was estimated by overlaying with 300 rpm patterns to compared relative intensity. The run was terminated after 220 hours as the powder appeared to be reddish-brown consistent with low BP fraction and based on the progression observed at 300 rpm, it was anticipated that an additional 1000 hours (42 days) of milling may be required to approach a similar level of conversion; such an extensive milling time in a high energy (and high collision frequency) ball mill was deemed impractical for further study. Some evidence of BP at earlier sampling periods (specifically at 16, 24, 48 hours) indicates nuclei were forming but not at a sufficient rate to initiate rapid growth.

XRD calibration curve obtained by the internal standard “spiking” method by mixing known concentrations of silicon (Si) and black phosphorus. Error bars indicate one standard deviation as an average of three scans for each target BP weight fraction. The adjusted  $R^2$  value for the polynomial fit indicates little effect of deviation due to sample preparation.<sup>77</sup>

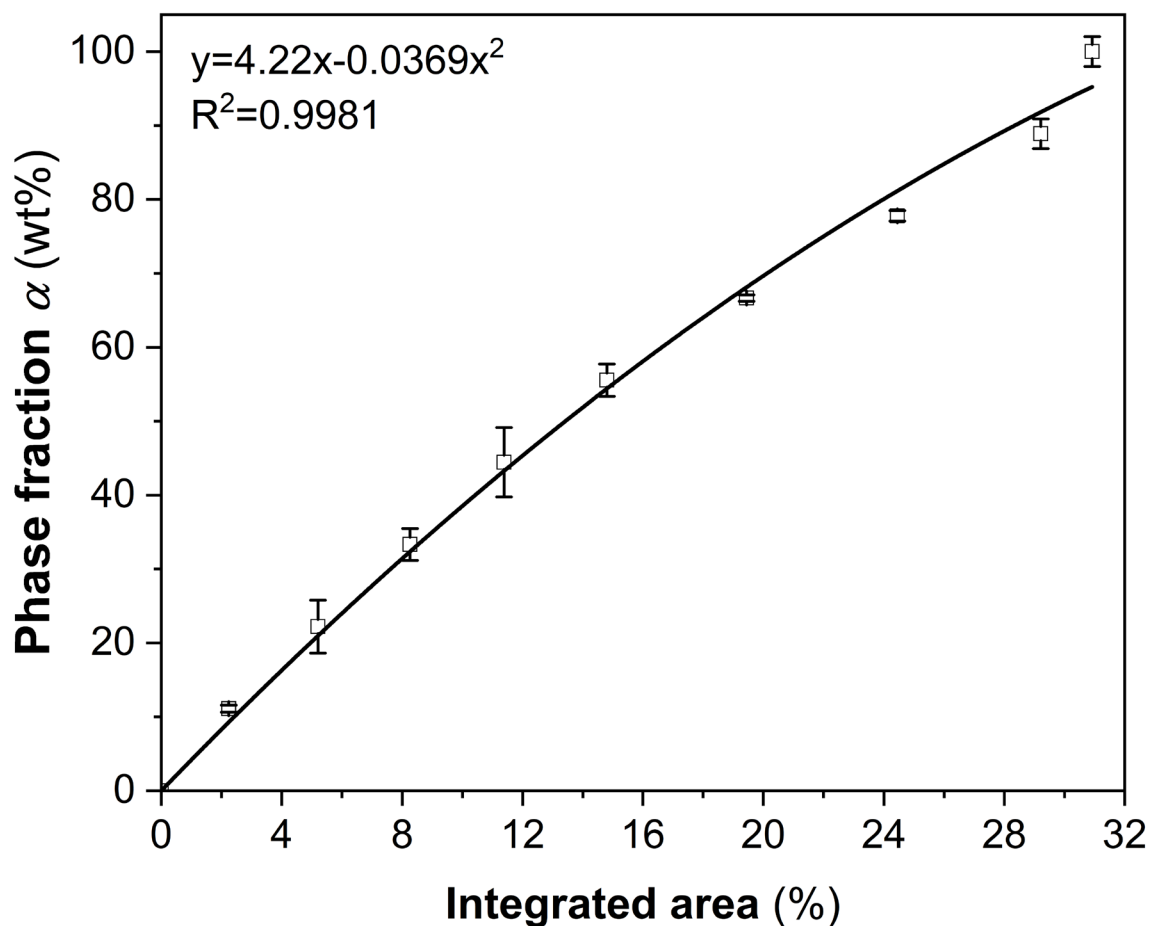


**Figure 2.6** XRD calibration curves using integrated area % of BP peaks (040 and 111) for determining black phosphorus weight fractions; error bars are one standard deviation obtained from three samples for each weight fraction.

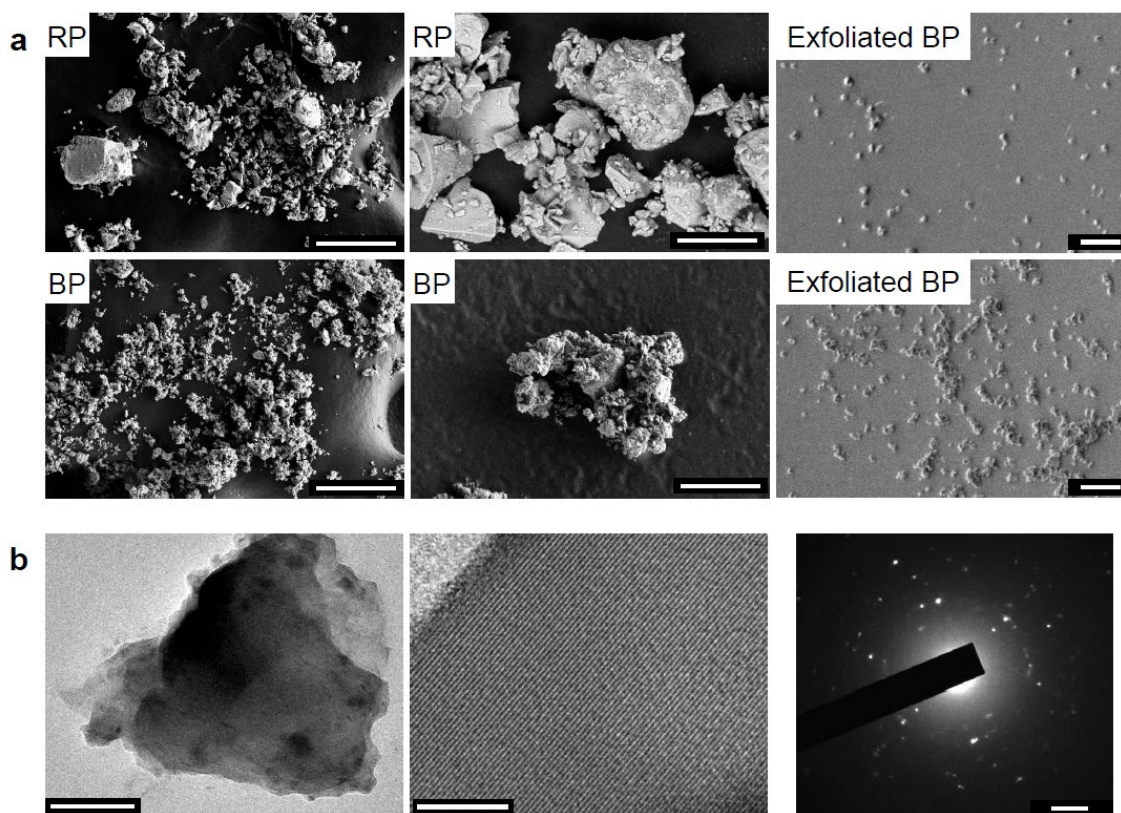


**Figure 2.7 Electron microscopy shows particle size reduction through BP synthesis and exfoliation while retaining polycrystallinity.**

(a) Scanning electron microscopy (SEM) images presenting faceted morphology of large particle sizes for RP, smaller particle sizes for BP, and narrow particle size for exfoliated BP flakes that consist of crystalline domains embedded in a larger bulk amorphous particle with plate-like morphology (SEM scale bars from left to right are 100  $\mu\text{m}$ , 10  $\mu\text{m}$  and 2  $\mu\text{m}$ , respectively). (b) Transmission electron microscopy (TEM) images and a selected area electron diffraction (SAED) pattern of polycrystalline BP manifesting large lattice domains and converted BP crystallinity. TEM scale bars from left to right are 50 nm, 10 nm, and 2  $\text{nm}^{-1}$  respectively.

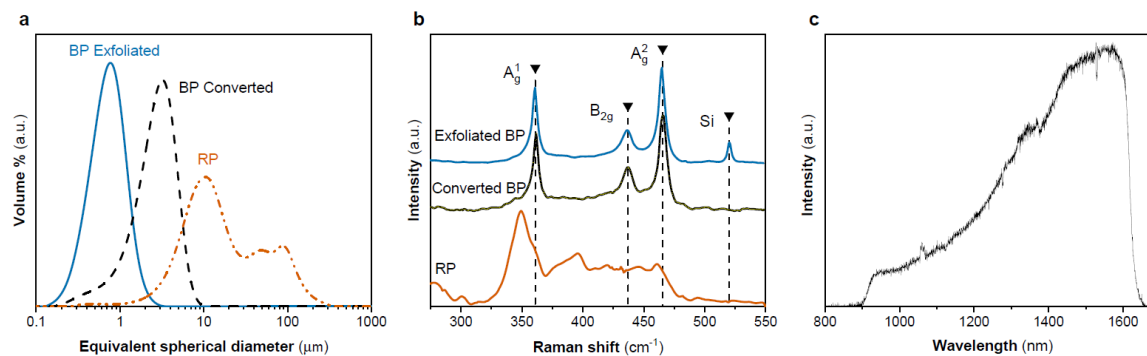


**Figure 2.8** Characterization of mechanochemically synthesized and exfoliated few-layer BP.

(a) Particle size analysis of RP, as-converted BP, and ball mill exfoliated BP showing progressively narrower and smaller size distributions as a result of conversion, comminution, and exfoliation. (b) Raman spectra confirming the amorphous nature of RP, as well as the crystalline nature of both converted and exfoliated BP. (c) Photoluminescence (PL) emission of exfoliated BP on SiO<sub>2</sub> with a broad spectrum due to the bilayer to multilayer BP in the exfoliated material.

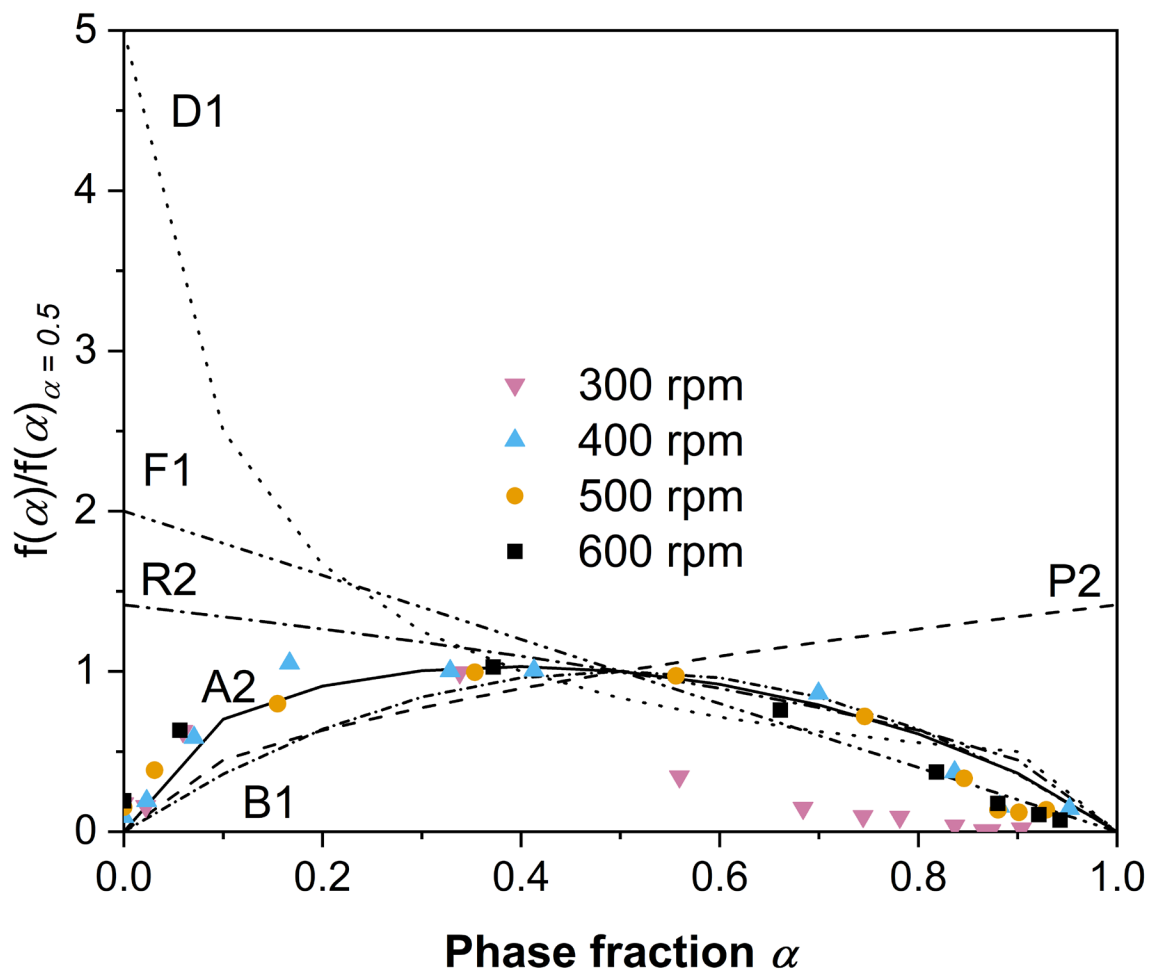


**Figure 2.9** Master plot method using  $f(\alpha)/f(\alpha)_{\alpha=0.5}$  ratios overlaid with experimental phase fractions; the A2 (JMAK), B1 (auto-catalytic) models best match the data while the F1 model (DC) loosely fits the data above 50%. The 300 rpm phase fraction deviates substantially above 50% which may indicate a mechanism change.

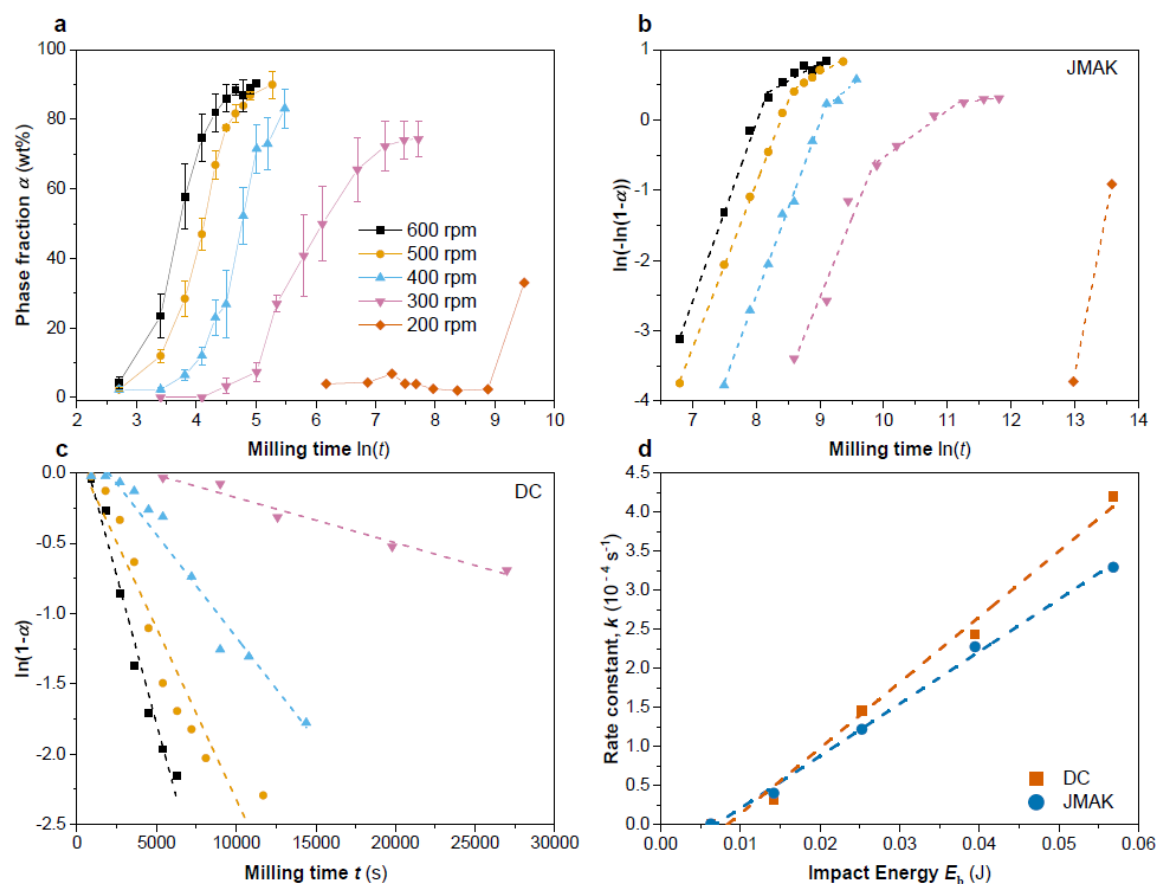


**Figure 2.10 Mechanochemically induced phase transformation kinetics of RP to BP using the JMAK and DC models.**

(a) XRD-based phase fraction versus logarithmic time showing representative S-curves for each rpm condition; higher rpm results in faster conversion while a dramatic reduction occurs at and below 300 rpm. An S-shape curve is typical of nucleation and growth dominated solid-state processes. Error bars represent one standard deviation, lines are visual aids. (b) JMAK linearization plots for extracting rate constants and exponents, lines are linear regression fits for each straight section; the slopes remain relatively constant indicating the conversion mechanism remains constant, while the kinks at higher phase fraction indicates a possible mechanism change. (c) DC model linearization plot excluding the 200 rpm data, lines are linear regression fits; the slopes become steeper (higher rate constant) with increasing rpm. (d) Linear regression fits for rate constants versus calculated impact energies; both the JMAK and DC models show the linear dependence of the rate constant on the impact energy confirming the assumption that a single impact is sufficient for converting the entrapped RP powder between media collisions to BP.

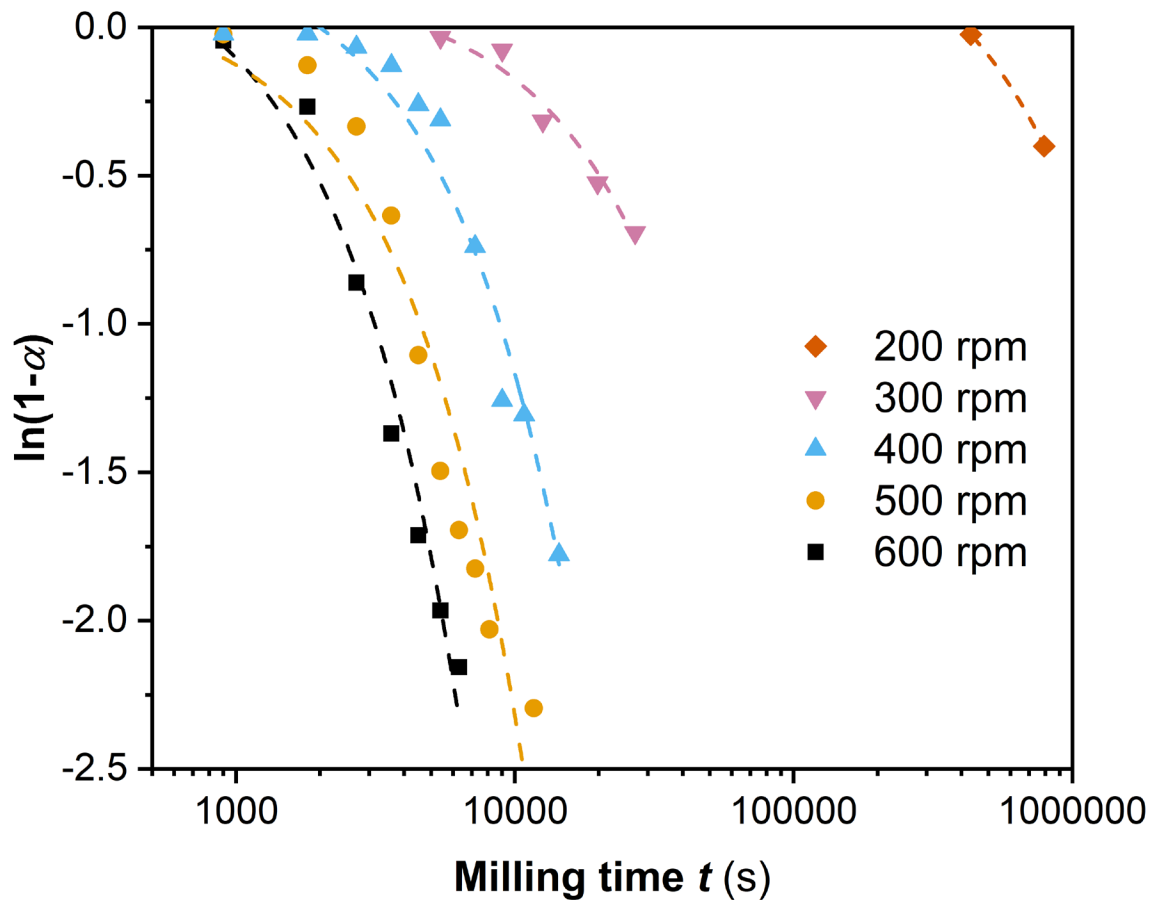


Figure 2.11 DC model including the 200 rpm dataset; the induction time obscures the trend of steeper slopes (larger rate constants) at higher rpms.

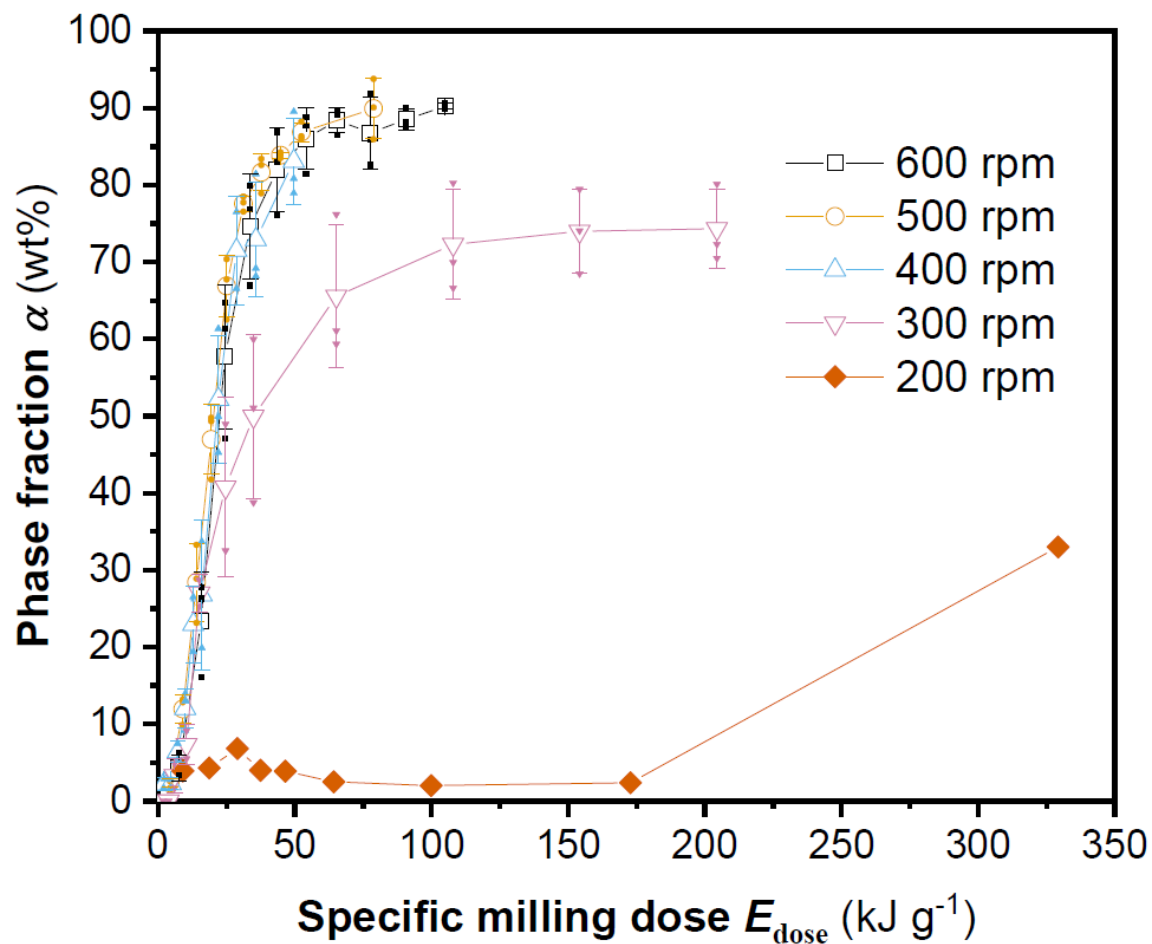
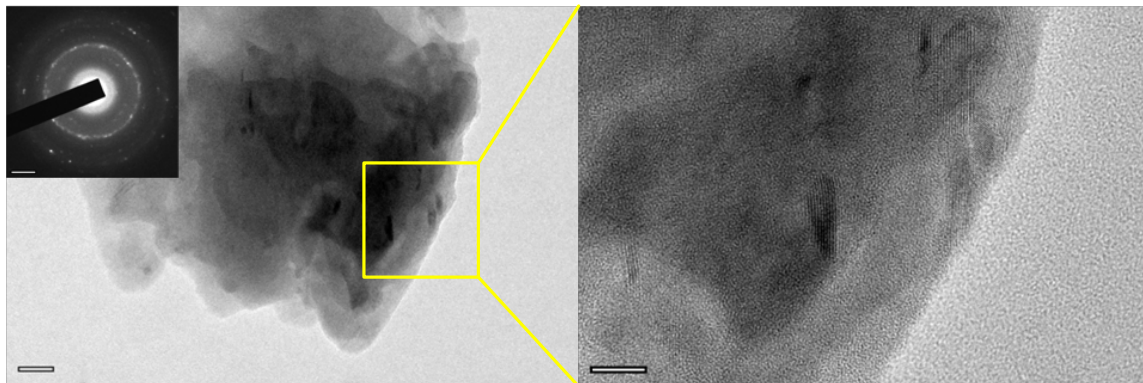
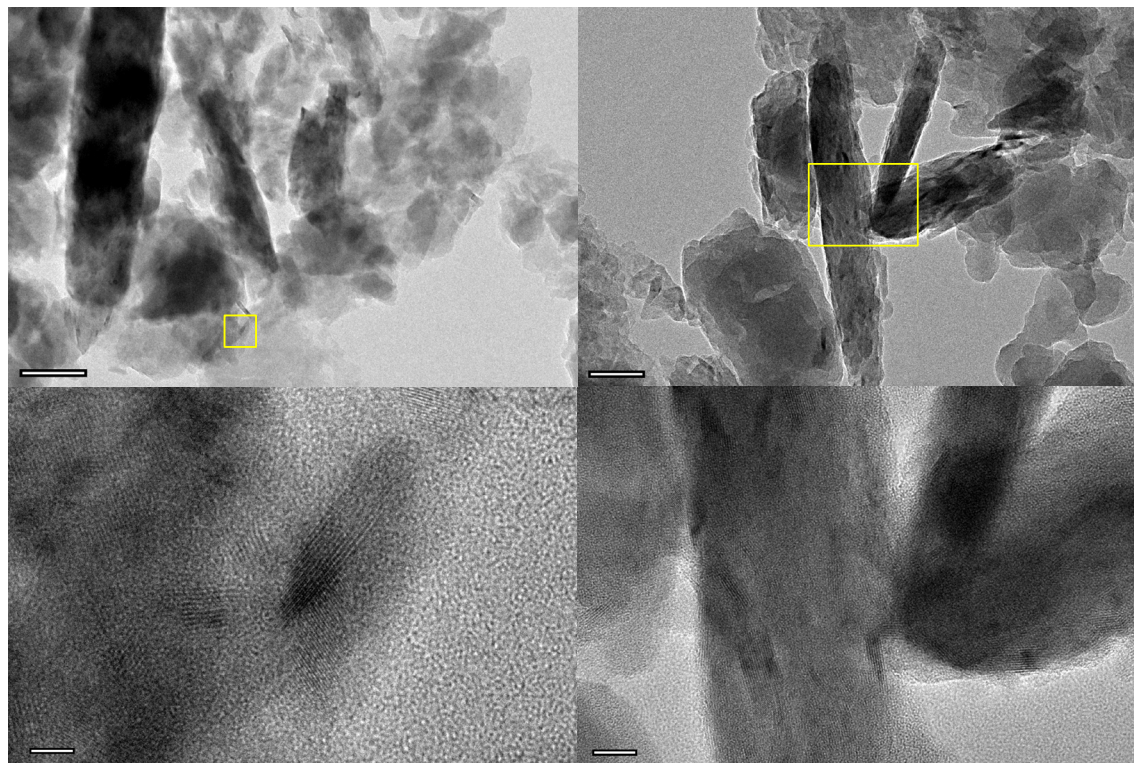


Figure 2.12 Extent of conversion for RP to BP as a function of specific milling dose.

Milling at 400 rpm or higher results in an equivalent energy dose to obtain the same extent of conversion. Milling at less than 400 rpm (i.e., 300 and 200 rpm) results in incomplete conversion due to an apparent energy threshold. Phase fraction data normalized by milling dose estimates. Error bars represent one standard deviation.



**Figure 2.13** TEM of BP flakes showing multiple crystalline domains with different orientations surrounded by an amorphous matrix (scale bars from left to right are 20 nm and 10 nm while the diffraction pattern scale bar is 2 nm<sup>-1</sup>, respectively).



**Figure 2.14** TEM images of BP flakes showing multiple crystalline domains with different orientations surrounded by an amorphous matrix (scale bars from left to right and top to bottom are 100 nm, 50 nm, 5 nm, and 10 nm, respectively).

Periods of cooling are required during high energy planetary ball milling using commercial ball mills such as the Retsch PM100. Continuous uninterrupted milling can potentially overheat the driveshaft; as such, it is common practice (and recommended by the manufacturer) to introduce cooling pauses. On the other hand, larger gravity-based production mills operate without pause.

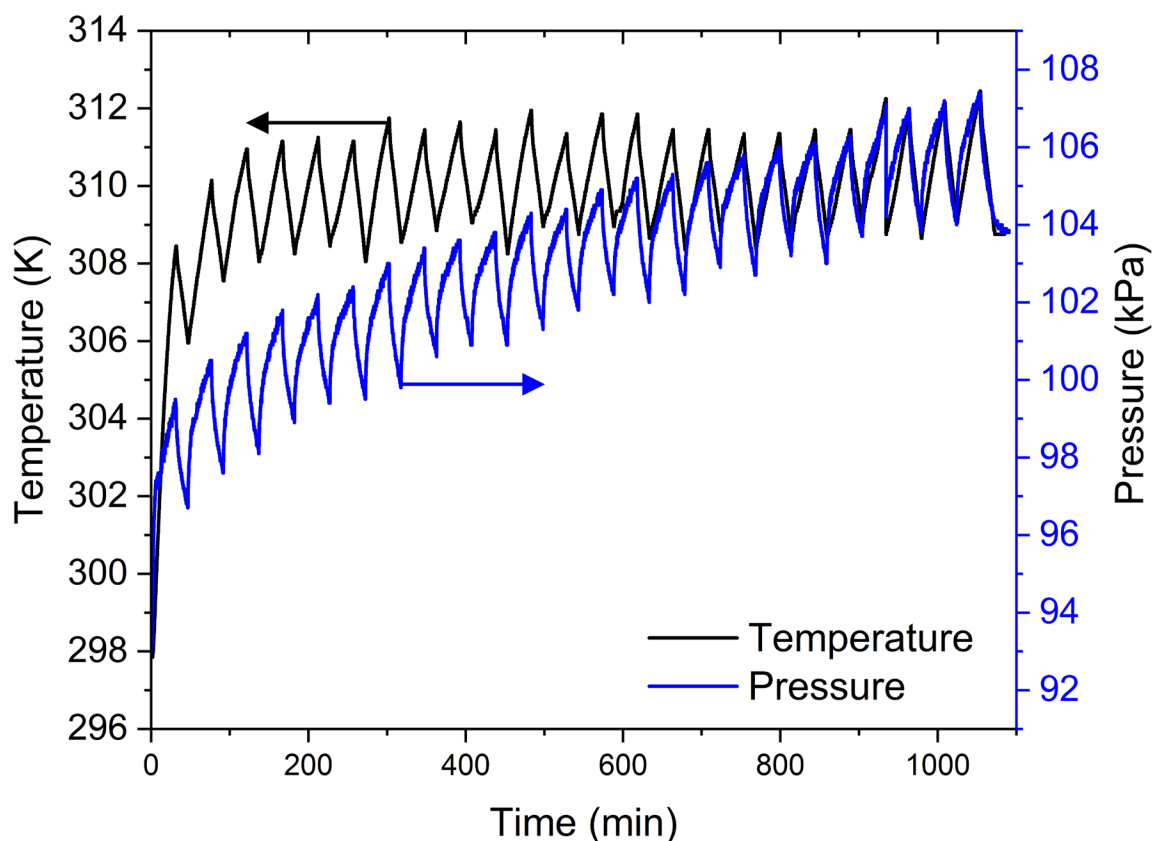


**Figure 2.15 In situ pressure and temperature cycle for a 600 rpm run with 5 grams of RP converted to BP.**

The sample was milled for an extended period of time to determine maximum temperature reached during the milling cycle. The oscillation of both temperature and pressure are due to 15 minute pauses every 30 minutes to prevent overheating of the PM100.

## Tables

Table 2.1 Solid state reaction models considered for the master-plot method<sup>73</sup>

Model	Differential form $f(\alpha)$
F1 (first-order)	1
R2 (contracting area)	$2(1 - \alpha)^{1/2}$
A2 (JMAK)	$2(1 - \alpha)(-\ln(1 - \alpha))^{1/2}$
D1 (1D diffusion)	$1/2\alpha$
P2 (power law)	$2\alpha^{1/2}$
B1 (Prout-Tompkins)	$\alpha(1 - \alpha)$

Table 2.2 PM 100 planetary ball mill parameters used for kinematic modeling.

Mill and Media Physical Constants			
Parameter	Symbol	Value	Units
<b>Mill Parameters</b>			
Vial / disk speed	$\omega_v / \omega_d$	-2:1	---
Disk radius	$r_d$	70.5	mm
Vial radius	$r_v$	37.5	mm
Corrected $r_v$	$r_v' = r_v - r_b$	35	mm
Vial / Disk radius	$r_v' / r_d$	0.496	---
<b>Media Parameters</b>			
Radius	$r_b$	5	mm
Density	$\rho_b$	7.8	$\text{g cm}^{-3}$
Mass	$m_b$	3.516	$\text{g cm}^{-3}$
Number of media	$N_b$	30	---

**Table 2.3 Comparison of kinetic models and calculated ball milling energies.**

Model	RPM	Rate Constants		Impact Energy	Impact Frequency	Milling Intensity (for 30 balls)	Fit (R <sup>2</sup> )
		$k [10^{-4} \text{ s}^{-1}]$	$n$	$E_b [\text{J}]$	$f_b [\text{s}^{-1}]$	$[\text{J s}^{-1}]$	
<b>DC</b>	200	0.01	1	0.006	250	1.6	1
	300	0.32	1	0.014	375	5.3	0.970
	400	1.46	1	0.025	499	12.6	0.947
	500	2.44	1	0.039	624	24.6	0.869
	600	4.20	1	0.056	749	42.6	0.959
<b>JMAK</b>	200	0.01	---	0.006	250	1.6	1
	300	0.40	2.3	0.014	375	5.3	0.950
	400	1.22	2.5	0.025	499	12.6	0.997
	500	2.27	2.3	0.039	624	24.6	0.999
	600	3.29	2.5	0.056	749	42.6	0.995

The kinematic model described by Kakuk *et al.* was implemented in MATLAB and solved numerically to obtain milling kinetic data such as impact frequency, impact energy, and total cumulative dose using the Retsch PM100 milling parameters above.<sup>14</sup> The reader is referred to Kakuk *et al.* for the mathematical expressions, variable definitions, and visual schematics of the kinematic model.<sup>14</sup>

CHAPTER THREE: MECHANOCHEMISTRY OF PHOSPHORUS-ARSENIC  
ALLOYS FOR VISIBLE AND INFRARED PHOTONICS

This chapter is submitted for publication by Wiley Publications in *Advanced Photonics Research* and should be referenced appropriately.

Reference:

S. V. Pedersen, F. Muramutsa, C. Greseth, J. D. Wood, C. Husko, J. Eixenberger, D. Estrada, B. J. Jaques, “Mechanochemistry of Phosphorus- Arsenic Alloys for Visible and Infrared Photonics.” *Advanced Photonics Research*. X (X) XX (2022)

Reproduced/modified by permission of Wiley Publications.

\*This chapter includes modifications from the originally published version, subheadings for clarity were incorporated into this version.

Mechanochemistry of Phosphorus- Arsenic Alloys for Visible and Infrared Photonics

Samuel V. Pedersen<sup>1,2</sup>

Florent Muramutsa<sup>1</sup>

Cade Greseth<sup>1,2</sup>

Joshua D. Wood<sup>3</sup>

Chad Husko<sup>4</sup>

Joshua Eixenberger<sup>1,2,5</sup>

David Estrada<sup>1,2,5</sup>

Brian J. Jaques<sup>1,2</sup>

Submitted for Published in:

Wiley Advanced Photonics Research

February 2022

<sup>1</sup>Micron School of Materials Science and Engineering, Boise State University,

Boise, ID 83725, USA

<sup>2</sup>Center for Advanced Energy Studies, Idaho Falls, ID 83401, USA

<sup>3</sup>Promethean Consulting, LLC, Oak Park, IL 60302, USA

<sup>4</sup>Iris Light Technologies, Inc., Chicago, IL 60622, USA.

<sup>5</sup>Idaho National Laboratory, Idaho Falls, ID 83402, USA

### **Abstract**

Incorporating few-layer two-dimensional phosphorus-arsenic alloys (PAs) into optoelectronic devices requires a synthesis technique that allows control of the alloy composition while producing volumes of material suitable for application development such as photodetectors, solar cells, and lasers. With that goal, high-energy ball milling allows production of both orthorhombic (o-PAs) and trigonal (t-PAs) alloys by reacting red phosphorus and metallic arsenic powders. The synthesis follows a two-step process in which arsenic rapidly reacts with red phosphorus to first produce t-PAs followed by a slower phase transformation into o-PAs; synthesis time and overall conversion rate are slightly enhanced by the presence of arsenic. Optical measurements on exfoliated alloys at the few-layer atomic limit of the two-dimensional PAs reveal emission spanning from the visible ( $\sim 1.9$  eV) into the near-infrared, covering a broad application space. Rapid powder synthesis within a closed system for stoichiometric control of the solid solution PAs alloys combined with solution-based exfoliation opens up opportunities for a whole new class of optoelectronic devices based on PAs nanomaterials.

### **3.1 Introduction**

In pursuit of two-dimensional (2D) materials for use in optoelectronics, binary alloys of pnictogens (group V semiconductor elements) at the few-layer limit are under investigation for their optical properties. While the orthorhombic structure of pure black phosphorus (BP) has a layer-dependent direct bandgap spanning 0.3–2.0 eV, orthorhombic phosphorus-arsenic (o-PAs) alloys have narrower bandgaps near 0.15 eV in the bulk. Theoretically, o-PAs alloys also have layer dependent widening of the direct

bandgaps up to 2.1 eV at the monolayer limit.<sup>1-3</sup> Pure orthorhombic arsenic is expected to have an indirect bandgap (0.73 eV) at the monolayer but becomes direct (0.52 eV) at two layers with the gap decreasing with increasing number of layers.<sup>4,5</sup> Experimentally, infrared spectroscopy performed on bulk o-PAs samples was used to infer an optical gap between 0.15-0.3 eV as a function of composition.<sup>6-9</sup> Similarly, naturally occurring trigonal grey arsenic exhibits a layer dependent bandgap ranging from 2.3 eV for monolayer, 0.37 for bilayer, and undergoes a transition to semi-metallic behavior in the bulk.<sup>10-12</sup> Alloying with phosphorus to produce trigonal PAs layered crystals (t-PAs) may enable bandgap tuning, thereby opening opportunities for optoelectronic devices in the visible-IR spectrum.<sup>13</sup> Anticipated applications of layered o-PAs and t-PAs alloys include transistors<sup>14,15</sup>, photodetectors<sup>6,7,16-18</sup>, saturable absorbers<sup>9</sup>, solar cells<sup>19</sup>, gas sensing<sup>20</sup>, lithium batteries<sup>21</sup>, lasers<sup>22</sup>, thermoelectrics<sup>23</sup>, and light radar.<sup>6</sup>

Nonetheless, synthesis of PAs compounds is challenging. The methods include high pressure (HP)<sup>24-26</sup>, use of mercury flux<sup>27,28</sup>, epitaxial growth on InP wafers<sup>14</sup>, and mineralizer assisted chemical vapor transport (CVT).<sup>6,29-32</sup> Recently, a mineralizer-free direct thermal synthesis for o-PAs (higher than 50 at% arsenic) in sealed silica tubes was demonstrated.<sup>33</sup> Such a possibility was alluded to in the 1940's with direct heating of arsenic and phosphorus together in sealed steel cans producing black crystals.<sup>34</sup> Direct synthesis of o-PAs alloys on silicon wafers without metallic seed layers (which quench optical properties) at moderate temperatures is lacking. Deposition of 2D materials onto silicon wafers using additive manufacturing may provide a viable route to optoelectronic devices provided that there exists a synthesis method to produce industrially scalable quantities of the 2D materials themselves.<sup>35-38</sup> Herein, we demonstrate high energy ball

milling (HEBM) as a synthesis route to produce the o-PAs and t-PAs alloys using a high energy planetary ball mill.

High energy ball milling, also referred to as mechanical alloying (MA), is a unique route for the production of black phosphorus.<sup>39-41</sup> MA exploits the rapid far-from-equilibrium thermomechanical condition which exists within compressed powders trapped in the collisions between media and between media and the vessel wall. These impact conditions can provide sufficient energy in the form of pressure and localized heat to enable the red to black phosphorus phase transformation.<sup>39-41</sup> MA avoids formation or use of toxic vapors, promotes control of stoichiometry of high vapor pressure elements, and requires no catalysts for alloy formation. While metal-rich phosphides have been explored, studies on the solubility limits and possible phases that can be produced by ball milling red phosphorus with other pnictogens, such as arsenic, are lacking.<sup>42,43</sup>

In this work, a high energy planetary ball mill was used to synthesize the o-PAs (1-70 at% arsenic) and the t-PAs (70-90 at% arsenic) alloys. The resulting powders were characterized using x-ray diffraction (XRD), Raman spectroscopy (Raman) and transmission electron microscopy (TEM) while details on compositions and bonding behavior were analyzed using energy dispersive spectroscopy (EDS) and x-ray photoelectron spectroscopy (XPS).

The kinetics of the conversion process and resultant rate constant were compared to that of pure BP synthesis and showed slightly faster conversion kinetics. It is thought that the faster kinetics are enabled by the rapid conversion of red phosphorus into the t-PAs phase. The slowest step is the gradual conversion of the t-PAs into o-PAs. The overall conversion rate is therefore limited by this slower transformation. Investigation

of the optical behavior using photoluminescence (PL) and UV-Vis absorption (UV-Vis) on ultrasonic probe tip exfoliated<sup>44</sup> few-layer solutions containing flakes from o-PAs and t-PAs shows an optical gap around 1.8-2 eV for all compositions. Both PAs solid solution alloy series exhibit emission in the visible and near IR making them promising for a wide range of optical applications.

### 3.2 Results and Discussion

The layered orthorhombic (*Cmca*) o-PAs alloys and layered trigonal ( $R\bar{3}m$ ) t-PAs alloys were successfully synthesized via HEBM as shown by the x-ray diffraction patterns and Raman spectra in **Figure 3.1**. The structural transition from the o-PAs to t-PAs occurred for the 70 at% arsenic composition is readily discerned by the appearance of two peaks at  $44^\circ$  and  $49^\circ$  in **Figure 3.1(a)**. At the 70 at% arsenic composition, a two-phase region is evident, as peaks from both o-PAs and t-PAs are present. Rietveld refinements on the 10-90 at% compositions are presented in **Figure 3.2**. Specifically, for the 70 at% arsenic composition, phase fraction analysis indicates approximately 5 wt% of the o-PAs phase is present while 95 wt% of the sample is the t-PAs phase. The narrow diffraction angle range in **Figure 3.1(b)** helps to reveal the peak shift to lower angles of the strong peaks (040 and 110 planes) near  $34^\circ$  which is consistent with the expansion of the unit cell with increasing arsenic content simply due to the larger atomic radius of arsenic.

Likewise, the Raman spectra in **Figure 3.1(c)** show vibrational modes related to As-As, As-P and P-P bonding. The peak positions and relative intensities of the HEBM synthesized o-PAs alloys qualitatively matches the results for CVT grown o-PAs single

crystals or thin films.<sup>6</sup> The Raman spectra for the t-PAs alloys with 70+ at% arsenic spectra show multiple broad peaks at 190-260  $\text{cm}^{-1}$  which implies bonding of phosphorus into the trigonal structure and qualitatively matches the expected wavenumber range for trigonal arsenic ( $\sim 200$ ,  $\sim 255$ , and  $\sim 366$   $\text{cm}^{-1}$ ).<sup>35</sup> The crystallographic details and vibrational modes of the orthorhombic and trigonal phases of phosphorus and arsenic along with reference phases from the Inorganic Crystal Structures Database (ICSD) are listed in **Table 3.1**.

**Figure 3.3** shows that the o-PAs alloys obey a Vegard-like linear trend in the lattice parameters  $a$ ,  $b$ , and unit cell volume,  $V$  (obtained from XRD Rietveld refinements as shown in **Figure 3.2**) which follow the relationship:  $A_{P_{1-x}As_x} = (1-x)A_P + xA_{As}$  (where  $A_x$  is the parameter of interest).<sup>45</sup> The Rietveld refined cell volumes for each ball milled composition agrees with the values obtained from CVT and mercury flux synthesized single crystals and polycrystalline powders including the apparent deviation from linearity for the  $c$  lattice parameter.<sup>29</sup>

**Figure 3.4** shows the low arsenic (0-10 at%) XRD and Raman spectra more clearly; even at low arsenic concentrations the peak shifts are apparent. Gaussian fits to the Raman peaks for arsenic compositions from 0-30 at% in **Figure 3.5** show a linear trend in the peak shifts of  $A^1_g$ ,  $B_{2g}$ , and  $A^2_g$  modes from 0-10 at% with deviation from linearity observed beyond 10 at% arsenic. The  $A^1_g$  mode was relatively unaffected only shifting approximately 2.5  $\text{cm}^{-1}$  between the 0 and 10 at% samples whereas the  $A^2_g$  mode had the largest shift of 7.9  $\text{cm}^{-1}$ . Multiple new modes at lower wavenumbers and severe peak distortion of the original three pure BP modes occurred above 10 at% arsenic indicating new phonon modes are formed with higher levels of arsenic alloying.

A study on the synthesis kinetics was performed on the o-PAs composition with 50 at% arsenic using the planetary ball mill with five-gram charges. Under nearly identical synthesis conditions as recently reported for pure BP production by ball milling, the addition of arsenic did not significantly alter the synthesis kinetics, energies, or times but the mechanistic steps are different.<sup>39</sup> Unlike pure BP milling which undergoes an amorphous to crystalline pressure induced phase transformation, addition of arsenic makes this process similar to a binary reaction between two elements. **Figure 3.6(a)** shows the XRD patterns from a time-resolved study on the PAs 50 at% arsenic composition while **Figure 3.6(b)** shows the estimated phase fraction for the same time intervals. From **Figure 3.6(c)**, the rate constant,  $k$  [ $\text{min}^{-1}$ ], is extracted by applying a linear regression on the logarithm of the unconverted phase fraction versus time.<sup>39,46</sup> The conversion at 600 rpm is comparable to that of pure BP with minor deviation from linearity from 0-30 wt% portion which was also observed in the pure BP trials. Within five minutes from the start of milling at 600 rpm, all of the red phosphorus powder has fully reacted with the arsenic powder to produce a nearly single phase of trigonal PAs powder; subsequent impacts then transform the t-PAs into the o-PAs phase. The rate constant for o-PAs 50 at% was slightly faster at  $3.4 \times 10^{-2} \text{ min}^{-1}$  versus pure BP at  $2.5 \times 10^{-2} \text{ min}^{-1}$  under identical milling conditions.<sup>39</sup>

To verify composition of the alloyed powders, scanning electron microscopy (SEM) combined with energy dispersive spectroscopy (EDS) was performed on loose powders adhered to carbon tape as shown in **Figure 3.7(a)**. The powder morphology consists of large plates up to  $\sim 100 \mu\text{m}$  in lateral extent intermixed with smaller irregular particles, all produced by comminution from the grinding media inside the steel vessel.

The EDS spectra for the PAs alloys in **Figure 3.7(b)** shows the expected relative intensity changes for the phosphorus K line and arsenic L line for the target compositions. Overall, each composition from 1-90 at% arsenic was successfully produced with minor variations as listed in **Table 3.2**.

To explore the bonding between phosphorus and arsenic atoms, x-ray photoelectron spectroscopy (XPS) was performed on the low arsenic content samples as shown in **Figure 3.8**. The spectra for arsenic 3d and phosphorus 2p core levels indicate covalent bonding between phosphorus and arsenic. Using orthorhombic arsenic as a reference, the arsenic 3d peak should reside near 41.6 eV.<sup>21,35,47,48</sup> At low arsenic content (<10 at%), arsenic forms a covalent bond with phosphorus and acts as a charge transfer element within the black phosphorus lattice – resulting in a shoulder sub-band at ~40.2 eV for the arsenic 3d spectrum and at ~128.6 eV for the phosphorus 2p spectrum. This is expected as the electronegativity difference between phosphorus and arsenic is about 0.01; phosphorus is slightly more electronegative and will tend to pull electrons away from arsenic possibly acting as a n-type dopant at low concentrations. Further electrical characterization is necessary to elucidate effects on carrier concentrations.

Transmission electron microscopy (TEM) with EDS and scanning TEM (STEM) was performed on ball mill exfoliated flakes of the o-PAs 20 at% alloy as shown in **Figure 3.9**. TEM results on the o-PAs 60 and t-PAs 80 at% arsenic samples are included in **Figure 3.10** and **Figure 3.11**. The selected area electron diffraction (SAED) pattern in **Figure 3.9(a)** shows bright rings (corresponding to the 040 and 111 planes; i.e., overlapped peaks near 34° in the XRD patterns) highlighting the polycrystalline structure of the flakes imaged in **Figure 3.9(b)**. Within this representative sample, flakes with

lateral sizes ranged from about 50–500 nm; whereas previous particle size analysis on exfoliated BP indicated that wet ball milling can produce size distributions from 100–1000 nm.<sup>39</sup> The STEM EDS map scans in **Figure 3.9(c,d)** show uniform distribution of phosphorus and arsenic atoms and no unreacted arsenic chunks were observed. The one-to-one correspondence of phosphorus and arsenic elemental maps suggests complete atomic mixing between the starting red phosphorus and grey arsenic powders producing a solid solution alloy. Lattice fringes from overlapped flakes shown in **Figure 3.9(e)** also confirm the crystallinity of the flakes after wet ball mill exfoliation in isopropanol. Particle size analysis in **Figure 3.12** on ultrasonic probe tip exfoliated samples used to produce the PL and UV solutions show comparable size distributions for all compositions similar to that observed on pure BP produced by wet ball milling.

The optical emission and absorption spectra on ultrasonic tip probe exfoliated few-layer PAs alloys are presented in **Figure 3.13(a)** and **Figure 3.14**, respectively. The exfoliated alloys were drop-cast onto high purity electrically fused quartz slides and encapsulated with a thick poly(methyl methacrylate) (PMMA) layer to prevent oxidation and degradation during exposure to the 532 nm excitation laser. The drop cast solutions are polydisperse and contain presumably monolayer through at least five-layer thick flakes. The optical transitions cover the visible (1-layer) to at least the long wavelength edge of the InGaAs detector (1700 nm).<sup>49</sup> The weak narrow peaks at 1.54 eV and 1.95 eV are artifacts from the 532 nm laser (808 nm pump) and from a strong PMMA or residual IPA Raman mode that appears at 630 nm when excited with a 532 nm laser source. Differences in the relative intensity from the underlying P-As flakes and the PMMA thickness or amount of IPA residue may mask these peaks. **Figure 3.13(b)** presents the

experimental PL and UV-Vis estimate for the optical transition for each composition comparing them to literature predictions for the monolayer electronic and optical bandgap as calculated using density functional theory and the GW approximation for the many body quasi-particle effects on the exciton binding energy.<sup>1,5,12</sup> The ball milled PAs alloys have transitions nearer to the electronic gap indicating a low exciton binding energy presumably due to a self-screening effect<sup>50-52</sup> since the PL was performed on clumps of multi-layer PAs. The dielectric constant of PAs is comparable to pure silicon resulting in a small exciton binding energy (<100 meV). This contrasts with other reports in the literature which use silicon dioxide substrates and thin materials (~nanometers) that results in a red shift of the peak due to a larger exciton binding energy on these substrates (300 meV).<sup>53-56</sup> While the majority of the existing literature focuses on the monolayer case for a few compositions (0, 25, 50, 75, 83 at% arsenic), new theoretical and experimental work should accurately predict (i.e., GW approximation) and measure the bandgap of 2-layer and thicker o-PAs and t-PAs alloys.

**Figure 3.15** shows the near infrared PL obtained with a thermoelectrically cooled InGasAs detector using a 532 nm laser for illumination. Like pure BP, the o-PAs alloys also exhibit strong PL response in the NIR with broad overlapped peaks near 0.8 eV (1500 nm). Due to the polydispersity of the exfoliated solutions, sub-micron flake sizes, and nanostructured grains obtained from ball mill synthesized powders, no attempt to obtain the layer-by-layer PL response was made. As observed in **Figure 3.9(e)**, the flakes are polycrystalline with individual grains fused together through the repeated media impacts within the planetary milling vessel. The lack of infrared emission in some compositions is attributed to insufficient sampling to find few-layer flakes with sufficient

emission to be detectable. Nonetheless, PL from several of the exfoliated samples demonstrate the visible and NIR optical properties of few-layer o-PAs and t-PAs alloys.

The HEBM synthesis of multi-gram scale quantities of PAs alloy powders for use in solution based additive manufacturing technologies (inkjet, aerosol, roll-to-roll, dipping, and spray-deposition, etc.) may enable high volume device fabrication and transform the optoelectronic industry. HEBM of PAs alloys provides a convenient source of stock powders for additive manufacturing; however, better understanding of the milling kinetics is paramount for commercial scale-up. In the initial stages of milling of the o-PAs 50 at% arsenic sample, red phosphorus and arsenic rapidly react to produce the t-PAs phase; even milling at a lower milling intensity (e.g. 300 rpm, not shown) resulted in the formation of this phase within only 30 minutes. Visually, the powder charge in the steel vessel appeared as a dull matte black, indicative of the complete consumption of the red phosphorus prior to the formation of any o-PAs as detectable by XRD. Only after about 15 minutes of ball milling at the highest milling intensity (i.e., 600 rpm) (or longer at lower rpm) did the o-PAs phase appear within the diffraction samples. This result is counterintuitive based on the CVT work by Osters *et al.*<sup>29</sup> They noted that o-PAs would form when the arsenic content was below 83 at% and they also calculated that the energy stability and thermodynamic free energy of the o-PAs phase was in all cases more favorable than the t-PAs phase below 70-83 at% arsenic.<sup>29</sup> Likewise, the recent vapor phase synthesis of o-PAs and t-PAs alloys indicated a preference for o-PAs when the arsenic content was less than 70 at%.<sup>33</sup> Since phosphorus and arsenic allotropes both share the same orthorhombic (Cmca) and trigonal ( $R\bar{3}m$ ) crystal structures (see **Table 3.1**), have the same valency, similar electronegativity, and atomic radii are within 15 %,

the formation of substitutional solid solution alloys is expected.<sup>57</sup> Addition of trigonal arsenic may stabilize the high-pressure phase of phosphorus. Hints from in-situ XRD and Raman studies on pure BP during high pressure experiments suggest that the trigonal phase may be more readily formed chemically but is not as stable as orthorhombic BP upon decompression.<sup>58</sup> Adding arsenic simply makes the trigonal phase stable enough to be retained at ambient pressure during the initial short milling times; longer milling times with successive high energy impacts then drives the system towards the kinetically hindered but more thermodynamically stable orthorhombic structure.

The transition from orthorhombic to trigonal PAs was observed near 70 at% arsenic. Recent room temperature HP experiments on pure black arsenic showed an irreversible phase transition from o-As to t-As upon decompression from the transition pressure regime (3.4-5.4 GPa) and this pressure is likely reduced when factoring in temperature and shear strain effects.<sup>59-65</sup> Inside a planetary ball mill, media collisions can produce localized pressure and temperature near 6 GPa and 200 °C, respectively.<sup>42</sup> It may be reasonably assumed that if trigonal arsenic is favored at higher pressures over orthorhombic black arsenic then, as the arsenic content approaches the solubility limit within o-PAs (near 83 at% arsenic), the high-pressure collisions may push the solid solution limit lower producing the t-PAs alloy at the lower observed limit of 70 at%. The transition at 70 at% arsenic observed in this work resides between the reported lower solubility near 60 at% arsenic as determined by HP<sup>24-26</sup> trials and the upper solubility limits of 74 at% (mercury flux)<sup>28</sup> or 83 at% (CVT).<sup>6</sup>

The overall reaction mechanism appears to consist of two steps; (fast step 1) alloying of amorphous red phosphorus and crystalline grey arsenic to form the trigonal

PAs alloy; (slow step 2) pressure induced phase transformation of trigonal PAs alloys into the orthorhombic PAs alloys. The limiting step is the slower transformation which took up to two hours of milling for the synthesis of five grams of o-PAs 50 at% arsenic.

Application of the deterministic impact model by Delogu and Cocco to that of phase transformations and binary reactions during mechanochemistry was used to estimate the rate constant and obtain a metric for comparing different synthesis conditions.<sup>46,66-69</sup> Although the process has two mechanistic steps, the majority of the synthesis time (>90%) reflects the second slower phase transformation of t-PAs to o-PAs. Therefore, fitting the conversion data excluding the initial (<5 at%) and final (>95 at%) phase fractions using an exponential model is a reasonable approximation. The rate constants between pure black phosphorus and o-PAs 50 at% arsenic synthesis were  $2.5 \times 10^{-2} \text{ min}^{-1}$  and  $3.4 \times 10^{-2} \text{ min}^{-1}$ , respectively; an increase of approximately 33%, indicating that arsenic (at this level) provides a modest conversion rate enhancement. Additional studies on the amount of arsenic needed for accelerating the conversion are warranted. A further study on the conversion kinetics of the t-PAs alloys should also be investigated.

From the definition of the unit cell where lattice parameter  $a$  is along the zigzag direction,  $b$  is along the stacking direction, and  $c$  is along the armchair direction as shown in **Figure 3.5**, it is instructive to compare the XRD results in **Figure 3.3** with the Raman results. The  $A^2_g$  mode (stretch along the armchair direction) shows the greatest peak shift while the  $c$  lattice parameter grows larger than that predicted by uniform lattice expansion. This may indicate a preference for arsenic to locate at specific sites that stretch the unit cell along the armchair direction which results in the dampening of the

highest frequency mode ( $A_g^2$ ) at  $460\text{ cm}^{-1}$ . Further studies using atomistic modeling of vibrational mode sensitivity to arsenic occupancy may better help reveal the atomic occupancies for low arsenic content o-PAs alloys.

As predicted by several theoretical works on the layer-dependent bandgaps of o-PAs alloys<sup>1-3</sup>, the photoluminescence on HEBM synthesized o-PAs and t-PAs powders exfoliated into few-layer flakes indicate a large optical transition near  $\sim 1.9\text{ eV}$  (corresponding to an emission centered near  $650\text{ nm}$ ). The main variable here is the exciton binding energy which is known to vary significantly for monolayer depending upon the substrate. Freestanding monolayer BP has an exciton binding energy of  $0.8\text{ eV}$ <sup>50</sup>, is reduced to  $0.3\text{ eV}$  on thick ( $90+\text{ nm}$ ) SiO<sub>2</sub>/Si, and further reduced to  $0.1\text{ eV}$  on silicon with a  $10\text{ nm}$  SiO<sub>2</sub> native oxide.<sup>56</sup> The measurements here were performed on thick non-centrifuged poly-dispersed drop-casted samples encapsulated with PMMA. Visually, under  $100\times$  magnification, the clumps appear to be large agglomerates of multilayer BP with some fraction likely consisting of monolayer flakes, possibly with turbostratic stacking. That is, the dielectric environment of the monolayer BP present is most likely that of other monolayers, or thicker flakes of BP, such that the exciton binding energy is negligible or less than  $0.1\text{ eV}$  since BP has a similar dielectric constant as silicon. The PL results in **Figure 3.13** show a relatively constant peak near  $1.8\text{-}2.0\text{ eV}$  for all compositions which is in line with theoretical predictions.

Additionally, the photoluminescence from exfoliated few-layer trigonal PAs alloys shown in **Figure 3.13(a)** matches the predicted and observed energy gaps for few-layer trigonal arsenene, although the reports are inconclusive if the gap is direct or indirect.<sup>12,19,70-73</sup> Presumably, adding  $10\text{-}30\text{ at}\%$  phosphorus into the trigonal arsenic

crystal may result in a direct gap; or at the very least, an optical transition that is readily observed at room temperature. A future study with detailed atomistic modeling of the effect of phosphorus alloying on the few-layer optical and electronic band structure of arsenene would be of great benefit.

From the data collected here, the optical transitions at 1.8-2.0 eV are inferred to be from monolayer o-PAs or t-PAs assuming a negligible exciton due to the surrounding BP self-screening the monolayer from the quartz substrate. The claim of monolayer is tentative as separating the nanomaterial agglomerates into individual flakes required to make accurate atomic force microscopy measurements to definitively show monolayer was challenging. The PL results here agree with GW approximations for monolayers. Arguably, optical transitions from thick flakes with higher order transitions (corresponding to the visible emission detected at 650 nm) are generally unresolved at room temperature. An outstanding question is if the addition of phosphorus into the trigonal arsenic structure expands the layer dependent bandgap range, such that 3- or 4- layers would also have a narrow bandgap before the onset of semimetal behavior. Confirmation of visible and NIR emission in both alloy series extends the wavelength regime from MWIR into the Vis-NIR spectrum. While recent literature emphasizes the mid-IR applications of orthorhombic black-arsenic alloys, emission within the visible spectrum suggests applications such as biomedical photothermal treatment, facial recognition, visible lasers and detectors.

In summary, we have demonstrated high energy planetary ball milling as a direct route to produce orthorhombic and trigonal phosphorus arsenic solid solution alloys and investigated the optical behavior at the few-layer limit. The rate limiting step in the

conversion process is the slow transformation of t-PAs into o-PAs; the synthesis time is comparable to pure BP synthesis. An enhanced solubility of phosphorus into the trigonal P-As alloy was observed. The exfoliated flakes contained crystalline domains within an amorphous matrix and arsenic and phosphorus were uniformly distributed within the crystals. Emission in the visible and NIR regimes from both orthorhombic and trigonal P-As alloys suggest an optical gap comparable to pure BP but a layer-by-layer study could help to delineate the layer dependency. High volume synthesis of commodity-grade P-As alloyed powers is a step forward towards nanomaterials in commercial optoelectronic devices.

### 3.3 Conclusion

In summary, we have demonstrated high energy planetary ball milling as a direct route to produce orthorhombic and trigonal phosphorus-arsenic solid solution alloys and investigated the optical behavior at the few-layer limit. The rate limiting step in the conversion process is the slow transformation of t-PAs into o-PAs; the synthesis time is comparable to pure BP synthesis. An enhanced solubility of phosphorus into the trigonal PAs alloy was observed. The exfoliated flakes contained crystalline domains within an amorphous matrix and arsenic and phosphorus were uniformly distributed within the crystals. Emission in the visible and NIR regimes from both orthorhombic and trigonal PAs alloys suggest an optical gap comparable to pure BP but a layer-by-layer study could help to delineate the layer dependency. More studies, both theoretical and experimental, are required to discern the layer by layer behavior of PAs alloys. High volume synthesis

of commodity-grade PAs alloyed powders is a step forward towards nanomaterials in commercial optoelectronic devices.

### 3.4 Methods

**In the milling experiment**, elemental red phosphorus (1-5 g) (Alfa Aesar, 97% purity, -60 mesh) and elemental arsenic (1-5 g) (Alfa Aesar, 99.99% purity, -200 mesh) and stainless steel media (10 mm diameter, 100 g) were weighed and loaded into a stainless steel vessel (250 mL) inside an argon atmosphere glovebox ( $P_{O_2} < 0.1$  ppm) and sealed under argon (90-95 kPa) at room temperature. The ball to powder mass ratio was 20:1. All milling experiments were conducted with the PM100 planetary ball mill (Retsch, Germany) with pauses in the milling cycles (15 minutes on, 30 minutes off) to prevent overheating of the unit and to switch the direction of flywheel rotation (promotes better mixing). Milling conditions (rpm and duration) were held constant at 600 rpm and 14 hours of milling.

**To obtain few-layer PAs suspensions**, the converted powder (0.1 g) are solvent exfoliated in isopropanol (30 mL) using a high-energy mixer mill (Spex 8000) with small (1 mm) diameter chrome steel ball media sealed inside a steel vessel (50 mL) for 12 hours at approximately 1000 cycles per minute. These solutions were used for TEM measurements. Exfoliation with anaerobic conditions with an ultrasonic probe tip sonicator with a cooling bath was used to obtain few-layer suspensions in IPA.<sup>49</sup> These solutions were dropcast onto high purity electrically fused quartz slides (to eliminate the Si peak in PL measurements). UV-Vis measurements were performed on ultrasonic tip

probe exfoliated solutions with optical densities between 0.3-1.0 and measured with a quartz cuvette using the SpectroVis Plus spectrometer (Vernier, USA).

**Powder X-ray diffraction (XRD)** data was obtained in the Bragg-Brentano geometry ( $\text{CuK}\alpha$ , Rigaku MiniFlex 600, Japan) on powder (0.165 g) sealed inside a polyimide dome within an argon glovebox to prevent ignition with air during x-ray measurements. The internal standard method using NIST Silicon 640D powder (ICSD #51688) was added in trace amounts to enable correction for vertical displacement errors with the polyimide dome x-ray accessory (Rigaku, accessory 2392B101). Rietveld refinement was performed using the GSAS-II software and the crystal information file of the  $\text{P}_{0.47}\text{As}_{0.53}$  compound (ICSD #611147) with occupancies set to the nominal composition of each sample. Refined factors included phase fraction, sample displacement, preferred orientation, unit cell parameters, strain, and crystallite size.

**Raman spectroscopy (Raman)** data was obtained (Horiba LabRam HR Evolution, Japan) on densely packed powder samples (0.01 g) prepared inside an argon glovebox that were sealed inside a custom-built enclosure with a sapphire window to prevent oxidation and ignition during measurements. A 50 mW 532nm laser source (Nd:YAG) was used to generate spectra collected with a Si CCD. Spectra obtained at 20X objective with repeat acquisitions for 60 seconds at ten random locations throughout the bulk surface using the 1800 lines/mm grating, at room temperature.

**Photoluminescence (PL)** measurements were obtained using two detectors for visible and infrared measurements. Exfoliated PAs samples were drop-cast in three locations onto electrically fused quartz slides, followed by immediate (<1 minute) PMMA encapsulation using a 200°C bakeout for 10 minutes to cure the PMMA film.

Each PAs spot was measured at least three times resulting in an average of 9 measurements per composition. A Princeton Aston spectrometer coupled with a silicon CCD (visible) and NIRvana InGaAs (NIR) thermoelectrically cooled array and an excitation wavelength of 532 nm at 40 mW was used to obtain the visible and infrared spectra. Data were collected for 5 seconds using a 100X near-infrared objective.

**Scanning electron microscopy (SEM)** was performed on powders pressed onto carbon tape and imaged at low beam currents (50 pA to 50 nA) and intermediate accelerating voltages (5-20 keV) using a FEI Teneo FESEM.

**X-ray photoelectron spectroscopy (XPS)** was performed on samples prepared inside an argon glovebox by pressing PAs powders into indium foil and transferred to the XPS with transfer chamber. XPS spectra were collected using a Physical Electronics Versaprobe system with a monochromatic Al  $K_{\alpha}$  X-ray source utilizing a beam diameter of 100  $\mu\text{m}$  and 25 W of power. For general survey scans, a pass energy of 117.4 eV and an energy step size of 0.8 eV was used. For higher resolution core level scans, a pass energy of 23.5 eV and an energy step size of 0.2 eV was used.

**Transmission electron microscopy (TEM)** was performed using a JEOL-JEM-2100, Japan, with Orius SC1000 CCD camera; samples were drop-cast onto lacy carbon grids and transferred into the vacuum chamber within 5 min. A low accelerating voltage of 100 keV was used with minimal dwell times roughly 30 seconds for imaging to prevent the amorphization of the flakes.

### **Acknowledgements**

This work has been funded, in part, by Boise State University College of Engineering Seed Funding Program and IGEM Commerce (grant number 003786). Materials were synthesized and processed in the Advanced Materials Laboratory (Boise State University, Boise, ID). XRD, SEM, and TEM were performed in the Boise State Center for Materials Characterization (Boise State University, Boise, ID). Acknowledgements to Dr. Karthik Chinnathambi for TEM support. Raman spectroscopy was performed in the Advanced Nanomaterials and Manufacturing Laboratory (Boise State University, Boise, ID). Photoluminescence Spectroscopy was performed at the Center for Nanoscale Materials, an Office of Science user facility, and was supported by the U.S. Department of Energy, Office of Science, Office of Basic Energy Sciences, under Contract No. DE-AC02-06CH11357. F.M., J.E., and D.E., acknowledge support through the Center for Advanced Energy Studies and AFWERX STTR award #FA8649-20-P-0986. S.P., C.G., and B.J. acknowledge support through the Center for Advanced Energy Studies and the IGEM Commerce (grant number 003786).

### **Author Contributions**

S.P. conceptualized and executed the milling studies, performed and analyzed the characterization data. C. G. performed SEM and PSA measurements. F. M. and J. E. performed XPS measurements. C.H. performed PL measurements. F.M. exfoliated and prepared the PMMA encapsulated samples. F.M. performed XPS measurements. J.W. discussed the data, analyzed the XPS data and provided useful suggestions. S.P. wrote the

manuscript with comments and edits from all co-authors. D.E. and B.J. supervised and directed the project.

### **Competing Interests**

C. Husko and J. Wood are equity holders in Iris Light Technologies.

## References

- 1 Shu, H. & Guo, J. Electronic and optical properties of phosphorene-like arsenic phosphorus: a many-body study. *Mater. Res. Express* **5**, 036302 (2018)
- 2 Luo, K., Chen, S. & Duan, C. Indirect-direct band gap transition of two-dimensional arsenic layered semiconductors—cousins of black phosphorus. *Sci China-Phys Mech Astron* **58**, 87301 (2015)
- 3 Shojaei, F. & Kang, H. S. Electronic Structure and Carrier Mobility of Two-Dimensional  $\alpha$  Arsenic Phosphide. *J Phys Chem C* **119**, 20210-20216 (2015)
- 4 Zhang, Z. *et al.* Manifestation of unexpected semiconducting properties in few-layer orthorhombic arsenene. *Appl. Phys. Express* **8**, 055201 (2015)
- 5 Kamal, C. & Ezawa, M. Arsenene: Two-dimensional buckled and puckered honeycomb arsenic systems. *Phys. Rev. B* **91**, 085423 (2015)
- 6 Liu, B. *et al.* Black Arsenic–Phosphorus: Layered Anisotropic Infrared Semiconductors with Highly Tunable Compositions and Properties. *Adv. Mater.* **27**, 4423-4429 (2015)
- 7 Long, M. *et al.* Room temperature high-detectivity mid-infrared photodetectors based on black arsenic phosphorus. *Sci. Adv.* **3**, e1700589 (2017)
- 8 Yu, L. *et al.* Electrically tunable optical properties of few-layer black arsenic phosphorus. *Nanotechnol.* **29**, 484001 (2018)
- 9 Shi, X. *et al.* Synthesis of black arsenic-phosphorus and its application for Er-doped fiber ultrashort laser generation. *Opt. Mater. Express* **9**, 2348-2357 (2019)
- 10 Chen, C. *et al.* Bandgap opening in layered gray arsenic alloy. *APL Mater.* **9**, 041102 (2021)
- 11 Liu, Y. *et al.* Band Structure, Band Offsets, and Intrinsic Defect Properties of Few-Layer Arsenic and Antimony. *J. Phys. Chem. C* **124**, 7441-7448 (2020)
- 12 Zhu, Z., Guan, J. & Tománek, D. Strain-induced metal-semiconductor transition in monolayers and bilayers of gray arsenic: A computational study. *Phys. Rev. B* **91**, 161404 (2015)
- 13 Liu, M.-Y., Huang, Y., Chen, Q.-Y., Cao, C. & He, Y. Unexpected electronic structure of the alloyed and doped arsenene sheets: First-Principles calculations. *Sci. Rep.* **6**, 29114 (2016)
- 14 Young, E. P. *et al.* Wafer-Scale Black Arsenic–Phosphorus Thin-Film Synthesis Validated with Density Functional Perturbation Theory Predictions. *ACS Appl. Nano Mater.* **1**, 4737-4745 (2018)
- 15 Zhong, M. *et al.* Thickness-Dependent Carrier Transport Characteristics of a New 2D Elemental Semiconductor: Black Arsenic. *Adv. Funct. Mater.* **28**, (2018)
- 16 Ryzhii, V., Ryzhii, M., Mitin, V., Shur, M. S. & Otsuji, T. Far-infrared photodetectors based on graphene/black-AsP heterostructures. *Opt. Express* **28**, 2480-2498 (2020)
- 17 Amani, M., Regan, E., Bullock, J., Ahn, G. H. & Javey, A. Mid-Wave Infrared Photoconductors Based on Black Phosphorus-Arsenic Alloys. *ACS Nano* **11**, 11724-11731 (2017)
- 18 Yuan, S. *et al.* Air-Stable Room-Temperature Mid-Infrared Photodetectors Based on hBN/Black Arsenic Phosphorus/hBN Heterostructures. *Nano Lett.* **18**, 3172-3179 (2018)

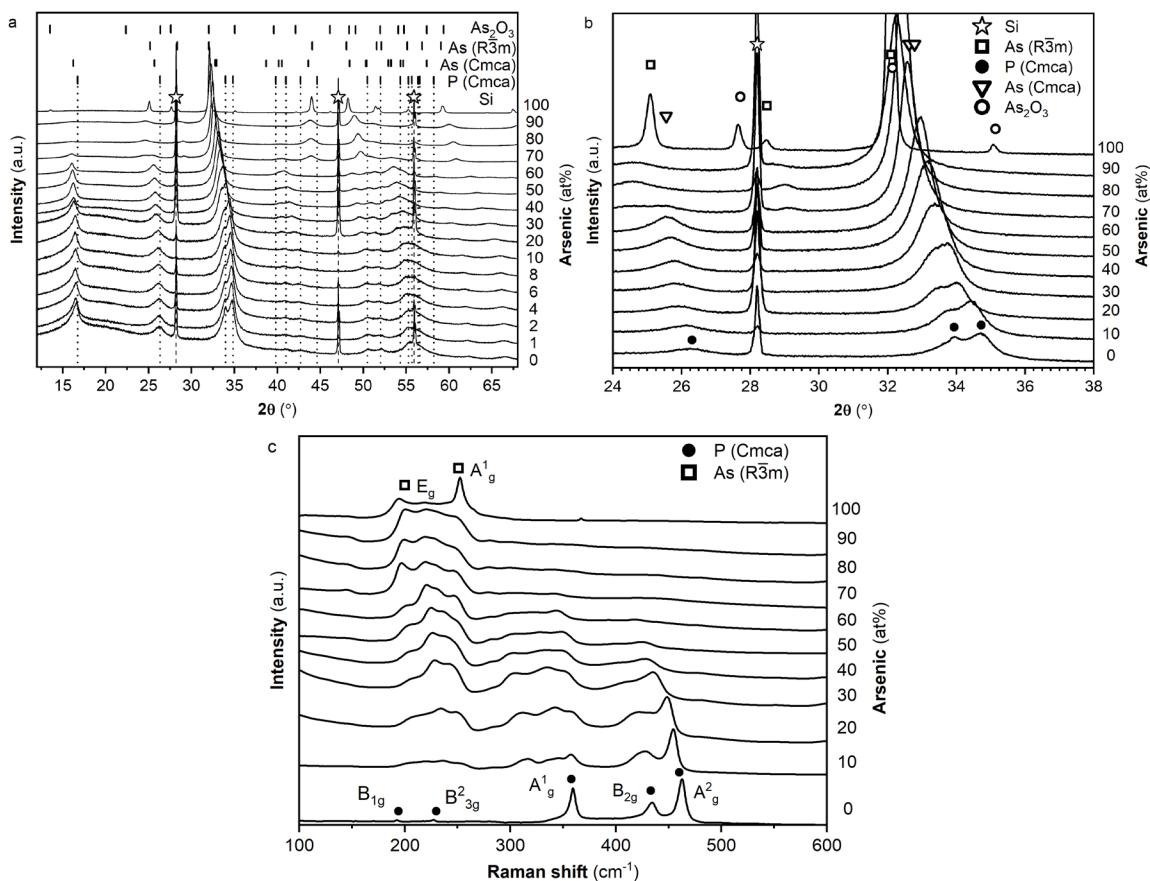
- 19 Xie, M. *et al.* A promising two-dimensional solar cell donor: Black arsenic–phosphorus monolayer with 1.54eV direct bandgap and mobility exceeding  $14,000\text{cm}^2\text{V}^{-1}\text{s}^{-1}$ . *Nano Energy* **28**, 433-439 (2016)
- 20 Abbas, A. N. *et al.* Black Phosphorus Gas Sensors. *ACS Nano* **9**, 5618-5624 (2015)
- 21 Luxa, J., Bouša, D., Zoller, F., Fattakhova-Rohlfing, D. & Sofer, Z. Black phosphorus–arsenic alloys for lithium ion batteries. *FlatChem* **19**, 100143 (2020)
- 22 Yun, S. H. & Kwok, S. J. J. Light in diagnosis, therapy and surgery. *Nat. Biomed. Eng.* **1**, 0008 (2017)
- 23 Karki, B., Rajapakse, M., Sumanasekera, G. U. & Jasinski, J. B. Structural and Thermoelectric Properties of Black Arsenic–Phosphorus. *ACS Appl. Energy Mater.* **3**, 8543-8551 (2020)
- 24 Shirotani, I., Kawamura, H., Tsuburaya, K. & Tachikawa, K. Superconductivity of Phosphorus and PhosphorusArsenic Alloy under High Pressures. *Jpn. J. Appl. Phys.* **26**, (1987)
- 25 Shirotani, I. *et al.* Superconductivity and phase transitions in phosphorus-arsenic alloy under high pressures. *Synth. Met.* **29**, 635-640 (1989)
- 26 Shirotani, I., Shiba, S., Takemura, K., Shimomura, O. & Yagi, T. Pressure-induced phase transitions of phosphorus-arsenic alloys. *Phys. B: Condens. Matter* **190**, 169-176 (1993)
- 27 Krebs, H., Weitz, H. & Worms, K. H. Über die Struktur und Eigenschaften der Halbmetalle. VIII. Die katalytische Darstellung des schwarzen Phosphors. *Z. Anorg. Allg. Chem.* **280**, 119-133 (1955)
- 28 Krebs, H., Holz, W. & Worms, K. H. Über die Struktur und die Eigenschaften der Halbmetalle, X. Eine Neue Rhombische Arsenmodifikation und Ihre Mischkristallbildung mit Schwarzem Phosphor. *Chem. Ber.* **90**, 1031-1037 (1957)
- 29 Osters, O. *et al.* Synthesis and Identification of Metastable Compounds: Black Arsenic—Science or Fiction? *Angew. Chem. Int. Ed* **51**, 2994-2997 (2012)
- 30 Xu, Y. *et al.* Epitaxial nucleation and lateral growth of high-crystalline black phosphorus films on silicon. *Nat. Commun.* **11**, 1330 (2020)
- 31 Izquierdo, N., Myers, J. C., Seaton, N. C. A., Pandey, S. K. & Campbell, S. A. Thin-Film Deposition of Surface Passivated Black Phosphorus. *ASC Nano* **13**, 7091-7099 (2019)
- 32 Izquierdo, N. *Thin Film Growth of Black Phosphorus and Black Arsenic Phosphorus* 28150586 thesis, University of Minnesota, (2020).
- 33 Antonatos, N., Mazánek, V., Plutnarová, I. & Sofer, Z. Mineralizer-Free Synthesis of Orthorhombic Arsenic-Phosphorus Alloys. *FlatChem* 100297 (2021)
- 34 Maple, T. G. *Thermodynamic properties of elemental phosphorus* Doctoral thesis, Massachusetts Institute of Technology, (1949).
- 35 Antonatos, N., Mazánek, V., Lazar, P., Sturala, J. & Sofer, Z. Acetonitrile-assisted exfoliation of layered grey and black arsenic: contrasting properties. *Nanoscale Adv.* **2**, 1282-1289 (2020)
- 36 Jin, X. *et al.* 102 fs pulse generation from a long-term stable, inkjet-printed black phosphorus-mode-locked fiber laser. *Opt. Express* **26**, 12506-12513 (2018)
- 37 Torrisi, F. *et al.* Inkjet-Printed Graphene Electronics. *ACS Nano* **6**, 2992-3006 (2012)

- 38 Hu, G. *et al.* Black phosphorus ink formulation for inkjet printing of optoelectronics and photonics. *Nat. Commun.* **8**, 278 (2017)
- 39 Pedersen, S. V. *et al.* Mechanochemical conversion kinetics of red to black phosphorus and scaling parameters for high volume synthesis. *npj 2D Mater Appl* **4**, 36 (2020)
- 40 Park, C. M. & Sohn, H. J. Black Phosphorus and its Composite for Lithium Rechargeable Batteries. *Adv. Mater.* **19**, 2465-2468 (2007)
- 41 Ferrara, C. *et al.* Efficiency and Quality Issues in the Production of Black Phosphorus by Mechanochemical Synthesis: A Multi-Technique Approach. *ACS Appl. Energy Mater.* **2**, 2794-2802 (2019)
- 42 Suryanarayana, C. Mechanical alloying and milling. *Prog. Mater. Sci.* **46**, 1-184 (2001)
- 43 Suryanarayana, C. Recent developments in mechanical alloying. *Rev. Adv. Mater. Sci.* **18**, 203-211 (2008)
- 44 Kang, J. *et al.* Solvent Exfoliation of Electronic-Grade, Two-Dimensional Black Phosphorus. *ACS Nano* **9**, 3596-3604 (2015)
- 45 Cullity, B. D. & Stock, S. R. *Elements of x-ray diffraction*. 3rd ed. edn, (Prentice Hall, Upper Saddle River, NJ, 2001).
- 46 Delogu, F. A combined experimental and numerical approach to the kinetics of mechanically induced phase transformations. *Acta Mater.* **56**, 905-912 (2008)
- 47 Antonatos, N., Luxa, J., Sturala, J. & Sofer, Z. Black arsenic: a new synthetic method by catalytic crystallization of arsenic glass. *Nanoscale* **12**, 5397-5401 (2020)
- 48 Bouša, D., Otyepková, E., Lazar, P., Otyepka, M. & Sofer, Z. Surface Energy of Black Phosphorus Alloys with Arsenic. *Chem. Nano. Mat.* **6**, 821-826 (2020)
- 49 Kang, J. *et al.* Stable aqueous dispersions of optically and electronically active phosphorene. *Proc. Natl. Acad. Sci.* **113**, 11688-11693 (2016)
- 50 Tran, V., Fei, R. & Yang, L. Quasiparticle energies, excitons, and optical spectra of few-layer black phosphorus. *2D Mater.* **2**, 044014 (2015)
- 51 Zhang, G. *et al.* Determination of layer-dependent exciton binding energies in few-layer black phosphorus. *Sci. Adv.* **4**, eaap9977 (2018)
- 52 Wang, X. *et al.* Highly anisotropic and robust excitons in monolayer black phosphorus. *Nat. Nanotechnol.* **10**, 517-521 (2015)
- 53 Gauffrès, E. *et al.* Momentum-Resolved Dielectric Response of Free-Standing Mono-, Bi-, and Trilayer Black Phosphorus. *Nano Lett.* **19**, 8303-8310 (2019)
- 54 Ross, A. M., Paterno, G. M., Dal Conte, S., Scotognella, F. & Cinquanta, E. Anisotropic Complex Refractive Indices of Atomically Thin Materials: Determination of the Optical Constants of Few-Layer Black Phosphorus. *Materials* **13**, 12, 5736 (2020)
- 55 Surrente, A. *et al.* Onset of exciton-exciton annihilation in single-layer black phosphorus. *Phys. Rev. B* **94**, 075425 (2016)
- 56 Surrente, A. *et al.* Excitons in atomically thin black phosphorus. *Phys. Rev. B* **93**, 121405 (2016)
- 57 Hume-Rothery, W., Mabbott, G., W & Channel Evans, K. The freezing points, melting points, and solid solubility limits of the alloys of silver and copper with the elements of the b sub-groups. *Philos. Trans. Royal Soc. A* **233**, 1-97 (1934)

- 58 Rissi, E. N., Soignard, E., McKiernan, K. A., Benmore, C. J. & Yarger, J. L. Pressure-induced crystallization of amorphous red phosphorus. *Solid State Comm.* **152**, 390-394 (2012)
- 59 Gao, C. *et al.* Stability and Phase Transition of Metastable Black Arsenic under High Pressure. *J. Phys. Chem. Lett.* **11**, 93-98 (2020)
- 60 Levitas, V. I. Strain-induced nucleation at a dislocation pile-up: a nanoscale model for high pressure mechanochemistry. *Phys. Lett. A* **327**, 180-185 (2004)
- 61 Ji, C. *et al.* Shear-induced phase transition of nanocrystalline hexagonal boron nitride to wurtzitic structure at room temperature and lower pressure. *Proc. Natl. Acad. Sci.* **109**, 19108-19112 (2012)
- 62 Delogu, F. Are processing conditions similar in ball milling and high-pressure torsion? The case of the tetragonal-to-monoclinic phase transition in ZrO<sub>2</sub> powders. *Scr. Mater.* **67**, 340-343 (2012)
- 63 Bridgman, P. W. Effects of High Shearing Stress Combined with High Hydrostatic Pressure. *Phys Rev* **48**, 825-847 (1935)
- 64 Bridgman, P. W. Shearing Phenomena at High Pressures, Particularly in Inorganic Compounds. *Proc. Am. Acad. Arts Sci.* **71**, 387-460 (1937)
- 65 Jacobs, R. B. Phosphorus at High Temperatures and Pressures. *J. Chem. Phys.* **5**, 945-953 (1937)
- 66 Delogu, F., Mulas, G., Schiffrini, L. & Cocco, G. Mechanical work and conversion degree in mechanically induced processes. *Mat. Sci. Eng. A* **382**, 280-287 (2004)
- 67 Delogu, F. & Cocco, G. Weakness of the “hot spots” approach to the kinetics of mechanically induced phase transformations. *J. Alloys Compd.* **465**, 540-546 (2008)
- 68 Napolitano, E., Mulas, G., Enzo, S. & Delogu, F. Kinetics of mechanically induced anatase-to-rutile phase transformations under inelastic impact conditions. *Acta Mater.* **58**, 3798-3804 (2010)
- 69 Delogu, F. & Takacs, L. Information on the mechanism of mechanochemical reaction from detailed studies of the reaction kinetics. *J Mater Sci* **53**, 13331-13342 (2018)
- 70 Kecik, D., Durgun, E. & Ciraci, S. Optical properties of single-layer and bilayer arsenene phases. *Phys. Rev. B* **94**, 205410 (2016)
- 71 Yu, J., Katsnelson, M. I. & Yuan, S. Tunable electronic and magneto-optical properties of monolayer arsenene: From  $\mathcal{G}\mathcal{W}_0$  approximation to large-scale tight-binding propagation simulations. *Phys. Rev. B* **98**, 115117 (2018)
- 72 Shah, J., Wang, W., Sohail, H. M. & Uhrberg, R. I. G. Experimental evidence of monolayer arsenene: an exotic 2D semiconducting material. *2D Mater.* **7**, 025013 (2020)
- 73 Vishnoi, P., Mazumder, M., Pati, S. K. & R. Rao, C. N. Arsenene nanosheets and nanodots. *New J. Chem.* **42**, 14091-14095 (2018)
- 74 Zanatta, A. R. Revisiting the optical bandgap of semiconductors and the proposal of a unified methodology to its determination. *Sci. Rep.* **9**, 11225 (2019)
- 75 Gilliam, S. J. *et al.* Raman spectroscopy of arsenolite: crystalline cubic As<sub>4</sub>O<sub>6</sub>. *J. Solid State Chem.* **173**, 54-58 (2003)

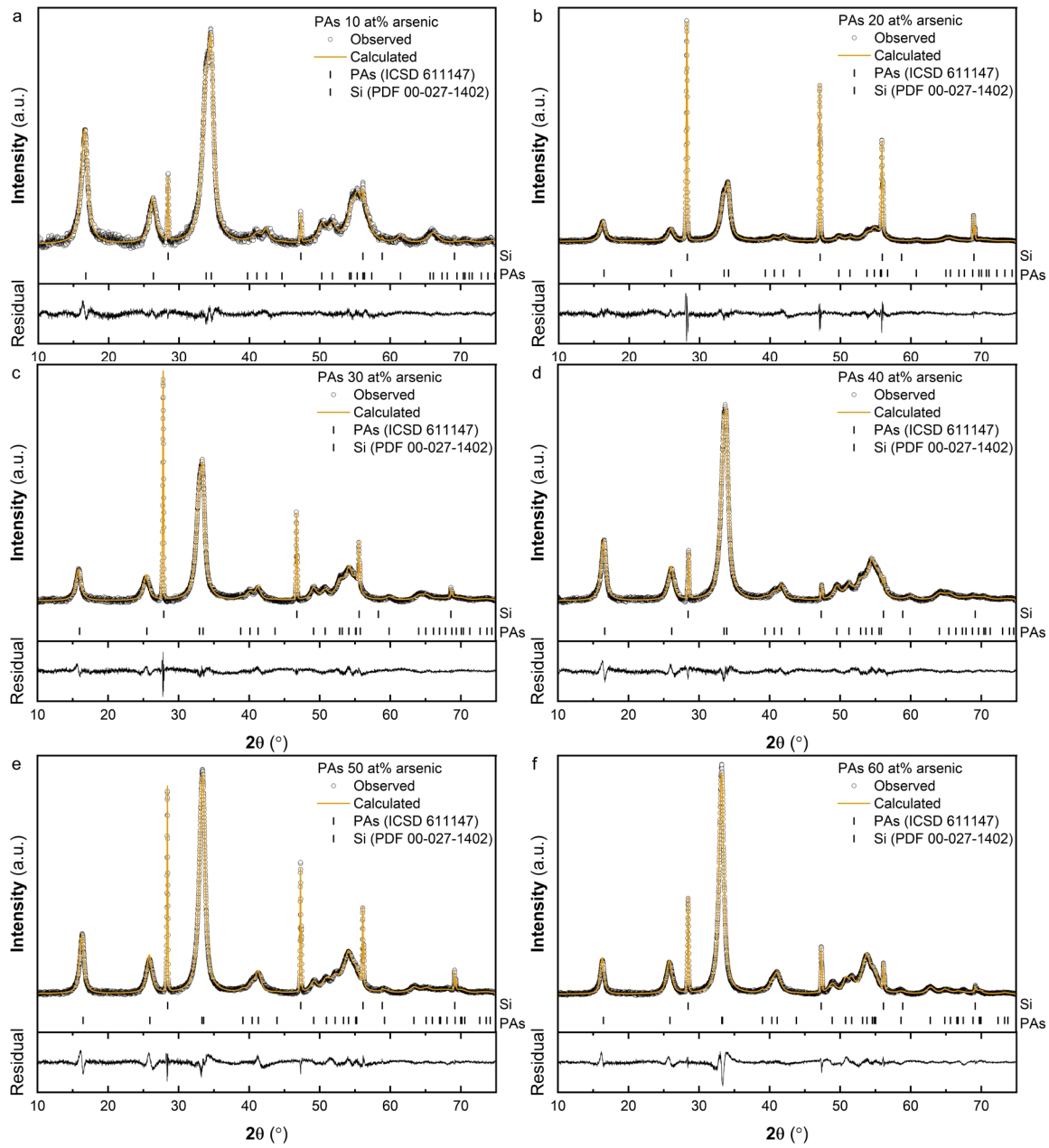
- 76 Grzechnik, A. Compressibility and Vibrational Modes in Solid As<sub>4</sub>O<sub>6</sub>. *J. Solid State Chem.* **144**, 416-422 (1999)

## Figures



**Figure 3.1 Structural characterization of mechanochemically synthesized P-As powders.**

(a) X-Ray diffraction (XRD) patterns with increasing arsenic content showing single phase o-PAs up to 60 at% and single-phase t-PAs at 80+ at%; patterns are normalized and vertically offset manually. Silicon (Si) reference standard (marked by stars, NIST 640D) added to samples to extract diffraction angles with high confidence during Rietveld refinements. Vertical markers are peak positions of reference patterns from ICSD for each phase, (b) XRD patterns focused on the main peaks near  $34^{\circ}$  show a steady decrease to lower diffraction angles due to lattice expansion. (c) Raman spectra of the same PAs powders showing the distinct vibrational modes resulting from the breakdown of the pure orthorhombic symmetry; additional modes at intermediate wavenumbers appear for the PAs alloys between the modes observed for pure orthorhombic BP and pure trigonal arsenic; all patterns are normalized and vertically offset.



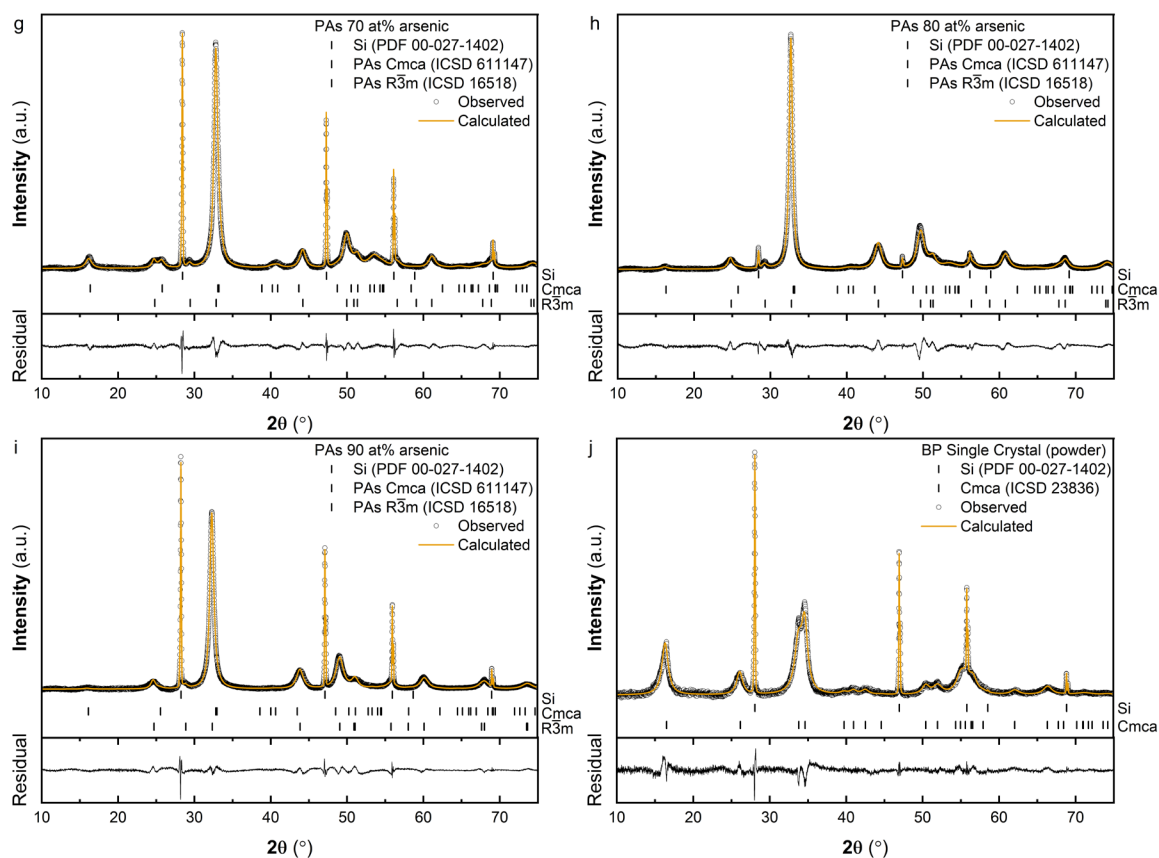


**Figure 3.2 Powder X-ray diffraction Rietveld refinement on ball mill synthesized P-As 10-90 at% arsenic composition.**

(a-f) single phase PAs alloys with the space group  $Cmca$ ; (g-i) the main phase is the trigonal  $R\bar{3}m$  phase with minor amounts of the  $Cmca$  phase (<5 wt%). (j) Refinement of a pure BP single crystal (HQ graphene) powdered using a Spex 8000 mixer mill for 5 minutes. Peaks from the NIST 640D silicon line standard (NIST PDF 00-027-1402, ICSD #51688) are also present and used to correct for sample displacement. Vertical markers indicate the peak positions for each phase. The crystal structure files for the  $Cmca$  and  $R\bar{3}m$  phases were manually adjusted such that the atomic occupancies of phosphorus and arsenic match the nominal composition based on the ICSD #61147 and #16518 crystallographic information files. Lattice parameters, peak broadening due to size and strain, and preferred orientation were refined sequentially after fitting the baseline with a Chebyshev polynomial. The silicon standard was separately refined using a La Bail extraction.

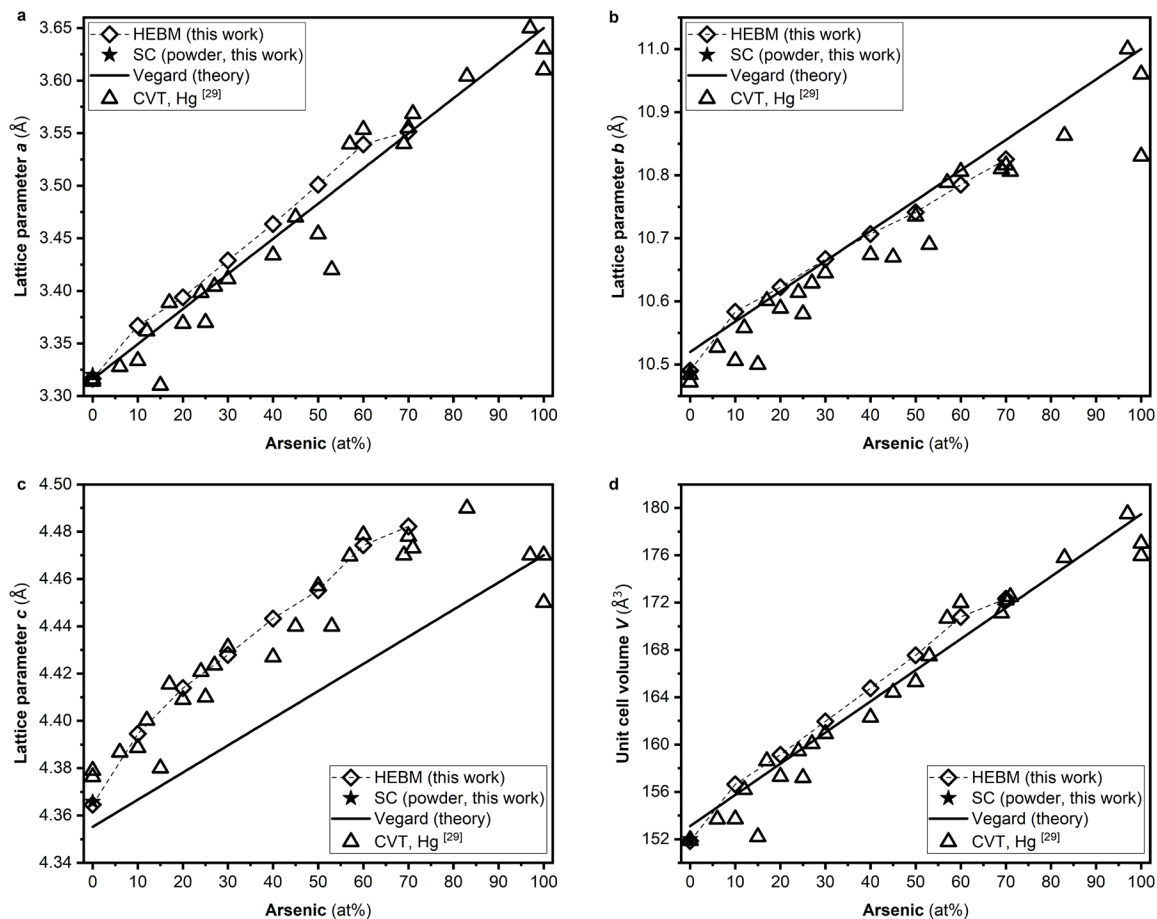


**Figure 3.3 Vegard behavior of lattice parameters and unit cell volume of o-PAs alloys.**

(a-c) Comparison of the theoretical linear Vegard trend for lattice parameters with results from ball mill synthesized o-PAs alloys (obtained by XRD Rietveld refinement) and literature values from CVT and mercury fluxed o-PAs alloys. The ball milled o-PAs lattice parameters a and b follow the linear trend as expected; a deviation consistent with literature is observed for the c lattice parameter, (d) The linear trend in the unit cell volume is clearly observed for all data sets.

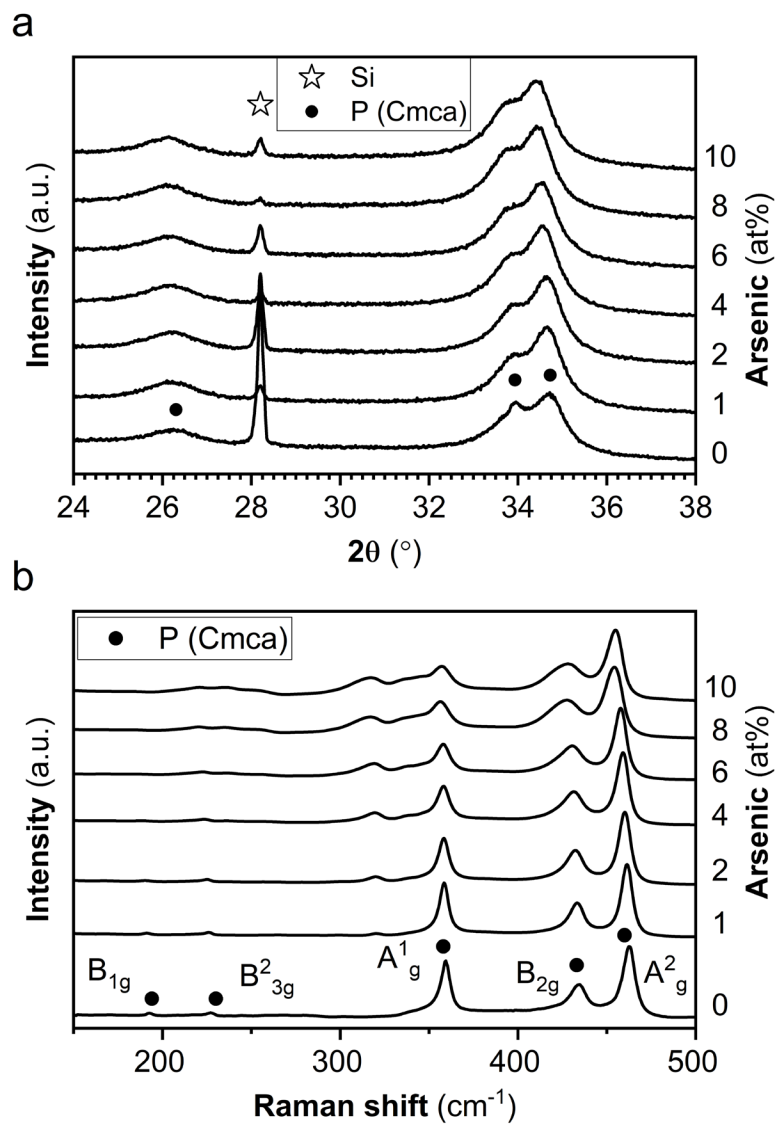


**Figure 3.4 Structural characterization of mechanochemically synthesized PAs powders at low arsenic content (0-10 at%).**

(a) X-Ray diffraction (XRD) patterns showing a slight shift of the main peaks; Si standard included for XRD refinement of sample displacement, (b) Raman spectra of the same PAs powders showing the distinct vibrational modes resulting from the breakdown of the pure orthorhombic symmetry; additional modes at intermediate wavenumbers. Markers for each phase detected are indicated for each pattern; all patterns normalized and vertically offset.

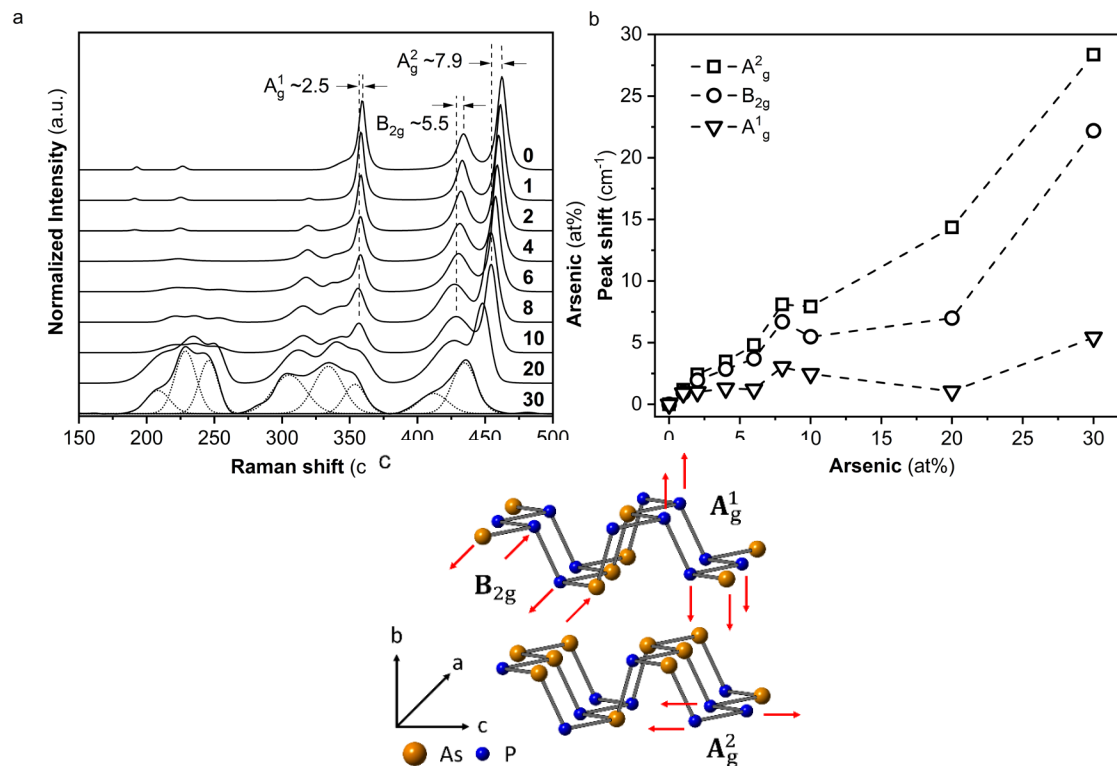


**Figure 3.5 Raman characterization of the P-As alloys from 0-30 at% arsenic.** (a) Raman spectra showing the gradual peak shifts of the main BP modes; vertical drop lines show the shift between the 0 and 10 at% samples for each mode. (b) Relative peak shift away from the 0 at% peak positions; a small linear region from 0-10 at% is evident, but deviation from nonlinear shift occurs between 10-20 at% which coincides with the loss of the distinct  $A_g^1$  mode and the merging of the  $B_{2g}$  and  $A_g^2$  modes along with multiple convoluted peaks between 200-375  $\text{cm}^{-1}$ . All patterns normalized and vertically offset, dashed lines are only visual aids, (c) Raman vibrations showing atom displacement, directions are indicated with red arrows.

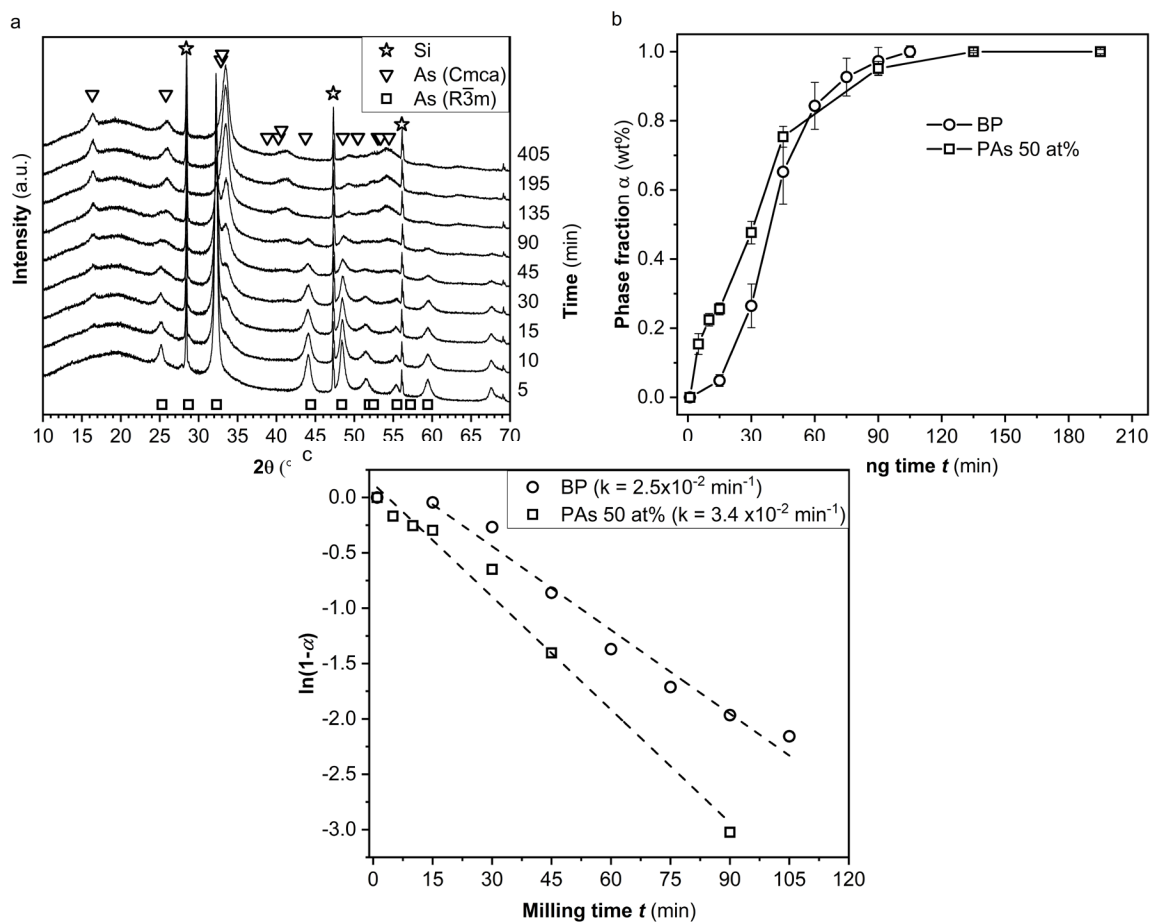


**Figure 3.6 Kinetics of orthorhombic PAs 50 at% synthesis.**

(a) XRD patterns of o-PAs 50 at% arsenic alloy sampled at incremental times for tracking phase evolution, (b) phase fraction versus milling time as compared to pure BP at 600 rpm; error bars are one standard deviation from three repeat runs, (c) plot of the logarithm of the unconverted phase fraction to obtain the rate constant,  $k$ , from the slope of the best fit straight line.

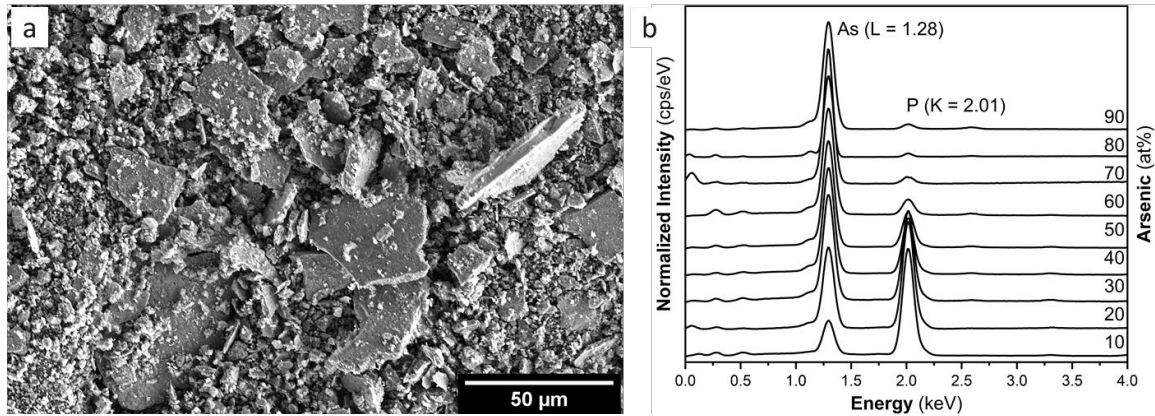


**Figure 3.7 Scanning electron microscopy of PAs alloyed powders.**

(a) The ball milled PAs alloy powders for all compositions exhibit large 100-micron plates intermixed with smaller irregular shaped particles as an outcome of the high pressure impacts and continuous grinding within the steel vessel, (b) representative energy dispersive x-ray spectra of the PAs samples showing the relative changes in the phosphorus K and arsenic L peak intensities as a function of alloy composition.

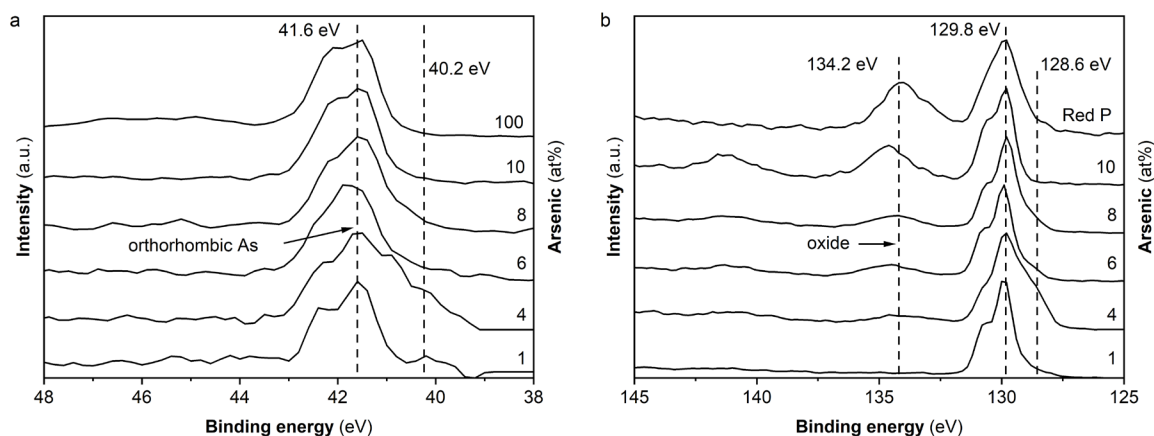


**Figure 3.8 X-ray photoelectron spectra (XPS) for P-As alloys generated by mechanochemical alloying.**

(a) As 3d and (b) P 2p core level spectra for increasing amounts of arsenic. At 41.6 eV, arsenic is configured in an orthorhombic form. At low arsenic concentration (<10 at%), the covalent arsenic acts as a charge transfer element within the host BP matrix, producing a new shoulder sub-band at ~40.2 eV for the As 3d spectrum and at ~128.6 eV for the P2p spectrum.

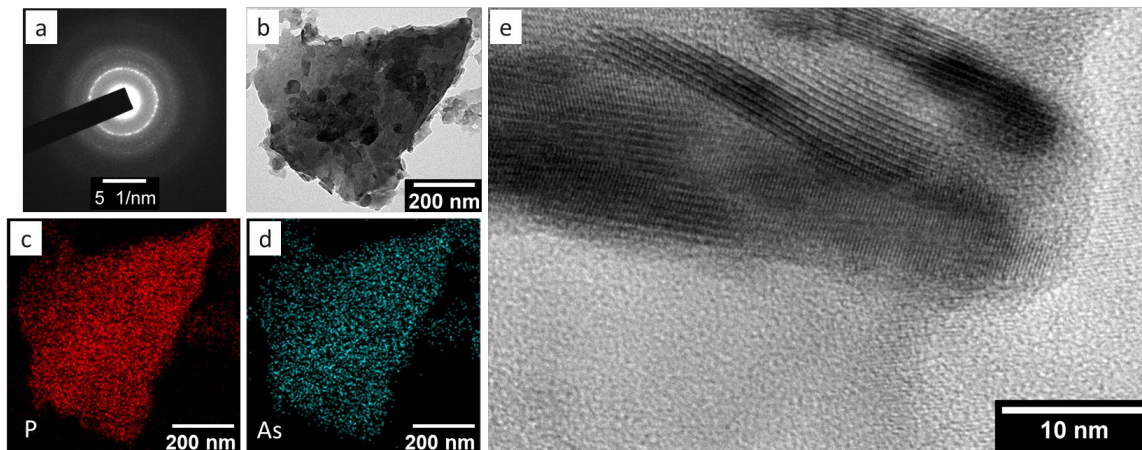


**Figure 3.9** Transmission electron microscopy on exfoliated flakes of an o-PAs 20 at% alloy.

(a) electron diffraction shows strong ring patterns (040, 111 planes) confirming the crystallinity of the exfoliated flakes and their match to the orthorhombic crystal structure, (b) exfoliated flakes with sizes ranging from 50 nm to 500 nm, (c,d) STEM EDS map scan for phosphorus and arsenic showing uniform distribution throughout the flakes, (e) lattice fringes of the crystalline flakes.

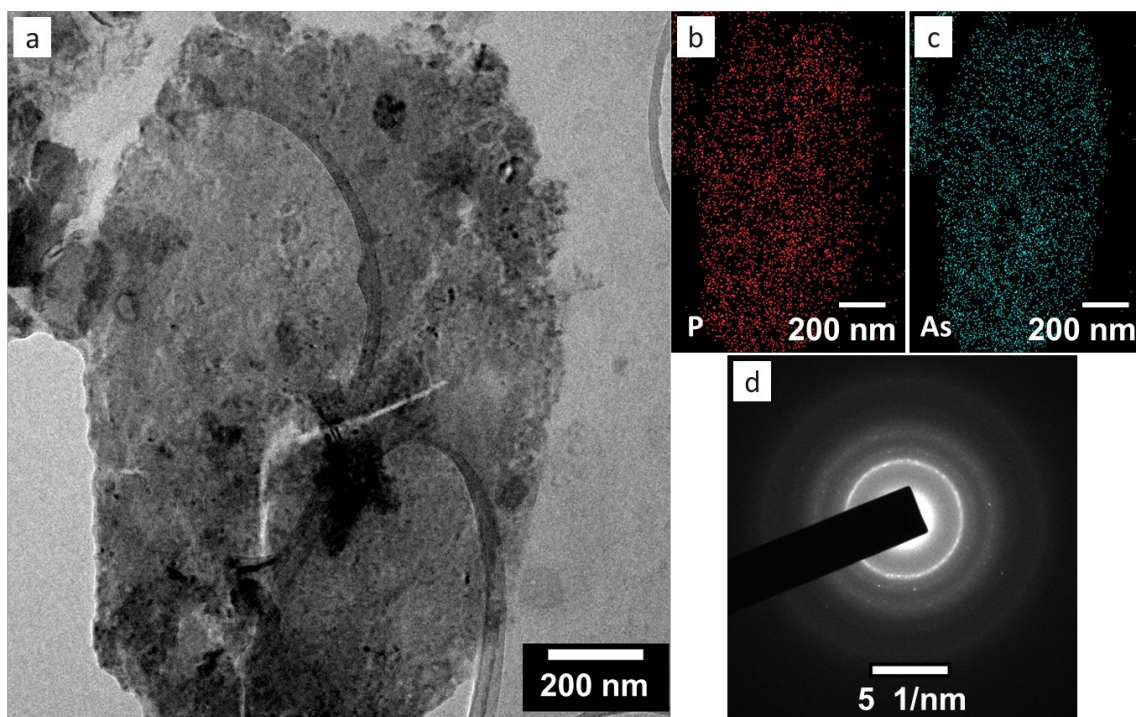


**Figure 3.10** Transmission electron microscopy on P-As 60 at % (*Cmca*) flakes. (a) Selected bright field image showing multiple overlapped flakes, (b,c) STEM maps showing the uniform distribution of phosphorus and arsenic throughout the flakes, (d) selected area electron diffraction pattern from the multi-flake confirming the crystallinity of the flakes.

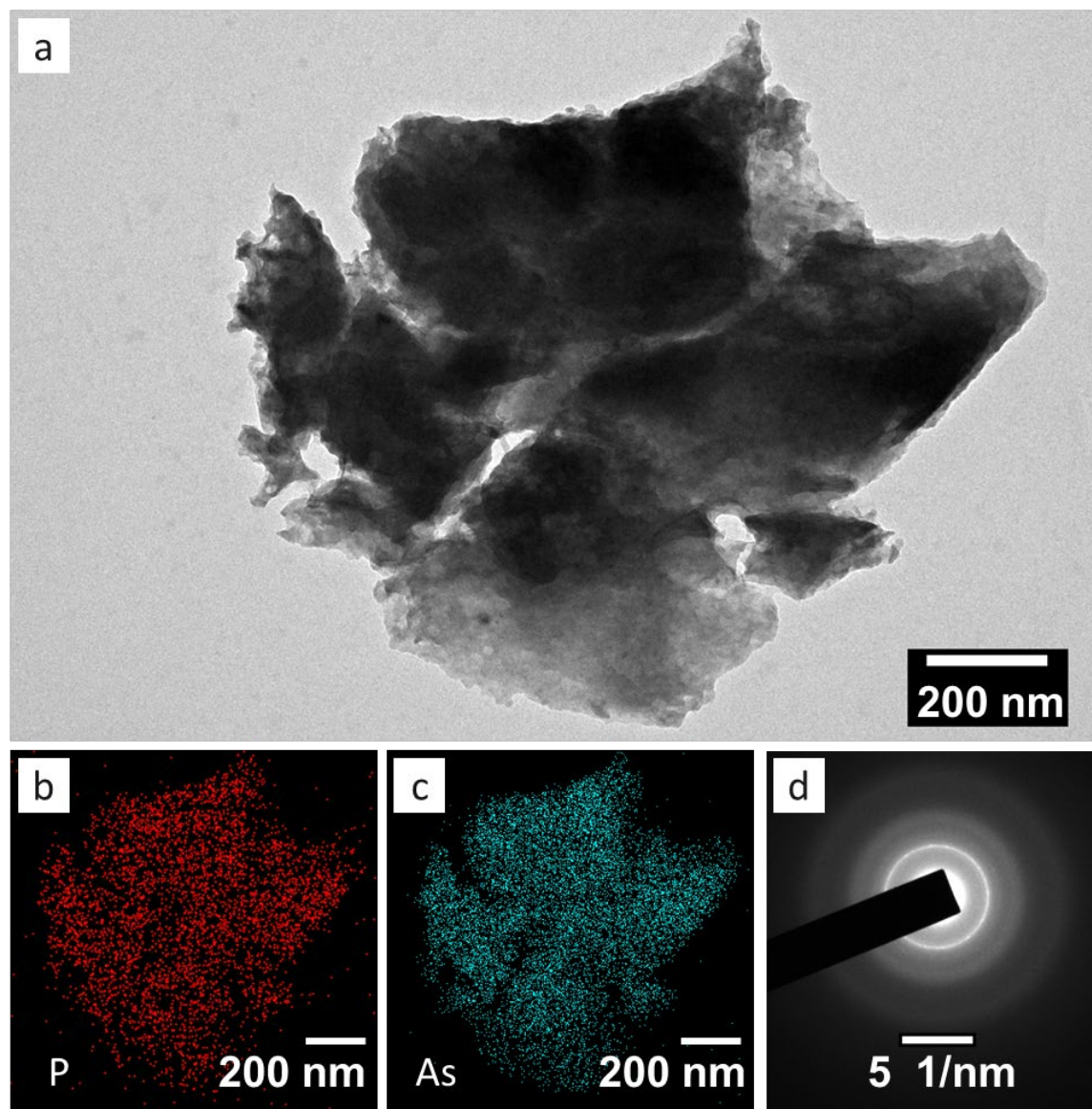


**Figure 3.11** Transmission electron microscopy on P-As 80 at % ( $R\bar{3}m$ ) flakes. **(a)** Selected bright field image showing multiple overlapped flakes, **(b,c)** STEM maps showing the uniform distribution of phosphorus and arsenic throughout the flakes, **(d)** selected area electron diffraction pattern from the multi-flake confirming the crystallinity of the flakes.

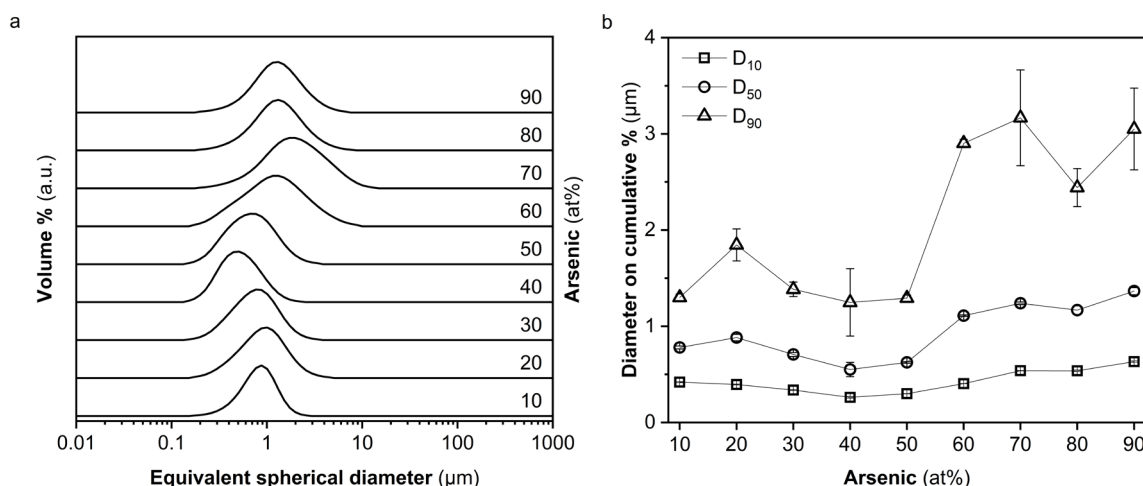


**Figure 3.12 Laser diffraction particle size analysis on ultrasonic probe tip exfoliated P-As compositions.**

(a) Volumetric size distributions as a function of the equivalent spherical diameter for flakes suspended in IPA. The distributions for all compositions consist of a single mode below ten microns, (b) the diameter on the cumulative distribution for which 10%, 50%, and 90% of the particles are below a given diameter as a function of arsenic content in the compositions; the distributions appear to be insensitive to the composition below 50 at% arsenic such that a single hour of probe tip exfoliation produces comparable size distributions; a slight trend upward at arsenic content greater than 50 at% does indicate greater difficulty in reducing the particle size during exfoliation. Nonetheless, the energy supplied by the ultrasonic probe tip is sufficient to overcome the breakage energy to fragment hard and soft agglomerated powders and the cleavage energy to separate 2D layers. Error bars is one standard deviation from at least three measurements.

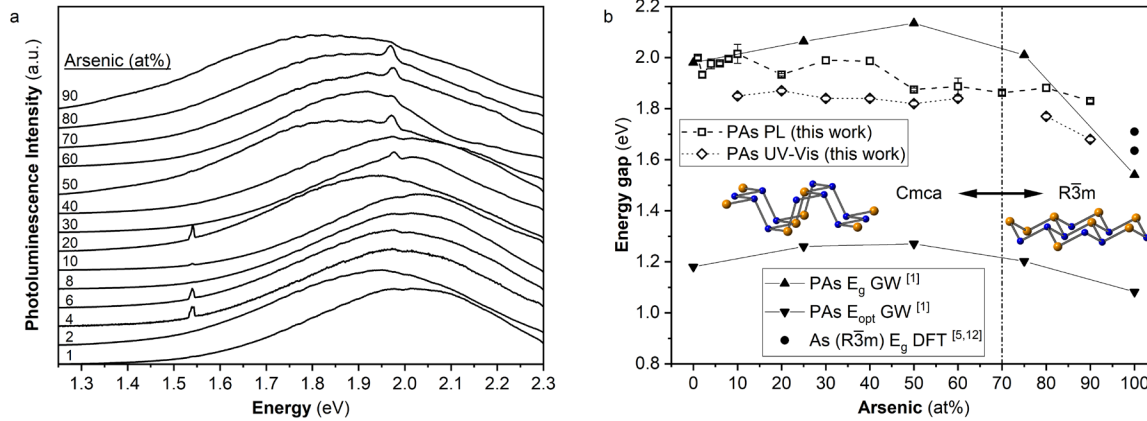


**Figure 3.13 Photoluminescence of orthorhombic P-As alloys.**

(a) broad visible PL emission from PMMA encapsulated exfoliated P-As dispersions centered near 1.8-2.0 eV indicating that 1-layer o-PAs and t-PAs is likely present within each of the polydisperse samples. Peaks at 1.54 and 1.95 eV are artifacts from the PMMA and laser pump (808 nm), (b) optical gap as obtained from PL and UV-Vis absorption as compared literature values of the theoretical fundamental bandgap  $E_g$  and optical gap  $E_{opt}$  calculated using DFT and GW methods; atomic models of the orthorhombic (Cmca) and trigonal ( $R\bar{3}m$ ) alloys are shown along with the transition between the two crystal types at 70 at%.

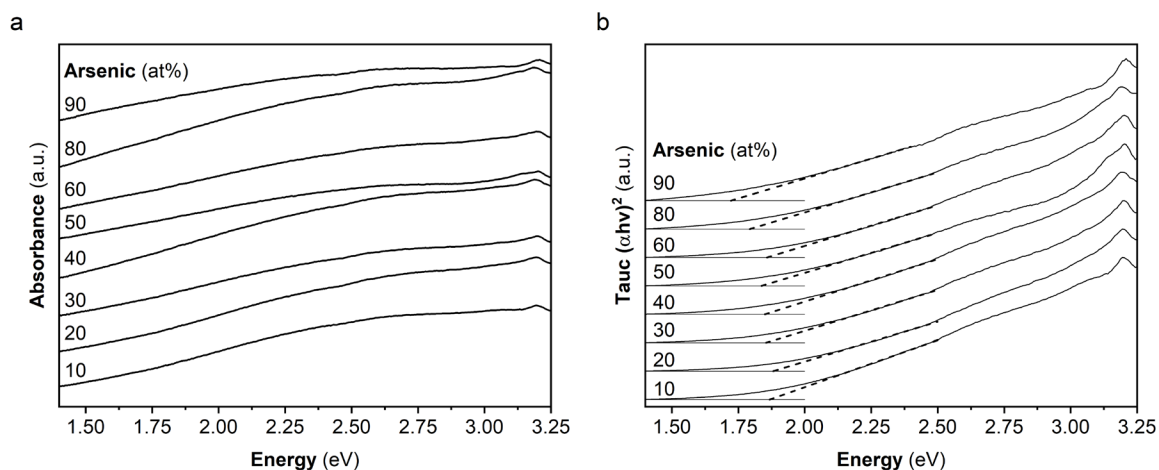


**Figure 3.14 UV-Visible absorption spectroscopy on ultrasonic probe tip exfoliated P-As compositions.**

(a) absorbance curves for the P-As alloys, (b) Tauc analysis (using expression for direct bandgap semiconductors) for obtaining the optical gaps by fitting a straight line (dash lines) along the low energy segment (all patterns manually offset for clarity, horizontal baseline representing zero absorbance added to show intersection with dashed line for optical gap estimate). The 70 at% sample was excluded as it consisted of a mixture of both orthorhombic and trigonal PAs phases.

The Tauc analysis for estimation of the bandgap employs fitting a straight line along the linear portion of the  $(\alpha hv)^2$  vs  $hv$  curve; the intersection with the abscissa gives the UV-Vis based optical bandgap<sup>74</sup>. The measured absorbance,  $A$ , was used in place of the absorption coefficient,  $\alpha$ , as it can be shown mathematically that  $A$  and  $\alpha$  merely scale the y-axis without altering the x-axis intercept value (gap estimate). For liquid suspensions  $\alpha = 2.303 \times 10^3 A \rho l^{-1} c^{-1}$  where  $l$ ,  $c$ ,  $\rho$  are all constants as a function of the wavelength or energy scale; hence  $\alpha$  is proportional to  $A$ . The path length,  $l$ , and material density,  $\rho$ , are known constants, while the loading of the colloid suspension,  $c$ , can be obtained from ion-coupled plasma mass spectroscopy measurements.

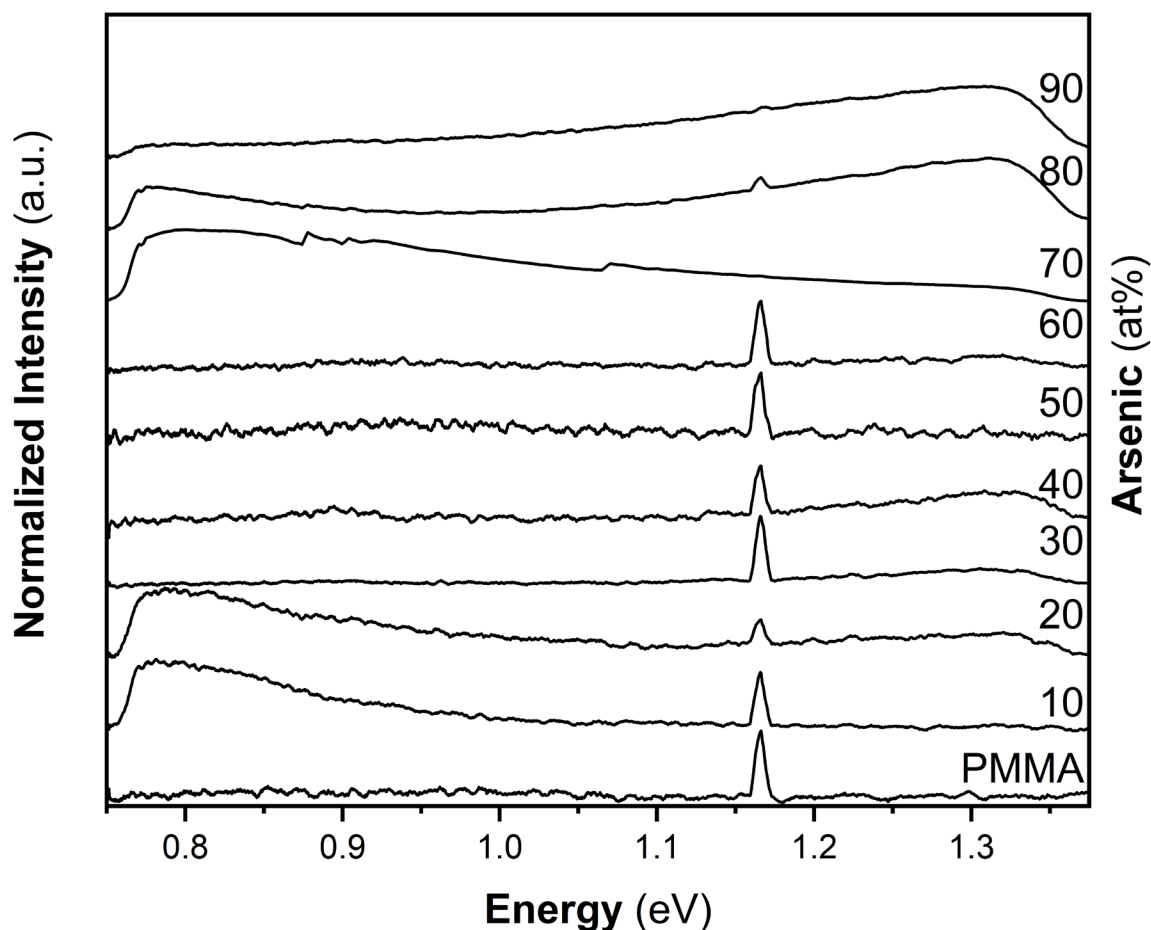


**Figure 3.15** Near Infrared photoluminescence on PMMA encapsulated P-As alloys.

Peaks near 0.8 eV are detected indicating some of the flakes under illumination are multilayer flakes; the detector cutoff at 0.75 eV (1700 nm) precludes determination of the peak centers. Small peaks at 1.33 eV (930 nm) may be from bilayer PAs alloys but these may also be the low energy tail of the peak detected in the visible photoluminescence measurements. The sharp peak at 1.17 eV (1064 nm) is an artifact from the 532 nm excitation laser. Not all samples measured had infrared emission but was likely due to insufficient PL sampling.

Trigonal phosphorus is a high-pressure phase of phosphorus at pressures  $> 5$  GPa. A note on nomenclature: the t-PAs series belongs to the trigonal crystal system but uses a rhombohedral lattice, hence the  $(R\bar{3}mR)$  designation, while pure metallic arsenic is also a part of the trigonal crystal system but is most often represented in the  $(R\bar{3}mH)$  with a hexagonal lattice. Cubic arsenic oxide ( $As_2O_3$ ) exists as a molecular solid with symmetry  $O_h$ ;<sup>75</sup> however, the Raman spectra is primarily from the  $As_2O_3$  "free" molecule with  $T_d$  symmetry<sup>76</sup> and is often discussed within this context.

## Tables

Table 3.1 Crystallographic details of phosphorus and arsenic structure.

Compound	Space Group	Lattice parameters (Å)			Volume (Å <sup>3</sup> )	Symmetry	Raman Peaks (cm <sup>-1</sup> ) <sup>[1-4]</sup>	ICSD
		a	b	c				
P (black)	Cmca	3.319	10.367	4.315	148.54	D <sup>2</sup> <sub>h</sub>	192, 228, 362, 439, 466	150873
As (black)	Cmca	3.620	10.85	4.480	175.96	D <sup>2</sup> <sub>h</sub>	98, 116, 221, 226, 255	609828
As (grey)	R $\bar{3}$ m	3.750	3.750	10.640	129.12	D <sup>3</sup> <sub>d</sub>	257, 195	16518
P (HP)	R $\bar{3}$ m	3.997	3.997	8.751	87.60	D <sup>3</sup> <sub>d</sub>	308, 388	258858
Si	Fd $\bar{3}$ m	5.430	5.430	5.430	160.15	O <sub>h</sub>	520	51688
As <sub>2</sub> O <sub>3</sub>	Fd $\bar{3}$ m	11.073	11.073	11.073	1357.83	O <sub>h</sub> (T <sub>d</sub> )	18 peaks	238612

**Table 3.2 EDS compositions of ball mill synthesized PAs powders.**

<b>Arsenic [at %]</b>	<b>1</b>	<b>2</b>	<b>4</b>	<b>6</b>	<b>8</b>	<b>10</b>	<b>20</b>	<b>30</b>	<b>40</b>	<b>50</b>	<b>60</b>	<b>70</b>	<b>80</b>	<b>90</b>
<b>Avg</b>	0.9	2.3	4.2	5.6	7.5	11.8	22.2	31.1	40.1	53.4	60.6	72.9	81.8	89.0
<b>St Dev</b>	0.1	0.1	0.7	1.2	0.9	0.2	0.8	0.8	3.9	3.5	9.2	1.5	4.8	3.3

CHAPTER FOUR: MECHANOCHEMISTRY OF THE PHOSPHORUS-GERMANIUM  
COMPOUNDS

This chapter is planned for submission to Elsevier Publications in *Journal of Solid State Chemistry* and should be referenced appropriately.

Reference:

S. V. Pedersen, J. D. Wood, C. Husko, D. Estrada, B. J. Jaques, “Mechanochemistry of the Phosphorus- Germanium compounds.” *Journal of Solid State Chemistry*. **X** (X) XX (2022)

Reproduced/modified by permission of Elsevier Publications.

\*This chapter includes formatting modifications from the originally submitted version.

Mechanochemistry of the Phosphorus-Germanium Compounds

Samuel V. Pedersen<sup>1,2</sup>

Joshua D. Wood<sup>3</sup>

Chad Husko<sup>4</sup>

David Estrada<sup>1,2,5</sup>

Brian J. Jaques<sup>1,2</sup>

<sup>1</sup>Micron School of Materials Science and Engineering, Boise State University,

Boise, ID 83725, USA

<sup>2</sup>Center for Advanced Energy Studies, Idaho Falls, ID 83401, USA

<sup>3</sup>Promethean Consulting, LLC, Oak Park, IL 60302, USA

<sup>4</sup>Iris Light Technologies, Inc., Chicago, IL 60622, USA.

<sup>5</sup>Idaho National Laboratory, Idaho Falls, ID 83402, USA

## Abstract

Layered germanium phosphides present unique properties at the few-layer limit. The trigonal Ge-P phase is an indirect semiconductor at the monolayer limit but undergoes a transition to metallic behavior in the bulk limit. The monoclinic GeP also possesses an indirect bandgap that decreases with increasing layer number much like black phosphorus. Incorporation of GeP nanomaterials into functional devices such as thermoelectrics, battery anodes, and opto-electronics requires an industrially scalable synthesis such as high energy planetary ball milling (HEPBM). Herein, we demonstrate the synthesis and characterization of Ge-P phases that can be produced by ball milling. During the milling process, high energy collisions effectively produce the pressure and temperatures needed to stabilize the high-pressure crystal structures Ge-P. A limited solid solution range (germanium content between 2 and 30 at%) for the trigonal ( $R\bar{3}m$ ) phase is revealed. The monoclinic phase at 50 at% germanium is also successfully produced by ball milling. This straightforward solid-state synthesis route of germanium phosphides could potentially enable scale-up of many applications exploiting their narrow bandgaps, high electrical conductivities, and layered structures.

## 4.1 Introduction

Interest in layered germanium phosphides has seen a resurgence following the isolation of graphene,<sup>1</sup> phosphorene,<sup>2</sup> germanene,<sup>3</sup> and, more recently, few-layer GeP compounds.<sup>4-11</sup> Within the phase diagram of Ge-P exists two phases consisting of van der Waals bonded layered crystals, including monoclinic ( $C2/m$ ) GeP and trigonal ( $R\bar{3}m$ ) GeP<sub>x</sub> (x=3,5).<sup>12</sup> Like many layered materials, quantum confinement alters the opto-

electronic behavior of monolayer and few-layer Ge-P layered crystals.<sup>5,6,8-10,13</sup> Although GeP<sub>5</sub> is a metallic conductor in both the bulk and monolayer,<sup>14</sup> GeP<sub>3</sub> (which shares the same trigonal crystal lattice) becomes an indirect bandgap semiconductor at the monolayer (0.55 eV) and bilayer (0.43 eV) limit.<sup>5,13</sup> Monoclinic GeP possesses a layer dependent indirect bandgap (eV) that can be tuned by strain engineering.<sup>15,16</sup> Few-layer Ge-P layered crystals have the potential to advance optoelectronic devices<sup>10</sup> and battery applications.<sup>15,17-19</sup>

Synthesis of bulk monoclinic GeP was first reported in 1939 but more detailed structural characterization occurred in the 1970's when high pressure anvil systems were used to produce small crystals.<sup>20,21</sup> More recently, monoclinic GeP crystals have been produced using a bismuth flux,<sup>6</sup> or tin flux,<sup>22</sup> a solvothermal route,<sup>17</sup> and by high energy ball milling.<sup>23</sup> Additionally, GeP<sub>3</sub> and GeP<sub>5</sub> have been produced by high pressure anvil routes as well as high energy ball milling (HEBM).<sup>4,24-28</sup> **Table 4.1** lists the known Ge-P phases along with their crystallographic details. Notably, the monoclinic GeP phase is metastable at ambient pressure with a positive free energy while the GeP<sub>3</sub> and GeP<sub>5</sub> phases are metastable high-pressure phases.<sup>12,29</sup>

Mechanochemistry, specifically high energy ball milling (HEBM), exploits the high energy collisions and grinding produced by grinding media (such as steel bearing balls) upon collision with each other and the milling container walls.<sup>30</sup> Global temperatures of up to 200 °C and pressures of up to 6 GPa at the point of impact have been estimated from Hertzian collision theory; however, these estimates are only rough approximations.<sup>30</sup> Collision geometry (head-on or glancing), volume of entrapped powder, elasticity of powder, and media characteristics all factor into the pressure and temperature

generated.<sup>31-34</sup> A qualitative range can be inferred from the experimental conditions for high-pressure phases such as pure black phosphorus (0.5 GPa at 500°C or 4 GPa at room temperature).<sup>35-38</sup> Due to limited studies of the pressure-temperature phase diagram of Ge-P and sporadic ball milling reports of Ge-P compounds there appears to be a significant knowledge gap. This opportunity is addressed by investigating the possible phases of Ge-P that can be obtained through HEBM and if alloys with black phosphorus (as the case for phosphorus-arsenic) could be formed.

In this work, the mechanochemical synthesis behavior of the Ge-P system is reported along with detailed processing conditions and structural characterization. Additionally, we highlight the compositional range for the trigonal phase,  $\text{GeP}_x$  ( $70 < x < 99$  at% phosphorus), and the lack of pressure induced solubility of phosphorus into the cubic Ge lattice. Lastly, ball mill doping of BP with germanium is demonstrated with a limited solubility ( $< 1$  at%).

## 4.2 Results

The layered trigonal  $\text{GeP}_x$  and monoclinic GeP compounds were successfully synthesized via HEBM as shown by the powder x-ray diffraction patterns in **Figure 4.1**. At less than one atomic percent germanium, phase pure black phosphorus was produced; which is in good agreement with the solubility of germanium reported in bismuth flux synthesized single crystals of black phosphorus.<sup>39</sup> Between 2 and 30 at% germanium, a trigonal solid solution alloy forms and this region contains the stoichiometric  $\text{GeP}_3$  (25 at% Ge) and  $\text{GeP}_5$  (16 at% Ge) compounds which share the same lattice symmetry. Donohue noted that the underlying crystal lattice is the same except for a doubling along

the *a*-axis to account for the stoichiometry difference.<sup>21</sup> The diffraction patterns for GeP<sub>3</sub> and GeP<sub>5</sub> milled powders are nearly the same except for a shift to lower angles in the GeP<sub>3</sub> pattern due to the increased lattice expansion resulting from the higher number of the larger germanium atoms. The 40 at% pattern shows a two-phase region consisting of monoclinic GeP and trigonal GeP<sub>3</sub>. The monoclinic GeP exists as a single phase for the milled mixture containing 50 at% germanium. The powder samples containing 60-90 at% germanium indicate mixtures of pure cubic germanium and the equimolar monoclinic GeP. **Table 4.2** lists the Ge-P phases produced by milling with approximate range of germanium (in at%) over which the Ge-P phases exist as single or two-phase regions. Of the known high-pressure phases, the cubic and tetragonal forms of GeP were not detected by XRD within powders targeting the GeP (50 at%).

Raman spectra for each composition is shown in **Figure 4.2** along with markers for the known vibrational modes for the stoichiometric compounds, which are listed in **Table 4.3**. For the trigonal phase with germanium content below <30 at%, a set of high frequency peaks that likely correspond to P-P bonding is evident near 420 cm<sup>-1</sup>, which is similar to the range wavenumbers for pure BP. The main germanium peak at 301 cm<sup>-1</sup> (for the 90 at% Ge pattern) may be the same peak at 291 cm<sup>-1</sup> (for the 60-80 at% Ge patterns) but shifted slightly to lower frequencies due to bonding with phosphorus. Excessive heating could also shift frequencies to lower wavenumbers. Steps to mitigate this by using neutral density filters to allow 0.1, 1, and 3.2% transmitted light with a 20X objective showed only minor shifts (<1 cm<sup>-1</sup>) with long exposures (240 seconds). Minor peaks in the 300-400 cm<sup>-1</sup> range in the 60-80 at% Ge patterns are from the minor amounts of monoclinic GeP present in the two-phase mixture (as observed by XRD). For the 10-

50 at% germanium samples, the vibrational modes match that of GeP and GeP<sub>3</sub>/GeP<sub>5</sub>. The modes mostly match that of single crystal GeP,<sup>8,10,11,40</sup> except for the mode near 430 cm<sup>-1</sup>, which is the main peak observed in single crystal GeP<sub>5</sub> produced by high pressure anvil method.<sup>14,41</sup> The results here match reports from ball mill synthesized GeP<sub>3</sub> and GeP<sub>5</sub> with vibrational modes at 190, 240, 300, 320, 350 cm<sup>-1</sup>;<sup>27,42</sup> however, modes at 300 and 400 cm<sup>-1</sup> are not present in high pressure synthesized single crystals which suggests disordering of the phosphorus and germanium atoms as well as the existence of Ge-Ge bonds.

### 4.3 Discussion

While GeP<sub>3</sub> and GeP<sub>5</sub> have been synthesized via MA, this work shows the existence of a trigonal solid solution alloy with a composition GeP<sub>x</sub> (1 < x < 70 at%). Donohue and Osugi both reported the similarity of the GeP<sub>3</sub> and GeP<sub>5</sub> structures but did not report the upper and lower limits of phosphorus content before a new phase formed.<sup>20,21</sup> The high-pressure phases of tetragonal and cubic GeP were not synthesized using the same ball milling conditions. Although the high pressure synthesis conditions for black phosphorus and the P-Ge phases are comparable as detailed in **Table 4.4**, only the monoclinic phase of GeP could be produced.<sup>38,43,44</sup> Monoclinic GeP is not considered a high pressure phase as it can be produced by directly heating elemental germanium and red phosphorus inside a sealed silica tube.<sup>20</sup> Monoclinic GeP will form before the tetragonal or cubic phases and will be retained during further milling. Additionally, little is known about the thermodynamic stability of germanium phosphides.<sup>29</sup> A comprehensive review of phosphides by Schlesinger indicated that monoclinic GeP is

thermodynamically unstable at ambient pressure and room temperature with a positive Gibbs free energy of  $19 \text{ kJ mol}^{-1}$ .<sup>29</sup> Results for the other high pressure phases of P-Ge were absent altogether and have not been experimentally determined in literature, to the best of the author's knowledge. While the impact energy does not directly correlate to specific combination of pressure and temperature, the ball mill synthesis of BP does suggest the impact energy is comparable to the high-pressure synthesis conditions for BP and, presumably, the high-pressure P-Ge phases. Factors besides impact energy, such as thermodynamic stability and kinetic pathways, must govern the synthesis of only monoclinic GeP at the 50 at% composition.<sup>12,21</sup>

Synthesis of the trigonal ( $R\bar{3}m$ ) P-Ge (2-30 at% Ge) phase can be rationalized based on the Hume-Rothery rules regarding solid solution alloy formation. Commonality between crystal structure, similar covalent radii, electronegativity, and valency are usually necessary; values for phosphorus, arsenic and germanium are listed in **Table 4.5**.<sup>45-49</sup> Generally, maximum solubility of two elements into the same crystal structure occurs when the valency, radii, and electronegativity is the same. The formation of trigonal P-Ge over orthorhombic P-Ge is likely due to the difference in valence electron count and the different ambient pressure stable phases available to pure phosphorus and pure germanium. Empirically, an atomic size difference less than 15% is often observed in solid solution alloys.<sup>50,51</sup> Both arsenic and germanium fit with the 15% difference threshold. The two stoichiometric phases  $\text{GeP}_3$  and  $\text{GeP}_5$  both are part of the trigonal crystal system with the  $R\bar{3}m$  symmetry. Likewise trigonal phosphorus is a metastable high-pressure phase synthesized at 5 GPa (using diamond anvils) but will transform into orthorhombic phosphorus upon decompression, as shown in **Figure 4.3**.<sup>36</sup> By

crystallographic convention, the trigonal crystal structure of the high-pressure semi-metallic phase of pure phosphorus is presented in a rhombohedral lattice setting ( $R\bar{3}mR$ ) and it provides a primitive lattice with two atoms. Mathematically, the rhombohedral lattice can be transformed into the hexagonal lattice ( $R\bar{3}mH$ ) with six atoms in the unit cell.<sup>52</sup> By visualizing the trigonal phosphorus and trigonal GeP<sub>5</sub> crystals within the same lattice setting, the substitution of one germanium atom into the trigonal phosphorus lattice would result in the GeP<sub>5</sub> phase. Although phosphorus and germanium both form orthorhombic structures, orthorhombic germanium (*Cmca*) is an exceptionally high pressure metastable phase (100 GPa).<sup>53</sup> Another orthorhombic allotrope of pure germanium (*Pbcm*) is metastable and can be obtained through de-lithiation of Li<sub>7</sub>Ge<sub>12</sub> precursors using ionic liquids.<sup>54</sup> Both the cubic and hexagonal diamond<sup>55</sup> forms of germanium contain 6-member rings, similar to the trigonal P-Ge and pure trigonal phosphorus phases. The propensity for phosphorus to form rings (i.e., red phosphorus, phosphorus sulfides, phosphorus selenides, and phosphorus stannides) suggests that the P-Ge compounds with rings would also be likely (as is observed for the monoclinic GeP phase). It is hypothesized that upon milling germanium and phosphorus, the lower pressure required to synthesize the trigonal phosphorus (5 GPa) versus orthorhombic germanium (100 GPa) favors the formation of the trigonal solid solution alloy over an orthorhombic alloy. Metallic arsenic possesses the same trigonal lattice as the high-pressure trigonal phosphorus with comparable lattice parameters as shown in **Table 4.1**. The ball mill synthesis results on P-As alloys revealed a limited trigonal crystal solid solution between P-As (70-90%) indicating that the atomic size of arsenic (comparable to germanium) was small enough to enable the alloy formation. From the literature,

modeling by Osters *et al.* showed only a minor difference in the energy stability ( $\approx 8 \text{ kJ mol}^{-1}$ ) of trigonal P-As over orthorhombic P-As as a function of composition.<sup>56</sup> From their CVT single crystal P-As work with DFT analysis shown in **Figure 4.4**, they showed that at 0 at% arsenic, the o-PAs phase has a free energy  $\Delta G^0_{298}$  of  $-7 \text{ kJ mol}^{-1}$ . They estimate the transition to t-PAs occurs at 90 at% arsenic. The  $\Delta G^0_{298}$  of t-PAs with 0 at% phosphorus is slightly positive near  $1 \text{ kJ mol}^{-1}$ . Hence only a small energy difference of about  $|8| \text{ kJ mol}^{-1}$  exists between the two structures. Substitution of phosphorus into trigonal arsenic is expected since phosphorus and arsenic are also isovalent. Considering the similarity between germanium and arsenic atoms from **Table 4.5**, the formation of trigonal P-Ge is not unsurprising. A future challenge would be use DFT to determine the energy stabilities of the trigonal phase of P-Ge as it compares to theoretical orthorhombic P-Ge and the P-As structural equivalents. Particularly, is the structure determination between orthorhombic or trigonal P-Ge mainly due to valency differences between phosphorus and germanium?

In the analysis of the x-ray diffraction data in **Figure 4.1**, it is observed that the expected  $\text{GeP}_3$  x-ray diffraction pattern (ICSD #16294) is markedly different than that of the expected  $\text{GeP}_5$  phase (PDF 00-024-0455), which is the least documented of the two phases in literature. Oddly enough, the solid solution alloy, when sampled at 2%, 10%, 20%, and 30% germanium, all produce the same diffraction pattern matching the  $\text{GeP}_5$  pattern from the calculated PDF 0024-0455 but with a shift to lower diffraction angles with increase germanium content (i.e., unit cell volume expansion). This result suggests a random solid solution alloy with site disorder. Ball milling of site ordered alloy or compound powders can result in in site disordering where one atom type substitutes onto

lattice sites specific to a different atom.<sup>30</sup> The distinct GeP<sub>3</sub> pattern (observed in single crystals)<sup>21</sup> is likely a special case due to perfect ordering of germanium and phosphorus atoms; whereas, in all other cases, disorder between sites produces x-ray diffraction results resembling pure trigonal phosphorus and the GeP<sub>5</sub> structure. MA synthesis of GeP<sub>3</sub> within the literature also confirms the match to the GeP<sub>5</sub> phase (PDF 0024-0455) instead of the known single crystal pattern of GeP<sub>3</sub>.<sup>4,24,25,42</sup> MA can often produce disordered alloys (where the underlying lattice stays the same but atoms swapping sites occurs) whereas slower and more controlled growth through solid state thermal reactions (heating powders in a tube furnace) or chemical vapor transport (heating powders in a tube furnace with mineralizers) will typically form ordered alloys.<sup>57-62</sup>

The XRD and Raman data in **Figure 4.1** and **Figure 4.2**, respectively, supports the lack of appreciable solubility of phosphorus into cubic germanium that was observed.<sup>12</sup> The samples targeting higher than 50 at% germanium resulted in a mixture of cubic germanium and monoclinic GeP. The Raman results in **Figure 4.2** indicate that all P-Ge phases formed via MA likely contain a Ge-Ge bond and may be related to the existence of the 6-member ring within cubic germanium, monoclinic GeP, and trigonal GeP<sub>x</sub>.<sup>10,14,18,54,63-66</sup> Cubic germanium has a strong vibrational mode at 300 cm<sup>-1</sup>, whereas all of the powder samples contained a mode near 290 cm<sup>-1</sup>. Considering that pure cubic germanium has a higher point symmetry ( $m\bar{3}m$ ), nearly all directional vibrations of Ge-Ge bonds are equal. The same cannot be said for the lower point symmetries of the GeP ( $C2/m$ ) or GeP<sub>x</sub> phases ( $\bar{3}m$ ). The reduced symmetry will result in a pair of Ge-Ge atoms having additional vibrational frequencies that are directionally dependent and should differ from the single observed frequency of cubic germanium.<sup>54,63,65</sup> Arguably, various

substitutions of phosphorus into the rings will result in new vibrational modes at higher and lower frequencies depending upon the degree of polarizability of each pair of bonded atoms. While no strict rule exists, longer bonds or heavier atoms tend to produce low frequency vibrations whereas shorter bonds with lighter elements are often at higher frequencies. Pure P-P bonding within the ring will have higher frequency vibrations than that of Ge-Ge within the same ring; likewise Ge-P bonds within the ring will exhibit their own vibrational frequencies likely between the modes of pure P-P or Ge-Ge bonds.<sup>67-70</sup> While polarization selection rules for optically active modes govern which vibrations will be Raman active or not<sup>71,72</sup>, one would expect that different bond distances and angles would result in different vibrational modes which is observed in **Figure 4.2**. Similar to the various allotropes of pure germanium, the lower symmetry crystals have additional vibrational modes beyond the primary mode observed near  $300\text{ cm}^{-1}$ .<sup>54,63</sup> A similar observation of additional modes due to local symmetry breakdown in  $\text{Si}_{1-x}\text{Ge}_x$  alloys was noted with germanium shifting pure Si-Si modes to lower frequency as the coordination of Ge atoms around the Si atom increased.<sup>73</sup> Comparison of the milled P-Ge powders in **Figure 4.2** to the P-As Raman spectra from **Figure 3.1**, within the same orthorhombic crystal lattice, the mixing of the two atoms (As and P) resulted in a range of modes sandwiched between the pure arsenic (*Cmca*) and pure phosphorus (*Cmca*) modes; no new vibrational modes below  $175\text{ cm}^{-1}$  and above  $460\text{ cm}^{-1}$  in the P-As alloys were evident. The same Raman behavior is observed for the  $\text{GeP}_x$  solid solution alloy in that no new modes appear above  $460\text{ cm}^{-1}$ . The same modes ( $\sim 125, 195, 240, 290, 340, 360, 420\text{ cm}^{-1}$ ) are present in the 10%, 20, and 30 at% germanium samples. The differences in intensity are likely both crystal orientation (polarization) and composition

dependent.<sup>70,74,75</sup> The random site disordering likely contributes to the similar patterns observed across the solid solution range in the trigonal  $\text{GeP}_x$  alloy series. A more detailed atomistic modeling of the vibrational modes as a function of crystal symmetry, atomic site position, and occupancy is needed to better understand the vibrational modes and possible assignment to phonon modes.

In conclusion, we have demonstrated high energy planetary ball milling as a direct route to produce (1) germanium substituted into black phosphorus, (2) the layered trigonal  $\text{Ge}_{1-x}\text{P}_x$  ( $70 < x < 99$ ) limited disordered solid solution alloy, (3) and the layered monoclinic GeP phase. Milling time (4-6 hours) and milling intensity (600 rpm) required to produce the P-Ge phases were comparable to pure black phosphorus.

Future work should include a conversion kinetics analysis to estimate the minimum impact energy and time required for synthesis of each Ge-P compound similar to the pure BP work and o-PAs 50 at% work described in **Figure 2.10** and **Figure 3.6**, respectively. A combination of experimental photoluminescence measurements and atomistic modeling of the composition and layer dependency on the nature of the bandgaps (direct, indirect) and vibrational modes would greatly aid in determining the suitability of these 2D layered Ge-P phases for opto-electronics. A considerable knowledge gap in the literature of the optical, thermal, vibrational and electrical properties of all of the P-Ge phases both in the bulk and the few-layer limit is quite apparent and warrant further study.

#### 4.4 Methods

**In the milling experiment**, elemental red phosphorus (1-5 g) (Alfa Aesar, 97% purity, -60 mesh, Alfa Aesar, 99.99% purity, chunks) and elemental germanium (1-5 g) (Alfa Aesar, 99.99% purity, -200 mesh) and stainless steel media (10 mm diameter, 100 g) were weighed and loaded into a stainless steel vessel (250 mL) inside an argon atmosphere glovebox ( $P_{O_2} < 0.1$  ppm) and sealed under argon (90-95 kPa) at room temperature. The ball to powder mass ratio was 20:1. All milling experiments were conducted with the PM100 planetary ball mill (Retsch, Germany) with pauses in the milling cycles (15 minutes on, 30 minutes off) to prevent overheating of the unit and to switch the direction of flywheel rotation (promotes better mixing). Milling conditions (rpm and duration) were held constant at 600 rpm and 14 hours of milling.

**Powder X-ray diffraction (XRD)** data was obtained in the Bragg-Brentano geometry ( $CuK_{\alpha}$ , Rigaku MiniFlex 600, Japan) on powder (0.165 g) sealed inside a polyimide dome within an argon glovebox to prevent possible reaction with air during XRD measurements.

**Raman spectroscopy (Raman)** data was obtained (Horiba LabRam HR Evolution, Japan) on densely packed powder samples (0.01 g) prepared inside an argon glovebox that were sealed inside a custom-built enclosure with a sapphire window to prevent oxidation and ignition during measurements. A 50 mW 532nm laser source (Nd:YAG) was used to generate spectra collected with a Si CCD. Spectra obtained at 20X objective with quadruple acquisitions for 60 seconds at ten random locations throughout the bulk surface using the 1800 lines/mm grating, at room temperature.

### **Acknowledgements**

This work has been funded, in part, by Boise State University College of Engineering Seed Funding Program and IGEM Commerce (grant number 003786). Materials were synthesized and processed in the Advanced Materials Laboratory (Boise State University, Boise, ID). XRD was performed in the Boise State Center for Materials Characterization (Boise State University, Boise, ID). C. Greseth and T. Nowling are acknowledged for their support with sample synthesis and characterization. Raman spectroscopy was performed in the Advanced Nano Materials and Manufacturing Laboratory (Boise State University, Boise, ID).

### **Author Contributions**

S.P. conceptualized and executed the milling studies, performed and analyzed the characterization data. B.J. supervised and directed the project.

### **Competing Interests**

The authors declare no competing interests.

## References

- 1 Novoselov, K. S. *et al.* Electric Field Effect in Atomically Thin Carbon Films. *Science* **306**, 666-669 (2004)
- 2 Liu, H. *et al.* Phosphorene: An Unexplored 2D Semiconductor with a High Hole Mobility. *ASC Nano* **8**, 4033-4041 (2014)
- 3 Acun, A. *et al.* Germanene: the germanium analogue of graphene. *J. Phys.: Condens. Matter* **27**, 443002 (2015)
- 4 Li, W. *et al.* Layered phosphorus-like GeP<sub>5</sub>: a promising anode candidate with high initial coulombic efficiency and large capacity for lithium ion batteries. *Energy Environ. Sci.* **8**, 3629-3636 (2015)
- 5 Jing, Y., Ma, Y., Li, Y. & Heine, T. GeP<sub>3</sub>: A Small Indirect Band Gap 2D Crystal with High Carrier Mobility and Strong Interlayer Quantum Confinement. *Nano Lett.* **17**, 1833-1838 (2017)
- 6 Li, L. *et al.* 2D GeP: An Unexploited Low-Symmetry Semiconductor with Strong In-Plane Anisotropy. *Adv. Mater.* **30**, 1706771 (2018)
- 7 Li, C. *et al.* Facile liquid-phase exfoliated few-layer GeP nanosheets and their optoelectronic device applications. *J. Mater. Chem. C* **8**, 5547-5553 (2020)
- 8 Wang, Z. *et al.* 2D GeP-based photonic device for near-infrared and mid-infrared ultrafast photonics. *Nanophotonics* **9**, 3645-3654 (2020)
- 9 Yu, T. *et al.* Two-Dimensional GeP-Based Broad-Band Optical Switches and Photodetectors. *Adv. Optical Mater.* **8**, 1901490 (2020)
- 10 Dushaq, G. & Rasras, M. Multilayer 2D germanium phosphide (GeP) infrared phototransistor. *Opt. Express* **29**, 9419-9428 (2021)
- 11 Zhao, S. *et al.* Flux Method Growth of Large Size Group IV–V 2D GeP Single Crystals and Photoresponse Application. *Crystals* **11**, 235 (2021)
- 12 Olesinski, R. W., Kanani, N. & Abbaschian, G. J. The Ge-P (Germanium-Phosphorus) System. *Bull. Alloy Phase Diagr.* **6**, (1985)
- 13 Wang, Q., Li, J.-W., Wang, B. & Nie, Y.-H. First-principles investigation of quantum transport in GeP<sub>3</sub> nanoribbon-based tunneling junctions. *Front. Phys.* **13**, 138501 (2018)
- 14 Song, J. *et al.* Pressure-driven significant phonon mode softening and robust superconductivity in layered germanium phosphide. *J. Mater. Chem. A* (2020)
- 15 Shojaei, F. & Kang, H. S. Electronic structure of the germanium phosphide monolayer and Li-diffusion in its bilayer. *Phys. Chem. Chem. Phys.* **18**, 32458-32465 (2016)
- 16 Cheng, A.-Q., He, Z., Zhao, J., Zeng, H. & Chen, R.-S. Monolayered Silicon and Germanium Monopnictide Semiconductors: Excellent Stability, High Absorbance, and Strain Engineering of Electronic Properties. *ACS Appl. Mater. Interfaces* **10**, 5133-5139 (2018)
- 17 Tseng, K.-W., Huang, S.-B., Chang, W.-C. & Tuan, H.-Y. Synthesis of Mesoporous Germanium Phosphide Microspheres for High-Performance Lithium-Ion and Sodium-Ion Battery Anodes. *Chem. Mater.* **30**, 4440-4447 (2018)
- 18 Yang, B. *et al.* Metallic layered germanium phosphide GeP<sub>5</sub> for high rate flexible all-solid-state supercapacitors. *J. Mater. Chem. A* **6**, 19409-19416 (2018)

- 19 Nam, K.-H., Jeon, K.-J. & Park, C.-M. Layered germanium phosphide-based anodes for high-performance lithium- and sodium-ion batteries. *Energy Storage Mater.* **17**, 78-87 (2019)
- 20 Osugi, J., Namikawa, R. & Tanaka, Y. Chemical reaction at high temperature and high pressure IV : high pressure phases in the Ge-P system. *Rev. Phys. Chem. Jpn.* **32**, 81-93 (1967)
- 21 Donohue, P. C. & Young, H. S. Synthesis, structure, and superconductivity of new high pressure phases in the systems Ge-P and Ge-As. *J. Solid State Chem.* **1**, 143-149 (1970)
- 22 Lee, K., Synnestvedt, S., Bellard, M. & Kovnir, K. GeP and  $(\text{Ge}_{1-x}\text{Sn}_x)(\text{P}_{1-y}\text{Ge}_y)$  ( $x \approx 0.12$ ,  $y \approx 0.05$ ): Synthesis, structure, and properties of two-dimensional layered tetrel phosphides. *J. Solid State Chem.* **224**, 62-70 (2015)
- 23 Li, W. *et al.* A self-healing layered GeP anode for high-performance Li-ion batteries enabled by low formation energy. *Nano Energy* **61**, 594-603 (2019)
- 24 Qi, W. *et al.* Facile Synthesis of Layer Structured GeP<sub>3</sub>/C with Stable Chemical Bonding for Enhanced Lithium-Ion Storage. *Sci Rep* **7**, 43582 (2017)
- 25 Wang, T. *et al.* Highly Reversible and Rapid Sodium Storage in GeP<sub>3</sub> with Synergistic Effect from Outside-In Optimization. *ACS Nano* **14**, 4352-4365 (2020)
- 26 Li, W. *et al.* Highly reversible sodium storage in a GeP<sub>5</sub>/C composite anode with large capacity and low voltage. *J. Mater. Chem. A* **5**, 4413-4420 (2017)
- 27 Liu, Y. *et al.* GeP<sub>5</sub>/C composite as anode material for high power sodium-ion batteries with exceptional capacity. *J. Alloys Compd.* **744**, 15-22 (2018)
- 28 Haghghat-Shishavan, S. *et al.* Exceptionally Reversible Li-/Na-Ion Storage and Ultrastable Solid-Electrolyte Interphase in Layered GeP<sub>5</sub> Anode. *ACS Appl. Mater. Interfaces* **11**, 32815-32825 (2019)
- 29 Schlesinger, M. E. The Thermodynamic Properties of Phosphorus and Solid Binary Phosphides. *Chem. Rev.* **102**, 4267-4302 (2002)
- 30 Suryanarayana, C. Mechanical alloying and milling. *Prog. Mater. Sci.* **46**, 1-184 (2001)
- 31 Rosenkranz, S., Breitung-Faes, S. & Kwade, A. Experimental investigations and modelling of the ball motion in planetary ball mills. *Powder Technol.* **212**, 224-230 (2011)
- 32 Rogachev, A. S. *et al.* Experimental investigation of milling regimes in planetary ball mill and their influence on structure and reactivity of gasless powder exothermic mixtures. *Powder Technol.* **274**, 44-52 (2015)
- 33 Schmidt, R., Martin Scholze, H. & Stolle, A. Temperature progression in a mixer ball mill. *Int. J. Ind. Chem.* **7**, 181-186 (2016)
- 34 Delogu, F. & Cocco, G. Weakness of the “hot spots” approach to the kinetics of mechanically induced phase transformations. *J. Alloys Compd.* **465**, 540-546 (2008)
- 35 Shoichi, E., Yuichi, A., Shin-ichi, T. & Shin-ichiro, N. Growth of Large Single Crystals of Black Phosphorus under High Pressure. *Jpn. J. Appl. Phys.* **21**, L482-L484 (1982)

- 36 Clark, S. M. & Zaug, J. M. Compressibility of cubic white, orthorhombic black, rhombohedral black, and simple cubic black phosphorus. *Phys. Rev. B* **82**, 134111 (2010)
- 37 Rissi, E. N., Soignard, E., McKiernan, K. A., Benmore, C. J. & Yarger, J. L. Pressure-induced crystallization of amorphous red phosphorus. *Solid State Comm.* **152**, 390-394 (2012)
- 38 Li, X. *et al.* Synthesis of thin-film black phosphorus on a flexible substrate. *2D Mater.* **2**, 031002 (2015)
- 39 Maruyama, Y., Inabe, T., He, L. & Oshima, K. Electrical conductivity of black phosphorous-germanium compound. *Synth. Met.* **43**, 4067-4070 (1991)
- 40 Barreteau, C., Michon, B., Besnard, C. & Giannini, E. High-pressure melt growth and transport properties of SiP, SiAs, GeP, and GeAs 2D layered semiconductors. *J. Cryst. Growth* **443**, 75-80 (2016)
- 41 Chang, Y. *et al.* Microwave absorbing properties of two dimensional materials GeP5 enhanced after annealing treatment. *Appl. Phys. Lett.* **114**, 013103 (2019)
- 42 Kim, D. *et al.* GeP3 with soft and tunable bonding nature enabling highly reversible alloying with Na ions. *Mater. Today Energy* **9**, 126-136 (2018)
- 43 Pedersen, S. V. *et al.* Mechanochemical conversion kinetics of red to black phosphorus and scaling parameters for high volume synthesis. *npj 2D Mater Appl* **4**, 36 (2020)
- 44 Park, C. M. & Sohn, H. J. Black Phosphorus and its Composite for Lithium Rechargeable Batteries. *Adv. Mater.* **19**, 2465-2468 (2007)
- 45 Cordero, B. *et al.* Covalent radii revisited. *Dalton Trans.* 2832-2838 (2008)
- 46 Gordy, W. & Thomas, W. J. O. Electronegativities of the Elements. *J. Chem. Phys.* **24**, 439-444 (1956)
- 47 Sanderson, R. T. Electronegativity and bond energy. *J. Am. Chem. Soc.* **105**, 2259-2261 (1983)
- 48 Allen, L. C. Electronegativity is the average one-electron energy of the valence-shell electrons in ground-state free atoms. *J. Am. Chem. Soc.* **111**, 9003-9014 (1989)
- 49 Hume-Rothery, W., Mabbott, G., W & Channel Evans, K. The freezing points, melting points, and solid solubility limits of the alloys of silver and copper with the elements of the b sub-groups. *Philos. Trans. Royal Soc. A* **233**, 1-97 (1934)
- 50 Li, S. *et al.* Study on the factors affecting solid solubility in binary alloys: An exploration by Machine Learning. *J. Alloy Compd.* **782**, 110-118 (2019)
- 51 He, Q. F., Ye, Y. F. & Yang, Y. Formation of Random Solid Solution in Multicomponent Alloys: from Hume-Rothery Rules to Entropic Stabilization. *J. Phase Equilib. Diffus.* **38**, 416-425 (2017)
- 52 Wondratschek, H., Aroyo, M. I., Souvignier, B. & Chapuis, G. *Transformations of coordinate systems in International Tables for Crystallography* 75-106.
- 53 Takemura, K. *et al.* High-Pressure Structures of Ge above 100 GPa. *phys. stat. sol. (b)* **223**, 385-390 (2001)
- 54 Tang, Z., Litvinchuk, A. P., Gooch, M. & Guloy, A. M. Narrow Gap Semiconducting Germanium Allotrope from the Oxidation of a Layered Zintl Phase in Ionic Liquids. *J. Am. Chem. Soc.* **140**, 6785-6788 (2018)

- 55 Zhao, Z. *et al.* Properties of the exotic metastable ST12 germanium allotrope. *Nat. Commun.* **8**, 13909 (2017)
- 56 Osters, O. *et al.* Synthesis and Identification of Metastable Compounds: Black Arsenic—Science or Fiction? *Angew. Chem. Int. Ed* **51**, 2994-2997 (2012)
- 57 Xie, H. *et al.* The intrinsic disorder related alloy scattering in ZrNiSn half-Heusler thermoelectric materials. *Sci. Rep.* **4**, 6888 (2014)
- 58 Ravel, B. *et al.* Atomic disorder in Heusler Co<sub>2</sub>MnGe measured by anomalous x-ray diffraction. *Appl. Phys. Lett.* **81**, 2812-2814 (2002)
- 59 Tobała, J. *et al.* Composition-induced metal-semiconductor-metal crossover in half-Heusler Fe<sub>1-x</sub>Ni<sub>x</sub>TiSb. *Phys. Rev. B* **64**, 155103 (2001)
- 60 Urban, P. *et al.* Temperature dependent resonant X-ray diffraction of single-crystalline Ge<sub>2</sub>Sb<sub>2</sub>Te<sub>5</sub>. *Cryst. Eng. Comm.* **15**, 4823-4829 (2013)
- 61 Mandrus, D. *et al.* Electronic transport in lightly doped CoSb<sub>3</sub>. *Phys. Rev. B* **52**, 4926-4931 (1995)
- 62 Cano-Torres, J. M. *et al.* Raman characterization and modelling of Cu<sub>2</sub>ZnSn<sub>1-x</sub>Ge<sub>x</sub>S<sub>4</sub> single crystals grown using chemical vapor transport. *Opt. Mater.* **66**, 671-677 (2017)
- 63 Zaikina, J. V. *et al.* Thermochemistry, Morphology, and Optical Characterization of Germanium Allotropes. *Chem. Mater.* **26**, 3263-3271 (2014)
- 64 Wakaki, M. *et al.* Raman spectroscopy of germanium films deposited with cluster-beam technique. *Phys. B: Condens. Matter* **219-220**, 535-537 (1996)
- 65 Kobliska, R. J. *et al.* Raman Scattering from Phonons in Polymorphs of Si and Ge. *Phys. Rev. Lett.* **29**, 725-728 (1972)
- 66 Weinstein, B. A. & Cardona, M. Second-Order Raman Spectrum of Germanium. *Phys. Rev. B* **7**, 2545-2551 (1973)
- 67 Soni, R. K. *et al.* Raman scattering in In<sub>1-x</sub>Ga<sub>x</sub>As<sub>y</sub>P<sub>1-y</sub> quaternary alloys. *J. Appl. Phys.* **59**, 2184-2188 (1986)
- 68 Sugiura, T., Hase, N., Iguchi, Y. & Sawaki, N. Raman Scattering Study of InGaAsP Quaternary Alloys Grown on InP in the Immiscible Region. *Jpn. J. Appl. Phys.* **37**, 544-549 (1998)
- 69 Tsang, J. C., Kesan, V. P., Freeouf, J. L., LeGoues, F. K. & Iyer, S. S. Raman spectroscopy of long-range order in epitaxial Si<sub>0.5</sub>Ge<sub>0.5</sub> alloys. *Phys. Rev. B* **46**, 6907-6914 (1992)
- 70 D'Costa, V. R. *et al.* Raman scattering in Ge<sub>1-y</sub>Sn<sub>y</sub> alloys. *Solid State Commun.* **144**, 240-244 (2007)
- 71 Edwards, D. F. Raman scattering in crystals. Report No. UCID-21510 DE89001284, (University of California, Lawrence Livermore National Laboratory, 1988).
- 72 Fateley, W. G., McDevitt, N. T. & Bentley, F. F. Infrared and Raman Selection Rules for Lattice Vibrations: The Correlation Method. *Appl. Spectrosc.* **25**, 155-173 (1971)
- 73 Alonso, M. I. & Winer, K. Raman spectra of c-Si<sub>1-x</sub>Ge<sub>x</sub> alloys. *Phys. Rev. B* **39**, 10056-10062 (1989)
- 74 Bouthillier, É., Assali, S., Nicolas, J. & Moutanabbir, O. Decoupling the effects of composition and strain on the vibrational modes of GeSn semiconductors. *Semicond. Sci. Technol.* **35**, 095006 (2020)

- 75 Zhu, Y. *et al.* Raman tensor of layered black phosphorus. *Photonix* **1**, 17 (2020)
- 76 Bergerhoff, G. & Brown, I. D. *Crystallographic Databases*. 77-95 (International Union of Crystallography, Chester, 1987).
- 77 Parker, J. H., Feldman, D. W. & Ashkin, M. Raman Scattering by Silicon and Germanium. *Phys. Rev.* **155**, 712-714 (1967)
- 78 Akahama, Y., Kobayashi, M. & Kawamura, H. Raman study of black phosphorus up to 13 GPa. *Solid State Commun.* **104**, 311-315 (1997)

## Figures

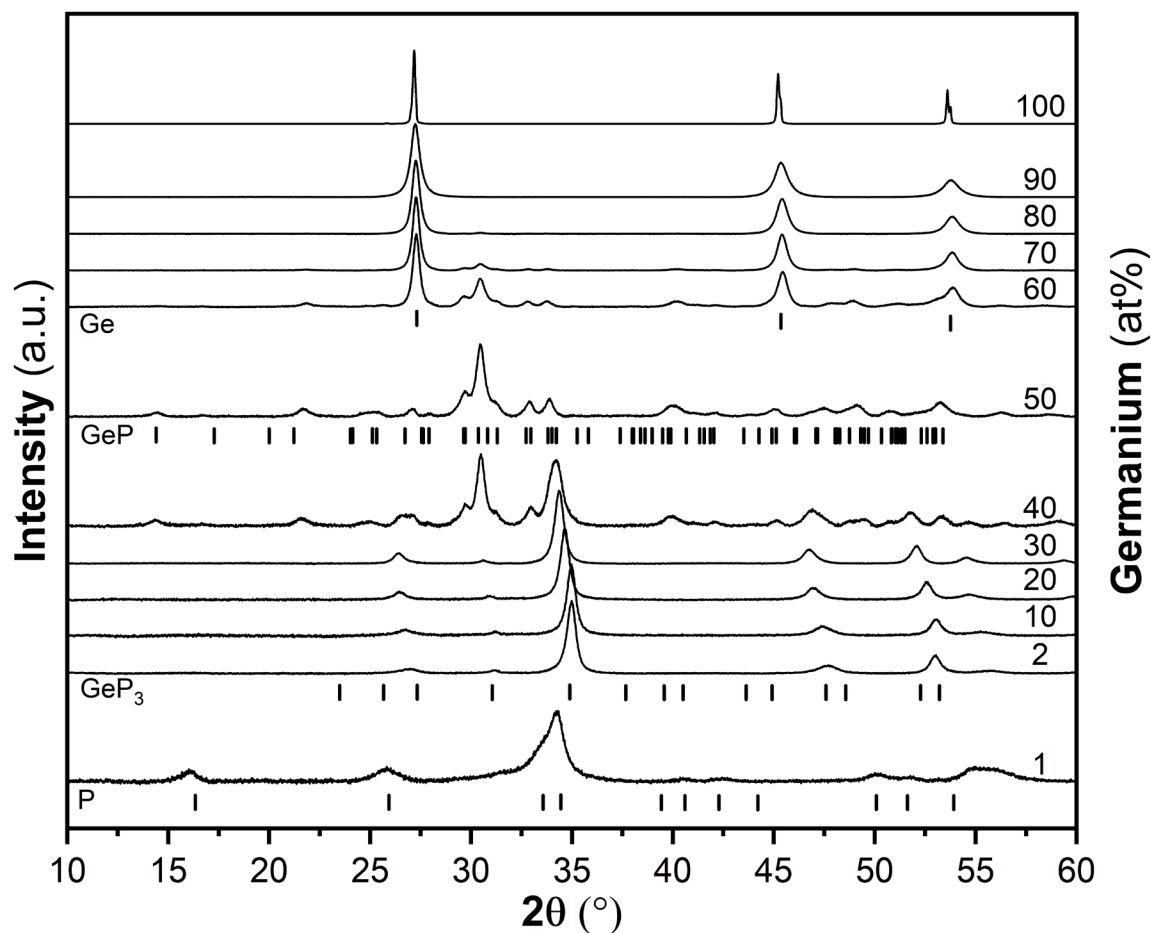


**Figure 4.1** Structural characterization of mechanochemically synthesized P-Ge powders.

X-Ray diffraction patterns with increasing germanium content reveal a limited solubility of germanium into the black phosphorus structure (<1 at% Ge), a limited solid solution alloy range for the trigonal GeP<sub>x</sub> (70 < x < 99 at% P), and several two-phase regions.

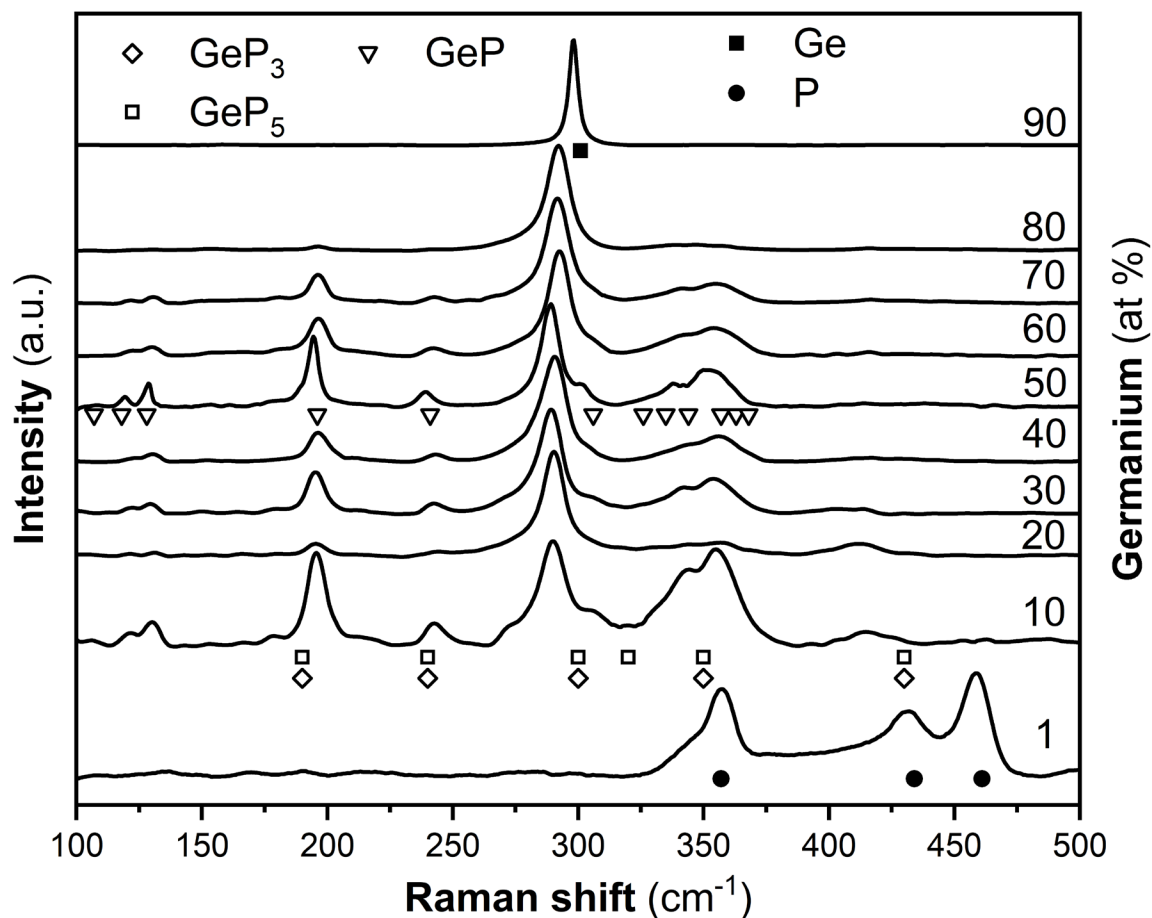


**Figure 4.2** Raman spectra of mechanochemically synthesized P-Ge compounds. Vibrational modes span the range from 100-450  $\text{cm}^{-1}$ , with the heavier germanium atom contributing more to the lower frequency modes. All samples contain a vibrational mode near 290  $\text{cm}^{-1}$  that likely corresponds to elemental germanium due to the instability of the P-Ge compounds.

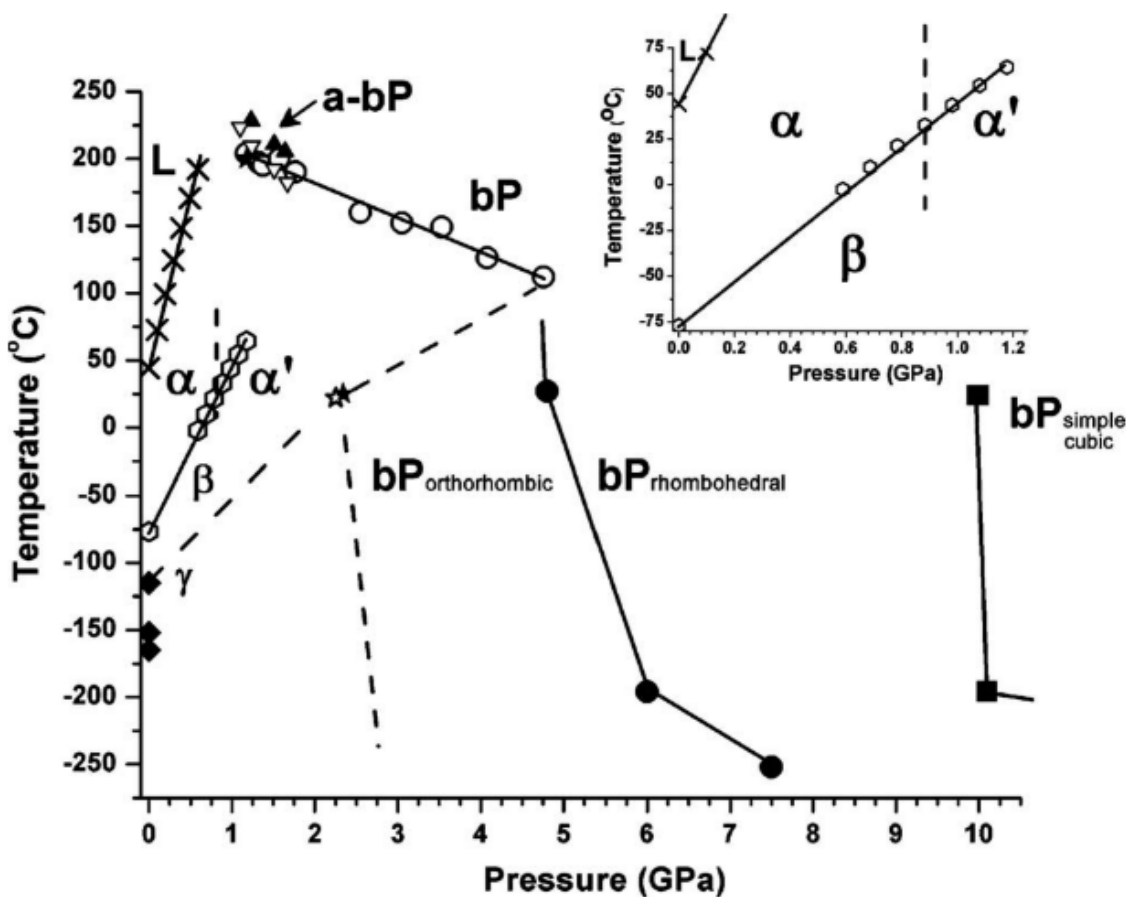


**Figure 4.3** Pressure and temperature phase diagram for elemental phosphorus. At 25°C, white phosphorus converts orthorhombic BP near 2 GPa, then transforms to the metastable rhombohedral BP structure near 5 GPa followed by the metastable simple cubic phase. Also shown are several white phosphorus transformations at near cryogenic conditions. Reproduced from Clark *et al.*<sup>36</sup>

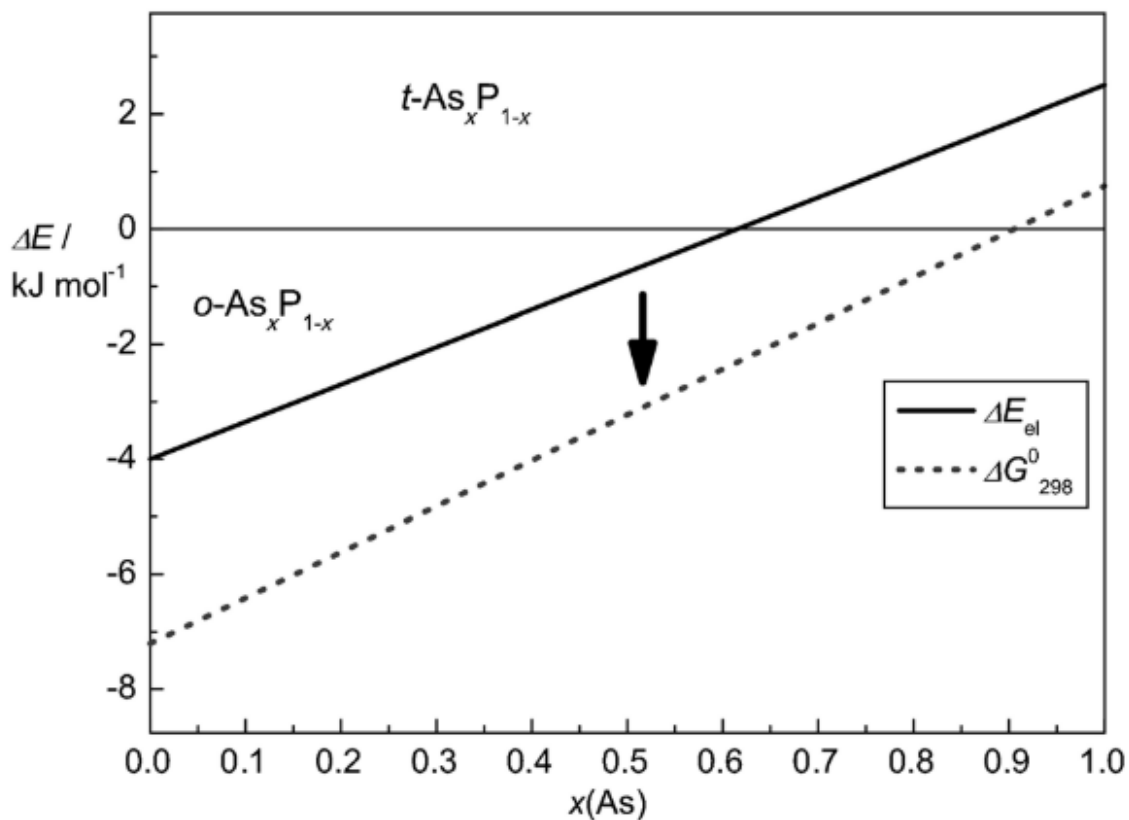


**Figure 4.4** Electron energy and Gibbs free energy stability of o-PAs and t-PAs alloys as function of arsenic concentration.

The solid line represents the electron stability between the two polymorphs while the dashed line represents the thermodynamic stability of the polymorphs as a function of arsenic content. The two methods provide different compositions (60 and 90 at%) for the transition point between the o-PAs and t-PAs structures. Reproduced from Osters *et al.*<sup>56</sup>

## Tables

Table 4.1 Crystallographic details of phosphorus-germanium compounds.

Compound	Space Group	Point Group	Lattice Parameters (Å)			Density	ICSD*
			a	b	c		
GeP	<i>C2/m</i>	<i>2/m</i>	15.14	3.638	9.19	4.15	637492
GeP	<i>F<math>\bar{4}3m</math></i>	$\bar{4}3m$	5.581	5.581	5.581	3.96	53874
GeP	<i>I4mm</i>	<i>4mm</i>	3.544	3.544	5.581	4.91	17032
GeP <sub>3</sub>	<i>R<math>\bar{3}mH</math></i>	$\bar{3}m$	7.05	7.05	9.932	3.86	16294
GeP <sub>5</sub>	<i>R<math>\bar{3}mH</math></i>	$\bar{3}m$	3.437	3.437	10.04	3.65	**
Ge	<i>F3dmS</i>	<i>m<math>\bar{3}m</math></i>	5.656	5.656	5.656	5.33	43422
P	<i>Cmca</i>	<i>mmm</i>	3.62	10.85	4.48	2.7	150873
P	<i>R<math>\bar{3}mH</math></i>	$\bar{3}m$	3.39	3.39	8.63	3.59	600019
Ge	<i>Pbcm</i>	<i>mmm</i>	8.15	11.57	7.76	5.18	263593
Ge	<i>Cmca</i>	<i>mmm</i>	7.885	4.655	4.651	11.30	94305
As	<i>R<math>\bar{3}mH</math></i>	$\bar{3}m$	3.759	3.759	10.547	5.78	16518
As	<i>Cmca</i>	<i>mmm</i>	3.62	10.85	4.48	5.66	609828
o-PAs (53 at%)	<i>Cmca</i>	<i>mmm</i>	3.53	10.71	4.45	4.28	611147

\*Inorganic Crystal Structures Database collection codes for the data presented.<sup>76</sup>

\*\* The data for GeP<sub>5</sub> was from PDF 00-024-0455 as it is not within ICSD.

Table 4.2 P-Ge phases produced by high energy ball milling.

Ge (at%)	Phases	Space Group
<1	P	<i>Cmca</i>
2 – 30	Trigonal P-Ge	<i>R<math>\bar{3}mH</math></i>
31-49	Trigonal P-Ge + monoclinic P-Ge	<i>R<math>\bar{3}mH</math> + C2/m</i>
50	Monoclinic GeP	<i>C2/m</i>
51 – 90	Monoclinic GeP + cubic Ge	<i>C2/m + F3dmS</i>

**Table 4.3 Raman modes of P-Ge phases.**

Compound	Space Group	Symmetry	Raman Peaks (cm <sup>-1</sup> )	Ref
GeP	<i>C2/m</i>	C <sub>2h</sub>	71, 79, 96, 114, 125, 135, 203, 248, 313, 333, 342, 351, 364, 370, 375	6,11,23
GeP	<i>F<math>\bar{4}3m</math></i>	T <sub>d</sub>	- - -	
GeP	<i>I4mm</i>	C <sub>4v</sub>	- - -	
GeP <sub>3</sub>	<i>R<math>\bar{3}mH</math></i>	D <sub>3d</sub>	190, 240, 300, 350, 430	25,42
GeP <sub>5</sub>	<i>R<math>\bar{3}mH</math></i>	D <sub>3d</sub>	190, 240, 300, 320, 350	14
Ge	<i>F3dmS</i>	O <sub>h</sub>	300.9	77
P	<i>Cmca</i>	D <sub>2h</sub>	192.4, 227.7, 361.7, 438.9, 465.9	78

**Table 4.4 High pressure synthesis conditions of P-Ge phases and black phosphorus.**

Compound	Space Group	Temperature (°C)	Pressure (GPa)	Ref
GeP	<i>C2/m</i>	1000	1	40
GeP	<i>F<math>\bar{4}3m</math></i>	1000-1400	3.5-4.0	20
GeP	<i>I4mm</i>	400-800	4.5	12,21
GeP <sub>3</sub>	<i>R<math>\bar{3}mH</math></i>	500-900	6.5	12,21
GeP <sub>5</sub>	<i>R<math>\bar{3}mH</math></i>	400-800	3-6.5	12,21
P	<i>Cmca</i>	0-500	0.5-4.5	38,43,44

**Table 4.5 Comparison of P, As, Ge atoms for solid solution formation.**

Element	Radii (ppm)	Electronegativity	Valency
P	107	2.19	5
As	119	2.18	5
Ge	120	2.01	4

Data obtained from Ref <sup>45-49</sup>

CHAPTER FIVE: MECHANOCHEMISTRY OF THE PHOSPHORUS-  
CHALCOGENIDE COMPOUNDS

This chapter is planned for submission to Elsevier Publications in *Journal of Solid State Chemistry* and should be referenced appropriately.

Reference:

S. V. Pedersen, J. D. Wood, C. Husko, D. Estrada, B. J. Jaques, “Mechanochemistry of the Phosphorus- Chalcogenide compounds.” *Journal of Solid State Chemistry*. **X** (X) XX (2022)

Reproduced/modified by permission of Elsevier Publications.

\*This chapter includes formatting modifications from the originally submitted version.

Mechanochemistry of the Phosphorus-Chalcogenide Compounds

Samuel V. Pedersen<sup>1,2</sup>

Joshua D. Wood<sup>3</sup>

Chad Husko<sup>4</sup>

David Estrada<sup>1,2,5</sup>

Brian J. Jaques<sup>1,2</sup>

<sup>1</sup>Micron School of Materials Science and Engineering, Boise State University,

Boise, ID 83725, USA

<sup>2</sup>Center for Advanced Energy Studies, Idaho Falls, ID 83401, USA

<sup>3</sup>Promethean Consulting, LLC, Oak Park, IL 60302, USA

<sup>4</sup>Iris Light Technologies, Inc., Chicago, IL 60622, USA.

<sup>5</sup>Idaho National Laboratory, Idaho Falls, ID 83402, USA

## 5.1 Introduction

The reactions of phosphorus with the members of the chalcogenide series (S, Se, Te) dates back several centuries. One of the earliest documented reactions is the synthesis of  $P_4S_{10}$  in 1843 by J. Berzelius.<sup>1</sup> Synthesis of low sulfur content compounds such as  $P_4S_3$ ,  $P_4S_5$ ,  $P_4S_7$ , and  $P_4S_9$  were obtained shortly afterwards using various thermal treatments with mixtures of P-S phases or P-S-I derivatives.<sup>1</sup> **Figure 5.1** shows the structural similarity of P-S compounds with increasing sulfur content. Notably, increasing the sulfur content decrease the number of P-P bonds and also results in terminal double bonds between phosphorus and sulfur. Fewer known binary P-Se compounds exist; notably, the  $P_4Se_3$  cage structure is structurally equivalent to caged  $P_4S_3$  monomer and is obtained in similar fashion by mixing molten white phosphorus and selenium in the presence of tetralin.<sup>2</sup> **Figure 5.2** shows the known  $P_4Se_3$  monomer along with local structural units that exist in P-Se amorphous glasses. No known binary compounds of phosphorus and tellurium exist although there is evidence for an amorphous phase containing 20 at% tellurium produced by prolonged ball milling.<sup>3</sup>

Traditionally, melt-quench methods are used to produce phosphorus sulfides and selenides.<sup>4-7</sup> Melt-quench synthesized  $P_2S_5$  forming the dimeric  $P_4S_{10}$  molecule is used to make dithiophosphoric acids which are reacted with zinc oxides to produce an additive that enhances the effectiveness of lubricating oils.<sup>1,8-11</sup> The zinc dialkyldithiophosphates family of additives were originally developed in the 1930's as anti-wear and anti-corrosion agents in mineral and synthetic oils and are still in use in nearly all lubricated oils today.<sup>8-11</sup> Sodium and ammonium salts with dithiophosphates are also used at flotation agents in metal extraction.<sup>12-14</sup>  $P_4S_{10}$  is also extensively used in organic synthesis

of sulfur containing heterocycles and in the synthesis of Lawesson's reagent.<sup>1,15,16</sup> The other notable P-S commercial compound is  $P_4S_3$ , which is used as component in strike-anywhere matches.<sup>17,18</sup> Recently,  $P_2S_5$  is also being investigated as an amorphous solid electrolyte in lithium ion batteries.<sup>6,19-25</sup> Applications of phosphorus and selenium are more limited. Phosphorus-selenium heterocycles as ligands have been explored in organometallic synthesis.<sup>16</sup> As for tellurium phosphides, no applications appear to exist, to the best of the author's knowledge. Presumably, the thermodynamic instability of any formed compound prevents its synthesis and use. Thermal reactions with white phosphorus and tellurium produce an unstable P-Te compound while high pressure (3-7 GPa) experiments with black phosphorus and tellurium indicate no compounds are formed.<sup>26</sup> Ternary reactions with phosphorus and the chalcogenides were aimed towards synthesis of non-oxide glasses for infrared transmission, mostly as ternary alloys of Ge-P-X (X = S, Se, Te).<sup>4-7</sup> In light of recent mechanochemical synthesis of black phosphorus,<sup>27-29</sup> phosphorus-arsenic alloys, and germanium phosphides,<sup>30-39</sup> the possibility of reacting phosphorus with the chalcogenides using mechanochemistry is explored. Milling studies to map the composition dependent ball mill accessible phase diagrams are reported.

Several of the crystalline P-S phases and glassy P-Se phases are synthesized for the first time using high energy planetary ball milling, to the best of the author's knowledge. This process avoids liquid processing of highly volatile phosphorus, sulfur, selenium and tellurium at elevated temperatures; instead, the use of sealed steel vessels under an inert gas environment alleviates the release of hazardous vapors and unwanted reactions with oxygen and moisture. Mixtures of P-S phases were always produced

indicating a complex milling behavior. Glassy P-Se powders were readily produced. At low concentrations, sulfur and selenium appear to bond into the crystal structure of black phosphorus, indicating these may be suitable dopants. However, electrical property measurements are still needed to confirm if carrier concentrations are improved. Milling P-Te together did not result in any compound which confirms the lack of chemical bonding between P-Te and indicates tellurium may not be a substitutional dopant for black phosphorus.

## 5.2 Results

For clarity, the mechanochemical synthesis results of P-S, P-Se, and P-Te are divided into three sections, starting with the lightest chalcogenide element, sulfur, and working towards the heaviest, tellurium. In each section, powder XRD results and powder Raman results showing the phases produced at a given chalcogenide concentration. Additionally, crystallographic details for the P-S, P-Se, and P-Te phases are presented in **Table 5.1**. The known Raman modes for applicable phases are split into separate tables and referred to specifically within each section.

### Results: Mechanical alloying of P-S compounds

For the P-S system, two sets of milling trials were conducted. In the first set, sulfur was added in increments of 10 at%; the XRD and Raman results are presented in **Figure 5.3** and **Figure 5.4**, respectively. **Table 5.1** lists the reference XRD Powder Diffraction Files (PDF) and the associated Inorganic Crystal Structures Database (ICSD) collection code for each phase identified.<sup>40</sup> Referring to **Figure 5.3** and **Figure 5.4**, at low sulfur content (below 30 at%), XRD peaks and vibrational modes corresponding to

pure BP appeared. At 10 at% sulfur, the XRD indicates the formation of black phosphorus and the Raman spectra show only vibrational modes corresponding to pure BP. Surprisingly, at the 20 at% sulfur content, vibrational modes that appear to partially match  $P_4S_3$  were present along with the pure BP modes; however, the XRD pattern was nearly amorphous; a small peak near  $33^\circ$  indicates a minor fraction of BP still present supporting the Raman results of a mixture of sulfur doped BP and  $P_4S_3$ . **Figure 5.5** depicts possible bonding arrangements with sulfur sitting at lattice sites or bridging across atoms on the surface of a single layer or across the van der Waals gap. Between 40-70 at% sulfur, several crystalline phases were present but the lack of sharp crystalline peaks made phase identification impractical. Only the pattern at 50 at% sulfur could be matched to  $P_4S_7$ . The Raman modes in **Figure 5.4** of the higher sulfur content samples indicate mixtures of  $P_4S_5$ ,  $P_4S_7$ , and  $P_4S_{10}$  along with amorphous selenium and sulfur-rich version of  $P_4S_{10+n}$ . The 80-90 at% sulfur runs show amorphous XRD structures and mostly match the  $P_4S_{10}$ ,  $P_4S_{10+n}$ , and amorphous sulfur Raman modes which is expected.

As the 10 at% sulfur increment milling trials sampled two phase regions of the P-S phase diagram,<sup>41</sup> a second set of trials targeting known stoichiometric phases were conducted. The XRD and Raman results are presented in **Figure 5.6** and **Figure 5.7**, respectively. To avoid confusion between the targeted phase and the actual phases detected, the patterns are labeled A through F and the nominal molar ratio of phosphorus to sulfur that was loaded into the stainless-steel milling vessel are listed in **Table 5.2**. Patterns A and B both were unsuccessful attempts to produce lower sulfur containing compounds ( $P_4S_3$ ,  $P_4S_4$ ); instead the formation of the higher sulfur containing phases (e.g.,  $P_4S_7$ ) was detected by XRD and Raman. The trial targeting the  $P_4S_3$  composition

consistently matched the  $P_4S_7$  structure. Repeated trials reproduced the  $P_4S_7$  structure at the  $P_4S_3$  molar ratio. From **Figure 5.7**, for pattern A, a set of low-frequency Raman modes ( $100\text{-}150\text{ cm}^{-1}$ ) and a pair of high-frequency modes ( $650\text{-}700\text{ cm}^{-1}$ ) are consistent with  $P_4S_7$  modes which are absent from the reference  $P_4S_3$  modes.<sup>42</sup> In fact, the Raman spectra targeting  $P_4S_3$  is nearly indistinguishable from the trials targeting PS,  $P_4S_5$ , and  $P_4S_7$  except for those modes at low frequency ( $100\text{-}150\text{ cm}^{-1}$ ) and at high frequency ( $650\text{-}700\text{ cm}^{-1}$ ). The pattern C targeted  $P_4S_5$  but instead appears to be a mixture of  $P_4S_6$ ,  $P_4S_7$  and a sub-stoichiometric (sulfur deficient) version of  $P_4S_7$  of the composition  $P_4S_{6.78}$ .<sup>43</sup> Thus pattern A is identified as  $P_4S_7$  while B and C are mixtures of  $P_4S_7$ ,  $P_4S_{6.78}$ , and  $P_4S_6$  based on the combined XRD and Raman results. Moving onto the higher sulfur content samples, patterns D and E targeted the  $P_4S_7$  and  $P_4S_9$  phases, respectively. Both patterns D and E mostly match the  $P_4S_{10}$  and sulfur reference XRD patterns. However, a few XRD peaks match the sub-stoichiometric FeS compound indicating iron contamination during the HEBM process. Additionally, a close inspection of **Figure 5.7** of the Raman mode near  $260\text{ cm}^{-1}$  that appears in patterns D, E, and F match one of the strongest modes from  $P_4S_{10}$ .<sup>42</sup> Pattern F targeting  $P_4S_{10}$  resulted in an XRD amorphous phase while the Raman mostly matches mixtures of  $P_4S_{10}$ , sulfur and the same iron sulfide phase.. Nearly all trials targeting a specific stoichiometry resulted in mixtures. The XRD and Raman confirm mixed phase samples that were either mostly  $P_4S_7$  (below the sulfur content required for pure phase  $P_4S_7$ ) or  $P_4S_{10}$  (above the sulfur content required for  $P_4S_7$ ).

### Results: Mechanical alloying of P-Se compounds

Milling of phosphorus with the larger selenium atom resulted in only amorphous phases above 10 at% selenium, as shown in the XRD patterns of **Figure 5.8**. The 10 at% selenium sample appears similar to the BP diffraction pattern, although a broad amorphous peak (centered at 31 degrees two theta) suggests that the selenium distorts the BP lattice. It is thought that this distortion is a result of either the nature of the position of the selenium atoms in the BP lattice, or the formation of an amorphous P-Se phase. The Raman results in **Figure 5.9** reveal distinct vibrational modes allowing differentiation of the x-ray amorphous phases to an extent. At 10 at% selenium, the vibrational modes of BP are still detected while a low frequency shoulder near  $340\text{ cm}^{-1}$  is overlapped with the BP  $A_g^1$  mode near  $360\text{ cm}^{-1}$ . Alternatively, this could be a mixture of BP with a P-Se molecular unit as indicated by roman numerals (I-IV) and listed in **Table 5.3**.<sup>44</sup> Only qualitative matching of the milled powders to vibrational frequencies listed in **Table 5.3** was conducted as the peaks were too convoluted and too broad to identify individual vibrational modes. Exposure of the sample to low laser power (less than 1 mW) with repeat acquisitions resulted in visible degradation of the sample at the location of the beam. Unfortunately, attempts to use lower power (0.01, 0.1 mW) with extended acquisition times (60+ minutes) resulted in poor signal to noise ratio with indistinguishable patterns. Yuan *et al.* and Georgiev *et al.* used Raman spectroscopy and phosphorus based nuclear magnetic resonance spectroscopy (P-NMR) results from a series of melt-quenched P-Se glasses to analyze the local P-Se structures, such as the  $\text{P}_4\text{Se}_3$  monomers,  $\text{P}(\text{Se}_{1/2})_3$  pyramidal units, and Se-Se chains that linked the units together.<sup>44-46</sup> These structural units are depicted in **Figure 5.2**. Raman modes of these

structural units appear to match those present in the ball mill synthesized P-Se powders.<sup>44-46</sup> A recent Raman study (2021) by Yuan *et al.* on conventional melt-quench P-Se glasses showed similar broad patterns at similar peak positions as a function of composition ( $30 > x > 95$  at% selenium) which confirms the results of the ball mill synthesized P-Se glasses.<sup>44-46</sup> The two strongest group of Raman modes from their melt-quench synthesized P-Se glasses include the peaks near  $250\text{ cm}^{-1}$  which correspond to Se-Se chains within the P-Se glasses, and the group of peaks between  $320\text{-}370\text{ cm}^{-1}$  that correspond to  $\text{P}_4\text{Se}_3$  monomers.<sup>45,47-50</sup> The ball milled patterns in **Figure 5.9** show the same grouping of peaks at  $250$  and  $320\text{-}370\text{ cm}^{-1}$  indicating the presence of Se-Se links and  $\text{P}_4\text{Se}_3$  monomer units, respectively. Additionally, the ethylene-like structure appears to be present as several of the modes within the  $325\text{-}375\text{ cm}^{-1}$  range appear that do not match the main  $\text{P}_4\text{Se}_3$  mode within the same wavenumber regime.

#### Results: Mechanical alloying of P-Te compounds

The XRD and Raman results of milling trials for the P-Te system are shown in **Figure 5.10** and **Figure 5.11**, respectively. A two-phase region with BP and tellurium is evident in the 10 and 20 at% tellurium compositions. Above 20 at% tellurium, the main phase was trigonal tellurium. It is not clear from the XRD patterns if phosphorus is bonded into the trigonal structure or exists in an amorphous state. The powders of the 20-90 at% samples were all of a metallic luster (like that of pure tellurium) and with no evidence of red phosphorus, as indicated by color, XRD, and Raman. Trigonal tellurium has Raman modes at  $120$  and  $140\text{ cm}^{-1}$ , well below the modes of pure BP.<sup>51</sup> The Raman spectra of the 1, 2, 10, 20, 30 and 40 at% tellurium samples all show the BP modes with

decreasing intensity while modes at low frequencies (120 and 140  $\text{cm}^{-1}$ ) increase in intensity with higher tellurium concentration. This implies that tellurium exists separately as a distinct phase rather than forming substitutional or interstitial bonding within the BP lattice.

### 5.3 Discussion

#### Discussion: Mechanical alloying of P-S compounds

Overall, to the best of the author's knowledge, this is the first report of the synthesis of the P-S and P-Se compounds exclusively by mechanical alloying in a high energy planetary ball mill starting from elemental powders. Mechanical alloying of phosphorus and sulfur may provide an alternative industrial synthesis for commercially relevant P-S compounds, provided that the process is able to produce single phase powders. As it stands, attempts to produce single phase  $\text{P}_4\text{S}_3$ ,  $\text{P}_4\text{S}_5$ ,  $\text{P}_4\text{S}_7$ ,  $\text{P}_4\text{S}_{10}$  were unsuccessful. Powder mixtures that favor the higher sulfur structures occurred even at low sulfur contents – the exact reason for this is currently unknown. Comparison to recent (2021) high pressure trials with diamond anvil cells on  $\text{P}_4\text{S}_3$  showed no new stable phases upon compression and decompression<sup>52</sup> – recovery of the original Raman peaks occurred upon decompression. Although a metastable phase was postulated from the appearance of several new Raman modes above 7 GPa, these were not quenchable for the  $\text{P}_4\text{S}_3$  composition. Within the same work, high pressure trials on the  $\text{P}_4\text{S}_{10}$  structure gave new additional Raman modes upon decompression only if the applied pressure was above 12 GPa.<sup>52</sup> Their DFT results indicated that terminal sulfur double bonded at phosphorus vertices on the  $\text{P}_4\text{S}_{10}$  molecule would split to form single bonds with adjacent sulfur atoms forming a polymeric structure. The end result would be retention of many of the

vibrational modes associated with the internal  $P_4S_{10}$  cage structure; however, new modes associated with the terminal sulfur atoms that restructured to form either dimers or polymeric chains were evident in their in-situ Raman data.<sup>52</sup> Therefore, it is postulated that ball milling may result in a similar behavior, where the cage-like structure of  $P_4S_7$  and  $P_4S_{10}$  are prevalent at the various compositions with the excess sulfur or phosphorus bonds forming distinct long-range organization of the molecular cages. Alternatively, the milling duration used may not be sufficient to fully homogenize at the atomic scale the phosphorus and sulfur atoms, resulting in atomic clusters of sulfur (hence the persistence of S-S bonds even at the lower stoichiometric compounds). One possibility is the evaporation of phosphorus during milling; although this is unlikely since hundreds of one-gram ball mill runs for the synthesis of black phosphorus powders were conducted over the course of this work with 95% or higher extraction of the starting mass. Chemical analysis of the P-S powders using EDS indicated significant deviation from the target compositions, notably all samples were sulfur deficient. Presumably, a detrimental interaction with sulfur and iron may be promoted during milling with stainless steel media and vessel. On-going efforts to determine the presence of iron sulfides in either the powder or the media surfaces may help to reveal if this is the reason for lack of compositional control.

There appears to be some degree of solubility and potential chemical substitutional doping of sulfur into the crystalline orthorhombic black phosphorus as is evident by the lack of sulfur or phosphorus-sulfide XRD peaks or Raman modes in both the XRD pattern in **Figure 5.3** and Raman spectra in **Figure 5.4** when the sulfur content less than 10 at%. Considering the P-S compounds have relatively high Raman peak

intensity and a wide range of vibrational frequencies spanning 100-500  $\text{cm}^{-1}$ , the absence of any additional modes within the 10 at% sample would suggest substitutional doping into the lattice sites of phosphorus. While there should be additional modes due to the 2-atom basis, the nearly identical atomic mass (30.97 and 32.07 amu) would only likely broaden the existing vibrational modes or produce shoulders.<sup>53-58</sup> The propensity of phosphorus and sulfur to produce molecular solids by forming adamantine cages with phosphorus or sulfur atoms acting as bridges between the cages may help to explain the unusual result at 20 at% sulfur addition. The XRD pattern in **Figure 5.3** shows two broad (amorphous) peaks at 17 and 32 degrees two theta (which are nearly identical in position and shape as that of the 30 at%) with the BP peaks overlapped; such a result by itself would likely indicate a two-phase region. The Raman spectra in **Figure 5.4** however shows mostly the BP modes, but with several extra modes within the same frequency range – these do not correspond to any known P-S compounds.<sup>42</sup> Instead, it is postulated that the presence of S-bonds link the 2D layers across the van der Waal gap, or in plane S-bridges linking distinct BP nanocrystals as shown in **Figure 5.5**.<sup>59</sup> The 30 at% sample mostly matches the  $\text{P}_4\text{S}_3$  phase but the Raman modes of BP are still present. Furthermore, a set of weak peaks between 260 and 300  $\text{cm}^{-1}$  does not match any known P-S compounds, further suggesting an unusual interaction of P-S molecular structures or links with the BP lattice.

#### Discussion: Mechanical alloying of P-Se compounds

Mechanical milling has been shown to produce amorphous pure selenium<sup>60,61</sup> and melt processing of P-Se compounds typically forms amorphous glasses.<sup>62</sup> Only in a

narrow window centered around the compound  $P_4Se_3$  ( $x=0.43$  at% Se) does a crystalline product form from the melt.<sup>44</sup> Presumably, within the planetary ball mill, the continuous comminution of large particles coupled with the effectiveness of milling to reduce crystalline grain sizes into the nanometer range, the appearance of only an x-ray amorphous  $P_4Se_3$  can be expected. The Raman spectra for the 40 at% composition in **Figure 5.9**, shows a distinct peak near  $365\text{ cm}^{-1}$ , which is close the primary mode (identified as marker IV) of  $P_4Se_3$  at  $370\text{ cm}^{-1}$ . The amorphous ball milled P-Se samples qualitatively match the recent Raman study on melt-quenched P-Se glasses at all compositions from 30+ at% selenium.<sup>44-46</sup> Selenium reacts with phosphorus in the same manner as arsenic does at concentrations below 10 at%. The XRD pattern in **Figure 5.8** at 10 at% selenium indicates a broad amorphous peak near 31 degrees two theta, while the Raman spectra in **Figure 5.9** shows vibrational modes that are consistent with black phosphorus. The appearance of a weak shoulder on the  $A_g^1$  mode ( $360\text{ cm}^{-1}$ ) and a lower frequency mode near  $318\text{ cm}^{-1}$  is comparable to the modes observed for the 10 at% arsenic alloyed sample (shoulder on the  $A_g^1$  and low frequency mode near  $320\text{ cm}^{-1}$ , as shown in **Figure 3.4**). As arsenic and selenium have comparable atomic sizes and masses, the substitution of selenium onto the BP lattice should produce similar vibrational frequencies.

#### Discussion: Mechanical alloying of P-Te compounds

Mechanical alloying of phosphorus with tellurium indicates the existence of a broad two-phase region consisting of BP and trigonal tellurium within the compositional range of 1-70 at% tellurium. This work using high energy planetary ball milling indicates

no compound formation or alloying of phosphorus and tellurium. The work here on ball milling P-Te contradicts results by Itoh *et al.*<sup>3</sup> In their ball mill synthesis work with P-Te compounds, they claimed P-Te bond formation in a fully amorphous sample based on pair distribution functions calculated from neutron and x-ray diffraction measurements.<sup>3</sup> They note that their sample was thermally unstable and decomposed rapidly at 200 °C, which is well below the melting temperature of black phosphorus (415 °C) or tellurium (449°C). This suggests a weak P-Te bond and is in agreement with literature, which states that P-Te bonds are easily broken and unfavorable in most chemical structures.<sup>63-65</sup> Furthermore, they observed elemental tellurium peaks in samples milled for 80 hours with 10 and 30 at% tellurium mixed within the amorphous phase. The lack of a crystalline BP phase in the work of Itoh *et al.* for the 10 at% sample suggests the impact energy of their milling system was insufficient to convert red phosphorus into black phosphorus,<sup>3</sup> unlike the milling results achieved in this work. A potential future study should repeat the 20 at% tellurium trial and ball mill for a similar time as used by Itoh *et al.* (~80 hours) to see if a fully amorphous phase is reproduced. Milling for long durations, particularly when the vessel and media configuration favors grinding (by loading the vessel with grinding media above 50-60% of the free volume) over high velocity impacts, has been noted by numerous groups to form amorphous phases of metals and compounds.<sup>39</sup> The lack of any known binary compounds of P-Te,<sup>3</sup> the weak bonding in ternary P-Te-X compounds (such as U-P-Te, Th-P-Te,<sup>66,67</sup> and BaP<sub>4</sub>Te<sub>2</sub><sup>63,67</sup>), and the weak bonding that does occur in P-Te organometallic compounds,<sup>63</sup> suggests that tellurium and phosphorus exist as a two phase mixture at all compositions. Although the

reported phase diagram shows a compound, PTe at 50 at% tellurium, no details on its structure were provided; its existence is unlikely or is highly unstable even if formed.<sup>68</sup>

Attempts to dope black phosphorus with 1-2 at% tellurium also showed a two-phase region as determined by Raman spectroscopy. **Figure 5.11** shows low frequency Raman modes clearly matched to trigonal tellurium indicating lack of substitution into the BP structure. These results also contradict BP doping experiments produced by chemical vapor transport.<sup>69-71</sup> In these CVT grown single crystals of BP, tellurium was added into the mixture of red phosphorus, tin iodide, and tin metal and subsequently reacted at temperatures near 600°C. Compositional analysis within those reports indicated <1 at% tellurium (using EDS or XPS) while Raman often showed slight peak shifts of 1-2 cm<sup>-1</sup> of the main BP modes. Absent in these works are electrical characterization such as Hall measurements to verify the type and concentration of the major charge carriers combined with chemical and structural characterization. Arguably, introducing tellurium using an in-situ molecular source (tellurium iodide) may increase the uniform incorporation of tellurium,<sup>70</sup> as compared to mechanical alloying, such that elemental tellurium vibrational modes are fully absent in Raman spectra. Early work by Akahama *et al.* reported Te-doped BP crystals by high pressure synthesis and their Hall measurements indicated n-type conduction – but their carrier concentration was only one order of magnitude higher (10<sup>16</sup> electrons per cm<sup>-3</sup>) than the undoped p-type (10<sup>15</sup> holes per cm<sup>-3</sup>) crystals.<sup>72</sup> While their results prove tellurium affects the electron concentration, the question arises to how many carriers (or fraction of a charge) each tellurium atom actually donates to total number of free carriers.<sup>72</sup> Since Akahama *et al.* did not report their actual tellurium levels introduced during the synthesis and the amount detected in the sample afterwards, it is

difficult to analyze the effectiveness of tellurium as a dopant from their work alone.<sup>72</sup>

Nonetheless, high energy planetary ball milling does not appear to be effective at driving tellurium into black phosphorus to produce an effective dopant.

In conclusion, we have demonstrated high energy planetary ball milling as a direct route to produce (1) mixtures of crystalline and amorphous phosphorus sulfides and crystalline sulfur substituted into black phosphorus powders, (2) amorphous phosphorus-selenium glasses spanning 20-90 at% selenium content and selenium substituted into black phosphorus powders, and (3) binary mixtures of crystalline tellurium metal and crystalline black phosphorus with no evidence of tellurium doping or bonding with phosphorus. Sulfur and selenium are likely candidates for n-type doping of black phosphorus provided these elements introduce shallow donor states near the conduction band rather than mid-gap states. Tellurium is likely a poor candidate for n-type doping due to thermal instability and prevalence to bond to itself over phosphorus even under high impact milling conditions.

Future work should further explore the P-S phases with a focus on determining if lower energy grinding conditions is sufficient to form P-S compounds, as larger commercial mills are of the tumbler (gravity) type that tend to favor grinding. Optimization of the process is needed to produce single phase powders with an emphasis on the commercially relevant  $P_4S_{10}$  compound. A more detailed study on sulfur and selenium below 10 at% in finer increments down to 1 at% (and less) would help to confirm their behavior as substitutional atoms using the trends observed in phosphorus-arsenic alloys as a benchmark. Complementary techniques such as x-ray photoelectron spectroscopy (binding energies, oxidation states), Fourier transformation infrared

spectroscopy (infrared active vibrational modes), and phosphorus nuclear magnetic resonance spectroscopy (chemical shifts, coordination) would further help to determine the local structure around the sulfur and selenium atoms. Atomistic modeling of the sulfur and selenium atomic positions and impacts to the optical and electrical properties would greatly aid in determining the suitability of these elements as dopants.

#### 5.4 Methods

**In the milling experiment**, elemental red phosphorus (1-5 g) (Alfa Aesar, 97% purity, -60 mesh, Alfa Aesar, 99.99% purity, chunks) and elemental sulfur (1-5 g) (Alfa Aesar, 99.99% purity, -200 mesh), elemental selenium (1-5 g) (Alfa Aesar, 99.99% purity, -200 mesh), and elemental tellurium (1-5 g) (Alfa Aesar, 99.99% purity, -200 mesh), and stainless steel media (10 mm diameter, 100 g) were weighed and loaded into a stainless steel vessel (250 mL) inside an argon atmosphere glovebox ( $P_{O_2} < 0.1$  ppm) and sealed under argon (90-95 kPa) at room temperature. The ball to powder mass ratio was 20:1. All milling experiments were conducted with the PM100 planetary ball mill (Retsch, Germany) with pauses in the milling cycles (15 minutes on, 30 minutes off) to prevent overheating of the unit and to switch the direction of flywheel rotation (promotes better mixing). Milling conditions (rpm and duration) were held constant at 600 rpm and 14 hours of milling.

**Powder X-ray diffraction (XRD)** data was obtained in the Bragg-Brentano geometry (CuK $\alpha$ , Rigaku MiniFlex 600, Japan) on powder (0.165 g) sealed inside a polyimide dome within an argon glovebox to prevent possible ignition with air during x-ray measurements.

**Raman spectroscopy (Raman)** data was obtained (Horiba LabRam HR Evolution, Japan) on densely packed powder samples (0.01 g) prepared inside an argon glovebox that were sealed inside a custom-built enclosure with a sapphire window to prevent oxidation and ignition during measurements. A 50 mW 532nm laser source (Nd:YAG) was used to generate spectra collected with a Si CCD. Spectra obtained at 20X objective with quadruple acquisitions for 60 seconds at ten random locations throughout the bulk surface using the 1800 lines/mm grating at room temperature.

### **Acknowledgements**

This work has been funded, in part, by Boise State University College of Engineering Seed Funding Program and IGEM Commerce (grant number 003786). Materials were synthesized and processed in the Advanced Materials Laboratory (Boise State University, Boise, ID). XRD was performed in the Boise State Center for Materials Characterization (Boise State University, Boise, ID). Raman spectroscopy was performed in the Advanced Nano Materials and Manufacturing Laboratory (Boise State University, Boise, ID). C. Greseth and T. Nowling are acknowledged for their support with sample synthesis and characterization.

### **Author Contributions**

S.P. conceptualized and executed the milling studies, performed and analyzed the characterization data. D.E. and B.J. supervised and directed the project.

### **Competing Interests**

The authors declare no competing interests.

## References

- 1 Ozturk, T., Ertas, E. & Mert, O. A Berzelius Reagent, Phosphorus Decasulfide (P<sub>4</sub>S<sub>10</sub>), in Organic Syntheses. *Chem. Rev.* **110**, 3419-3478 (2010)
- 2 Wood, P. T. *Phosphorus-sulfur and phosphorus-selenium heterocycles* Doctoral thesis, Imperial College, (1988).
- 3 Itoh, K., Mizuhara, Y. & Otomo, T. Mechanochemical synthesis of binary phosphorus telluride: Short range structure and thermal properties. *J. Solid State Chem.* **267**, 119-123 (2018)
- 4 Hilton, A. R. Nonoxide Chalcogenide Glasses as Infrared Optical Materials. *Appl. Opt.* **5**, 1877-1882 (1966)
- 5 Eckert, H. Structural Characterization of Non-Oxide Chalcogenide Glasses using Solid State NMR. *Angew. Chem. Int. Ed. Engl.* **28**, 1723-1732 (1989)
- 6 Eckert, H., Liang, C. S. & Stucky, G. D. Phosphorus-31 magic angle spinning NMR of crystalline phosphorus sulfides: correlation of phosphorus-31 chemical shielding tensors with local environments. *J. Phys. Chem.* **93**, 452-457 (1989)
- 7 Cui, S. *et al.* *Selenide and telluride glasses for mid-infrared bio-sensing*. Vol. 8938 PWB (SPIE, 2014).
- 8 Spikes, H. The History and Mechanisms of ZDDP. *Tribol. Lett.* **17**, 469-489 (2004)
- 9 Zhang, J. & Spikes, H. On the Mechanism of ZDDP Antiwear Film Formation. *Tribol. Lett.* **63**, 24 (2016)
- 10 Johnson, D. W. & Hils, J. E. Phosphate Esters, Thiophosphate Esters and Metal Thiophosphates as Lubricant Additives. *Lubricants* **1**, 132-148 (2013)
- 11 Canter, N. ZDDP's uncertain future. *Tribol. Lubr. Technol.* **75**, 12-22 (2019)
- 12 Wang, X., Liu, W., Jiao, F., Qin, W. & Yang, C. New insights into the mechanism of selective flotation of copper and copper-tin alloy. *Sep. Purif. Technol.* **253**, 117497 (2020)
- 13 Chen, W. *et al.* The selective flotation of chalcopyrite against galena using alginate as a depressant. *Miner. Eng.* **141**, 105848 (2019)
- 14 Zhou, X., Zhao, C., Li, Y., Chen, J. & Chen, Y. The flotation process, smelting process and extraction products on jamesonite: A review. *Miner. Eng.* **172**, 107146 (2021)
- 15 Ozturk, T., Ertas, E. & Mert, O. Use of Lawesson's Reagent in Organic Syntheses. *Chem. Rev.* **107**, 5210-5278 (2007)
- 16 Hua, G. & Woollins, J. D. Organophosphorus-selenium/tellurium reagents: from synthesis to applications. *Phys. Sci. Rev.* **4**, (2019)
- 17 Bricklebank, N. *et al.* *Handbook of Chalcogen Chemistry: New Perspectives in Sulfur, Selenium and Tellurium*. (Royal Society of Chemistry, 2007).
- 18 Corbridge, D. E. C. *Phosphorus : an outline of its chemistry, biochemistry, and technology*. 3rd ed. edn, (Elsevier Science Publishers, Amsterdam, 1985).
- 19 Shibao, R. K., Xia, Y., Srdanov, V. I. & Eckert, H. Plasma-Enhanced Chemical Vapor Deposited Phosphorus Sulfide Films. Characterization by Raman and Solid-State NMR Spectroscopies and Comparison to Melt-Quenched Glassy Materials. *Chem. Mater.* **7**, 1631-1638 (1995)

- 20 Tatsumisago, M., Hama, S., Hayashi, A., Morimoto, H. & Minami, T. New lithium ion conducting glass-ceramics prepared from mechanochemical Li<sub>2</sub>S–P<sub>2</sub>S<sub>5</sub> glasses. *Solid State Ion.* **154-155**, 635-640 (2002)
- 21 Lin, Z., Liu, Z., Fu, W., Dudney, N. J. & Liang, C. Phosphorous Pentasulfide as a Novel Additive for High-Performance Lithium-Sulfur Batteries. *Adv. Funct. Mater.* **23**, 1064-1069 (2013)
- 22 Zu, C., Klein, M. & Manthiram, A. Activated Li<sub>2</sub>S as a High-Performance Cathode for Rechargeable Lithium–Sulfur Batteries. *J. Phys. Chem. Lett.* **5**, 3986-3991 (2014)
- 23 Baba, T. & Kawamura, Y. Structure and Ionic Conductivity of Li<sub>2</sub>S–P<sub>2</sub>S<sub>5</sub> Glass Electrolytes Simulated with First-Principles Molecular Dynamics. *Front. Energy Res.* **4**, (2016)
- 24 Kudu, Ö. U. *et al.* A review of structural properties and synthesis methods of solid electrolyte materials in the Li<sub>2</sub>S – P<sub>2</sub>S<sub>5</sub> binary system. *J. Power Sources* **407**, 31-43 (2018)
- 25 Li, Y. *et al.* Interface engineering for composite cathodes in sulfide-based all-solid-state lithium batteries. *J. Energy Chem.* **60**, 32-60 (2021)
- 26 Maisashvili, N. G., Vinogradova, G. Z., Timofeeva, N. V. & Luzhnaya, N. P. Interaction of Various Phosphorus Modifications with Tellurium. *Russian J. Inorg. Chem.* **25**, p 680-683 (1980)
- 27 Pedersen, S. V. *et al.* Mechanochemical conversion kinetics of red to black phosphorus and scaling parameters for high volume synthesis. *npj 2D Mater Appl* **4**, 36 (2020)
- 28 Ferrara, C. *et al.* Efficiency and Quality Issues in the Production of Black Phosphorus by Mechanochemical Synthesis: A Multi-Technique Approach. *ACS Appl. Energy Mater.* **2**, 2794-2802 (2019)
- 29 Park, C. M. & Sohn, H. J. Black Phosphorus and its Composite for Lithium Rechargeable Batteries. *Adv. Mater.* **19**, 2465-2468 (2007)
- 30 Li, W. *et al.* Layered phosphorus-like GeP<sub>5</sub>: a promising anode candidate with high initial coulombic efficiency and large capacity for lithium ion batteries. *Energy Environ. Sci.* **8**, 3629-3636 (2015)
- 31 Qi, W. *et al.* Facile Synthesis of Layer Structured GeP<sub>3</sub>/C with Stable Chemical Bonding for Enhanced Lithium-Ion Storage. *Sci Rep* **7**, 43582 (2017)
- 32 Li, W. *et al.* A self-healing layered GeP anode for high-performance Li-ion batteries enabled by low formation energy. *Nano Energy* **61**, 594-603 (2019)
- 33 Baláž, P. *et al.* Semi-industrial Green Mechanochemical Syntheses of Solar Cell Absorbers Based on Quaternary Sulfides. *ACS Sustainable Chem. Eng.* **6**, 2132-2141 (2018)
- 34 Baláž, P., Ohtani, T., Bastl, Z. & Boldižárová, E. Properties and Reactivity of Mechanochemically Synthesized Tin Sulfides. *J. Solid State Chem.* **144**, 1-7 (1999)
- 35 Zhao, L.-D., Zhang, B.-P., Liu, W.-S., Zhang, H.-L. & Li, J.-F. Enhanced thermoelectric properties of bismuth sulfide polycrystals prepared by mechanical alloying and spark plasma sintering. *J. Solid State Chem.* **181**, 3278-3282 (2008)
- 36 Baláž, P. *et al.* Kinetics of mechanochemical synthesis of Me/FeS (Me=Cu, Pb, Sb) nanoparticles. *J. Alloy Compds.* **483**, 484-487 (2009)

- 37 Shen, T. D., Wang, K. Y., Quan, M. X. & Hu, Z. Q. Formation of amorphous Ge-S semiconductor alloys by mechanical alloying. *Appl. Phys. Lett.* **63**, 1637-1639 (1993)
- 38 Sabooni, S., Karimzadeh, F. & Abbasi, M. H. Thermodynamic aspects of nanostructured Ti<sub>5</sub>Si<sub>3</sub> formation during mechanical alloying and its characterization. *Bull. Mater. Sci.* **35**, (2012)
- 39 Suryanarayana, C. Mechanical alloying and milling. *Prog. Mater. Sci.* **46**, 1-184 (2001)
- 40 Bergerhoff, G. & Brown, I. D. *Crystallographic Databases*. 77-95 (International Union of Crystallography, Chester, 1987).
- 41 Okamoto, H. P-S (Phosphorus-sulfur). *J. Phase Equilibria* **12**, 706-707 (1991)
- 42 Gardner, M. Infrared and Raman spectra of some phosphorus sulphides. *J. Chem. Soc. Dalton Trans.* 691-696 (1973)
- 43 Dixon, D. T., Einstein, F. W. B. & Penfold, B. R. The molecular and crystal structure of sulphur-deficient tetraphosphorus heptasulphide ( $\beta$ -P<sub>4</sub>S<sub>7</sub>). *Acta Cryst.* **18**, 221-225 (1965)
- 44 Georgiev, D. G. *et al.* Molecular structure, glass transition temperature variation, agglomeration theory, and network connectivity of binary P-Se glasses. *Phys. Rev. B* **64**, 134204 (2001)
- 45 Yuan, B., Aitken, B., Hung, I., Gan, Z. & Sen, S. Compositional Evolution of the Structure and Connectivity in Binary P–Se Glasses: Results from 2D Multinuclear NMR and Raman Spectroscopy. *J. Phys. Chem. B* **125**, 13057-13067 (2021)
- 46 Lister, G. M. S. & Jones, R. Ab initio calculations on the structure and vibrational properties of some phosphorus-selenium molecules: applications to zero-dimensional glasses. *J. Phys.: Condens. Matter* **1**, 6039-6048 (1989)
- 47 Sarfati, J. D., Burns, G. R. & Morgan, K. R. Tetraphosphorus tetraselenide: crystalline and amorphous phases analysed by X-ray diffraction, Raman and magic angle spinning <sup>31</sup>P NMR spectroscopy and differential scanning calorimetry. *J. Non Cryst. Solids* **188**, 93-97 (1995)
- 48 Cao, Y. *et al.* P<sub>4</sub>Se<sub>3</sub> as a new anode material for sodium-ion batteries. *J. Alloy Compd.* **775**, 1286-1292 (2019)
- 49 Rollo, J. R. *et al.* A new polymorph of tetraphosphorus triselenide,  $\alpha'$ -P<sub>4</sub>Se<sub>3</sub>: an x-ray, Raman, and XPS study of the normal crystalline phases and a DSC study of the crystalline and the orientationally disordered phases of P<sub>4</sub>Se<sub>3</sub>. *Inorg. Chem.* **29**, 2889-2894 (1990)
- 50 Burns, G. R., Rollo, J. R. & Sarfati, J. D. Phases of tetraphosphorus triselenide analysed by magic angle spinning <sup>31</sup>P NMR and Raman spectroscopy, and the Raman spectrum of tetraphosphorus tetraselenide. *Spectrochimica Acta* **47A**, 811-818 (1991)
- 51 Pine, A. S. & Dresselhaus, G. Raman Spectra and Lattice Dynamics of Tellurium. *Phys. Rev. B* **4**, 356-371 (1971)
- 52 Liu, D. *Structural Tuning and Spectroscopic Characterizations of Polysulfide as Battery Materials*, (2021).
- 53 Soni, R. K. *et al.* Raman scattering in In<sub>1-x</sub>Ga<sub>x</sub>As<sub>y</sub>P<sub>1-y</sub> quaternary alloys. *J. Appl. Phys.* **59**, 2184-2188 (1986)

- 54 Sugiura, T., Hase, N., Iguchi, Y. & Sawaki, N. Raman Scattering Study of InGaAsP Quaternary Alloys Grown on InP in the Immiscible Region. *Jpn. J. Appl. Phys.* **37**, 544-549 (1998)
- 55 Tsang, J. C., Kesan, V. P., Freeouf, J. L., LeGoues, F. K. & Iyer, S. S. Raman spectroscopy of long-range order in epitaxial Si<sub>0.5</sub>Ge<sub>0.5</sub> alloys. *Phys. Rev. B* **46**, 6907-6914 (1992)
- 56 D'Costa, V. R. *et al.* Raman scattering in Ge<sub>1-y</sub>Sn<sub>y</sub> alloys. *Solid State Commun.* **144**, 240-244 (2007)
- 57 Bouthillier, É., Assali, S., Nicolas, J. & Moutanabbir, O. Decoupling the effects of composition and strain on the vibrational modes of GeSn semiconductors. *Semicond. Sci. Technol.* **35**, 095006 (2020)
- 58 Zhu, Y. *et al.* Raman tensor of layered black phosphorus. *PhotonIX* **1**, 17 (2020)
- 59 Li, M. *et al.* Revealing Dopant Local Structure of Se-Doped Black Phosphorus. *Chem. Mater.* (2021)
- 60 Fan, G. J., Guo, F. Q., Hu, Z. Q., Quan, M. X. & K., L. Amorphization of selenium induced by high-energy ball milling. *Phys. Rev. B* **55**, (1997)
- 61 Joraid, A. A., Alamri, S. N., Abu-Sehly, A. A. & Benghanem, M. Nonisothermal crystallisation kinetics of amorphous selenium prepared by high-energy ball milling: A comparison with the melt-quenching and thin-film techniques. *J. Non Cryst. Solids* **358**, 1268-1273 (2012)
- 62 Bytchkov, A. *et al.* Intermediate- and short-range order in phosphorus-selenium glasses. *Phys. Rev. B* **83**, 144201 (2011)
- 63 Nordheider, A., Woollins, J. D. & Chivers, T. Organophosphorus–Tellurium Chemistry: From Fundamentals to Applications. *Chem. Rev.* **115**, 10378-10406 (2015)
- 64 Chivers, T. & Laitinen, R. S. Tellurium: a maverick among the chalcogens. *Chem. Soc. Rev.* **44**, 1725-1739 (2015)
- 65 Lyda, C. M., Leone, J. M., Bankert, M. A., Xia, Y. & Eckert, H. Structural Studies of Phosphorus-Sulfur-Tellurium Glasses by <sup>31</sup>P MAS NMR and Vibrational Spectroscopies. *Chem. Mater.* **6**, 1934-1939 (1994)
- 66 Tschulik, K. *et al.* Chemistry and Physical Properties of the Phosphide Telluride Zr<sub>2</sub>PTe<sub>2</sub>. *Eur. J. Inorg. Chem.* **2009**, 3102-3110 (2009)
- 67 Jörgens, S., Johrendt, D. & Mewis, A. BaP<sub>4</sub>Te<sub>2</sub>—A Ternary Telluride with P-Te Bonds and a Structural Fragment of Black Phosphorus. *Chem. Eur. J.* **9**, 2405-2410 (2003)
- 68 Okamoto, H. P-Te (Phosphorus-Tellurium). *J. Ph. Equilibria Diffus.* **31**, 405-406 (2010)
- 69 Akahama, Y., Endo, S. & Narita, S. Electrical Properties of Black Phosphorus Single Crystals. *J. Phys. Soc. Jpn.* **52**, 2148-2155 (1983)
- 70 Zhang, Z., Khurram, M., Sun, Z. & Yan, Q. Uniform Tellurium Doping in Black Phosphorus Single Crystals by Chemical Vapor Transport. *Inorg. Chem.* **57**, 4098-4103 (2018)
- 71 Yu, Y. *et al.* N-type doping of black phosphorus single crystal by tellurium. *Nanotechnol.* **31**, 315605 (2020)
- 72 Yang, B. *et al.* Te-Doped Black Phosphorus Field-Effect Transistors. *Adv. Mater.* **28**, 9408-9415 (2016)

- 73 Schönberger, S. *Phosphorus, sulfur and pyridine a unique combination to a great structural diversity* Doctoral thesis, LMU Munich, (2013).

## Figures

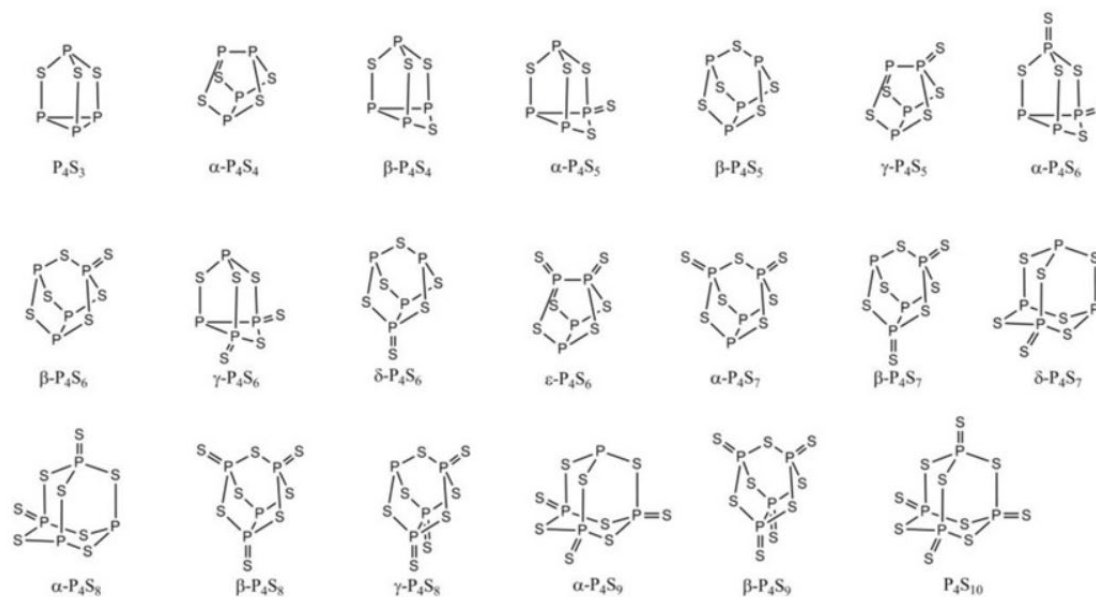


**Figure 5.1** Known phosphorus-sulfur compounds.

Numerous phosphorus-sulfur compounds consisting of cages containing single bonds of phosphorus to itself or sulfur and terminal double bonds of sulfur to phosphorus. Greek letters are variations of a given stoichiometric compound. Reproduced from Schonberger.<sup>73</sup>

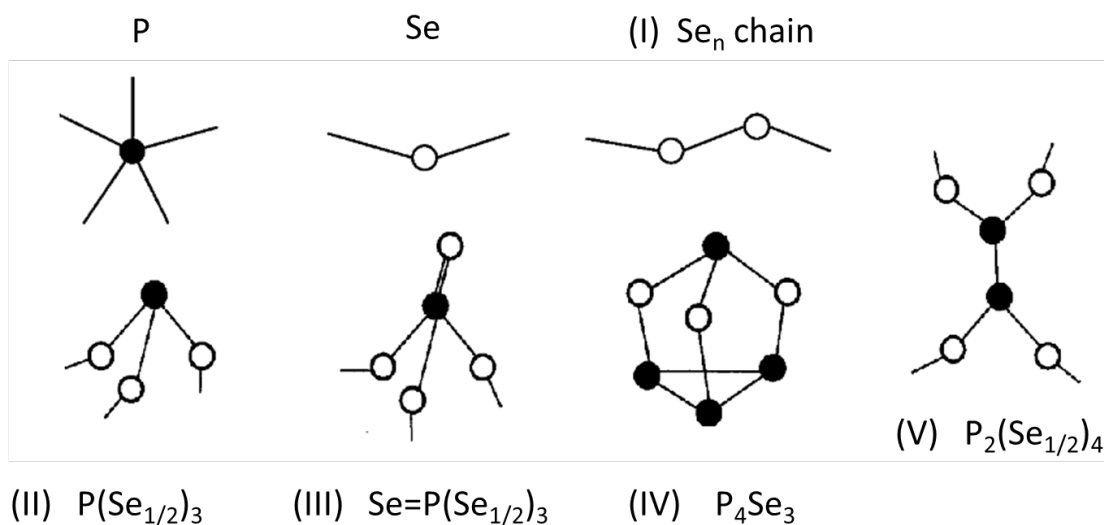


**Figure 5.2 Local structural units in P-Se glasses.**

Five-fold coordinated phosphorus (closed circle) and two-fold coordinated selenium (open circle) can link up to form local structural units such as (I) Se-Se chains, (II)  $P(\text{Se}_{1/2})_3$  pyramidal, (III) double bonded  $\text{Se}=\text{P}(\text{Se}_{1/2})_3$  quasi-tetrahedral unit, (IV)  $\text{P}_4\text{Se}_3$  cage monomer, (V) ethylene-like  $\text{P}_2(\text{Se}_{1/2})_4$  unit. (The  $\frac{1}{2}$  subscripts for Se within the formulas indicate each Se atom has one of two bonds linked to a phosphorus atom. The other bond could be either phosphorus or selenium). Figure adapted from Georgiev *et al.*<sup>44</sup>

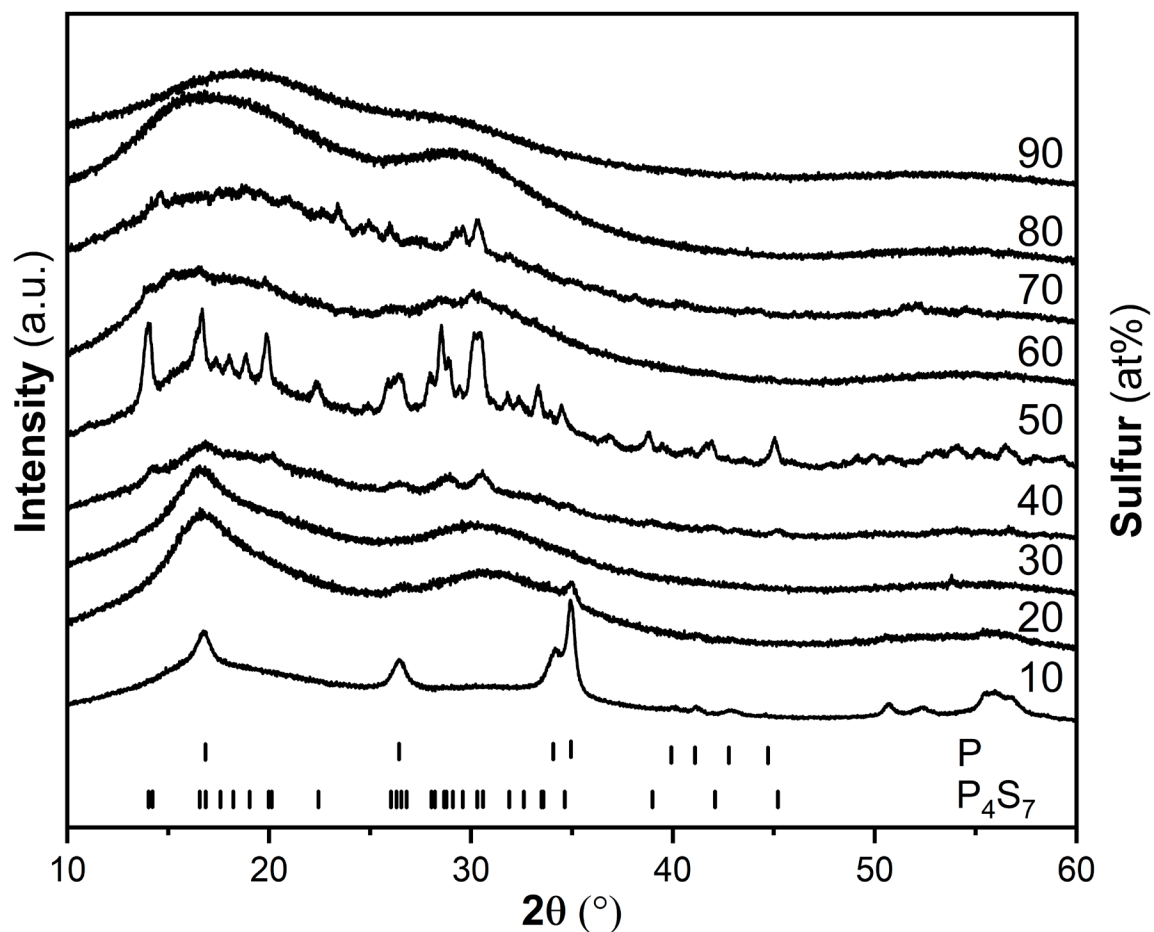


**Figure 5.3** Structural characterization of mechanochemically synthesized P-S powders.

X-Ray diffraction patterns with increasing sulfur content indicate the synthesis of both amorphous and crystalline P-S compounds along with limited solubility in the black phosphorus crystal structure. Patterns are normalized and manually offset vertically.

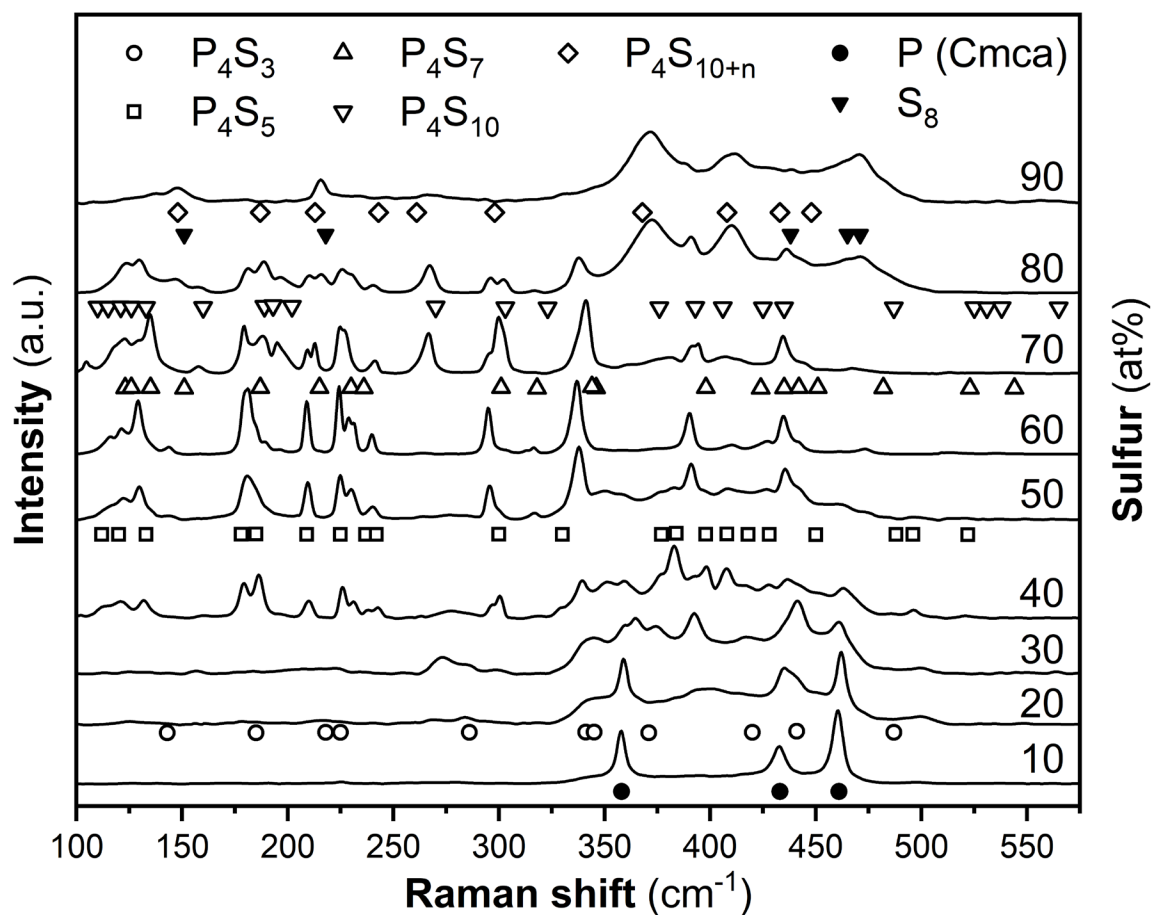


**Figure 5.4 Raman characterization of mechanochemically synthesized P-S powders produced in 10 at% sulfur increments.**

Raman spectra of the P-S powders showing the distinct vibrational modes corresponding to the various P-S cage-like structures. At low sulfur content, vibrational modes of black phosphorus are observed. Markers for each phase detected are indicated for each pattern<sup>42</sup>; all patterns normalized and vertically offset.

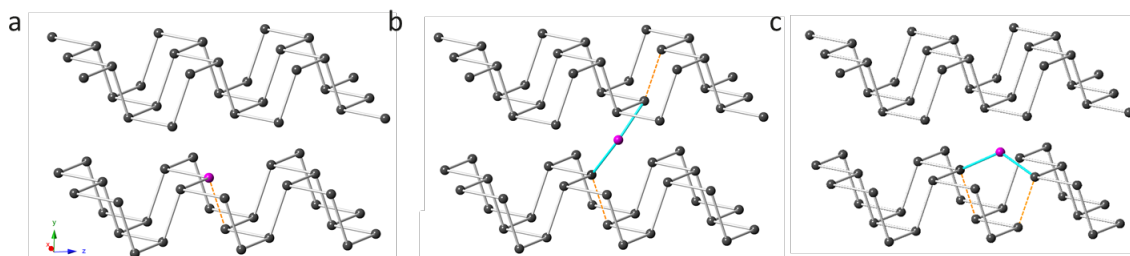


**Figure 5.5 Postulated BP structure with sulfur atoms**

**(a)** Sulfur substitutes directly onto the BP lattice replacing a phosphorus atom but also resulting in a missing bond with the phosphorus atom beneath it; unless a second sulfur atom replaces the adjacent phosphorus atom, satisfying all bonds, **(b)** sulfur bridges across the van der Waals gap, linking two adjacent layers, **(c)** sulfur bridges across the armchair within the same layer. In all cases, phosphorus atoms with missing bonds are present, as indicated by orange dashed lines.

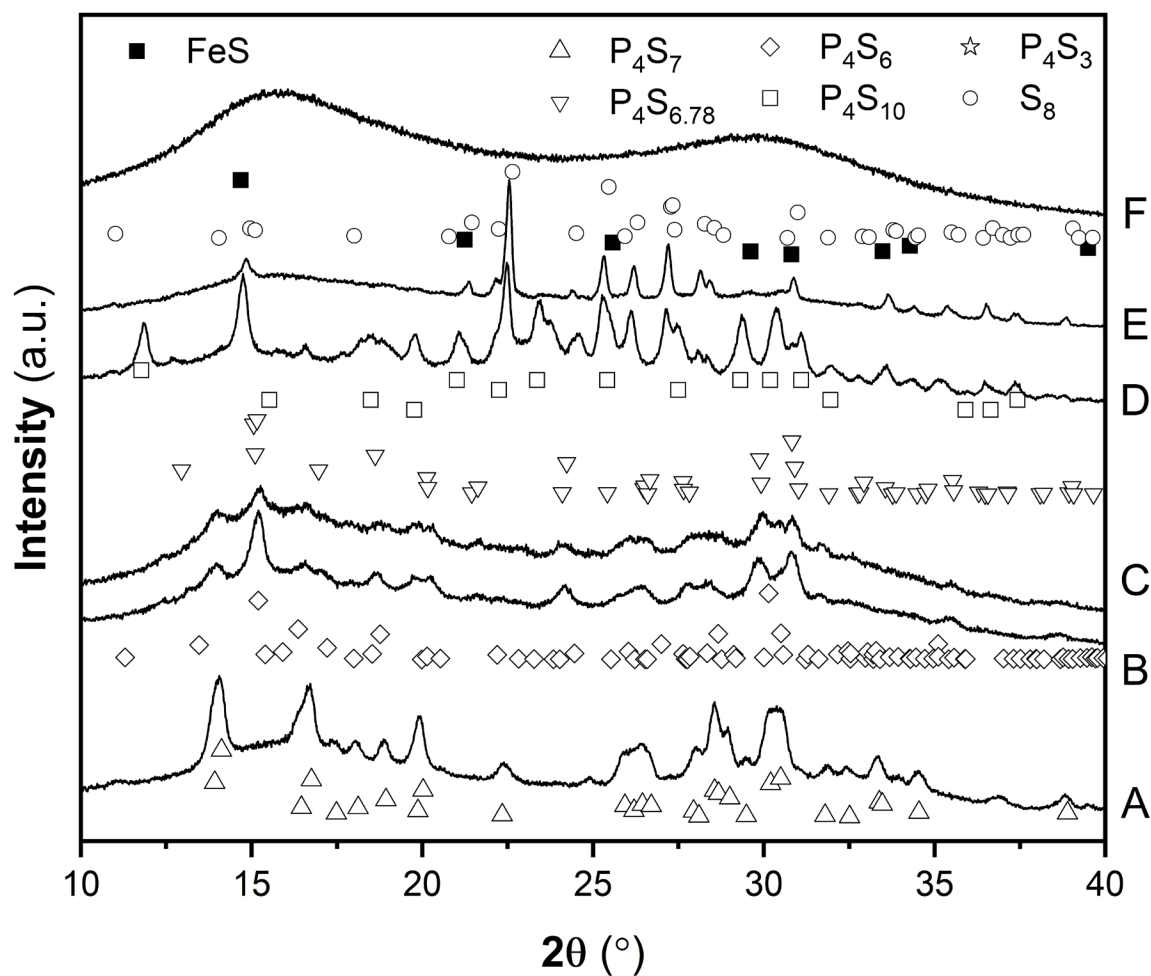


**Figure 5.6 Structural characterization of mechanochemically synthesized P-S powders.**

X-Ray diffraction patterns of the P-S powders with specific molar ratio show presence of multiple crystalline phases in most samples. Molar ratios P:S targeted: (A = 4:3, B = 1:1, C = 4:5, D = 4:7, E = 4:9, F = 4:10). Patterns are normalized and manually offset vertically.

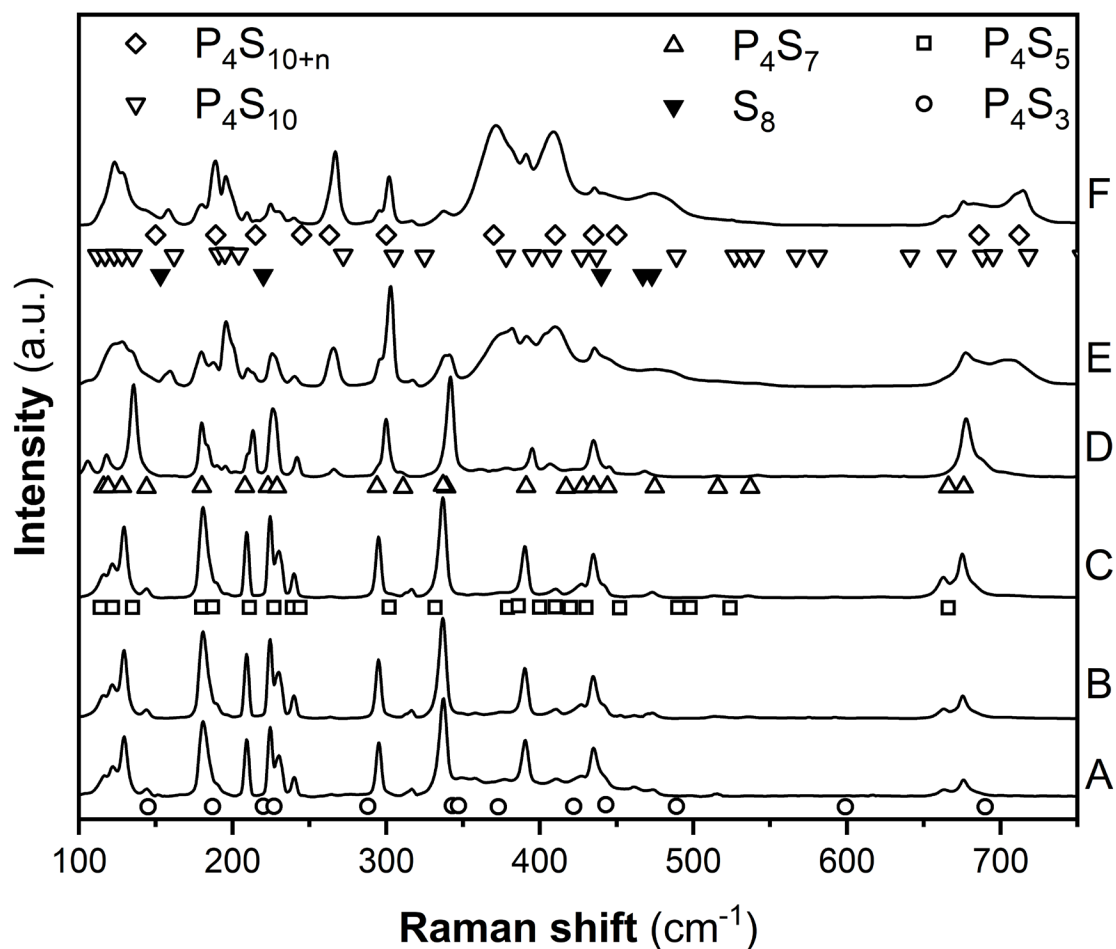


**Figure 5.7 Raman characterization of mechanochemically synthesized P-S powders.**

Raman spectra of the P-S powders with specific stoichiometries exhibit vibrational modes from multiple known phases with distinct cage-like structures and terminal bonds.

Molar ratios P:S targeted: (A = 4:3, B = 1:1, C = 4:5, D = 4:7, E = 4:9, F = 4:10).

Markers for each phase detected are indicated for each pattern; all patterns normalized and vertically offset.

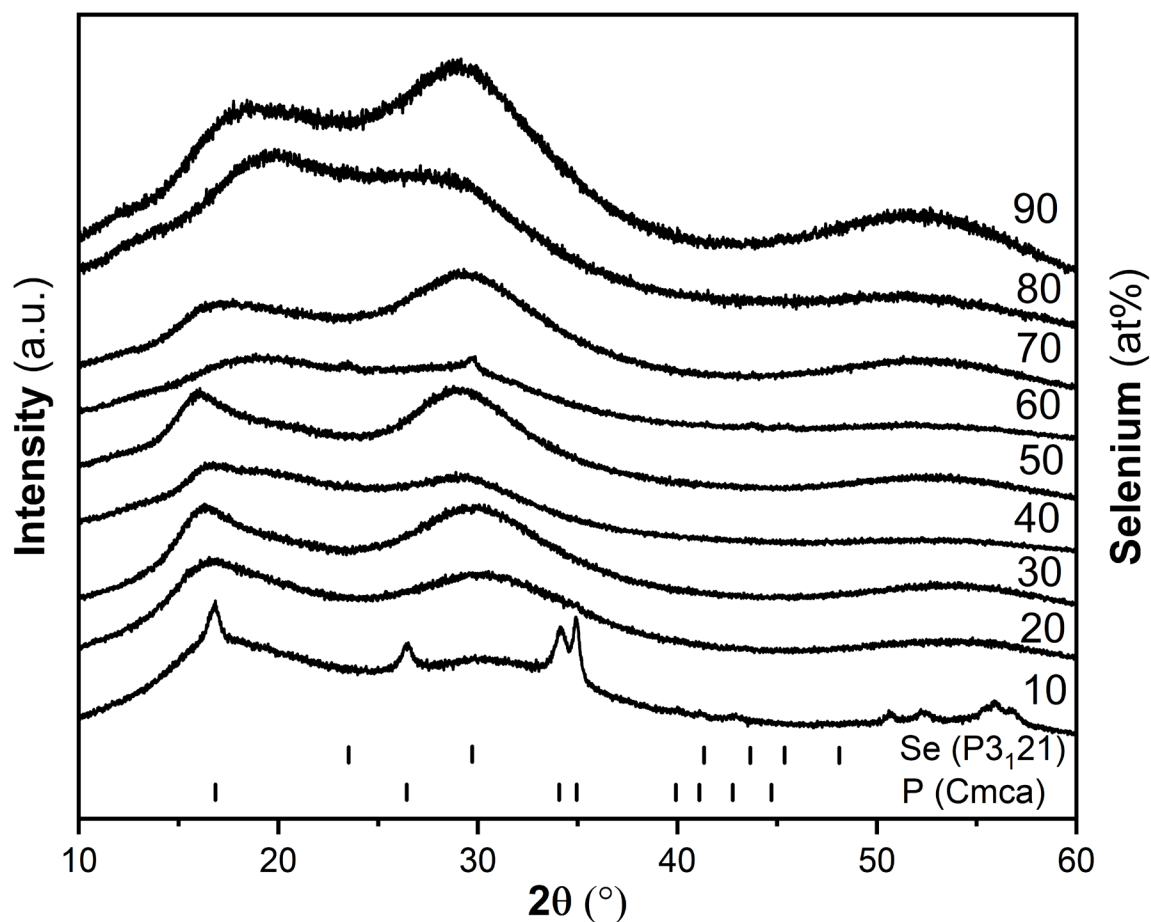


**Figure 5.8** Structural characterization of mechanochemically synthesized P-Se powders.

X-Ray diffraction patterns with increasing selenium content indicate the synthesis of amorphous P-Se compounds along with limited solubility in the black phosphorus crystal structure. Patterns are normalized and manually offset vertically.

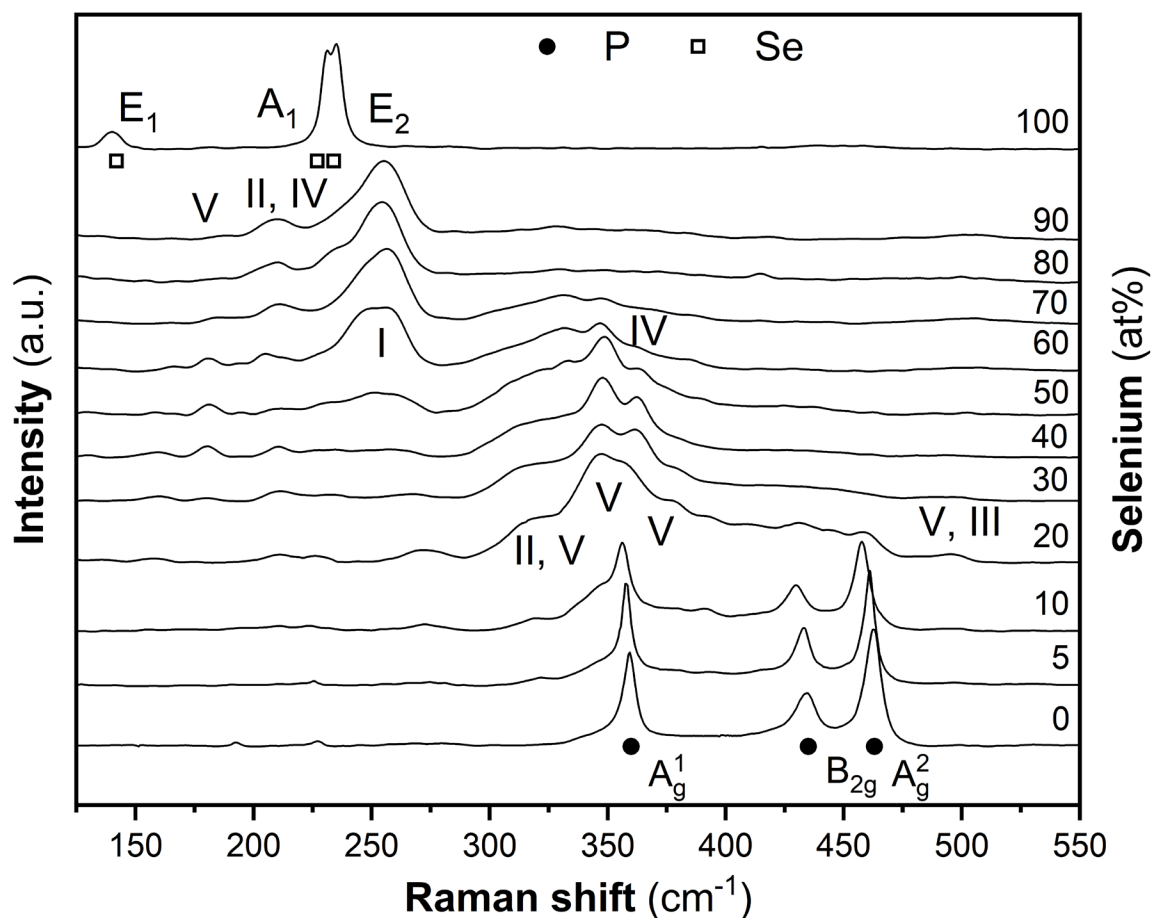


**Figure 5.9** Structural characterization of mechanochemically synthesized P-Se powders.

Raman spectra of the P-Se powders showing the distinct vibrational modes corresponding to the various P-Se structures local structures indicated by roman numerals I-V: (I) Se-Se chains and rings, (II)  $\text{P}(\text{Se}_{1/2})_3$  pyramidal unit, (III) double bonded  $\text{Se}=\text{P}(\text{Se}_{1/2})_3$  quasi-tetrahedral unit, (IV)  $\text{P}_4\text{S}_3$  monomers, (V)  $\text{P}_2(\text{Se}_{1/2})_4$  ethylene-like unit. Roman numerals indicate approximate peak positions.<sup>44</sup> All patterns are normalized and vertically offset.

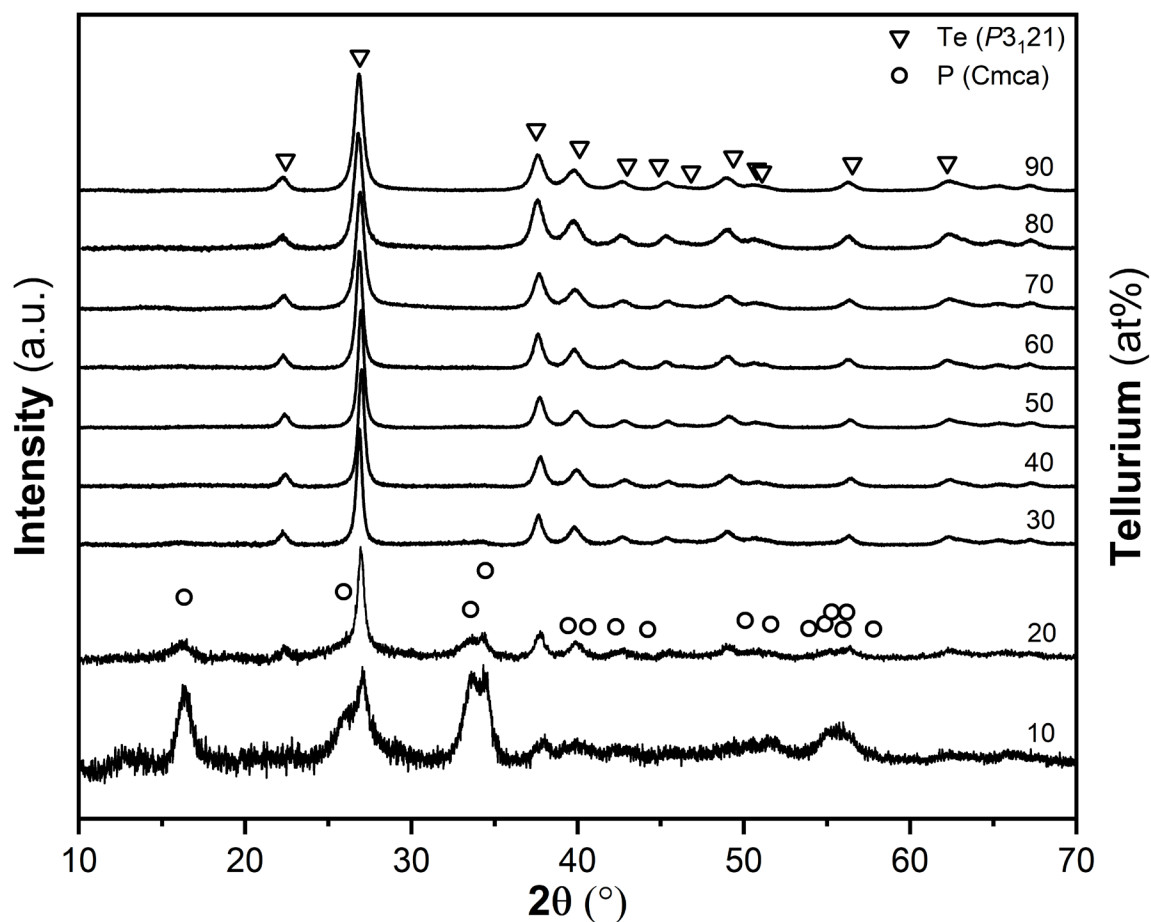


**Figure 5.10** Structural characterization of mechanochemically synthesized P-Te powders.

X-Ray diffraction patterns with increasing tellurium content indicate no compound or alloy formation; minor solubility of tellurium into the BP crystal structure is evident.

Patterns are normalized and manually offset vertically.

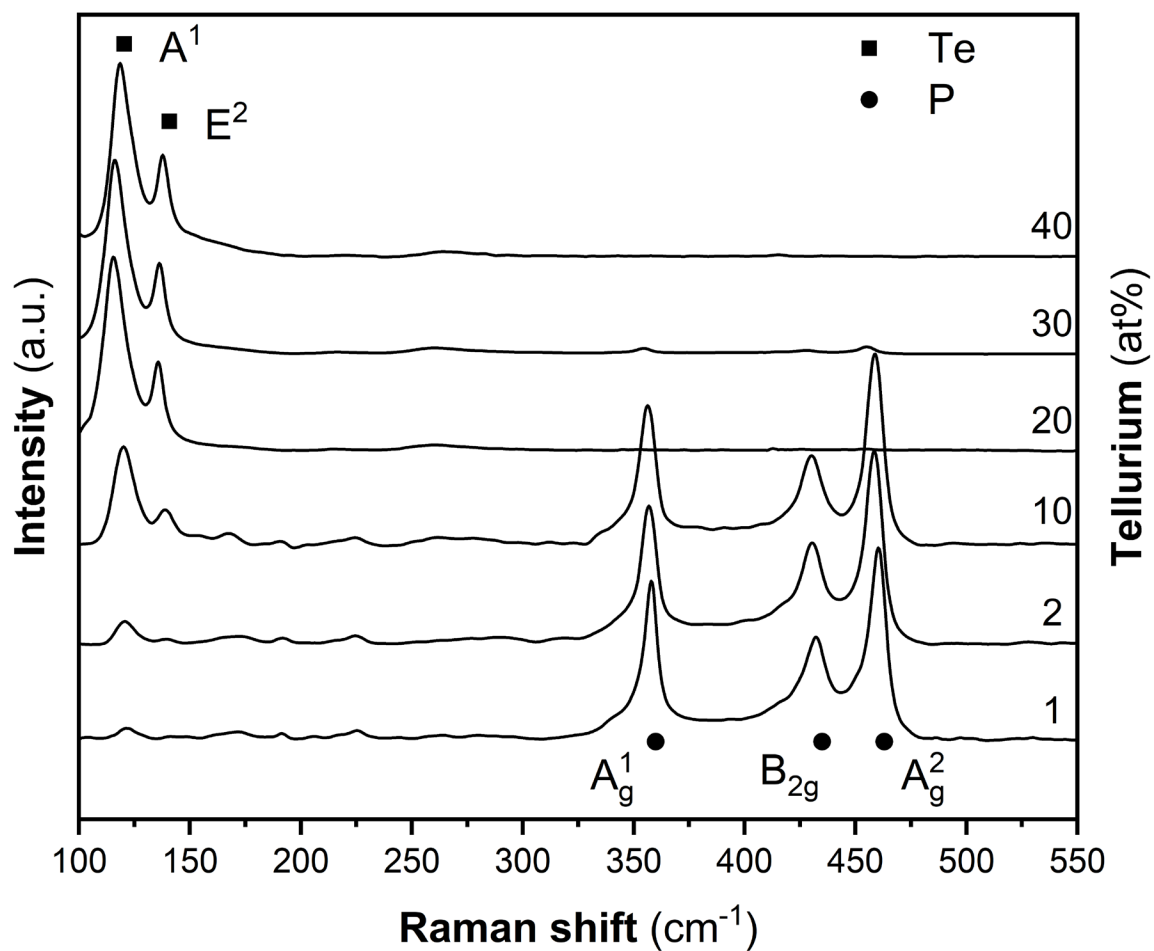


**Figure 5.11** Structural characterization of mechanochemically synthesized P-Te powders.

Raman spectra of the P-Te powders showing only the distinct vibrational modes of black phosphorus and tellurium indicating lack of bonding between the two elements. Markers for each phase detected are indicated for each pattern; all patterns normalized and vertically offset.

## Tables

**Table 5.1** XRD phases within mechanochemically synthesized P-S, P-Se, P-Te powders

XRD phases	Space Group	PDF	ICSD
P <sub>4</sub> S <sub>7</sub>	<i>P21/n</i>	01-073-1364	023842
P <sub>4</sub> S <sub>6</sub>	<i>P21/c1</i>	01-089-0292	078765
P <sub>4</sub> S <sub>6.78</sub>	<i>Pbcn</i>	072-1627	018138
P <sub>4</sub> S <sub>10</sub>	<i>P-1</i>	01-073-1365	023843
S <sub>8</sub>	<i>FdddZ</i>	01-074-1465	027261
Fe <sub>0.91</sub> S	<i>Ccmm</i>	01-075-2377	032651
Se	<i>P3<sub>1</sub>21</i>	01-086-2246	40018
Te	<i>P3<sub>1</sub>21</i>	01-085-0555	023059
P	<i>Cmca</i>	01-073-1358	023836

**Table 5.2** Structural units within mechanochemically synthesized P-S powders

Marker	Targeted P:S molar ratio	XRD phases	Raman phases
A	4:3	P <sub>4</sub> S <sub>7</sub>	P <sub>4</sub> S <sub>3</sub> , P <sub>4</sub> S <sub>7</sub>
B	1:1	P <sub>4</sub> S <sub>7</sub> , P <sub>4</sub> S <sub>6.78</sub> , P <sub>4</sub> S <sub>6</sub>	P <sub>4</sub> S <sub>3</sub> , P <sub>4</sub> S <sub>7</sub>
C	4:5	P <sub>4</sub> S <sub>7</sub> , P <sub>4</sub> S <sub>6.78</sub> , P <sub>4</sub> S <sub>6</sub>	P <sub>4</sub> S <sub>7</sub> , P <sub>4</sub> S <sub>5</sub>
D	4:7	P <sub>4</sub> S <sub>10</sub> , P <sub>4</sub> S <sub>6.78</sub> , S <sub>8</sub> , Fe <sub>0.91</sub> S	P <sub>4</sub> S <sub>7</sub> , P <sub>4</sub> S <sub>10</sub>
E	4:9	P <sub>4</sub> S <sub>10</sub> , S <sub>8</sub> , Fe <sub>0.91</sub> S	P <sub>4</sub> S <sub>7</sub> , P <sub>4</sub> S <sub>10</sub> , S <sub>8</sub>
F	4:10	Amorphous	P <sub>4</sub> S <sub>7</sub> , P <sub>4</sub> S <sub>10</sub> , S <sub>8</sub>

P-S Raman modes<sup>42</sup>**Table 5.3** Structural units within mechanochemically synthesized P-Se amorphous glasses

Marker	Raman shift (cm <sup>-1</sup> )	Structure
I	237, 350	Se-Se
II	210, 330	P(Se <sub>1/2</sub> ) <sub>3</sub>
III	510	Se=P(Se <sub>1/2</sub> ) <sub>3</sub>
IV	184, 212, 320, 371	P <sub>4</sub> Se <sub>3</sub>
V	180, 330, 350, 370	P <sub>2</sub> (Se <sub>1/2</sub> ) <sub>4</sub>

P-Se Raman modes<sup>44</sup>

## CHAPTER SIX: CONCLUSIONS

Collectively, this body of work investigates the mechanochemistry of functional materials. A common theme throughout each chapter is the synthesis of phosphorus containing materials and the use of mechanical energy to drive high pressure phase transformations, synthesize binary alloys, form crystalline compounds, and create amorphous glasses. This dissertation emphasizes layered 2D materials formed with phosphorus, arsenic, and germanium, and then branches out to explore reactions of phosphorus with the chalcogenides to address knowledge gaps in their synthesis by high energy ball milling. The understanding of the reaction kinetics governing the pressure induced phase transformation of red phosphorus to black phosphorus is highlighted in Chapter Two. This theme of ball mill synthesis of high-pressure phases is extended to orthorhombic and trigonal black phosphorus-arsenic alloys in Chapter Three and to layered monoclinic and trigonal germanium phosphides in Chapter Four. Delineation between doping, alloying, or compound formation of phosphorus with the chalcogenides is presented in Chapter Five. Together, through the exploration of the mechanochemically accessible phase diagrams of P-As, P-Ge, P-S, P-Se, and P-Te, along with minor studies with P-Sn, P-Sb, P-Bi, P-B, and P-Nb presented in the appendix, the feasibility of doping crystalline black phosphorus is discussed.

High energy ball milling of black phosphorus was first demonstrated in 2007 but details regarding the synthesis kinetics were lacking. Chapter Two represents a major contribution to the literature regarding the optimum milling conditions and scaling

parameters necessary for industrial scale-up to produce optically viable black phosphorus nanomaterials. Application of solid-state kinetic models revealed the stochastic process governing the incremental conversion of red phosphorus to black phosphorus as a function both the energy imparted and minimum impact energy per media impact needed for practical conversion rates. A specific milling dose near 100 kJ per gram and an impact energy near 25 mJ per impact is shown to produce BP efficiently. The nucleation of nanosized BP crystals within an amorphous matrix follows a sigmoidal behavior with milling time. Furthermore, in light of the renewed interest in the few-layer properties of BP, the optical emission of ball mill synthesized BP demonstrates this process as a viable route for producing layered nanomaterials for visible and infrared photonics.

Chapter Three answers the question of how arsenic will affect the synthesis of layered BP, both in terms of kinetics and optical properties. Synthesis of the orthorhombic and trigonal PAs alloys by high energy ball milling is a first in the scientific community, and provides a convenient method to produce these 2D materials that are suitable for visible, near-infrared, and mid-infrared applications. From a kinetics standpoint, milling arsenic with phosphorus follows a two-step mechanism. First, arsenic rapidly reacts with red phosphorus to produce the *trigonal* PAs crystal structure. Second, trigonal PAs is transformed into orthorhombic PAs with further milling. This result is surprising as orthorhombic PAs is supposedly thermodynamically more stable than trigonal PAs over most of the P-As composition range. From an energetics standpoint, the same milling conditions for pure BP is sufficient to produce PAs alloys from 1-90 at% arsenic. Photoluminescence of exfoliated PAs powders show emission in the visible

spectrum which confirms theoretical predictions on the monolayer optical properties of PAs alloys.

Similar to Chapter Three, Chapter Four describes the mechanochemical synthesis of germanium phosphides with the aim to address doping and compound formation. Specifically, germanium solubility below 1 at% within black phosphorus is shown. Above 2 at%, the metastable high-pressure trigonal P-Ge alloys form with XRD and Raman results indicating site disorder present in alloys from 2-30 at% germanium. The layered monoclinic P-Ge at 50 at% germanium was also synthesized by high energy ball milling. Although an indirect bandgap semiconductor, the straightforward synthesis of monoclinic GeP may still enable its use in applications exploiting its 2D nature such as intercalation of sodium and lithium for battery anodes.

Mechanochemically synthesized P-S, P-Se, and P-Te compounds are the subject of Chapter Five. In keeping up with the theme of doping black phosphorus by ball milling phosphorus with candidate dopants, results indicate sulfur and selenium may be substitutional dopants as they create similar distortions in the vibrational modes of pure BP when doped with arsenic as discussed in Chapter Three. High energy ball mill synthesis of P-S crystalline phases and the P-Se amorphous glasses (30-90 at% selenium) is also a first within the scientific community, to the best of the author's knowledge. While BP, PAs, and PGe are all crystalline layered semiconductors, the phosphorus sulfides and selenides represent a series of molecular solids that can be either crystalline or solid. Their synthesis via ball milling represents a novel processing route that avoids melting white or red phosphorus and yellow sulfur, and demonstrates the versatility of ball mills to produce a wide range of structures. The milling results of P-S mixtures with low sulfur

content indicate an unusual behavior in that the formed products matched the crystalline structure and vibrational modes of polymeric structures normally assigned to sulfur-rich compounds. Presumably, the high-pressure collisions enable sulfur links between basic monomer units that do not normally form without excess sulfur. Further investigations are warranted to better understand the local structural units both as a function of composition and milling conditions.

A compilation of the results from the preceding chapters and Appendix A that are related to mechanochemically producing doped black phosphorus with Ge, Sn, S, Se, Te, Sb, Bi, and As elements is as follows (absent electrical measurements):

**(1)** Arsenic may be a dopant depending upon how the electron charge distribution plays out at various arsenic concentrations; XPS results indicate slight n-type behavior, consistent with DFT literature. The structural characterization results for arsenic provide a solid framework to compare all other dopants for BP.

**(2)** Germanium is likely a p-type substitutional atom for BP with a solubility near  $\approx 1-2$  at%. Germanium stabilizes a trigonal solid solution alloy at higher concentrations with the same lattice type as trigonal PAs alloys.

**(3)** Tin is likely a p-type impurity dopant at levels below 10 at% considering the atomic size difference between phosphorus, germanium, and tin. The low solubility of germanium into BP, the lack of strongly doped p-type crystals via CVT, and literature evidence of tin inclusions between layers indicate impurity doping rather than substitutional doping.

(4) Sulfur and selenium may be dopants with solubility no greater than 10 at%.

Both sulfur and selenium may substitute into the BP lattice; however, the nature of doping (n- or p-type) is still unknown.

(5) Tellurium is not likely a substitutional dopant as neither the XRD or Raman support bonding of phosphorus with tellurium (which is consistent with literature stating that P-Te bonds within crystalline structures are nearly non-existent).

(6) the heavier pnictogens (Sb and Bi) do not form compounds with phosphorus and are not expected to be substitutional dopants.

Mechanochemistry of phosphorus to produce layered crystals that possess desirable optical properties has the potential to enable large scale device fabrication when coupled with compatible deposition methods. Black phosphorus, black phosphorus-arsenic alloys, layered germanium phosphides, and crystalline and amorphous phosphorus sulfides and selenides can all be produced readily using high energy ball milling. As a novel synthesis route, direct reactions without forming volatile vapors of phosphorus greatly simplifies the synthesis of these compounds.

Potential research opportunities with mechanochemically synthesized phosphorus-based nanomaterials include the following:

(1) Evaluation of pure black phosphorus for applications not requiring good conductivity such as infrared absorption. Challenges with residual amorphous material may prevent effective electrical conductivity in ball mill synthesized BP. Alternative applications that exploit the near-infrared absorption behavior of BP are more likely

to be realized commercially. Saturable absorbers for mode-lock lasers may also be a viable alternative.<sup>1</sup> Similarly, photothermal therapy that uses targeted infrared light to thermally active BP nanoparticles introduced into biological tissues or organs could also be an effective application for ball milled BP.<sup>2-5</sup> Another application includes use as a flame-retardant additive in plastics or polymer composites.<sup>6</sup>

- (2) Evaluation of dopant behavior in the phosphorus-arsenic alloys. The larger unit cell volume may accommodate germanium and selenium atoms more readily and potentially act to stabilize these dopant atoms within the orthorhombic crystal structure.
- (3) Post-processes to remove amorphous BP or RP from mechanochemically synthesized BP: exploration of reactive gases that target amorphous RP or amorphous BP preferentially over crystalline BP could enable conductive BP nanoparticles. Similarly, reactive solvents that could strip the amorphous phosphorus may be a viable approach to produce conductive BP nanoparticles produced by ball milling.
- (4) Beyond opto-electronics, phosphorus-arsenic alloys could be effective thermoelectrics.<sup>7</sup> The relatively good conductivity, decent Seebeck coefficient, and possibly low thermal conductivity (due to heteroatomic bonding) could result in modest thermoelectric figure of merit provided the carrier concentration (via doping) is within the correct range ( $10^{18}$ - $10^{20}$  carriers  $\text{cm}^{-3}$ ).
- (5) A deeper kinetic analysis on P-As alloys, looking specifically at the low arsenic content alloys could help to reveal if arsenic acts as a catalyst in the conversion of amorphous red phosphorus into a crystalline product (be it a trigonal or orthorhombic phase). Determination of the minimum impact energy needed to convert RP into BP in

- the presence of minor amounts of arsenic could substantiate its use as even marginal improvements in conversion times translates into considerable savings in electricity usage of large scale industrial mills.
- (6) Addition of a binder (such as metallic tin) in low amounts for enabling low pressure sintering may consume amorphous RP and form a two-phase composite consisting of crystalline BP and an electrically conductive tin phosphide. Such a composite may find use in optoelectronics or thermoelectrics.
- (7) Thermoelectric measurements on bulk and few-layer trigonal and monoclinic Ge-P phases could help to reveal if the narrow bandgap of these crystals could make useful as thermoelectrics.
- (8) Alloying of arsenic into the monoclinic GeP phase (GeAs also shares the same crystal structure) could alter the bandgap favorably into a direct bandgap semiconductor.<sup>8</sup> The thermal stability of GeAs could balance out the thermal instability of GeP and provide a means of tuning the opto-electronic-thermal properties of the ternary monoclinic Ge-As-P crystal.<sup>9,10</sup>
- (9) Use of a ceramic milling system (ie.,  $\text{Si}_3\text{N}_4$ ) may alleviate challenges for P-S compound synthesis by avoiding reactions with iron. A more in-depth impact energy study on the attainable P-S compounds (ie., variation of the RPM and media size) may allow for the direct synthesis of phase pure P-S compounds. As an extension, recent publications using  $\text{P}_2\text{S}_5$  as a precursor for the synthesis of  $\text{Li}_2\text{S-P}_2\text{S}_5$  amorphous glasses as solid electrolytes, suggest the possibility of the direct synthesis of  $\text{Li}_2\text{S-P}_2\text{S}_5$  using mechanochemistry in a single step.

## References

- 1 Chen, Y. *et al.* Mechanically exfoliated black phosphorus as a new saturable absorber for both Q-switching and Mode-locking laser operation. *Opt. Express* **23**, 12823-12833 (2015)
- 2 Sun, C. *et al.* One-pot solventless preparation of PEGylated black phosphorus nanoparticles for photoacoustic imaging and photothermal therapy of cancer. *Biomaterials* **91**, 81-89 (2016)
- 3 Zhao, Y. *et al.* Stable and Multifunctional Dye-Modified Black Phosphorus Nanosheets for Near-Infrared Imaging-Guided Photothermal Therapy. *Chem. Mater.* **29**, 7131-7139 (2017)
- 4 Liu, Z. *et al.* A two-dimensional fingerprint nanoprobe based on black phosphorus for bio-SERS analysis and chemo-photothermal therapy. *Nanoscale* **10**, 18795-18804 (2018)
- 5 Ou, W. *et al.* Plug-and-Play Nanorization of Coarse Black Phosphorus for Targeted Chemo-photoimmunotherapy of Colorectal Cancer. *ACS Nano* **12**, 10061-10074 (2018)
- 6 Qu, Z. *et al.* Surface functionalization of few-layer black phosphorene and its flame retardancy in epoxy resin. *Chem. Eng. J.* **382**, 122991 (2020)
- 7 Karki, B., Rajapakse, M., Sumanasekera, G. U. & Jasinski, J. B. Structural and Thermoelectric Properties of Black Arsenic–Phosphorus. *ACS Appl. Energy Mater.* **3**, 8543-8551 (2020)
- 8 Barreteau, C., Michon, B., Besnard, C. & Giannini, E. High-pressure melt growth and transport properties of SiP, SiAs, GeP, and GeAs 2D layered semiconductors. *J. Cryst. Growth* **443**, 75-80 (2016)
- 9 Feng, L., Lu, J., Zhang, X. & Xiang, G. Tuning electronic structure and optical properties of monolayer GeAs and GeAs<sub>2</sub> by alloying with nitrogen and phosphorus elements. *Phys. B: Condens. Matter* **614**, 413033 (2021)
- 10 Zhao, T., Sun, Y., Shuai, Z. & Wang, D. GeAs<sub>2</sub>: A IV–V Group Two-Dimensional Semiconductor with Ultralow Thermal Conductivity and High Thermoelectric Efficiency. *Chem. Mater.* **29**, 6261-6268 (2017)

## APPENDIX A

**Appendix A. Miscellaneous Phosphorus Ball Milling Results**

### Miscellaneous Phosphorus Ball Milling Results

What follows is an attempt to document results that are related to ball milling but were either inconclusive, incomplete, or one-off experiments to explore possible avenues for further studies for myself or those that continue such work. Unlike the preceding Chapters 2-3 which were completed studies with enough rigor for publication, or Chapters 4-5 which were complete enough to comprise their own chapters, the following results are mainly powder XRD plots indicating either the successful formation of a desired product or the formation of the undesired product or the formation of an unidentified phase (or phases). In most cases, after verifying the phases with XRD, no further attempts were made at either characterization or experimentation primarily as the main source of funding of this dissertation work was focused on synthesis and characterization of black phosphorus and its alloys. For brevity, only a short statement about the intended outcome and results summary will be made for each group of experiments.

In preparing for the work on mechanochemical doping of black phosphorus, an immediate question of concern are what elements would likely be dopants for BP. The criteria for an effective dopant are that it introduces a donor state just below the conduction band minimum (CBM) for n-type doping or an acceptor state just above the valence band maximum (VBM) for p-type doping.

Unfortunately, within the literature, the nature of dopants evaluated by various DFT approximations with a chosen lattice (monolayer, bilayer, or multilayer) leads to contradictory outcomes (S, Se, Te, Si, Ge, Sn, B, Al, Ga, Zn, Cu, Ni, Co, Fe, Ti, O, C, N, As).<sup>1-17</sup> For example, sulfur is calculated to induce metallic behavior in monolayer,<sup>4,8,15</sup>

or introduces deep states in the middle of the bandgap indicating poor n-type donor,<sup>2,5</sup> or indirect gap if two sulfur atoms are present,<sup>5</sup> or even acts as an acceptor making the monolayer p-type.<sup>10</sup> Likewise, arsenic may or may not introduce impurity donor states.<sup>12,16</sup>

The literature with experimental results from field effect transistors on exfoliated flakes or hall bars from bulk crystals was in favor of boron (B),<sup>18</sup> germanium (Ge),<sup>19</sup> and tellurium (Te)<sup>20</sup> as dopants. Sulfur,<sup>21-23</sup> selenium,<sup>17,23-26</sup> tellurium,<sup>23,26-29</sup> and boron,<sup>18</sup> are reported as n-type dopants while tin and germanium<sup>23</sup> are p-type dopants. Adatom doping for n-type behavior with aluminum,<sup>30</sup> potassium,<sup>31-33</sup> or copper,<sup>34</sup> has also been investigated. Electrostatic doping by interface engineering,<sup>35-39</sup> or by surface functionalization through various surface treatments (typically organic compounds)<sup>40-43</sup> can modulate the carrier concentration to a limited extent. Intercalation of dopant atoms in between the atomic layers of BP may also produce a change in electrical properties;<sup>44-46</sup> however, none of these reports have discussed actual carrier concentrations achieved by such means. Most report the carrier mobility as a function of doping while few publish the carrier concentration achieved for a given dopant concentration produced by their synthesis process. Pioneering works on the electrical properties of undoped BP have shown carrier concentrations near  $1 \times 10^{15} \text{ cm}^{-3}$  and  $1 \times 10^{16} \text{ cm}^{-3}$  at  $25^\circ\text{C}$ .<sup>47,48</sup> The broad range could be attributed to the purity of the starting red phosphorus or inclusion of reagents such as mercury, bismuth, or tin.<sup>49</sup> These studies provide a baseline to which dopant studies should reference. As stated previously, boron, germanium, and tellurium are the most promising dopants.<sup>18-20</sup> Kim *et al.* introduced boron via a plasma deposition into BP flakes and applied electrical contacts with lithography; the I-V curve threshold

voltage switched from +4V to -4.5V after boron doping.<sup>18</sup> Unfortunately, they did not report the actual carrier concentration achieved by means of Hall measurements.

Maruyama *et al.* introduced germanium via the bismuth-flux crystal growth method and claim 2-4 at% based on electron probe microanalysis.<sup>19</sup> No hall measurements were reported. Instead, they noted the resistivity at room temperature changed by three orders of magnitude, which is to the best of the author's knowledge, the largest change in resistivity by doping of BP reported to date (hence the focus on germanium-phosphorus reactions in Chapter Four). Lastly, the work by Akahama *et al.* demonstrated n-type behavior with tellurium and they reported the Hall measurements for carrier concentration; unfortunately, they did not report the tellurium target or actual dopant levels achieved.<sup>20</sup> Comparing their reported p-type and n-type resistivities and carrier concentrations revealed a troubling outcome for the efficiency of tellurium doping. The reported hole concentration was between  $10^{15}$  and  $10^{16}$  holes per  $\text{cm}^3$ . The reported electron concentration was  $\approx 3 \times 10^{15}$  electrons per  $\text{cm}^3$  for the same p-type single crystals. For the Te-doped sample, the reported electron concentration was  $2 \times 10^{16} \text{ cm}^{-3}$ , about 1 order of magnitude higher than the electron concentration in the p-type crystal.<sup>20</sup> At -73°C, the p-type crystal in-plane mobility was  $\approx 500\text{-}1000 \text{ cm}^2\text{V}^{-1}\text{s}^{-1}$  while the n-type in-plane mobility was  $\approx 400 \text{ cm}^2\text{V}^{-1}\text{s}^{-1}$ . While their results prove tellurium affects the electron concentration, the question arises to how many carriers (or fraction of a charge) each tellurium atom actually donates to total number of free carriers.<sup>20</sup> As Akahama *et al.* did not report their actual tellurium levels introduced during the synthesis and the amount detected in the sample afterwards, it is difficult to analyze the effectiveness of tellurium as a dopant. Yang *et al.* reported experimental values of tellurium (0.1 at%) by high

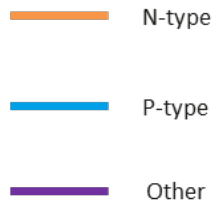
pressure synthesis but retained the p-type nature of BP based on hall measurements.<sup>27</sup> Attempts to increase the concentration to 0.5 at% resulted in tellurium inclusions rather than doping.<sup>27</sup> Zhang *et al.* claims Te-doping up to 0.5 at% via CVT but only provides XPS and EDS data – absent electrical measurements to confirm the semiconducting behavior (n or p type, carrier concentration).<sup>28</sup> Yu *et al.* claims Te-doping (EDS reports 0.1 at%) via CVT and provides I-V curves showing a shift of the threshold voltage towards the negative voltage – but the threshold voltage is still positive; the sample was still p-type.<sup>29</sup> Electron mobility or carrier concentration may have been improved but not enough to counteract the majority hole carriers.<sup>29</sup>

In the literature for BP, most of the electrical measurements have focused on the carrier mobility but have not adequately determined the carrier concentration. When electrical semiconducting devices are designed, the most important parameter that affects device performance is carrier concentration – this can be changed by several orders of magnitude whereas far less control over carrier mobility exists. Typically, silicon is doped from  $10^{17}$  to  $10^{21}$  carriers per  $\text{cm}^3$ , particularly for opto-electronics where a high number of recombination is desired to produce light emission. Over this same carrier concentration range, the mobility slightly changes, and less than an order of magnitude. At concentrations in the range of  $10^{19}$  –  $10^{21}$   $\text{cm}^{-3}$ , the semiconductor may become degenerate in that the individual impurity states form an energy band that can merge with the valence band or conduction band, causing the semiconductor to act more like metals – which is often the case for lasers and opto-electronics which need the high carrier concentrations for sufficient photon generation. Hence, the term “doping” versus “alloying” should be used in context of electrical behavior in addition to structural

behavior. Doping consists of altering the carrier concentration to improve conductivity and recombination events while retaining the semiconducting nature – a transition to metallic behavior would push the system into the “alloying” regime. In both “doping” and “alloying” the impurity atom is ideally substituted into the host lattice. The main point of emphasis is that as device performance primarily depends on carrier concentration, it is paramount that electrical measurements on BP should estimate the actual carrier concentration achieved by doping rather than focusing on minute changes of the carrier mobility as a function of the various doping schemes (substitutional, interstitial, intercalation, interfacial, electrostatic). Theoretical work suggests that BP may resemble the compound semiconductors GaAs or amorphous semiconductors for determining the type and number of free carriers introduced<sup>2</sup>. Experimentally, no seminal work on black phosphorus has elucidated the effective dopants, carrier concentrations achieved, and resultant conductivities to date.

A second motivation for ball milling phosphorus with these elements (Ge, Sn, S, Se, Te, As, Sb, Bi) was an apparent knowledge gap within the mechanochemical literature.<sup>50</sup> Accordingly, milling studies showing what compounds, if any, would form as a function of composition were lacking. A few isolated reports on P-Te<sup>51</sup> and P-Ge<sup>52-55</sup> existed but were either limited in scope (the P-Te work used low impact energy) or only synthesized a single composition (GeP<sub>5</sub> or GeP<sub>3</sub>). Absent from the literature, however, are works related to phosphides with Groups 4, 5, and 6 elements which surround phosphorus in the periodic table as shown in **Figure A.1**. Since the anticipated dopants include germanium and tin (group 4), possibly arsenic (group 5), and the chalcogenide set of sulfur, selenium, and tellurium (group 6), it seemed worthwhile to explore the

reactions of phosphorus with these elements across the entire range of compositions from 0 to 100 at% of each element as achieved through mechanochemistry. The outcomes of these phase diagram studies were reported in Chapter 3 (arsenic) Chapter 4 (germanium) and Chapter 5 (sulfur, selenium, tellurium) and were focused around the various compounds or alloys that were formed. What follows is a separate discussion of the dopant elements (Ge, Sn, S, Se, Te, and As) in reference to doping black phosphorus rather than compound or alloy formation. As these results were not discussed collectively as a group within each chapter, they are presented here within Appendix A. Results for milling with antimony, bismuth, boron, oxygen, and niobium are also included with their own rationale.

III	IV	V	VI	
Boron 5 B 10.81	Carbon 6 C 12.01	Nitrogen 7 N 14.00	Oxygen 8 O 15.99	
Aluminum 13 Al 26.98	Silicon 14 Si 28.08	Phosphorus 15 P 30.97	Sulfur 16 S 32.06	
Gallium 31 Ga 69.72	Germanium 32 Ge 72.63	Arsenic 33 As 74.92	Selenium 34 Se 78.97	
Indium 49 In 114.82	Tin 50 Sn 118.71	Antimony 81 Sb 121.76	Tellurium 52 Te 127.60	
Thallium 81 Pb 204.38	Lead 82 Pb 207.20	Bismuth 83 Bi 208.98	Polonium 84 Po 208.98	

**Figure A.1 Phosphorus and its periodic neighbors.**

Phosphorus, element number 15 (highlighted magenta) resides in group V while likely dopants are from groups III, IV, and VI. Predicted n-type and p-type dopants are highlighted in orange and blue respectively. Other elements reacted with phosphorus via ball milling are highlighted in purple. Each block lists the element name, number, symbol and atomic mass.

A compilation of the results from the preceding chapters and Appendix A that are related to mechanochemically producing doped black phosphorus with Ge, Sn, S, Se, Te, Sb, Bi, and As elements is as follows (absent electrical measurements):

(1) Arsenic may be a dopant depending upon how the electron charge distribution plays out at various arsenic concentrations; XPS results indicate slight n-type behavior, consistent with DFT literature. The structural characterization results for arsenic provide a solid framework to compare all other dopants for BP.

(2) Germanium is likely a p-type substitutional atom for BP with a solubility near  $\approx 1-2$  at%. Germanium stabilizes a trigonal solid solution alloy at higher concentrations with the same lattice type as trigonal PAs alloys.

(3) Tin is likely a p-type impurity dopant at levels below 10 at% considering the atomic size difference between phosphorus, germanium, and tin. The low solubility of germanium into BP, the lack of strongly doped p-type crystals via CVT, and literature evidence of tin inclusions between layers indicate impurity doping rather than substitutional doping.

(4) Sulfur and selenium may be dopants with solubility no greater than 10 at%. Both sulfur and selenium may substitute into the BP lattice; however, the nature of doping (n- or p-type) is still unknown.

(5) Tellurium is not likely a substitutional dopant as neither the XRD or Raman support bonding of phosphorus with tellurium (which is consistent with literature stating that P-Te bonds within crystalline structures are nearly non-existent).

(6) the heavier pnictogens (Sb and Bi) do not form compounds with phosphorus and are not expected to be substitutional dopants.

While not explicitly stated in Chapter 3, a primary motivation for working with phosphorus and arsenic was to produce a known substitutional alloy of phosphorus with another element and use it as a reference to compare other dopants. Namely, arsenic obeys the Hume-Rothery rules (empirical guidelines) when forming a solid solution alloy with phosphorus. That is phosphorus and arsenic share the same valency, atomic radii do not differ more than 15%, same crystal structure or shared allotrope structure, and similar

electronegativity. XRD refinement shows that arsenic expands the lattice even at 1-10 at% arsenic concentrations – hence any atom of a similar size as arsenic that substitutes into BP and replaces phosphorus on its site should exhibit similar unit cell expansion. Raman spectroscopy shows that arsenic at the 1-10 at% concentration causes distortion of the three main BP and produces lower wavenumber modes between 200-350  $\text{cm}^{-1}$ . Therefore, a dopant atom such as germanium or selenium should also produce similar modes and distortion based on the simple harmonic oscillator approach. Arsenic, selenium, and germanium all have similar atomic radii and masses. Selenium produces modes well below that of arsenic suggesting an atomic position other than the BP lattice sites, or higher degree of movement due to phosphorus forming two bonds to the selenium atom or selenium is double bonded to a single phosphorus atom.

Given the limited solubility of germanium into BP, and the limited solubility of arsenic (up to 70 at%), the results for tin and antimony can be better understood. First, although antimony has the same valency as phosphorus and similar electronegativity as arsenic, it does not produce an alloy, which confirms the known phase diagram of P-Sb.<sup>56</sup> Surprisingly, while antimony fails to bond with phosphorus, tin does form compounds with phosphorus.<sup>57,58</sup> This suggests a more complex explanation that requires analysis of the bond formation between the  $\text{sp}^3$  hybridized orbitals of phosphorus and the outer ‘*d*’ or ‘*f*’ states of the larger metal atoms. The XRD does not, however, show a comparable lattice expansion with tin doping (10 at%). Given that tin is a poor dopant (and most probably an inclusion when introduced with iodine)<sup>59</sup> and that antimony forms no binary compounds with phosphorus (although trace amounts of antimony appear to be incorporated into the Hittorf’s and violet phosphorus structure),<sup>60,61</sup> the evaluation of

tellurium as a dopant can also be better addressed. While several hundred P-Te organometallic compounds exist, all of these contain a weak bond between phosphorus and tellurium that is light and heat sensitive.<sup>62</sup> No known binary P-Te compounds exist.<sup>51</sup> The ball mill work by Itoh *et al.* indicates that an amorphous black powder containing 20 at% tellurium contained P-Te bonds based on the total pair distribution functions (from XRD and neutron diffraction), but the 10 and 30 at% samples did not.<sup>51</sup> No rationale as to why only the 20 at% tellurium sample had P-Te bonds whereas the 10 and 30 at% samples did not. Furthermore, the greatest reason to suspect tellurium is not a substitutional dopant is that studies on the electron distribution between constituent elements of X-P-Te ternary compounds (X is any other element) indicate little to no bonding between P-Te atom in most crystalline structures. Instead, tellurium forms bonds with X, and phosphorus forms bonds with X while X acts as a bridge between phosphorus and tellurium atoms. Classic examples of this are U-P-Te and Th-P-Te.<sup>63,64</sup> This does not mean that P-Te bonding is impossible; the compound BaP<sub>4</sub>Te<sub>2</sub> was shown to possess weak P-Te bonds.<sup>62,64</sup> However, the tendency of tellurium to bond to itself over phosphorus suggests that Te-Te chains may somehow be incorporated between the BP layers (likely accompanied by vacancy defects) with weak P-Te bonds may that form;<sup>65-67</sup> this may explain the weak broad amorphous peak near 28 degrees two theta observed in the 10 at% tellurium pattern in **Figure 5.10**. Even if such P-Te bonds form, they are likely to be destroyed upon solvent exfoliation or suffer from rapid oxidation.

In light of these results, a possible step forward is to explore doping of the P-As system. The larger unit cell volume of P-As combined with existence of Ge-As-Te, Ge-As-Se, and Ge-As-P glasses suggests that Ge, S, Se, and possibly Te may be stabilized in

the presence of arsenic and enable doping of binary black phosphorus-arsenic alloys in both the bulk and few-layer limit.

## Appendix A.1 Mechanochemical Doping Study of Phosphorus with Germanium and Selenium

To evaluate germanium and selenium as dopants for black phosphorus, a set of milling trials using high purity powder sources (RP, 99.999%, Ge, 99.99%, Se, 99.99%) were conducted. While most of the milling work with phosphorus was conducted using stainless steel vessel and stainless steel media and low purity red phosphorus (97%), the doping trials were conducted with high purity red phosphorus lumps and tungsten carbide media and tungsten carbide vessel to avoid incorporation of iron into the powder. The contamination from the stainless steel vessel was determined by performing trace metal analysis (ppb sensitivity) using ion-coupled-plasma mass spectroscopy (ICP-MS) on a high purity red phosphorus conversion run. The results suggest that up to 1000 ppm of iron was present. Accordingly, doping trials with germanium and selenium were performed using the tungsten carbide milling vessel and milling media. **Figure A.1.1** shows the powder XRD results confirming the synthesis of phase pure BP with increasing levels of germanium or selenium targeting  $10^{18}$ ,  $10^{19}$ ,  $10^{20}$  dopant atoms per  $\text{cm}^{-3}$  corresponding to (0.001, 0.01, 0.1 at% Ge or Se). **Table A.1.1** lists the ICPMS trace metal analysis confirming the amounts of germanium, selenium, as well as other impurity elements. Iron contaminates were detected at less than 100 ppm, which is the same as was detected in the as-received high purity red phosphorus, suggesting that no additional contamination was introduced. These results are in agreement with bismuth flux synthesized single crystals doped with germanium up to 2-4 at%.<sup>19</sup> However, it is possible that germanium or selenium may be present as secondary phases if these formed amorphous or nanosized crystals which are often undetectable by XRD.<sup>50</sup> Additionally,

long term stability of germanium atoms in black phosphorus should be investigated since the lack of thermodynamic stability of P-Ge phases at ambient pressure suggests instability of bonds between germanium and phosphorus. The formation of yellow phosphorus on the inside of glass vials of the trigonal P-Ge phase 2 at% germanium powders stored within an argon glovebox further supports lack of long-term (3 month) stability as shown in **Figure A.1.2**.

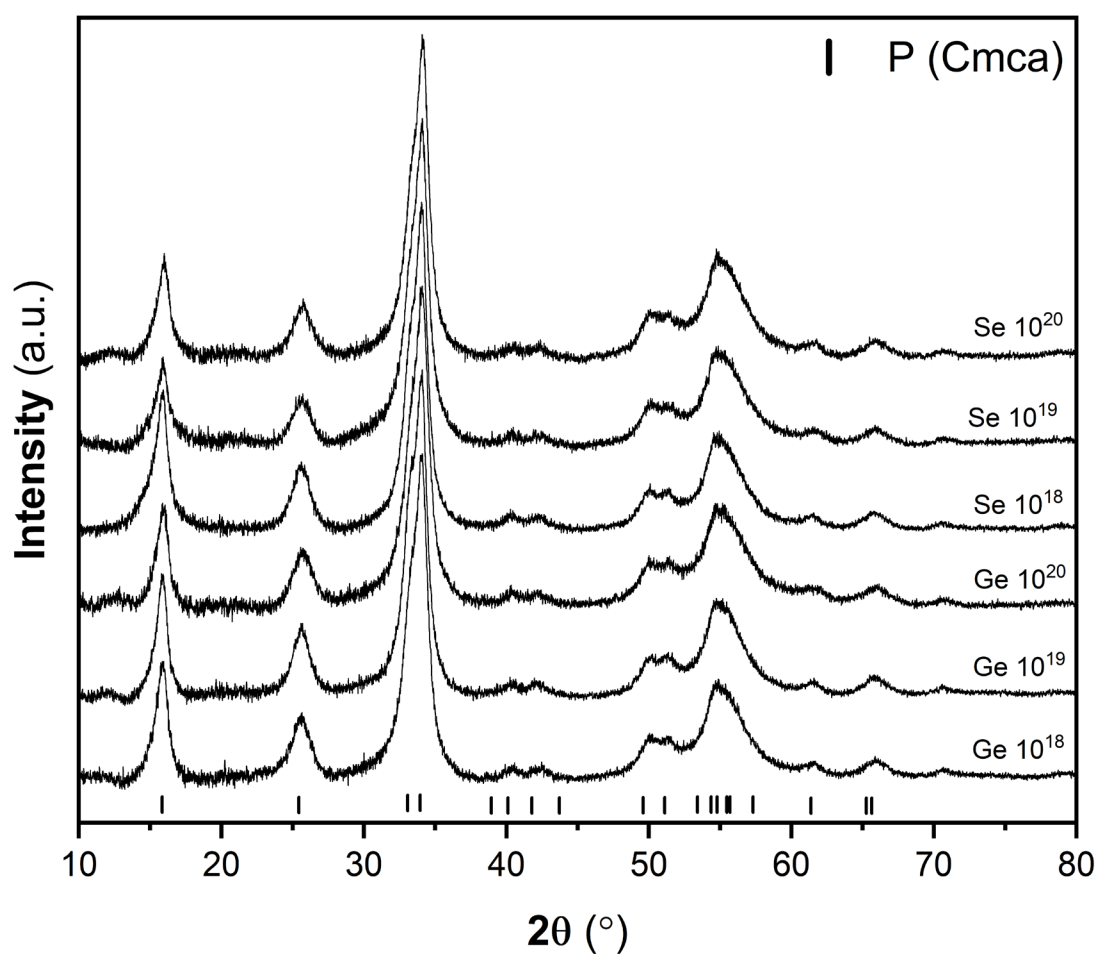


**Figure A.1.1 Structural characterization of mechanochemically synthesized germanium and selenium doped BP powders.**

X-Ray diffraction patterns with germanium and selenium content ( $10^{18} - 10^{20}$  dopants  $\text{cm}^{-3}$ ) indicate incorporation into the black phosphorus structure. No evidence of unreacted germanium or selenium is present within the samples. All patterns normalized and vertically offset manually.



**Figure A.1.2 Optical image of P-Ge 2 at% powders after long term storage.**

The optical image of a glass vial containing trigonal P-Ge (2 at% germanium) shows discoloration of the powders, the inside walls of the vial, cap, and slow damage to the paper label on the exterior of the vial due to instability of the P-Ge sample. The yellowish discoloration is presumably oxidized white phosphorus. Sample was stored inside argon glovebox (double sealed inside a secondary glass vial).

**Table A.1.1 Target dopant concentrations of the Ge- and Se- doped phosphorus ball milling runs along with the impurities from milling as determined by ICPMS. The samples were milled with WC balls and vessel in order to reduce contamination introduced during milling.**

Dopant	Target			ICPMS (ppm)						
	at%	atoms cm <sup>-3</sup>	ppm	Ge	Se	W	Fe	K	Ni	Co
Ge	0.001	10 <sup>18</sup>	10	150	3	20	100	0	3	4
	0.01	10 <sup>19</sup>	100	150	14	20	0	0	5	4
	0.1	10 <sup>20</sup>	1000	3557	6	20	0	0	13	5
Se	0.001	10 <sup>18</sup>	10	0.3	200	150	30	180	10	8
	0.01	10 <sup>19</sup>	100	0.7	500	180	40	315	16	7
	0.1	10 <sup>20</sup>	1000	0.7	4439	50	50	433	10	10

**In the milling experiment**, elemental red phosphorus (1-5 g, Alfa Aesar, 99.99% purity, chunks) and elemental germanium and selenium (1-5 g) (Alfa Aesar, 99.99% purity, -200 mesh) and tungsten carbide (WC) milling vessel and media (10 mm, 30 spheres) were weighed and loaded into the WC vessel (250 mL) inside an argon atmosphere glovebox ( $P_{O_2} < 0.1$  ppm) and sealed under argon (90-95 kPa) at room temperature. All milling experiments were conducted with the PM100 planetary ball mill (Retsch, Germany). As the high purity red phosphorus consisted of larger 1-3 mm chunks, a short 30-minute milling cycle at 300 rpm was used to grind and distribute the red phosphorus inside the vessel to reduce bare WC media to WC vessel collisions at higher rpm. The main milling sequence was conducted at 600 rpm and 18 hours of milling with pauses (15 minutes on, 45 minutes off) to prevent overheating of the unit.

**Ion-coupled plasma mass spectroscopy (ICPMS)** was performed on powders. The powders were dissolved into 2% nitric acid and analyzed in solution mode using a ThermoElectron X-Series II quadrupole ICPMS. A set of phosphorus geological standards were used to calibrate the results.<sup>68</sup>

Dr. Swartz and Dr. Schmitz are gratefully acknowledged their support with ICPMS trace metal analysis in the Isotope Geoscience Laboratory (Boise State University, Boise, ID).

## Appendix A.2 Mechanochemical study of Phosphorus and Tin compounds

Using nearly identical milling conditions needs to produce pure black phosphorus (as described in Chapter 2.4), milling trials with low purity red phosphorus (98 at%) and high purity tin powder (99.99 at%) were conducted. **Figure A.2.1** shows the powder XRD samples from 10 to 70 at% tin alloying with phosphorous. At 10 at% tin, the pattern appears to be single phase with no elemental tin or tin phosphides peaks detectable. At 20-30 at%, the trigonal  $\text{SnP}_3$  phase was produced. At 40 at%, a mixture with  $\text{SnP}_3$  and possibly SnP exists. At 50 at%, the powder was mostly SnP but a strong peak at 33 degrees two theta suggests an impurity phase such as  $\text{Sn}_4\text{P}_3$ . At 60 at%  $\text{Sn}_4\text{P}_3$  was present while 70 at% appears to match elemental tin was some  $\text{Sn}_4\text{P}_3$  also present. The 80 and 90 at% samples were not synthesized due to cold welding of tin to the stainless-steel media and vessel. For the 70 at% tin trial using 1 gram of powder, only about 0.15 grams of free powder could be extracted. As tin is a soft metal, it appears to cold weld during impacts to the vessel wall and media, producing a lustrous metallic coating. At the lower tin levels, phosphorus acts as a process control agent preventing the cold welding of tin.<sup>50</sup> A similar processing result was observed for trials at the higher levels with antimony and tellurium which are also relatively soft metals (as compared to transition metals).

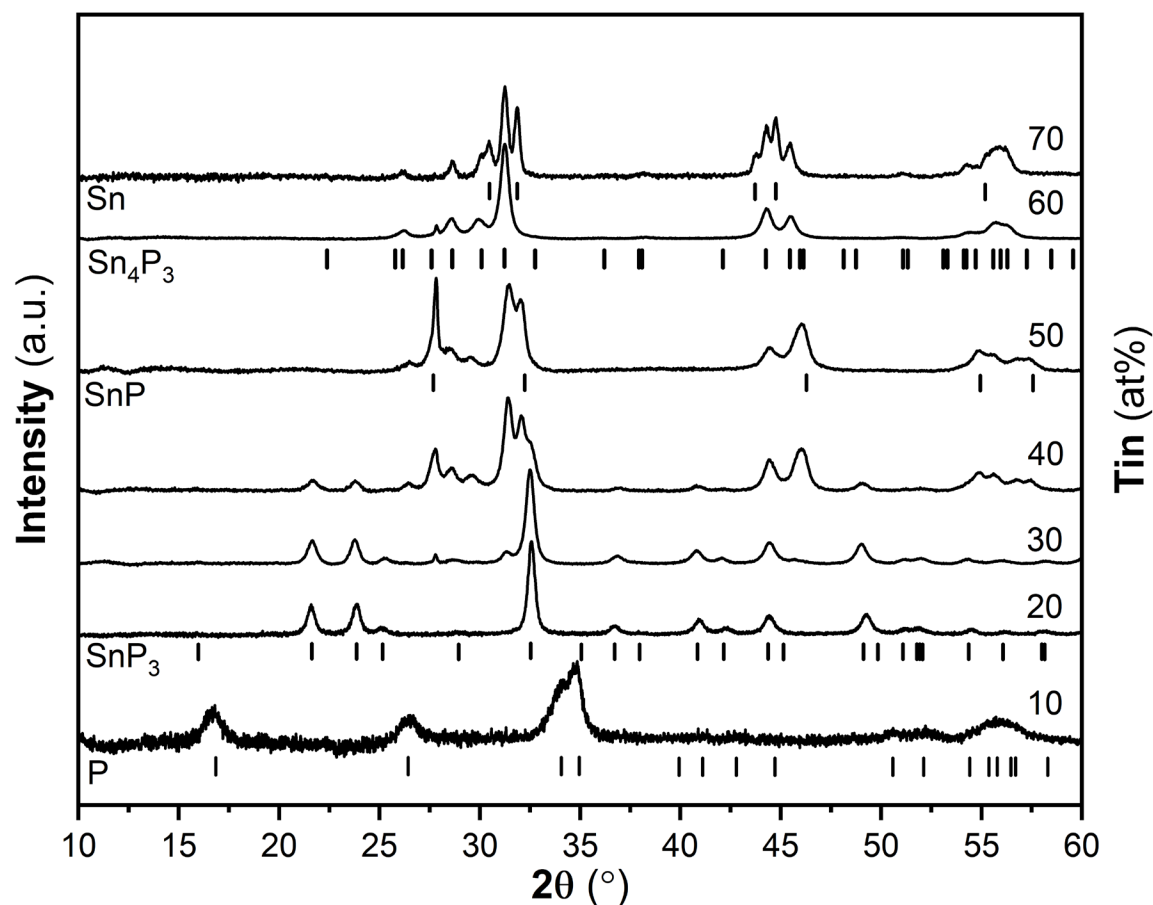


**Figure A.2.1 Structural characterization of mechanochemically synthesized P-Sn powders**

X-Ray diffraction patterns with increasing tin content reveal a limited solubility of tin into the black phosphorus structure (<10 at% Sn), a limited solid solution alloy range for the trigonal  $\text{Sn}_x\text{P}_{1-x}$  ( $10 < x < 30$  at% Sn), and several two-phase regions.

The main outcomes are: (1) that phosphorus and tin form binary compounds which indicate stable P-Sn bonding and (2) BP crystals were detected below 10 at% tin addition. That is, at low levels of tin addition, phosphorus will still form the BP crystal structure. Whether or not tin is actually doped by substitution into the lattice sites or is present as an impurity (interstitial, intercalated) remains to be proven conclusively. Literature results with CVT and high resolution TEM indicates tin exists as a tin iodide impurity when added via the mineralizer approach.<sup>59</sup>

### Appendix A.3 Mechanochemistry of Phosphorus in the Presence of Heavy Pnictogens: Antimony and Bismuth

While trials with lead (Pb) were considered, it seemed unnecessary as several reports of violet or Hittorf's phosphorus production by lead flux indicates that phosphorus-lead alloys were unlikely to form.<sup>61,69</sup> As antimony substituted violet phosphorus is produced using the lead flux route<sup>61</sup>, the question is if antimony could be substituted into the black phosphorus structure via mechanical alloying. Since PAs alloys with extended solubility of arsenic up to ~70 at% are stable in the orthorhombic BP structure, the question is if antimony or bismuth (the heavier pnictogens below arsenic) behave in a similar manner. The bismuth flux route will produce BP instead of Hittorf's violet phosphorus whereas antimony has not been demonstrated as a flux for black phosphorus.<sup>48,70</sup> Therefore, a series of trials with bismuth and antimony were conducted with the XRD results shown in **Figure A.3.1**. The first pattern (P + Bi, 4 at%) is an attempt to mimic the bismuth flux BP crystal growth method. In this trial, 0.25 grams of bismuth metal (4 at% Bi) is added to 1-gram of red phosphorus and milled in the normal stainless-steel vessel with 10 mm diameter stainless steel media at 600 rpm for 14 hours (15/30 minutes on/off cycle). The result is metallic bismuth and black phosphorus powders. The traditional bismuth flux method uses white phosphorus (as red does not readily dissolve into molten bismuth).<sup>48</sup> It was hoped that the high-pressure impacts during milling would provide enough energy to drive phosphorus atoms into the bismuth structure and that upon decompression (as the media rebound away from each other) the phosphorus would precipitate out as BP. More work is needed to better understand if bismuth benefits the conversion process in anyway. The ball mill settings (speed, media

size and density, vessel volume, etc.,) are alone sufficient to produce BP directly from RP without any additive. This trial by itself cannot answer if bismuth helps – but it does show that bismuth does not prevent the formation of BP (unlike antimony). It was hoped that bismuth, if it acted to precipitated BP, would increase the grain size and produce sharper XRD peaks. Visually, the peak widths in **Figure A.3.1** are quite broad indicating nanosized crystalline domains indicating no appreciable improvement by bismuth.

Similar trials with antimony show a somewhat different behavior: At 5, 10 and 20 at% antimony, the phases present are metallic antimony, white phosphorus, and an amorphous hump near the 111 and 040 peaks of BP are visible. At the lower 10-40 at% Sb compositions, an amorphous hump near 32-34 degrees two theta is evident – this may be an interaction of phosphorus with antimony and is similar to the result with 20 at% tellurium (See **Figure 5.10**). Like the soft tin metal, antimony cold welds at the 70 at% addition – no appreciable amount of powder could be extracted from the milling vessel and media. Lastly, glass vials containing the P-Sb powders appear to slowly decompose over time forming a yellowish film on the insides of the glass vial containers (stored inside the glovebox); this suggests an unstable mixture of metallic antimony and phosphorus. It is observed that a yellowish film formed on the compact powder bed during the XRD measurement of the 5 and 10 at% samples even when using the argon XRD holder (Kapton dome accessory); upon exposure to air the powder immediately ignited. The sharp peaks at 20-25 degrees two theta match the known peaks for white/yellowish phosphorus which possesses a cubic crystal structure. Overall, while bismuth does not prevent the formation of black phosphorus, antimony appears to produce an amorphous compound with phosphorus that is extremely oxygen sensitive

and slowly decomposes under inert gas environments.

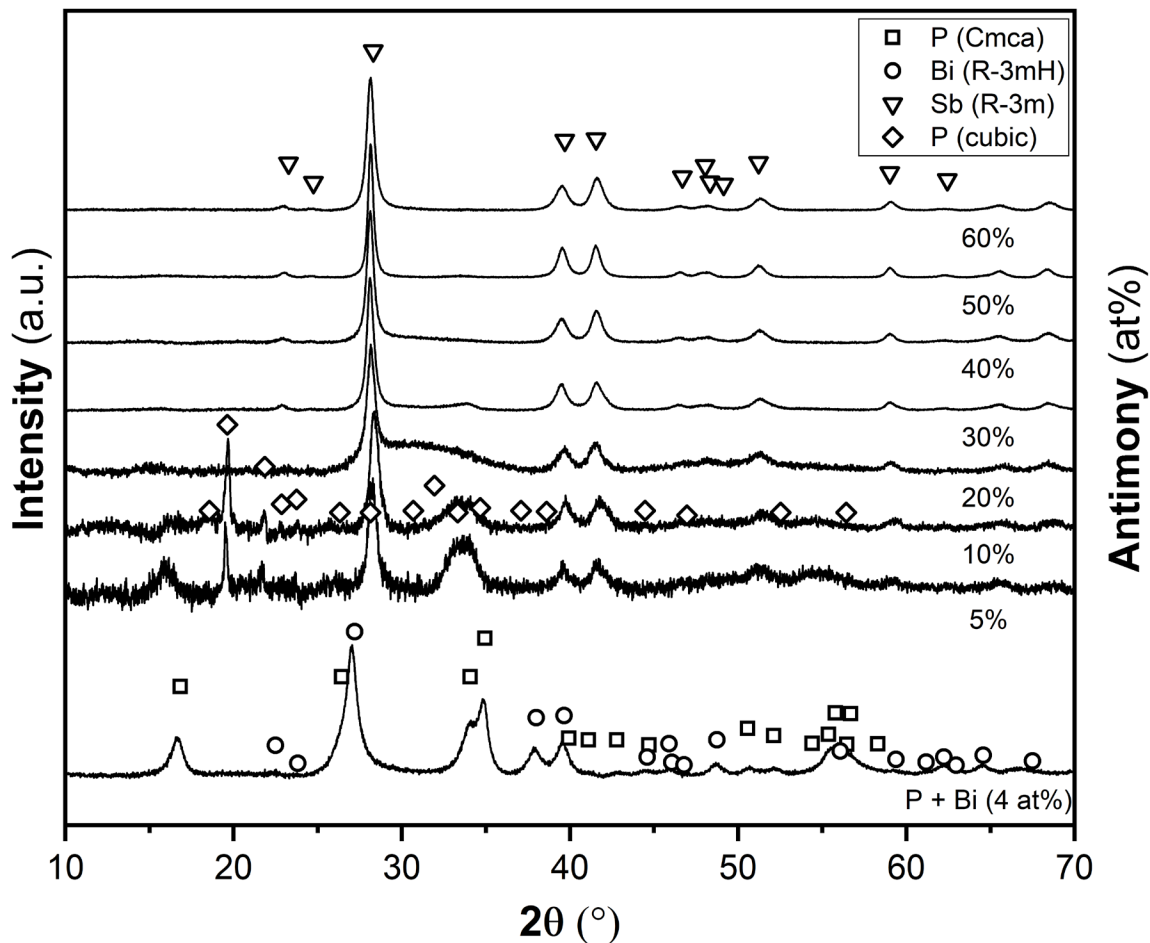


**Figure A.3.1 Structural characterization of mechanochemically synthesized P-Sb powders.**

X-Ray diffraction patterns with increasing antimony content indicate that only metallic antimony (Sb) and an amorphous phase exist at 20 at% Sb or less. At higher antimony content, only the crystal structure of antimony appears to be present. A single trial with bismuth metal at 4 at% shows a two-phase mixture of BP and bismuth metal. Patterns are normalized and manually offset vertically.

## Appendix A.4 Mechanochemical reactions of Phosphorus with Oxygen, Boron, and Niobium

The following results are milling trials that explore reactions of phosphorus with oxygen, boron, and niobium. Black phosphorus synthesis trials using tungsten carbide (WC) and silicon nitride ( $\text{Si}_3\text{N}_4$ ) grinding media were also conducted. While most of the milling work with phosphorus was conducted using stainless steel vessel and stainless steel media, the doping trials were conducted with tungsten carbide media and vessel to avoid incorporation of iron into the powder. The contamination from the stainless steel vessel was determined by performing trace metal analysis (ppb sensitivity) using ion-coupled-plasma mass spectroscopy (ICP-MS) on a high purity red phosphorus conversion run. The results suggest that up to 1000 ppm of iron was present. From a reaction standpoint, the Gibbs free energy of formation of tungsten phosphide, WP, is near  $-8 \text{ kJ mol}^{-1}$  whereas BP is near  $-11 \text{ kJ mol}^{-1}$  and pure WC is near  $-38 \text{ kJ mol}^{-1}$ . The reaction of WC with phosphorus is thermodynamically unfavorable. A similar analysis with  $\text{Si}_3\text{N}_4$  (gibbs free energy of  $-647 \text{ kJ mol}^{-1}$ ) and the likely products SiP ( $-58 \text{ kJ mol}^{-1}$ ) and PN ( $-195 \text{ kJ mol}^{-1}$ ) suggests a possible reaction that favors SiP and PN but the thermodynamic stability of  $\text{Si}_3\text{N}_4$  suggests the reaction would not proceed readily. Other vessels such as alumina ( $\text{Al}_2\text{O}_3$ ) or zirconia ( $\text{ZrO}_2$ ) could likely react with phosphorus to form highly stable phosphates,  $\text{AlPO}_4$  and  $\text{ZrP}_2\text{O}_7$ , with Gibbs free energy of formation near  $-1600$  and  $-2645 \text{ kJ mol}^{-1}$ , respectively. Iron phosphides ( $\text{Fe}_3\text{P}$ ,  $\text{Fe}_2\text{P}$ ,  $\text{FeP}$ ) are all thermodynamically more stable than BP ( $-146$ ,  $-134$ ,  $-97 \text{ kJ mol}^{-1}$ , respectively) and thus are expected to form with extensive cold welding and abrasion of the chrome steel vessel and media.<sup>71-74</sup>

To investigate potential contamination from WC or  $\text{Si}_3\text{N}_4$  media and vessel systems; high purity red phosphorus lumps (99.99%) (1-5g) were milled at 600 rpm for 1440 minutes (24 hours) (15:45 minute on/off cycle). The XRD patterns from the powders produced are shown in **Figure A.4.1**. The bottom most pattern is that of a purchased black phosphorus single crystal ground into powder using the planetary ball mill. The second pattern is that of red phosphorus milled with regular air (20% oxygen, 80% nitrogen) instead of argon – BP was produced with some amorphous material still present after 1 hour of milling at 600 rpm. Although this trial indicates that oxygen does not prevent BP formation, when the vessel is opened inside the fumehood, visible fumes (smoke) was released and the powder ignited inside the vessel. Therefore, it is much safer to produce BP by milling under argon atmosphere than under air.

The third pattern (WC satellite media) was the first attempt at BP synthesis using a WC milling vessel (250 mL) and 10 mm diameter WC satellites. WC satellite media have a band with a slight edge along the circumference of the media – this type of grinding ball is less expensive to produce than polished round balls without the band. While BP was produced, the satellite media chipped along the bands creating WC contamination in the free BP powder. The fourth pattern is a follow-up run using polished WC media without the band (purchased separately) in the same WC milling vessel. The result was BP powder without any WC media contamination (at least detectable by XRD). The fifth pattern from the bottom is the BP powder obtained using silicon nitride ( $\text{Si}_3\text{N}_4$ ) grinding media (10 mm diameter) and vessel (250 mL). No silicon nitride contamination was detected.

The next two patterns (P + B) are boron-phosphide synthesis trials at 10 at% boron. The reasons for ball milling phosphorus and boron together were to first determine if boron could be doped into black phosphorus and to synthesis, if possible, the theoretically predicted hexagonal boron phosphide, hBP, (a 2D monolayer analog to hexagonal boron nitride).<sup>18,75-83</sup> The powder appears to be a match of trigonal B<sub>12</sub>P<sub>2</sub> and cubic boron phosphide. Two peaks at 46 and 48 degrees two theta were however unidentified. Attempt to match oxygen by-products such as B<sub>2</sub>O<sub>3</sub>, P<sub>2</sub>O<sub>5</sub>, etc., did not match the two peaks either. Milling runs at 500 rpm and 600 rpm appeared to produce different proportions of the cubic and trigonal boron phosphide phases. Due to the similarity of hBN and hBP (direct analogues),<sup>76,77,84</sup> the formation of hBP via ball milling is probably impossible – milling hBN powder for long periods of time will irreversibly produce cubic hBN.<sup>85-88</sup> Even if hBP was formed from red phosphorus and boron powder, the powder will likely transform to cubic boron phosphide. Furthermore, the powders were highly flammable when exposed to oxygen and likely contained residual white or yellow phosphorus; yellow phosphorus films were observed to form on the inside of the sealed glass vials (stored in an argon glovebox).

Niobium phosphides were briefly discussed during a conversation in our research group about an unrelated project involving niobium metal doped with phosphorus. After a brief literature search, it seemed that ball mill synthesis of Nb-P phases may not have been demonstrated experimentally. Prior work on Half-Heuslers (the subject of Appendix B) with refractory metals such as zirconium, hafnium, and also niobium alloyed with tin, nickel, and iron indicated that some of the refractory metals are amenable to mechanical alloying.<sup>89</sup> Therefore, a simple 1-gram trial with niobium and red phosphorus at 600 rpm

for 18 hours (15/45 minutes on/off cycle) was performed with the same milling configuration (250 mL vessel, 10 mm stainless steel grinding media). The XRD pattern shown in **Figure A.4.1** appears to match the NbP (I41md) phase (ICSD 81493) with some metallic niobium still unreacted. A few peaks were not identified and did not match peaks from other Nb-P phases. Considering that several of the Nb-P compounds are high pressure phases, ball milling of Nb-P may provide a straightforward route to obtain these phases and possibly explore their unusual properties.<sup>90-93</sup>

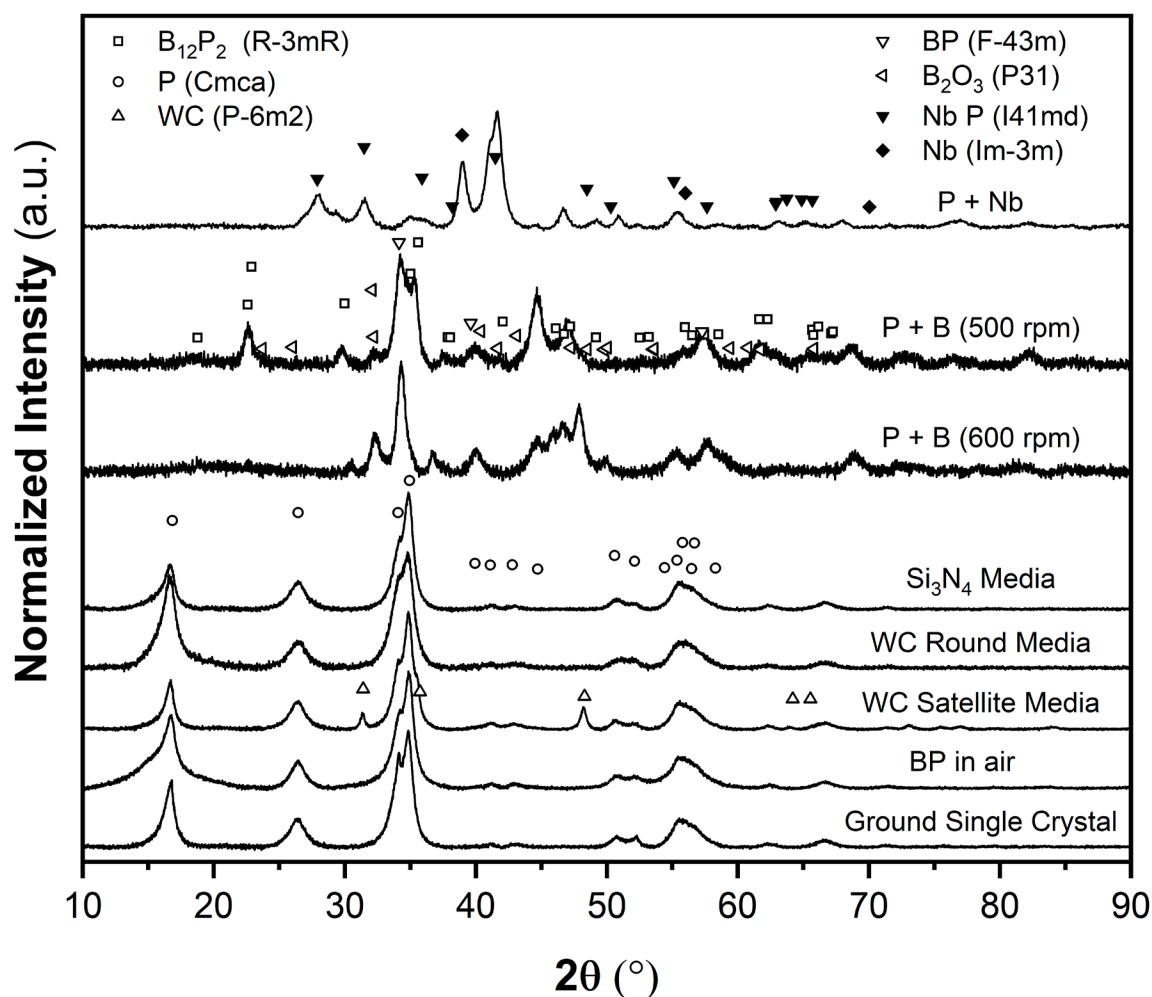


**Figure A.4.1 Structural characterization of phosphorus milling trials with oxygen, boron, and niobium.**

X-Ray diffraction patterns of ball mill synthesized powders; patterns are background corrected, normalized, and vertically offset manually.

## References

- 1 Hashmi, A. & Hong, J. Transition Metal Doped Phosphorene: First-Principles Study. *J. Phys. Chem. C* **119**, 9198-9204 (2015)
- 2 Guo, Y. & Robertson, J. Vacancy and Doping States in Monolayer and bulk Black Phosphorus. *Sci. Rep.* **5**, 14165 (2015)
- 3 Hu, T. & Hong, J. First-Principles Study of Metal Adatom Adsorption on Black Phosphorene. *J. Phys. Chem. C* **119**, 8199-8207 (2015)
- 4 Khan, I. & Hong, J. Manipulation of magnetic state in phosphorene layer by non-magnetic impurity doping. *New J. Phys.* **17**, (2015)
- 5 Li, X. B. *et al.* Structures, stabilities, and electronic properties of defects in monolayer black phosphorus. *Sci. Rep.* **5**, 10848 (2015)
- 6 Sui, X. *et al.* Tunable Magnetism in Transition-Metal-Decorated Phosphorene. *J. Phys. Chem. C* **119**, 10059-10063 (2015)
- 7 Xiang, D. *et al.* Surface transfer doping induced effective modulation on ambipolar characteristics of few-layer black phosphorus. *Nat. Commun.* **6**, 6485 (2015)
- 8 Yu, W. *et al.* Anomalous doping effect in black phosphorene using first-principles calculations. *Phys. Chem. Chem. Phys.* **17**, 16351-16358 (2015)
- 9 Koenig, S. P. *et al.* Electron Doping of Ultrathin Black Phosphorus with Cu Adatoms. *Nano Lett.* **16**, 2145-2151 (2016)
- 10 Suvansinpan, N. *et al.* Substitutionally doped phosphorene: electronic properties and gas sensing. *Nanotechnol.* **27**, 065708 (2016)
- 11 Gaberle, J. & Shluger, A. L. Structure and properties of intrinsic and extrinsic defects in black phosphorus. *Nanoscale* **10**, 19536-19546 (2018)
- 12 Wang, K., Wang, H., Zhang, M., Liu, Y. & Zhao, W. Electrical properties of phosphorene systems doped with fourth-period elements. *Appl. Phys. Lett.* **112**, 202101 (2018)
- 13 Xuan, X., Zhang, Z. & Guo, W. Doping-stabilized two-dimensional black phosphorus. *Nanoscale* **10**, 7898-7904 (2018)
- 14 Goulart, L., da S. Fernandes, L., Lange dos Santos, C. & Rossato, J. Electronic and structural properties of black phosphorene doped with Si, B and N. *Phys. Lett. A* **383**, 125945 (2019)
- 15 Wang, K., Wang, H., Zhang, M., Liu, Y. & Zhao, W. Electronic and magnetic properties of doped black phosphorene with concentration dependence. *Beilstein J Nanotechnol* **10**, 993-1001 (2019)
- 16 Guo, H., Chu, W., Zheng, Q. & Zhao, J. Tuning the Carrier Lifetime in Black Phosphorene through Family Atom Doping. *J. Phys. Chem. Lett.* **11**, 4662-4667 (2020)
- 17 Li, M. *et al.* Revealing Dopant Local Structure of Se-Doped Black Phosphorus. *Chem. Mater.* (2021)
- 18 Kim, D.-K. *et al.* P-N Junction Diode Using Plasma Boron-Doped Black Phosphorus for High-Performance Photovoltaic Devices. *ACS Nano* **13**, 1683-1693 (2019)
- 19 Maruyama, Y., Inabe, T., He, L. & Oshima, K. Electrical conductivity of black phosphorous-germanium compound. *Synth. Met.* **43**, 4067-4070 (1991)

- 20 Akahama, Y., Endo, S. & Narita, S. Electrical Properties of Black Phosphorus  
Single Crystals. *J. Phys. Soc. Jpn.* **52**, 2148-2155 (1983)
- 21 Chang, Y. *et al.* Liquid-exfoliation of S-doped black phosphorus nanosheets for  
enhanced oxygen evolution catalysis. *Nanotechnol.* **30**, 035701 (2018)
- 22 Lv, W. *et al.* Sulfur-Doped Black Phosphorus Field-Effect Transistors with  
Enhanced Stability. *ACS Appl. Mater. Interfaces* **10**, 9663-9668 (2018)
- 23 Antonatos, N. *et al.* In Situ Doping of Black Phosphorus by High-Pressure  
Synthesis. *Inorg. Chem.* (2019)
- 24 Ge, Y. *et al.* Few-layer selenium-doped black phosphorus: synthesis, nonlinear  
optical properties and ultrafast photonics applications. *J. Mater. Chem. C* **5**, 6129-  
6135 (2017)
- 25 Xu, Y. *et al.* Selenium-Doped Black Phosphorus for High-Responsivity 2D  
Photodetectors. *Small* **12**, 5000-5007 (2016)
- 26 Liu, M. *et al.* High yield growth and doping of black phosphorus with tunable  
electronic properties. *Mater. Today* **36**, 91-101 (2020)
- 27 Yang, B. *et al.* Te-Doped Black Phosphorus Field-Effect Transistors. *Adv. Mater.*  
**28**, 9408-9415 (2016)
- 28 Zhang, Z., Khurram, M., Sun, Z. & Yan, Q. Uniform Tellurium Doping in Black  
Phosphorus Single Crystals by Chemical Vapor Transport. *Inorg. Chem.* **57**,  
4098-4103 (2018)
- 29 Yu, Y. *et al.* N-type doping of black phosphorus single crystal by tellurium.  
*Nanotechnol.* **31**, 315605 (2020)
- 30 Prakash, A., Cai, Y., Zhang, G., Zhang, Y. W. & Ang, K. W. Black Phosphorus  
N-Type Field-Effect Transistor with Ultrahigh Electron Mobility via Aluminum  
Adatoms Doping. *Small* **13**, (2017)
- 31 Kim, J. *et al.* Electronic band structure of surface-doped black phosphorus. *J.*  
*Electron Spectrosc. Relat. Phenom.* **219**, 86-91 (2017)
- 32 Kim, S.-W. *et al.* Microscopic mechanism of the tunable band gap in potassium-  
doped few-layer black phosphorus. *Phys. Rev. B* **96**, 075416 (2017)
- 33 Chen, Z. *et al.* Spectroscopy of buried states in black phosphorus with surface  
doping. *2D Mater.* (2020)
- 34 Kumar, A. *et al.* Black Phosphorus n-Type Doping by Cu: A Microscopic Surface  
Investigation. *J. Phys. Chem.* **125**, 13477-13484 (2021)
- 35 Robbins, M. C. & Koester, S. J. Black Phosphorus p- and n-MOSFETs With  
Electrostatically Doped Contacts. *IEEE Electron Device Lett.* **38**, 285-288 (2017)
- 36 Xu, Y. *et al.* Field-Induced n-Doping of Black Phosphorus for CMOS Compatible  
2D Logic Electronics with High Electron Mobility. *Adv. Funct. Mater.* **27**,  
1702211 (2017)
- 37 Park, H. & Kim, J. Enhancing ambipolar carrier transport of black phosphorus  
field-effect transistors with Ni-P alloy contacts. *Phys. Chem. Chem. Phys.* **20**,  
22439-22444 (2018)
- 38 Wang, L. *et al.* Unipolar n-Type Conduction in Black Phosphorus Induced by  
Atomic Layer Deposited MgO. *IEEE Electron Device Lett.* **40**, 471-474 (2019)
- 39 Wang, C.-H. *et al.* Unipolar n-Type Black Phosphorus Transistors with Low  
Work Function Contacts. *Nano Lett.* **18**, 2822-2827 (2018)

- 40 Sofer, Z. *et al.* The Covalent Functionalization of Layered Black Phosphorus by Nucleophilic Reagents. *Angew. Chem. Int. Ed* **56**, 9891-9896 (2017)
- 41 van Druenen, M. *et al.* Covalent Functionalization of Few-Layer Black Phosphorus Using Iodonium Salts and Comparison to Diazonium Modified Black Phosphorus. *Chem. Mater.* **30**, 4667-4674 (2018)
- 42 He, G., Dong, T., Yang, Z. & Ohlckers, P. Tuning 2D Black Phosphorus: Defect Tailoring and Surface Functionalization. *Chem. Mater.* **31**, 9917-9938 (2019)
- 43 Jia, J., Jeon, S., Jeon, J., Park, J.-H. & Lee, S. Versatile Doping Control of Black Phosphorus and Functional Junction Structures. *J. Phys. Chem. C* **123**, 10682-10688 (2019)
- 44 Zhang, R., Waters, J., Geim, A. K. & Grigorieva, I. V. Intercalant-independent transition temperature in superconducting black phosphorus. *Nat. Commun.* **8**, 15036 (2017)
- 45 Lin, Z. *et al.* Interstitial copper-doped edge contact for n-type carrier transport in black phosphorus. *InfoMat* **1**, 242-250 (2019)
- 46 Vanni, M. *et al.* Interlayer Coordination of Pd-Pd Units in Exfoliated Black Phosphorus. *J. Am. Chem. Soc.* (2021)
- 47 Hu, S. *et al.* Intrinsic and extrinsic electrical and thermal transport of bulk black phosphorus. *Phys. Rev. B* **97**, 045209 (2018)
- 48 Baba, M., Izumida, F., Morita, A., Koike, Y. & Fukase, T. Electrical properties of black phosphorus single crystals prepared by the bismuth-flux method. *Jpn. J. Appl. Phys.* **30**, 1753-1758 (1991)
- 49 Mayorga-Martinez, C. C. *et al.* Metallic impurities in black phosphorus nanoflakes prepared by different synthetic routes. *Nanoscale* **10**, 1540-1546 (2018)
- 50 Suryanarayana, C. Mechanical alloying and milling. *Prog. Mater. Sci.* **46**, 1-184 (2001)
- 51 Itoh, K., Mizuhara, Y. & Otomo, T. Mechanochemical synthesis of binary phosphorus telluride: Short range structure and thermal properties. *J. Solid State Chem.* **267**, 119-123 (2018)
- 52 Qi, W. *et al.* Facile Synthesis of Layer Structured GeP<sub>3</sub>/C with Stable Chemical Bonding for Enhanced Lithium-Ion Storage. *Sci Rep* **7**, 43582 (2017)
- 53 Wang, T. *et al.* Highly Reversible and Rapid Sodium Storage in GeP<sub>3</sub> with Synergistic Effect from Outside-In Optimization. *ACS Nano* **14**, 4352-4365 (2020)
- 54 Li, W. *et al.* Layered phosphorus-like GeP<sub>5</sub>: a promising anode candidate with high initial coulombic efficiency and large capacity for lithium ion batteries. *Energy Environ. Sci.* **8**, 3629-3636 (2015)
- 55 Liu, Y. *et al.* GeP<sub>5</sub>/C composite as anode material for high power sodium-ion batteries with exceptional capacity. *J. Alloys Compd.* **744**, 15-22 (2018)
- 56 Okamoto, H. P-Sb (Phosphorus-Antimony). *J. Ph. Equilibria Diffus.* **30**, 303-304 (2009)
- 57 Okamoto, H. P-Sn (phosphorus-tin). *J. Ph. Equilibria Diffus.* **14**, 263-264 (1993)
- 58 Ritscher, A., Schmetterer, C. & Ipsen, H. Pressure dependence of the tin-phosphorus phase diagram. *Monatsh. Chem.* **143**, 1593-1602 (2012)

- 59 Izquierdo, N., Myers, J. C., Seaton, N. C. A., Pandey, S. K. & Campbell, S. A. Thin-Film Deposition of Surface Passivated Black Phosphorus. *ACS Nano* **13**, 7091-7099 (2019)
- 60 Jason, M. E. Transfer of Sulfur from Arsenic and Antimony Sulfides to Phosphorus Sulfides. Rational Syntheses of Several Less-Common P4Sn Species. *Inorg. Chem.* **36**, 2641-2646 (1997)
- 61 Baumer, F. *et al.* Synthesis, Characterization, and Device Application of Antimony-Substituted Violet Phosphorus: A Layered Material. *ACS Nano* **11**, 4105-4113 (2017)
- 62 Nordheider, A., Woollins, J. D. & Chivers, T. Organophosphorus–Tellurium Chemistry: From Fundamentals to Applications. *Chem. Rev.* **115**, 10378-10406 (2015)
- 63 Tschulik, K. *et al.* Chemistry and Physical Properties of the Phosphide Telluride  $Zr_2PTe_2$ . *Eur. J. Inorg. Chem.* **2009**, 3102-3110 (2009)
- 64 Jörgens, S., Johrendt, D. & Mewis, A.  $BaP_4Te_2$ —A Ternary Telluride with P-Te Bonds and a Structural Fragment of Black Phosphorus. *Chem. Eur. J.* **9**, 2405-2410 (2003)
- 65 Chivers, T. & Laitinen, R. S. Tellurium: a maverick among the chalcogens. *Chem. Soc. Rev.* **44**, 1725-1739 (2015)
- 66 Du, Y. *et al.* One-Dimensional van der Waals Material Tellurium: Raman Spectroscopy under Strain and Magneto-Transport. *Nano Lett.* **17**, 3965-3973 (2017)
- 67 Zhu, J. *et al.* Synergy of tellurium and defects in control of activity of phosphorene for oxygen evolution and reduction reactions. *Phys. Chem. Chem. Phys.* **21**, 22939-22946 (2019)
- 68 Jochum, K. P. *et al.* Reference Values Following ISO Guidelines for Frequently Requested Rock Reference Materials. *Geostand. Geoanalytical Res.* **40**, 333-350 (2016)
- 69 Ruck, M. *et al.* Fibrous red phosphorus. *Angew Chem Int Ed Engl* **44**, 7616-7619 (2005)
- 70 Baba, M., Takeda, Y. & Morita, A. Preparation of black phosphorus single crystals by a completely closed bismuth-flux method and their crystal morphology. *Jpn. J. Appl. Phys.* **28**, 4 (1989)
- 71 Coltters, R. G. & Belton, G. R. High temperature thermodynamic properties of the tungsten carbide WC determined using a galvanic cell technique. *Metall. Mater. Trans. A* **14**, 1915-1919 (1983)
- 72 Lesnyak, V. V., Stratiichuk, D. A., Sudavtsova, V. S. & Slobodyanik, M. S. Preparation of Al, Cr, Nb, Mo, and W Monophosphides from a Lithium Metaphosphate Melt. *Russ. J. Appl. Chem.* **74**, 1274-1277 (2001)
- 73 Gingerich, K. A. Vaporization Behavior and Phosphorus Decomposition Pressures of Tungsten Monophosphide. *J. Phys. Chem.* **68**, 768-772 (1964)
- 74 Barin, I.  $O-Pu(SO_4)_2$  in *Thermochemical Data of Pure Substances* 1238-1358 (1995).
- 75 Zhuang, H. L. & Hennig, R. G. Electronic structures of single-layer boron pnictides. *Appl. Phys. Lett.* **101**, 153109 (2012)

- 76 Hallioglu, L. *Formation and functionalization of boron phosphide monolayers* Masters thesis, Bilkent University, (2015).
- 77 Yu, J. & Guo, W. Strain tunable electronic and magnetic properties of pristine and semihydrogenated hexagonal boron phosphide. *Appl. Phys. Lett.* **106**, 043107 (2015)
- 78 Zeng, B. *et al.* First-Principles Prediction of the Electronic Structure and Carrier Mobility in Hexagonal Boron Phosphide Sheet and Nanoribbons. **120**, 25037-25042 (2016)
- 79 Onat, B., Hallioglu, L., İpek, S. & Durgun, E. Tuning Electronic Properties of Monolayer Hexagonal Boron Phosphide with Group III–IV–V Dopants. *J. Phys. Chem. C* **121**, 4583-4592 (2017)
- 80 Bhattacharyya, G., Choudhuri, I. & Pathak, B. High Curie temperature and half-metallicity in an atomically thin main group-based boron phosphide system: long range ferromagnetism. *Phys. Chem. Chem. Phys.* **20**, 22877-22889 (2018)
- 81 Cheng, Y., Meng, R., Tan, C., Chen, X. & Xiao, J. Selective gas adsorption and I–V response of monolayer boron phosphide introduced by dopants: A first-principle study. *Appl. Surf. Sci.* **427**, 176-188 (2018)
- 82 Ullah, S., Denis, P. A. & Sato, F. Hexagonal boron phosphide as a potential anode nominee for alkali-based batteries: A multi-flavor DFT study. *Appl. Surf. Sci.* **471**, 134-141 (2019)
- 83 Zhou, Z. Z., Liu, H. J., Fan, D. D., Cao, G. H. & Sheng, C. Y. High thermoelectric performance in the hexagonal bilayer structure consisting of light boron and phosphorus elements. *Phys. Rev. B* **99**, (2019)
- 84 Mukhanov, V. A., Vrel, D., Sokolov, P. S., Le Godec, Y. & Solozhenko, V. L. Ultra-fast mechanochemical synthesis of boron phosphides, BP and B<sub>12</sub>P<sub>2</sub>. *Dalton Trans.* **45**, 10122-10126 (2016)
- 85 Ji, C. *et al.* Shear-induced phase transition of nanocrystalline hexagonal boron nitride to wurtzitic structure at room temperature and lower pressure. *Proc. Natl. Acad. Sci.* **109**, 19108-19112 (2012)
- 86 Ghosh, J., Mazumdar, S., Das, M., Ghatak, S. & Basu, A. K. Microstructural characterization of amorphous and nanocrystalline boron nitride prepared by high-energy ball milling. *Mater. Res. Bull.* **43**, 1023-1031 (2008)
- 87 Gasgnier, M., Szwarc, H. & Ronez, A. Low-energy ball-milling: Transformations of boron nitride powders. Crystallographic and chemical characterizations. *J. Mater. Sci.* **35**, 3003-3009 (2000)
- 88 Li, L. H. *et al.* Large-scale mechanical peeling of boron nitride nanosheets by low-energy ball milling. *J. Mater. Chem.* **21**, (2011)
- 89 Pedersen, S. V. *et al.* Novel synthesis and processing effects on the figure of merit for NbCoSn, NbFeSb, and ZrNiSn based half-Heusler thermoelectrics. *J. Solid State Chem.* 121203 (2020)
- 90 Liu, X. *et al.* High-Pressure Crystal Growth, Superconducting Properties, and Electronic Band Structure of Nb<sub>2</sub>P<sub>5</sub>. *Chem. Mater.* **32**, 8781-8788 (2020)
- 91 Sergelius, P. *et al.* Berry phase and band structure analysis of the Weyl semimetal NbP. *Sci. Rep.* **6**, 33859 (2016)
- 92 Jiang, Y. *et al.* Landau Quantization in Coupled Weyl Points: A Case Study of Semimetal NbP. *Nano Lett.* **18**, 7726-7731 (2018)

- 93 Gooth, J. *et al.* Experimental signatures of the mixed axial–gravitational anomaly in the Weyl semimetal NbP. *Nat.* **547**, 324-327 (2017)

## APPENDIX B

**Novel synthesis and processing effects on the figure of merit for NbCoSn, NbFeSb,  
and ZrNiSn based half-Heusler thermoelectrics**

**Novel synthesis and processing effects on the figure of merit for NbCoSn, NbFeSb,  
and ZrNiSn based half-Heusler thermoelectrics**

This Appendix is published by Elsevier in the *Journal of Solid State Chemistry* and should be referenced appropriately.

Reference:

S. V. Pedersen, J. R. Croteau, N. Kempf, Y. Zhang, D. P. Butt, B. J. Jaques, “Novel synthesis and processing effects on the figure of merit for NbCoSn, NbFeSb, and ZrNiSn based half-Heusler thermoelectrics.” *JSSC*. **285** 121203 (2020)

Reproduced/modified by permission of Elsevier.

\*This chapter includes formatting modifications from the originally published version.

Novel synthesis and processing effects on the figure of merit for NbCoSn, NbFeSb, and  
ZrNiSn based half-Heusler thermoelectrics

Samuel V. Pedersen<sup>a,b</sup>

Joseph R. Croteau<sup>a,b</sup>

Nicholas Kempf<sup>a,b,c</sup>

Yanliang Zhang<sup>a,b,c</sup>

Darryl P. Butt<sup>a,b,d</sup>

Brian J. Jaques<sup>a,b</sup>

Published in:

Journal of Solid State Chemistry

January 2020

<sup>a</sup>Micron School of Materials Science and Engineering, Boise State University,  
Boise, ID 83725, USA

<sup>b</sup>Center for Advanced Energy Studies, Idaho Falls, ID 83401, USA

<sup>c</sup>Department of Aerospace and Mechanical Engineering, University of Notre Dame,  
Notre Dame, IN, 46556, USA

<sup>d</sup>College of Mines and Earth Sciences, University of Utah,  
Salt Lake City, UT, 84112, USA.

## Abstract

The n-type NbCoSn, ZrNiSn and p-type NbFeSb half-Heuslers are promising thermoelectric materials with high figures of merit (ZT) for applications between 575 and 1000 K. By eliminating hafnium and utilizing low cost scalable production methods, the widespread commercialization of high temperature thermoelectrics could be achieved. In this work, half-Heuslers containing refractory metals (Nb and Zr) were produced by high energy planetary ball milling and their thermoelectric performance compared to half-Heuslers prepared by the conventional arc-melting synthesis route. Starting materials, as-milled powders, and consolidated samples were characterized by XRD, SEM, and EDS. The thermoelectric performance parameters were characterized using simultaneous Seebeck and electrical resistivity measurements and laser flash analysis. The mechanically alloyed NbCoSn and NbFeSb achieved ZT of approximately 0.53 (873 K) and 0.72 (873 K), respectively, comparing well to literature and prepared arc-melted monoliths. The results demonstrate mechanical alloying as a viable synthesis technique for refractory metal containing half-Heusler thermoelectrics.

## B.1 Introduction

Since the late 1990's, interest continues to grow in the thermoelectric compounds known as half-Heuslers, named based on their unique crystal structure. These materials are typified by high Seebeck coefficient ( $S$ ) and electrical conductivity ( $\sigma$ ) and operate in the temperature ( $T$ ) range of 575-1000 K while retaining good mechanical strength and thermal stability.<sup>1-4</sup> Half-Heuslers have, however, been unable to achieve high figures of merit (ZT) above a value of 2 because of their high thermal conductivity ( $\kappa$ ) (7-9 Wm<sup>-1</sup>K<sup>-1</sup>).<sup>3,4</sup> The performance of a thermoelectric material relies directly on the ratio of several

material properties given by the expression  $ZT = S^2\sigma T/\kappa$ , which is a ratio between the electrical power and thermal conductivity.<sup>2</sup> Of the half-Heuslers, the most studied have been of the (M)NiSn and the (M)CoSb type compounds, where (M = Hf, Zr, or Ti).<sup>3-6</sup> By optimizing the intermetallic compositions and carrier dopant concentrations, ZT values within the range of 1-1.5 are routinely achievable in the n-type (M)NiSn<sub>1-x</sub>Sb<sub>x</sub> when prepared by the sequential process of arc-melting powder into an ingot, crushing and milling the ingot into powder, and then consolidating the powder by hot-pressing or spark plasma sintering (SPS).<sup>3,4</sup> Recent work with the TaFeSb half-Heusler synthesized by ball milling and hot pressing demonstrated a ZT of 1.5 at 973 K.<sup>7</sup> Generally, p-type half-Heuslers of the (M)CoSb<sub>1-x</sub>Sn<sub>x</sub> compositions suffer from low carrier mobility and have not achieved the same levels of success as their n-type counterparts.<sup>4,6</sup> Significant reductions in thermal conductivity (resulting in increased performance, ZT) by phonon scattering from point defects, nano-inclusions, and interfaces within nano-grained materials have been demonstrated<sup>2-5,8-17</sup> and the half-Heusler compounds are moving ever-closer to the presumed minimum ZT of 2 necessary for widespread commercialization.<sup>3,17</sup>

Although the (M)NiSn and (M)CoSb type compounds have received the most attention, there are nearly a hundred other half-Heusler compounds.<sup>18</sup> In the last decade, advancements in computational materials science have led to rapid discoveries from materials-by-design approaches. First principle calculations applied to half-Heuslers have been used to explain the semi-conducting behavior observed in these compounds<sup>6</sup>, and have been used to screen new, potentially high-performing compositions.<sup>19,20</sup> Of those compounds, compositions with 18 valence electrons per unit cell (VEC) should be

narrow band-gap semiconductors and have potentially promising thermoelectric properties. Using the 18 VEC criteria, Yang et al. evaluated the thermoelectric properties of more than thirty half-Heusler compounds using an ab initio approach.<sup>20</sup> Half-Heusler compounds with the compositions NbCoSn and NbFeSb stand out among those calculated, having higher power factors,  $PF = S^2\sigma$ , compared to the traditional n-type (M)NiSn and p-type (M)CoSb. Table 1 compares experimentally reported peak thermoelectric performance ( $ZT$ ) in select Nb-based half-Heusler compositions with the corresponding synthesis routes. Our results, using high energy planetary ball milling (HEPBM), are also included and are comparable to the  $ZT$  results of half-Heuslers obtained by conventional synthesis routes.

The advantage of HEPBM is the scalable production of large quantities of phase pure powder consisting of high and low melting temperature elements without evaporative loss and resultant stoichiometry deficiencies which occur in solid state, arc-melting, optical zone floating, and levitation melting synthesis methods.<sup>4</sup> Pioneering work by J. S. Benjamin at the INCO company demonstrated mechanical alloying for oxide dispersion strengthened nickel superalloys at the 10's of kg scale using a commercial Model 100-S attrition mill (Szegvari) while larger production mills could operate at the 100's of kg scale.<sup>21</sup>

Under optimal milling conditions, nano-grained powders with reduced particle size and increased surface areas can be produced which enable a reduction in sintering time when rapid sintering methods such as SPS are used. The resulting monoliths will retain the nanostructure that improves phonon scattering and results in a lower thermal conductivity.<sup>22</sup> Increasing the number of grain boundaries improves phonon scattering

with minimal impact to the electrical conductivity due to differences in phonon versus electron mean free paths; the overall effect is an increase in the ZT.<sup>23-25</sup>

Previous studies investigating the  $\text{Ti}_x\text{Zr}_{1-x}\text{NiSn}$  alloys indicate an inability to obtain a phase pure half-Heusler via planetary ball milling.<sup>26,27</sup> However, a few reports indicate other zirconium-based half-Heuslers, such as  $\text{Zr}_{0.5}\text{Hf}_{0.5}\text{Co}_{0.4}\text{Rh}_{0.6}\text{Sb}_{1-x}\text{Sn}_x$  or  $\text{Zr}_{0.5}\text{Hf}_{0.5}\text{Ni}_{0.8}\text{Pd}_{0.2}\text{Sn}_{0.99}\text{Sb}_{0.01}$  can be mechanically alloyed such that zirconium substitutes into the half-Heusler structure but these still had minor impurities from the milling process ( $\text{HfO}_2$  and  $\text{CoSb}$ ).<sup>28,29</sup>

This work first presents a milling study that evaluates the minimum intensity and duration required to achieve a phase pure half-Heusler  $\text{Ti}_{0.75}\text{Zr}_{0.25}\text{Ni}_{0.98}\text{Sn}_{0.02}$  powder. It is important to note that further milling at longer durations or higher intensity than necessary for conversion/ alloying leads to increased levels of contamination and can degrade the performance of the alloy.<sup>30</sup> While the milling intensity is a function of multiple variables, the most studied are the milling media material and size, ball to powder charge ratio, vessel and flywheel rotation speeds, and vial filling ratio.<sup>30</sup> This research investigates optimization of alloy synthesis via milling intensity by altering the rotation speed and milling duration while keeping the other variables constant.

The current work demonstrates, hafnium-free  $\text{NbCoSn}$ ,  $\text{NbFeSb}$ , and  $\text{Ti}_x\text{Zr}_{1-x}\text{NiSn}$  based half-Heusler alloys synthesized by mechanical alloying via high energy planetary ball milling followed by consolidation with spark plasma sintering. The work presented here compares the mechanically alloyed half-Heuslers to those produced by conventional methods and demonstrates that comparable performance is achieved for  $\text{NbCoSn}$ . Improvements for the milling operation are recommended to close the performance gap

between the traditionally fabricated and state of-the-art  $\text{Ti}_x\text{Zr}_{1-x}\text{NiSn}$  and  $\text{NbFeSb}$  thermoelectrics.

## B.2 Materials and Methods

### B.2.1 Powder synthesis

Three synthesis routes were compared for the half-Heusler compounds with the structures XYZ ( $X = \text{Nb, Ti, Hf}$ ;  $Y = \text{Co or Fe}$ ,  $Z = \text{Sn and Sb}$ ) and  $\text{XNiY}$  ( $X = \text{Ti, Zr, Hf}$ ;  $Y = \text{Sn, Sb}$ ). Monoliths were prepared from (1) arc-melted and crushed powder, (2) arc-melted powder further refined by ball milling, and (3) mechanically alloyed powders. The arc-melted ingots were produced from nominal amounts of the elemental powders (with 5 wt% extra Sn to account for evaporative loss<sup>4</sup>) that were then homogenized, crushed, and sintered by spark plasma sintering; these are referred to as arc-melted monoliths (AM). Details for the arc-melting method is presented elsewhere.<sup>31</sup> The mechanically alloyed monoliths (MA) were produced by HEPBM using a total of 15 g of the stoichiometric amounts of elemental powders (All powders: Alfa Aesar, 99.5% pure or greater, 60 mesh or finer) using a milling profile of 4 h at 350 rpm, 24 h at 500 rpm, and 1 h at 350 rpm. The refined arc-melted monoliths (RAM) were produced with the addition of a mechanical milling step at 500 rpm for 12 h followed by sintering by SPS. All milling for both the RAM and MA samples was performed in a high-energy planetary ball mill (Retsch PM100). The powders were loaded into a 250 mL hardened-steel milling vessel inside an argon glovebox (<10 ppm of  $\text{O}_2$ ) with 5 mm diameter 440C stainless steel balls to achieve a 10:1 ball-to-powder ratio (BPR). The vessel was sealed, transferred out of the glovebox, and milled continuously with the vessel switching direction of rotation at 10-min intervals. For the  $\text{Ti}_x\text{Zr}_{1-x}\text{NiSn}_{1-y}\text{Sb}_y$  milling study, the

milling vessel, powder charge, and media configuration was kept constant while the milling intensity was varied from 200 to 500 rpm and the duration was varied between 1 and 6 h with 10-min switching intervals.

### B.2.2 Monolith synthesis

The synthesized powders (AM, MA, RAM) were loaded into grafoil lined (99.8%, Alfa Aesar, USA) 12.5 mm bore diameter graphite dies (I85, Electrodes Inc) and compacted using 30 MPa of applied pressure in the SPS (Dr. Sinter SPS-515S). After achieving a vacuum (<75 millitorr), 100 MPa of pressure was applied at the start of the temperature ramp which increased at a rate of 150 K/min to 1250 K. The temperature and pressure were held for 10 min before the pressure was released and the sample cooled naturally to ambient temperature. Temperature was measured with a K-type thermocouple inserted into a hole bored halfway through the wall of the graphite die. Further details on SPS sintering profiles for half-Heuslers are presented elsewhere.<sup>32</sup>

### B.2.3 Characterization methods

Powder x-ray diffraction (XRD) data ( $\text{CuK}\alpha$ , Rigaku MiniFlex 600) was obtained on 0.1 g of powder mixed with vacuum grease to prevent oxidation and self-ignition; the grease adds a small amorphous background at low angles. Particle size analysis (Horiba LA-950) was obtained with powders dispersed in water. All monoliths were prepared for microscopy by grinding with SiC grit paper and polished with water-based polycrystalline diamond suspensions. Grain structure was revealed by submerging in Marble's reagent (50 mL H<sub>2</sub>O, 50 mL HCl, 10 g CuSO<sub>4</sub>) for 10 s, then rinsing with

deionized water, sonicating in isopropyl alcohol, and compressed air drying. Monolith density was obtained using the Archimedes method in water. Monolith XRD was obtained on polished, un-etched pellets and compared to reference diffraction files from the Inorganic Crystal Structure Database (ICSD) for phase identification. Rietveld refinement using crystallographic information files from ICSD modified to account for the targeted stoichiometry was performed for the mechanically alloyed powders and sintered monoliths. Optical microscopy (OM) (Olympus B-51) and scanning electron microscopy (SEM) (Hitachi S-3400 N or Teneo Field Emission SEM) with energy dispersive x-ray spectroscopy (EDS) data on microstructure, morphology, and stoichiometry were obtained on etched pellets. Grain size was determined using the linear intercept method from OM and SEM images. The parallel faces of 12.5 mm diameter disks were ground using 1200 grit SiC to a thickness of approximately 1.5 mm and coated using an aerosol spray graphite powder. Temperature dependent thermal diffusivity was measured with a laser flash apparatus (LFA) (Linseis LFA 1000). The thermal conductivity was determined using the measured diffusivity, the measured density, and the calculated specific heat of the compound estimated by the Kopp-Neumann law<sup>33-36</sup> and the published values of specific heat in either the JANAF<sup>37</sup> or Barin tables.<sup>38</sup> Rectangular bars were cut from monoliths that measure approximately 1.5 x 1.5 x 12 mm<sup>3</sup> (T x W x L). The temperature-dependent Seebeck coefficient and electrical resistivity were measured simultaneously with a commercial device (Linseis LSR-3 Seebeck).

## B.3 Results

### B.3.1 Half-Heusler powder characterization

In order to study the effect of milling intensity, the mechanochemical synthesis of the  $\text{Ti}_{0.75}\text{Zr}_{0.25}\text{NiSn}_{0.98}\text{Sb}_{0.02}$  powders at different milling rpm was investigated. As seen in the top half of the XRD patterns in **Figure B.1**, a milling speed of 400 rpm is necessary for synthesis of the half-Heusler phase. The bottom half of **Figure B.1** shows a time study at a constant milling speed of 500 rpm which shows half-Heusler conversion after 3 h of milling. Below a milling intensity of 400 rpm, the formation of the half-Heusler crystal structure is not achieved. The loose powder sampled after 6 h of milling consisted of primarily unalloyed nickel with small amounts of tin. The result from the investigation on  $\text{Ti}_{0.75}\text{Zr}_{0.25}\text{NiSn}_{0.98}\text{Sb}_{0.02}$  (500 rpm threshold, minimum of 6 h) was applied to the synthesis of the NbCoSn and NbFeSb alloys. As seen in **Figure B.2**, ball milling at a speed of 500 rpm was sufficient produce the various half-Heusler powders except for the  $\text{Hf}_{0.25}\text{Zr}_{0.75}\text{NiSn}_{0.99}\text{Sb}_{0.01}$  composition. The characteristic peak positions (slightly offset for each unique composition) match the reference NbFeSb powder diffraction file. Even after milling for 24 h at 500 rpm, the hafnium peaks still persist in the  $\text{Hf}_{0.25}\text{Zr}_{0.75}\text{NiSn}_{0.99}\text{Sb}_{0.01}$  pattern. As seen in **Figure B.3**, a representative Rietveld refinement on the  $\text{Nb}_{0.75}\text{Ti}_{0.25}\text{FeSb}$  mechanically alloyed powder shows good agreement with the targeted composition while the lattice parameter obtained ( $a = 5.95 \text{ \AA}$ ) is in good agreement with value reported elsewhere ( $a = 5.90 \text{ \AA}$ ).<sup>39</sup> Provided within the supplemental information file, are additional Rietveld refinements on each mechanically alloyed half-Heusler that show good agreement with the targeted compositions. Slight deviations in peak intensities between the (111) (200) and (220) can be attributed to site

disorder wherein the constituent elements swap lattice positions.<sup>24</sup> Additionally, incomplete anti-site filling can also result in deviations from the theoretical peak intensities.<sup>24</sup> The high backgrounds at low angles in the powder refinements are due to the presence of the amorphous vacuum grease used to prevent rapid oxidation of the finely sized powders.

To compare the effect of ball milling for particle size reduction, the half-Heusler powders synthesized by arc-melting were ball milled for 12 additional hours at a milling speed of 500 rpm. As seen in **Figure B.4** for the  $\text{Nb}_{0.75}\text{Ti}_{0.25}\text{FeSb}$  half-Heusler powders, the particle size distribution is reduced progressively with the mechanically alloyed powder having the narrowest distribution. Additionally, SEM images of the  $\text{Nb}_{0.75}\text{Ti}_{0.25}\text{FeSb}$  arc-melted and refined powders show the clear difference in particle sizes with large 100- $\mu\text{m}$  sized particles only present in the arc-melted powders.

### B.3.2 Half-Heusler microstructural characterization

To produce bulk monoliths for thermoelectric characterization, the mechanically alloyed powders (milled at 500 rpm for at least 6 h) were consolidated via SPS at 1250 K for 10 min. The resultant phases of the sintered monoliths produced from the mechanically alloyed powders are shown in **Figure B.5** along with markers for each phase reference. Since the same milling profile was used for all the alloys, the synthesis was not optimized for each specific alloy. As a result, each alloy contains minor amounts of unalloyed or binary phases which could be mitigated by extending the milling duration. On the other hand, repeated attempts to incorporate Hf into either ZrNiSn or

NbFeSb proved unsuccessful. The NbCoSn, NbFeSb and (Hf,Zr)NiSn alloys were further characterized for their microstructure and studied for their thermoelectric performance.

The microstructure and homogeneity of the half-Heusler alloys were examined to verify the elemental distribution and relative grain sizes. The impurities detected in the XRD patterns in **Figure B.5**, were clearly seen in the SEM and EDS mapping of the alloys. As shown in **Figure B.6** for the  $\text{Ti}_{0.75}\text{Zr}_{0.25}\text{NiSn}_{0.98}\text{Sb}_{0.02}$  monolith, the elemental maps show clustering of zirconium (that overlaps with oxygen) and iron with some minor inhomogeneity of the other elements. Rietveld refinement of each monolith produced from mechanically alloyed powders also indicates that the intended half-Heusler is the primary phase (typically greater than 95%) with the exception of the hafnium containing alloy (included in the supplementary file). Additionally, the lattice parameter for each alloy corresponds to the smaller half-Heusler unit cell.<sup>40,41</sup>

As previously stated, an advantage of mechanical alloying followed by rapid spark plasma sintering is the production of fine-grained or submicron grain structure which has been shown to increase  $ZT$  by lowering the thermal conductivity.<sup>22</sup> As evidenced by **Figure B.7** the fractured and polished surfaces of the n-type  $\text{NbCoSn}_{0.9}\text{Sb}_{0.1}$  reveal a nanostructured microstructure with an average grain size of  $300 \pm 40$  nm as calculated by the ASTM E112 linear intercept method.<sup>42</sup> Under the same sintering profile of 1250 K at 100 MPa for 10 min, the other alloys have larger micron sized grains.

The most common method of producing half-Heuslers containing refractory metals is arc-melting, while few reports of mechanical alloying have been produced. Often, in order to improve homogeneity of the powders and to reduce the crystallite size

within the powders before sintering, the arc-melted ingot is crushed and mechanically milled to produce sub-micron grained powders.<sup>4,16,17,31</sup> Within **Figure B.8**, for the  $\text{Nb}_{0.75}\text{Ti}_{0.25}\text{FeSb}$  composition, the XRD and SEM results for the three synthesis routes after SPS show the half-Heusler phase is obtained with comparable grain sizes between the ball mill refined arc-melted and mechanically alloyed starting powders. The monolith produced by the ball mill refined arc-melted powders shows a bimodal grain size distribution with large micron sized grains surrounded by much smaller submicron grains. Ideally, the presence of nanometer grains should suppress the thermal conductivity to a greater extent than the electrical conductivity. A small Fe peak ( $44^\circ$ ) in the mechanically alloyed pattern appeared after sintering, either unalloyed Fe or as a decomposition of the  $\text{Nb}_{0.75}\text{Ti}_{0.25}\text{FeSb}$  structure. The arc-melting of powders often produces an inhomogeneous ingot which is evidenced by the impurity peaks (Fe, Nb,  $\text{FeSb}_2$ ,  $\text{Nb}_5\text{Sb}_4$ ,  $\text{NbSb}_2$  phases).

### B.3.3 Thermoelectric performance comparison

The choice of synthesis route affected the overall ZT performance achieved for each n- and p-type half-Heusler. **Figure B.9** shows the figure of merit (ZT) of the different synthesis routes and compositions while Table 2 lists the peak ZT value and temperature. The three synthesis routes compared including AM powders, RAM powders, and MA powders that were spark plasma sintered to produce monoliths. A higher ZT value indicates a higher expected conversion efficiency.

The Seebeck coefficients as a function of temperature for both n-type

and p-type are plotted on an absolute scale in **Figure B.10**. The general trend observed is an increase of the Seebeck with increasing temperature with a peak maximum near 800 K for most of the alloys.

The thermal conductivity as a function of temperature for the half-Heuslers are shown in **Figure B.11**. The general trend observed is a decrease in thermal conductivity with increasing temperature. A similar trend is observed for electrical conductivity that decreases with increasing temperature as shown in **Figure B.12**. The power factors ( $PF = S^2\sigma$ ) also increase to a maximum with increasing temperature as a direct outcome of its dependence on the square of the Seebeck coefficients as shown in **Figure B.13**.

#### **B.4 Discussion**

Overall, to the best of the author's knowledge, this is the first report of the synthesis of the n-type  $\text{NbCoSn}_{1-x}\text{Sb}_x$  (ZT of 0.53 at 773 K) and p-type  $\text{Nb}_{1-x}\text{Ti}_x\text{FeSb}$  (ZT of 0.72 at 773 K) half-Heuslers exclusively by mechanical alloying in a high energy planetary ball mill starting from elemental powders. Furthermore, these mechanically alloyed half-Heuslers achieve peak ZT values at 773 K approaching the values obtained by the traditional arc-melting synthesis route as noted in Table 2.

This work demonstrates mechanical alloying via high energy planetary ball milling as viable synthesis route for refractory metal half-Heuslers. Furthermore, it represents a synthesis route that can, in a single step, produce the half-Heusler alloy and reduce the crystallite size of the powders which can be preserved as nanostructured grains via rapid consolidation with spark plasma sintering. As noted before, grain size reduction

into the sub-micron regime can enhance the overall ZT by preferentially suppressing phonon transport with limited reduction in electrical conduction.

The  $\text{Ti}_{0.75}\text{Zr}_{0.25}\text{NiSn}_{0.98}\text{Sb}_{0.02}$  milling intensity study (**Figure B.1**) determined that a milling speed of 400 rpm was required for appreciable alloying of the various elements into the half-Heusler crystal structure within 6 h. Generally, higher milling speeds increase the kinetic energy of impacts reducing the time to conversion. However, from a practical standpoint, a trade-off exists between milling efficiency, media and vessel wear, and powder contamination. In this case, the half-Heuslers were synthesized at 500 rpm for 24 h to improve the efficiency of mechanical alloying and for particle size reduction. Under the same conditions for milling and sintering the NbCoSn alloy which had a grain size of  $300 \pm 40$  nm (24 h milling at 500 rpm, sintered at 1250 K for 10 min), the  $\text{Nb}_{0.75}\text{Ti}_{0.25}\text{FeSb}$  contained larger 5-10  $\mu\text{m}$  sized grains whereas the  $\text{Ti}_{0.75}\text{Zr}_{0.25}\text{NiSn}_{0.98}\text{Sb}_{0.02}$  consisted of  $1.07 \pm 0.30$   $\mu\text{m}$  grains (**Figure B.7**). According to Suryanarayana, particle size reduction generally begins after alloy formation and homogenization, which are governed by solubility, formation energy of the intermetallic, and melting temperatures of the constituent elements.<sup>43</sup> The extent of grain refinement is then dependent upon milling conditions, alloy compositions, grain boundary energy, melting point, and defect creation/recovery rates.<sup>43-45</sup> Likewise, grain growth during sintering will also be material dependent. The main criteria for sintering was to achieve high densification (greater than 95%) with the shortest holding time. The result for the  $\text{NbCoSn}_{0.9}\text{Sb}_{0.1}$  demonstrates the feasibility of obtaining a nanostructured monolith. A systematic study investigating the crystallite size of milled powders before sintering as a function of milling intensity for the various compositions is recommended.

During mechanical milling, the metals will coat the media and vessel and through repeated impacts cold welding will occur. As a result, alloying of iron from the stainless-steel media into the powders will also occur and can have detrimental effects on thermoelectric performance. Unalloyed iron increases the metallic character of the monolith, increasing both the thermal and electrical conductivities, and in turn lowering the ZT. The poor performance of the  $\text{Ti}_{0.75}\text{Zr}_{0.25}\text{NiSn}_{0.98}\text{Sb}_{0.02}$  mechanically alloyed monolith is due to low electrical conductivity and low Seebeck coefficient arising from the formation of zirconium oxide and iron contamination introduced by the stainless-steel media and vessel as can be seen in the EDS maps of **Figure B.6**. In particular, this characterization shows the presence of oxygen and iron from the ball milling process along with minor amounts of zirconium oxide which had negative impacts on the Seebeck coefficient and electrical conductivity and therefore a detrimental impact on the thermoelectric performance. Experimental work by Hohl et al.<sup>46</sup> demonstrated that substitution of iron for nickel dramatically reduced the Seebeck coefficient.

In general, the mechanically alloyed  $\text{Nb}_{0.75}\text{Ti}_{0.25}\text{FeSb}$  composition retains a higher thermal conductivity (about 33% larger than the refined and arc-melted products) while the Seebeck coefficient was relatively consistent across all the synthesis routes. Although the grain size is smaller in the mechanically alloyed product than either of the arc-melted products (average size approximately 5  $\mu\text{m}$  versus 20  $\mu\text{m}$ , respectively), the thermal conductivity was not reduced substantially; such an effect is not often observed unless the grain size distribution is sub-micron.<sup>22</sup> The other mechanically alloyed composition,  $\text{Nb}_{0.6}\text{Ti}_{0.4}\text{Sb}_{0.95}\text{Sn}_{0.05}$ , achieved a lower ZT of 0.47 at 873 K than the product achieved through the ball mill refined arc-melting route<sup>31</sup> with ZT of 0.80 at 873 K. While the

Seebeck coefficient of the mechanically synthesized material was indeed higher ( $250 \mu\text{VK}^{-1}$ ) than the refined arc-melted product ( $177 \mu\text{VK}^{-1}$ ), so too were both the thermal conductivity ( $6.31$  vs  $4.6 \text{ WmK}^{-1}$ ) and the electrical resistivity ( $19.01$  vs  $6.8 \mu\Omega\text{m}$ ).

Mechanical alloying generally achieved lower ZT values while refinement of arc-melted powders by additional ball milling generally produced comparable results to unmilled arc-melted samples. The mechanically alloyed half-Heuslers generally have lower peak ZT values which can be attributed to either a low Seebeck coefficient, **Figure B.10**, or high thermal or low electrical conductivities, **Figure B.11** and **Figure B.12**, respectively. The notable exception is the mechanically alloyed  $\text{NbCoSn}_{0.9}\text{Sb}_{0.1}$  alloy which obtained a peak ZT of 0.54 at 773 K as compared to the reference refined arc-melted alloy of the same composition which had a similar ZT of 0.50 at 773 K. As Table 2 shows, the peak ZT values of the mechanically alloyed  $\text{NbCoSn}_{0.9}\text{Sb}_{0.1}$  and  $\text{Nb}_{0.75}\text{Ti}_{0.25}\text{FeSb}$  are comparable to the arc-melted values. The effect of a lower thermal conductivity and higher Seebeck offset the reduced electrical conductivity in the mechanically synthesized  $\text{NbCoSn}_{0.9}\text{Sb}_{0.1}$  compound. The reduced thermal conductivity may be attributed to phonon-scattering across grain boundaries in the nano-grained monolith (average grain size  $300 \pm 40 \text{ nm}$ ). The reduction in electrical conductivity is likely influenced by the minor secondary phases present. Incomplete alloying could be improved by additional milling time or other factors that increase the cumulative impact energy a given powder particle experiences throughout a milling cycle while refinement in the sintering parameters may prevent the decomposition. For the mechanically alloyed  $\text{Nb}_{0.75}\text{Ti}_{0.25}\text{FeSb}$  monolith, the uniform micron sized grains did not reduce the thermal conductivity. The mechanically refined and mechanically alloyed powders appear to be

nearly phase pure and match the reference NbFeSb (PDF 01-087-2169). Removal of minor impurity phases is often achieved by lengthy homogenization thermal treatments (2 weeks at 1250 K, sealed under argon).<sup>40,41,47</sup>

For the (M)NiSn derivatives (M = Ti, Zr, Hf), these results indicate that further optimization of the high energy ball milling process is required. As stated earlier, the attempts to alloy Hf into ZrNiSn and NbFeSb by high energy planetary ball milling did not incorporate appreciable amounts of hafnium; rather Zr alloyed into TiNiSn with small amounts of zirconium oxide detected. The low ZT of the mechanically alloyed  $\text{Hf}_{0.25}\text{Zr}_{0.75}\text{NiSn}_{0.99}\text{Sb}_{0.01}$  alloy is due to the low Seebeck coefficient which reached a peak value of  $80 \mu\text{VK}^{-1}$  whereas the arc-melt alloy had a peak at  $200 \mu\text{VK}^{-1}$ . The lack of alloying of hafnium into the half-Heusler crystal resulted in an inadequate carrier concentration which greatly reduced the Seebeck coefficient. Furthermore, titanium can contain up to 33 atomic % oxygen within its lattice at 1000 K while zirconium can contain up to 35 atomic % at 2338 K and when incorporated into a half-Heusler, the oxygen may decompose the TiNiSn into nickel tin compounds and  $\text{TiO}_2$  or  $\text{ZrO}_2$ .<sup>48,49</sup> Any oxygen present will preferentially bind to zirconium as it has a higher affinity to oxygen. Within the literature<sup>26-29</sup>, synthesis of Hf- or Zr- substituted TiNiSn compounds have been performed in tungsten carbide vessels and media to eliminate the iron contamination but the trade-off exists in that harder media may simply fracture and embed into the softer metals and can be present at sufficient concentration to be detectable by XRD.<sup>30</sup>

Mechanical alloying of refractory metals including niobium, titanium and zirconium via high energy ball milling within the milling configuration evaluated (10:1

BPR, 250 mL stainless steel vessel, 5 mm diameter 440C media, 15 g powder charge) was demonstrated successfully while the incorporation of hafnium has proven challenging and was not successful in this work; presumably due to its high melting temperature (2506 K).<sup>30</sup> However, considering the successful formation of a niobium based half-Heusler (melting temperature of 2750 K) (NbCoSn) via mechanical alloying, the higher melting temperature of hafnium alone cannot explain the resistance of hafnium to alloy into the half-Heusler intermetallic. Others have successfully demonstrated synthesis of tantalum<sup>7</sup>, zirconium<sup>50</sup> or hafnium-based half-Heusler using a different milling device (shaker mill) and configuration (lower BPR, media type and size, smaller powder charge) which changes the energy deposition due to differences in the kinematic behavior of planetary versus shaker ball mills.<sup>28-30,51</sup> Although not demonstrated in this work, it is postulated that use of the denser WC media of similar size (5 mm or 10 mm) would provide sufficient impact energy to alloy hafnium within a planetary ball mill.

## B.5 Conclusion

Synthesis of both n- and p-type half-Heusler thermoelectrics (NbFeSb and NbCoSn) containing high melting temperature refractory metals, Ti, Zr, and Nb were successfully produced by high energy planetary ball milling. While the ZT performance was less than typically reported for the conventional synthesis route of arc-melting, the thermoelectric performance of Nb<sub>0.75</sub>Ti<sub>0.25</sub>FeSb (ZT = 0.72 at 873 K) and NbCoSn<sub>0.9</sub>Sb<sub>0.1</sub> (ZT = 0.53 at 873 K) demonstrates these are potentially promising candidate thermoelectrics for intermediate service temperatures (575-1000 K). A comparison of synthesis routes show that arc-melting routes consistently produce higher ZT values and

that further optimization of the mechanical alloying process is necessary to produce similar performance. A minimum milling intensity (500 rpm, 3 h) was determined for the conversion of  $\text{Ti}_{0.75}\text{Zr}_{0.25}\text{NiSn}_{0.98}\text{Sb}_{0.02}$  half-Heusler and demonstrated that Zr-alloying by high energy ball milling is feasible. However, reduction in milling contamination by use of harder milling materials ( $\text{ZrO}_2$  or WC) is likely necessary to achieve comparable thermoelectric performance. Ideally, an optimized mechanical alloying synthesis route for nano-grained, phase pure powders would lower fabrication costs to enable competitive commercialization of thermoelectrics.

### **Acknowledgements**

This work has been partially funded by the US Department of Energy (award #DE-NE0008255). Bryan Forsmann at Boise State University is gratefully acknowledged for his valuable support at the Center for Advanced Energy Studies (Idaho Falls, ID). Dr. Zhifeng Ren (University of Houston, Houston, TX) is acknowledged for providing arc-melted powders. Materials were synthesized and processed in the Advanced Materials Lab (Boise State University, Boise, ID; Center for Advanced Energy Studies, Idaho Falls, ID). XRD and SEM was performed in the Boise State Center for Materials Characterization (Boise, ID).

### **Author Contributions**

Samuel V. Pedersen: Investigation, Formal analysis, Visualization, Writing - original draft, Writing - review & editing. Joseph R. Croteau: Investigation, Formal analysis, Conceptualization, Visualization, Writing - original draft, Writing - review & editing. Nicholas Kempf: Investigation, Data curation, Formal analysis. Yanliang Zhang: Funding acquisition, Project administration, Conceptualization. Darryl P. Butt: Funding

acquisition, Project administration. Brian J. Jaques: Funding acquisition, Project administration, Conceptualization, Supervision, Writing - review & editing, Resources.

### **Competing Interests**

The authors declare that they have no known competing financial interests or personal relationships that could have appeared to influence the work reported in this paper.

## References

- 1 Sootsman, J. R., Chung, D. Y. & Kanatzidis, M. G. New and old concepts in thermoelectric materials. *Angew Chem Int Ed Engl* **48**, 8616-8639 (2009)
- 2 Radousky, H. B. & Liang, H. Energy harvesting: an integrated view of materials, devices and applications. *Nanotechnol.* **23**, 502001, 502001 (2012)
- 3 Bos, J. W. & Downie, R. A. Half-Heusler thermoelectrics: a complex class of materials. *J Phys Condens Matter* **26**, 433201 (2014)
- 4 Chen, S. & Ren, Z. F. Recent progress of half-Heusler for moderate temperature thermoelectric applications. *Mater. Today* **16**, 387-395 (2013)
- 5 Chen, L. *et al.* Uncovering high thermoelectric figure of merit in (Hf,Zr)NiSn half-Heusler alloys. *Appl. Phys. Lett.* **107**, 1-5, 041902 (2015)
- 6 Zeier, W. G. *et al.* Engineering half-Heusler thermoelectric materials using Zintl chemistry. *Nat Rev Mater* **1**, 16032 (2016)
- 7 Zhu, H. *et al.* Discovery of TaFeSb-based half-Heuslers with high thermoelectric performance. *Nat. Commun.* **10**, 270 (2019)
- 8 Li, J. F., Liu, W. S., Zhao, L. D. & Zhou, M. High-performance nanostructured thermoelectric materials. *Npg Asia Mater* **2**, 152-158 (2010)
- 9 Snyder, G. J. & Toberer, E. S. Complex thermoelectric materials. *Nat Mater* **7**, 105-114 (2008)
- 10 Liu, W. S., Yan, X., Chen, G. & Ren, Z. F. Recent advances in thermoelectric nanocomposites. *Nano Energy* **1**, 42-56 (2012)
- 11 Joshi, G. *et al.* Enhancement in Thermoelectric Figure-Of-Merit of an N-Type Half-Heusler Compound by the Nanocomposite Approach. *Adv Energy Mater* **1**, 643-647 (2011)
- 12 Joshi, G. *et al.* Enhancement of thermoelectric figure-of-merit at low temperatures by titanium substitution for hafnium in n-type half-Heuslers Hf<sub>0.75-x</sub>Ti<sub>x</sub>Zr<sub>0.25</sub>NiSn<sub>0.99</sub>Sb<sub>0.01</sub>. *Nano Energy* **2**, 82-87 (2013)
- 13 Chen, L. D., Huang, X. Y., Zhou, M., Shi, X. & Zhang, W. B. The high temperature thermoelectric performances of Zr<sub>0.5</sub>Hf<sub>0.5</sub>Ni<sub>0.8</sub>Pd<sub>0.2</sub>Sn<sub>0.99</sub>Sb<sub>0.01</sub> alloy with nanophase inclusions. *J. Appl. Phys.* **99**, 1-6, 064305 (2006)
- 14 Bhattacharya, S. *et al.* Effect of Sb doping on the thermoelectric properties of Ti-based half-Heusler compounds, TiNiSn<sub>1-x</sub>Sb<sub>x</sub>. *Appl. Phys. Lett.* **77**, 2476-2478 (2000)
- 15 Szczech, J. R., Higgins, J. M. & Jin, S. Enhancement of the thermoelectric properties in nanoscale and nanostructured materials. *J. Mater. Chem.* **21**, 4037-4055 (2011)
- 16 Yan, X. *et al.* Enhanced thermoelectric figure of merit of p-type half-Heuslers. *Nano Lett.* **11**, 556-560 (2011)
- 17 Minnich, A. J., Dresselhaus, M. S., Ren, Z. F. & Chen, G. Bulk nanostructured thermoelectric materials: current research and future prospects. *Energ Environ Sci* **2**, 466-479 (2009)
- 18 Wong-Ng, W. & Yang, J. International Centre for Diffraction Data and American Society for Metals database survey of thermoelectric half-Heusler material systems. *Powder Diffr.* **28**, 32-43 (2013)

- 19 Page, A., Poudeu, P. F. P. & Uher, C. A first-principles approach to half-Heusler thermoelectrics: Accelerated prediction and understanding of material properties. *J Materomics* **2**, 104-113 (2016)
- 20 Yang, J. *et al.* Evaluation of Half-Heusler Compounds as Thermoelectric Materials Based on the Calculated Electrical Transport Properties. *Adv. Funct. Mater.* **18**, 2880-2888 (2008)
- 21 Gilman, P. S. & Benjamin, J. S. Mechanical alloying. *Ann. Rev. Mater. Sci.* **13**, 279-300 (1983)
- 22 Zhang, Y. *et al.* Lattice thermal conductivity diminution and high thermoelectric power factor retention in nanoporous macroassemblies of sulfur-doped bismuth telluride nanocrystals. *Appl. Phys. Lett.* **100**, 193113 (2012)
- 23 Gayner, C. & Kar, K. K. Recent advances in thermoelectric materials. *Prog Mater Sci* **83**, 330-382 (2016)
- 24 Graf, T., Felser, C. & Parkin, S. S. P. Simple rules for the understanding of Heusler compounds. *Prog Solid State Ch* **39**, 1-50 (2011)
- 25 Fitriani *et al.* A review on nanostructures of high-temperature thermoelectric materials for waste heat recovery. *Renew Sust Energ Rev* **64**, 635-659 (2016)
- 26 Karati, A. & Murty, B. S. Synthesis of nanocrystalline half-Heusler TiNiSn by mechanically activated annealing. *Mater. Lett.* **205**, 114-117 (2017)
- 27 Zou, M. M., Li, J. F., Du, B., Liu, D. W. & Kita, T. Fabrication and thermoelectric properties of fine-grained TiNiSn compounds. *J. Solid State Chem.* **182**, 3138-3142 (2009)
- 28 Maji, P. *et al.* Thermoelectric performance of nanostructured p-type  $Zr_{0.5}Hf_{0.5}Co_{0.4}Rh_{0.6}Sb_{1-x}Sn_x$  half-Heusler alloys. *J. Solid State Chem.* **202**, 70-76 (2013)
- 29 Misra, D. K. *et al.* Microstructure and Thermoelectric Properties of Mechanically Alloyed  $Zr_{0.5}Hf_{0.5}Ni_{0.8}Pd_{0.2}Sn_{0.99}Sb_{0.01}/WO_3$  Half-Heusler Composites. *Sci Adv Mater* **3**, 607-614 (2011)
- 30 Suryanarayana, C. Mechanical alloying and milling. *Prog Mater Sci* **46**, 1-184 (2001)
- 31 Joshi, G. *et al.* NbFeSb-based p-type half-Heuslers for power generation applications. *Energ Environ Sci* **7**, 4070-4076 (2014)
- 32 Zhang, Y., Butt, D. & Agarwal, V. Nanostructured Bulk Thermoelectric Generator for Efficient Power Harvesting for Self-powered Sensor Networks. Report No. INL/EXT-15-36260, 1-38 (Idaho National Lab. (INL), Idaho Falls, ID (United States), 2015).
- 33 Sekimoto, T., Kurosaki, K., Muta, H. & Yamanaka, S. Thermoelectric properties of Sn-doped TiCoSb half-Heusler compounds. *J Alloy Compd* **407**, 326-329 (2006)
- 34 Kawaharada, Y., Kurosaki, K., Muta, H., Uno, M. & Yamanaka, S. High temperature thermoelectric properties of  $CoNb_{1-M}Sn$  half-Heusler compounds. *J Alloy Compd* **384**, 303-307 (2004)
- 35 Leitner, J., Voňka, P., Sedmidubský, D. & Svoboda, P. Application of Neumann-Kopp rule for the estimation of heat capacity of mixed oxides. *Thermochim. Acta* **497**, 7-13 (2010)

- 36 Birkel, C. S. *et al.* Rapid Microwave Preparation of Thermoelectric TiNiSn and TiCoSb Half-Heusler Compounds. *Chem. Mater.* **24**, 2558-2565 (2012)
- 37 Chase, M. W., Jr. *NIST-JANAF thermochemical tables*. 4th edn, (American Chemical Society; American Institute of Physics for the National Institute of Standards and Technology, Washington, DC, 1998).
- 38 Barin, I. & Platzki, G. *Thermochemical data of pure substances*. 3rd edn, (VCH Publishers, New York, NY, 1995).
- 39 Ferluccio, D. A. *et al.* Low thermal conductivity and promising thermoelectric performance in  $A_x\text{CoSb}$  ( $A = \text{V, Nb or Ta}$ ) half-Heuslers with inherent vacancies. *J Mater Chem C* **7**, 6539-6547 (2019)
- 40 Ferluccio, D. A., Smith, R. I., Buckman, J. & Bos, J. G. Impact of Nb vacancies and p-type doping of the NbCoSn-NbCoSb half-Heusler thermoelectrics. *Phys. Chem. Chem. Phys.* **20**, 3979-3987 (2018)
- 41 Gürth, M. *et al.* Thermoelectric high ZT half-Heusler alloys  $\text{Ti}_{1-x-y}\text{Zr}_x\text{Hf}_y\text{NiSn}$  ( $0 \leq x \leq 1$ ;  $0 \leq y \leq 1$ ). *Acta Mater.* **104**, 210-222 (2016)
- 42 Baláž, P. *et al.* Hallmarks of mechanochemistry: from nanoparticles to technology. *Chem. Soc. Rev.* **42**, 7571-7637 (2013)
- 43 Froes, F. H., Suryanarayana, C., Russell, K. & Li, C. G. Synthesis of Intermetallics by Mechanical Alloying. *Mat Sci Eng A* **192**, 612-623 (1995)
- 44 Amornpitoksuk, P. & Suwanboon, S. Correlation of milling time on formation of TiCoSb phase by mechanical alloying. *J Alloy Compd* **462**, 267-270 (2008)
- 45 Delogu, F. & Cocco, G. Crystallite size refinement in elemental species under mechanical processing conditions. *Mat Sci Eng A* **422**, 198-204 (2006)
- 46 Hohl, H. *et al.* Efficient dopants for ZrNiSn-based thermoelectric materials. *J. Phys.: Condens. Matter* **11**, 1697-1709 (1999)
- 47 Fu, C. *et al.* Realizing high figure of merit in heavy-band p-type half-Heusler thermoelectric materials. *Nat Commun* **6**, 8144, 8144 (2015)
- 48 Berche, A. & Jund, P. Oxidation of half-Heusler NiTiSn materials: Implications for thermoelectric applications. *Intermetallics* **92**, 62-71 (2018)
- 49 Puchala, B. & Van der Ven, A. Thermodynamics of the Zr-O system from first-principles calculations. *Phys Rev B* **88**, 1-15, 094108 (2013)
- 50 Germond, J. D., Schilling, P. J., Takas, N. J. & Poudeu, P. F. P. Thermoelectric Performance of Nanostructured ZrNiSn Compounds Synthesized by Mechanical Alloying. *MRS Proceedings* **1267**, 1267-DD1203-1212, 1267-dd03-12 (2011)
- 51 Makongo, J. P. A., Zhou, X. Y., Misra, D. K., Uher, C. & Poudeu, P. F. P. Correlation between processing conditions, microstructure and charge transport in half-Heusler alloys. *J. Solid State Chem.* **201**, 280-287 (2013)
- 52 Ono, Y., Inayama, S., Adachi, H. & Kajitani, T. in *2006 25th International Conference on Thermoelectrics*. 124-127 (IEEE).
- 53 He, R. *et al.* Enhanced thermoelectric properties of n-type NbCoSn half-Heusler by improving phase purity. *Apl Mater* **4**, 1-9, 104804 (2016)
- 54 Kimura, Y., Tamura, Y. & Kita, T. Thermoelectric properties of directionally solidified half-Heusler compound NbCoSn alloys. *Appl. Phys. Lett.* **92**, 1-4, 012105 (2008)

## Figures

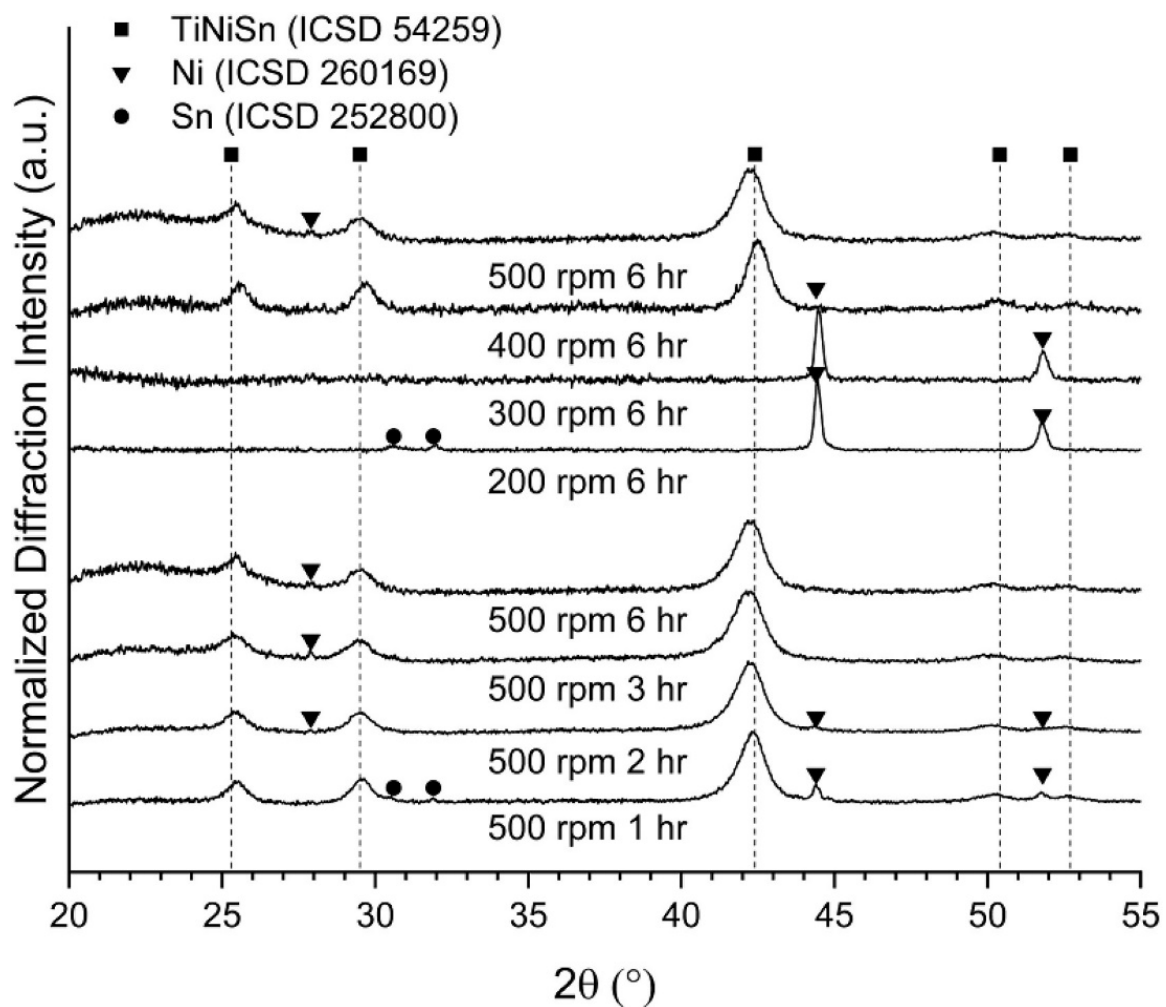


**Figure B.1** Normalized x-ray diffraction patterns of planetary ball milled  $\text{Ti}_{0.75}\text{Zr}_{0.25}\text{NiSn}_{0.98}\text{Sb}_{0.02}$  half-Heusler powders showing the effects of time and milling speed on phase conversion. Unalloyed phases are indicated by markers and characteristic half-Heusler peaks are indicated by vertical drop lines (shown for the half-Heusler TiNiSn).

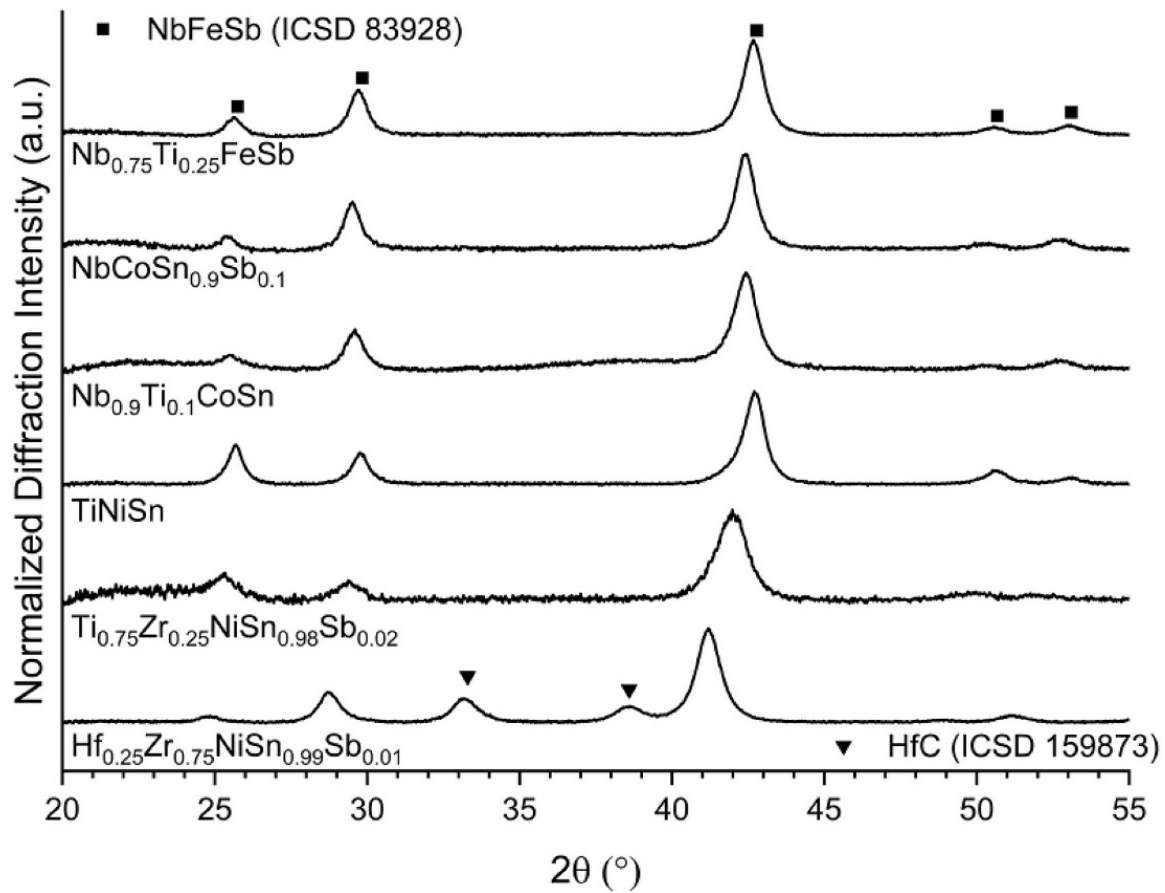


**Figure B.2** Normalized x-ray diffraction patterns of mechanochemically synthesized half-Heuslers powders. Characteristic peaks of the half-Heusler structure and impurity peaks are marked.

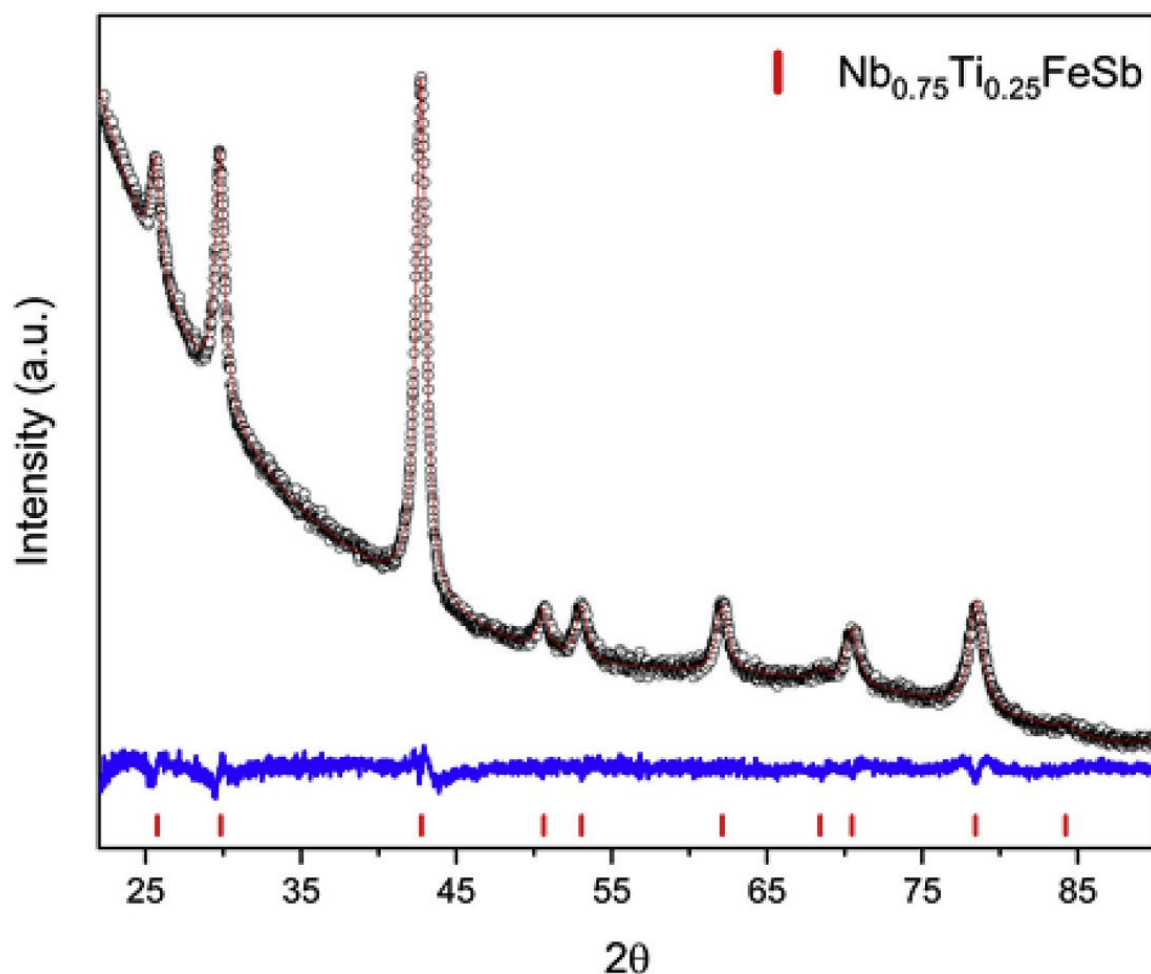


**Figure B.3** A typical powder x-ray diffraction Rietveld refinement result on the mechanically alloyed  $\text{Nb}_{0.75}\text{Ti}_{0.25}\text{FeSb}$  half-Heusler. Black circles are observed data, red lines are the calculated profiles, blue lines are difference curves (obs-calc). Vertical lines indicate Bragg reflection positions (phase indicated in figure).

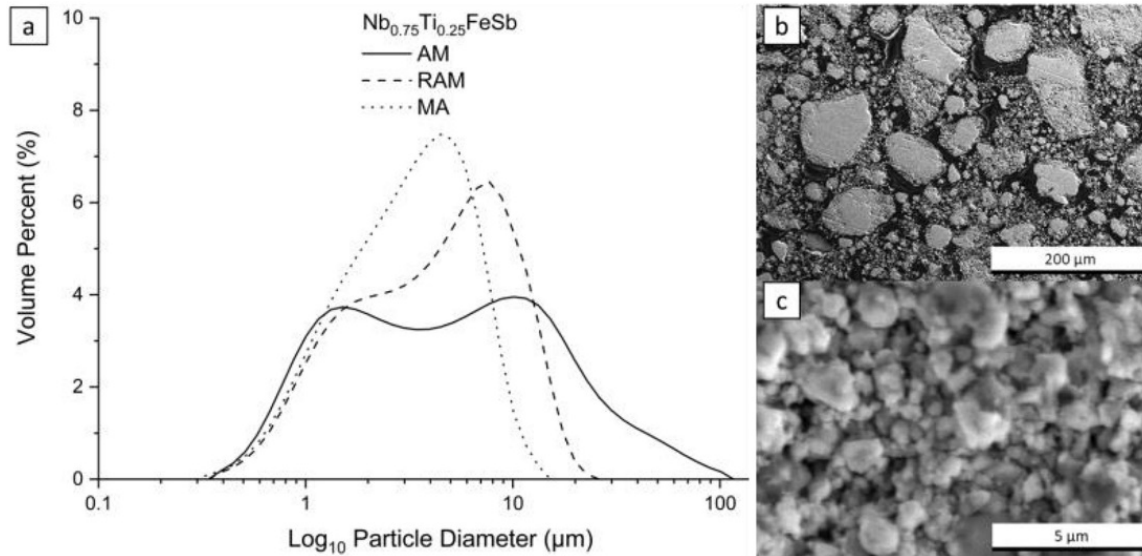


**Figure B.4** (a) Solution-based laser scattering particle size analysis of arc-melted (AM), ball mill refined arc-melted (RAM) and ball mill mechanically alloyed (MA) half-Heusler  $\text{Nb}_{0.75}\text{Ti}_{0.25}\text{FeSb}$  powders shows that the arc-melted powder size distribution is much broader while the ball milled samples have a narrower size distribution; SEM images of  $\text{Nb}_{0.75}\text{Ti}_{0.25}\text{FeSb}$  arc-melted powders before milling (b) and after refinement (c) by high energy ball milling.

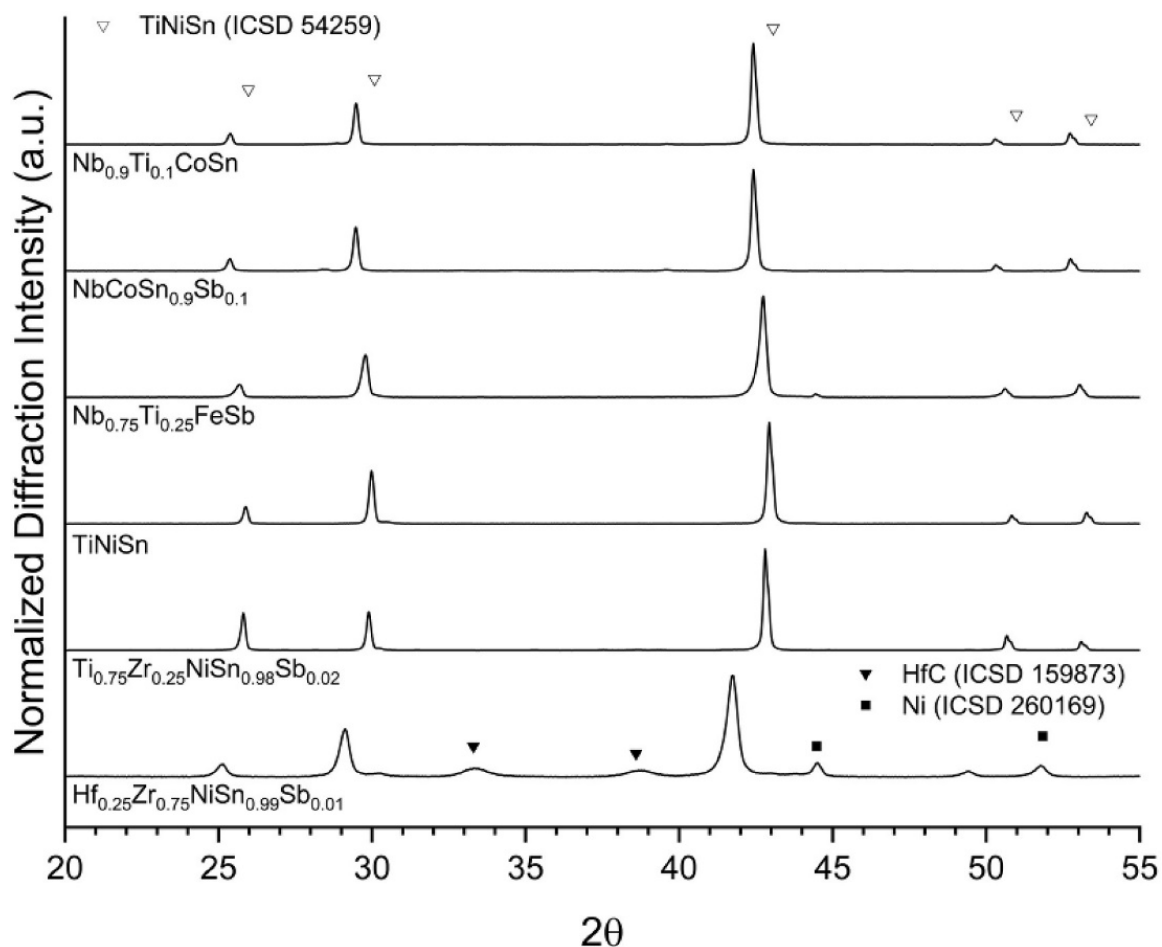


**Figure B.5** Normalized x-ray diffraction patterns of spark plasma sintered half-Heuslers synthesized by mechanically alloying in a planetary ball mill. Unalloyed starting elements and minor impurity peaks are marked. Characteristic peaks for a typical half-Heusler (TiNiSn) are indicated.

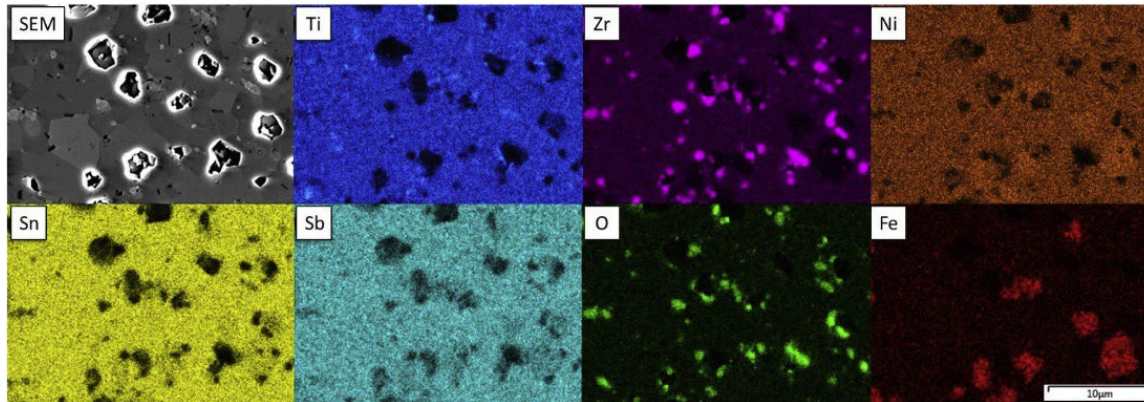


**Figure B.6** Chemical map of the surface of the  $\text{Ti}_{0.75}\text{Zr}_{0.25}\text{NiSn}_{0.98}\text{Sb}_{0.02}$  monolith (mechanically alloyed and SPS'd) showing the heterogeneous chemical structure of the alloy.

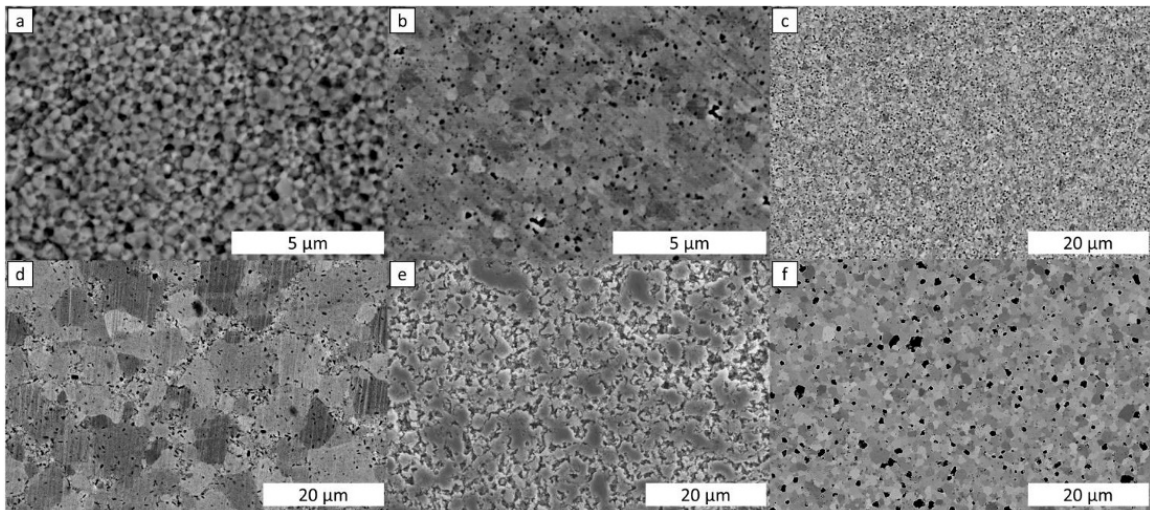


**Figure B.7** SEM micrographs of the microstructures obtained through MA and SPS of half-Heusler materials where (a) and (b) show the fracture surface and polished surface of  $\text{NbCoSn}_{0.9}\text{Sb}_{0.1}$  while (c) shows the polished surface of  $\text{NbCoSn}_{0.9}\text{Sb}_{0.1}$  at lower magnification for comparison to (d)  $\text{Nb}_{0.75}\text{Ti}_{0.25}\text{FeSb}$  (e)  $\text{Hf}_{0.25}\text{Zr}_{0.75}\text{NiSn}_{0.99}\text{Sb}_{0.01}$  (f)  $\text{Ti}_{0.75}\text{Zr}_{0.25}\text{NiSn}_{0.98}\text{Sb}_{0.02}$ .

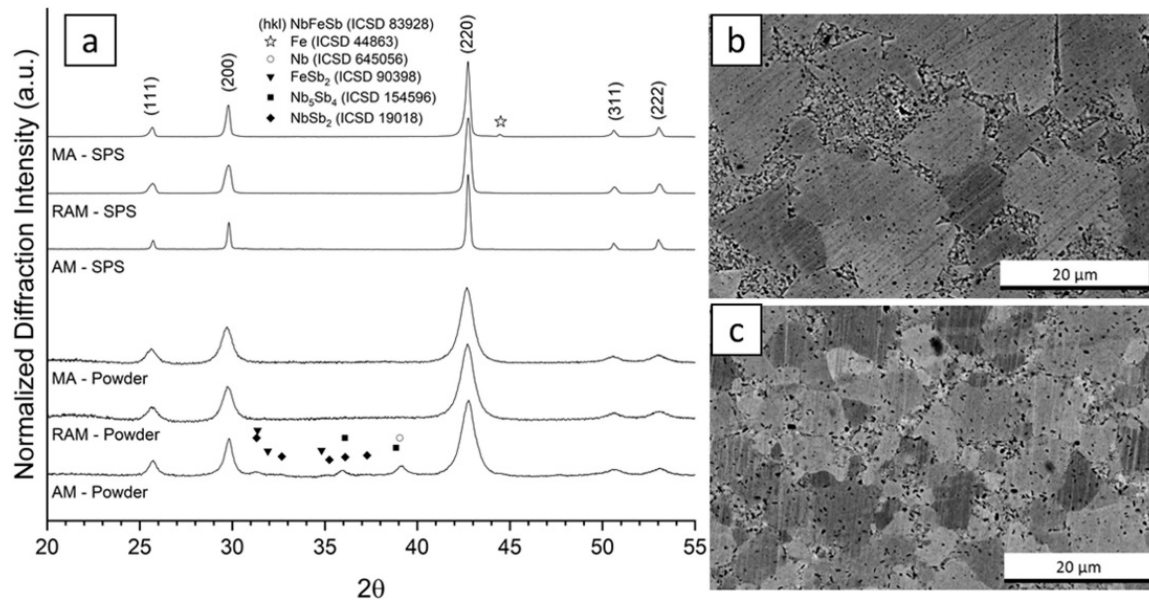


**Figure B.8** (a) X-ray diffraction patterns for  $\text{Nb}_{0.75}\text{Ti}_{0.25}\text{FeSb}$  synthesized by arc-melting powders (AM), these same arc-melted powders refined through additional planetary ball milling (RAM), and elemental powders that were mechanically alloyed via HEPBM (MA). The top set of patterns are for the monoliths produced by consolidation of the three powder sets via spark plasma sintering (AM-SPS, RAM-SPS, and MA-SPS). Peaks of the ternary NbFeSb half-Heusler compound are indexed and impurity phases are indicated. (b) SEM of monolith of  $\text{Nb}_{0.75}\text{Ti}_{0.25}\text{FeSb}$  produced with RAM powder as compared to (c) the SPS monolith produced from MA powder, with both monoliths having similar micron sized grains.

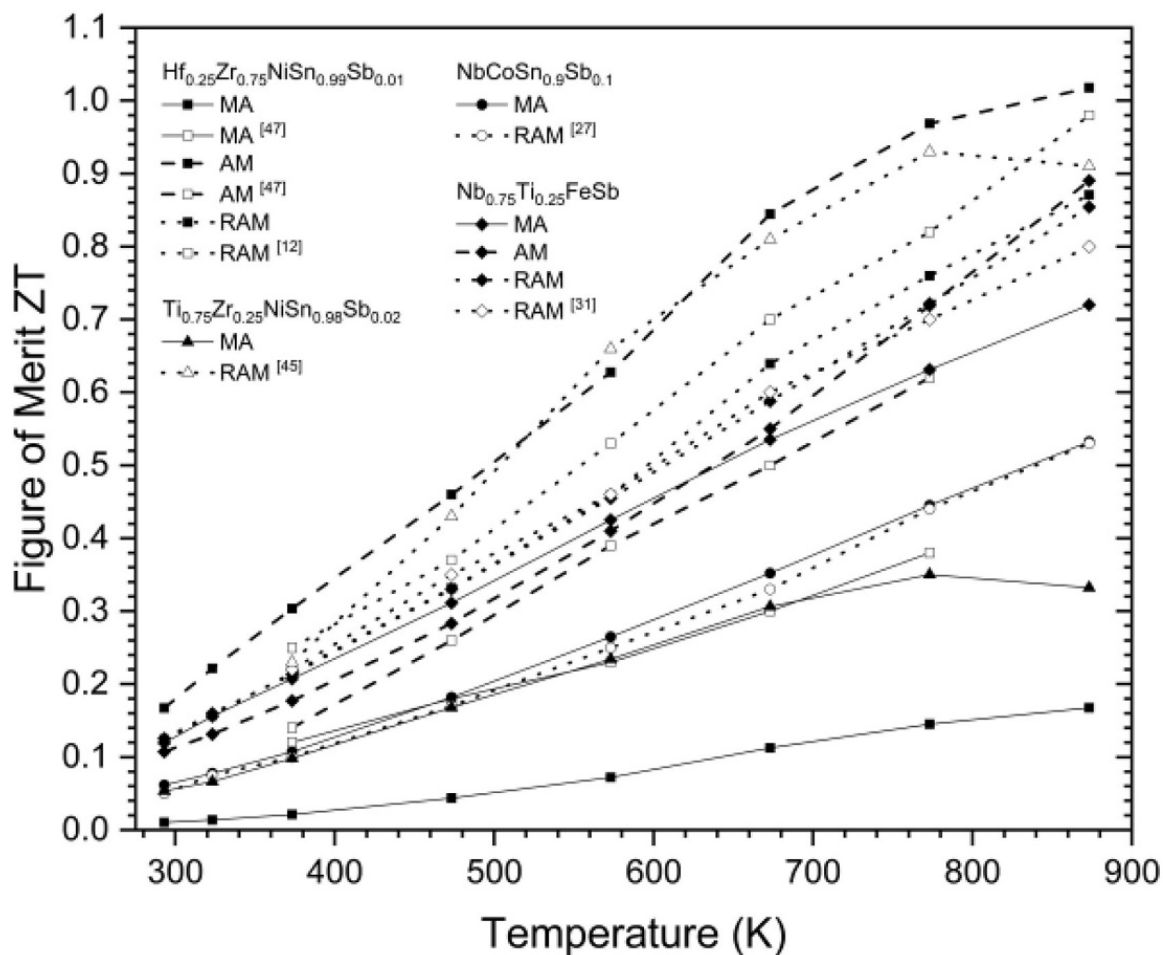


**Figure B.9** The thermoelectric performance (ZT) of synthesized half-Heuslers (indicated by symbol shape) made via arc-melting (AM, dashed lines), mechanical alloying (MA, solid lines), and ball mill refined arc-melting method (RAM, dotted lines) along with comparable reference data indicated with open symbols.

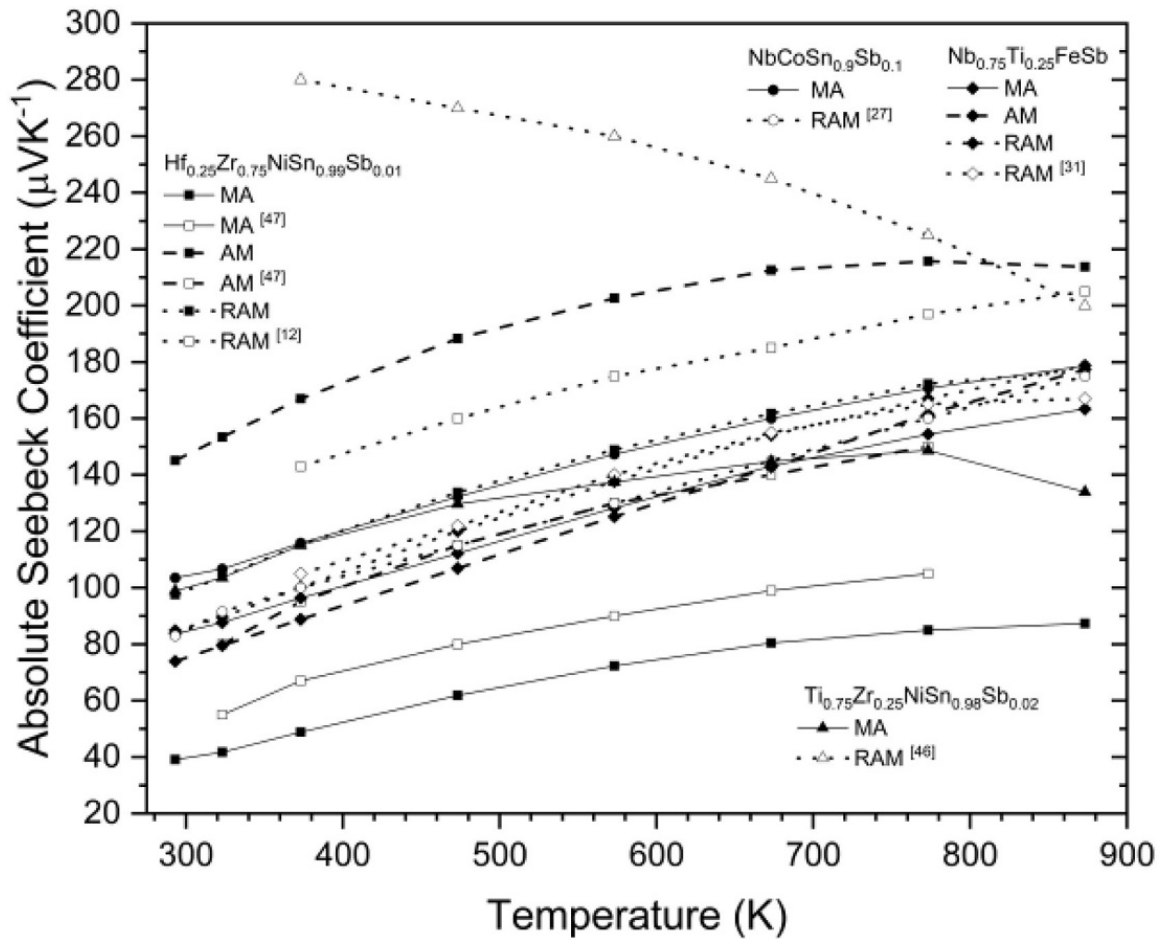


**Figure B.10** The absolute Seebeck coefficient of both n- and p-types plotted for synthesized half-Heusler (indicated by symbol shape) made via arc-melting (AM, dashed lines), mechanical alloying (MA, solid lines), and ball mill refined arc-melting method (RAM, dotted lines) along with comparable reference data indicated with open symbols.

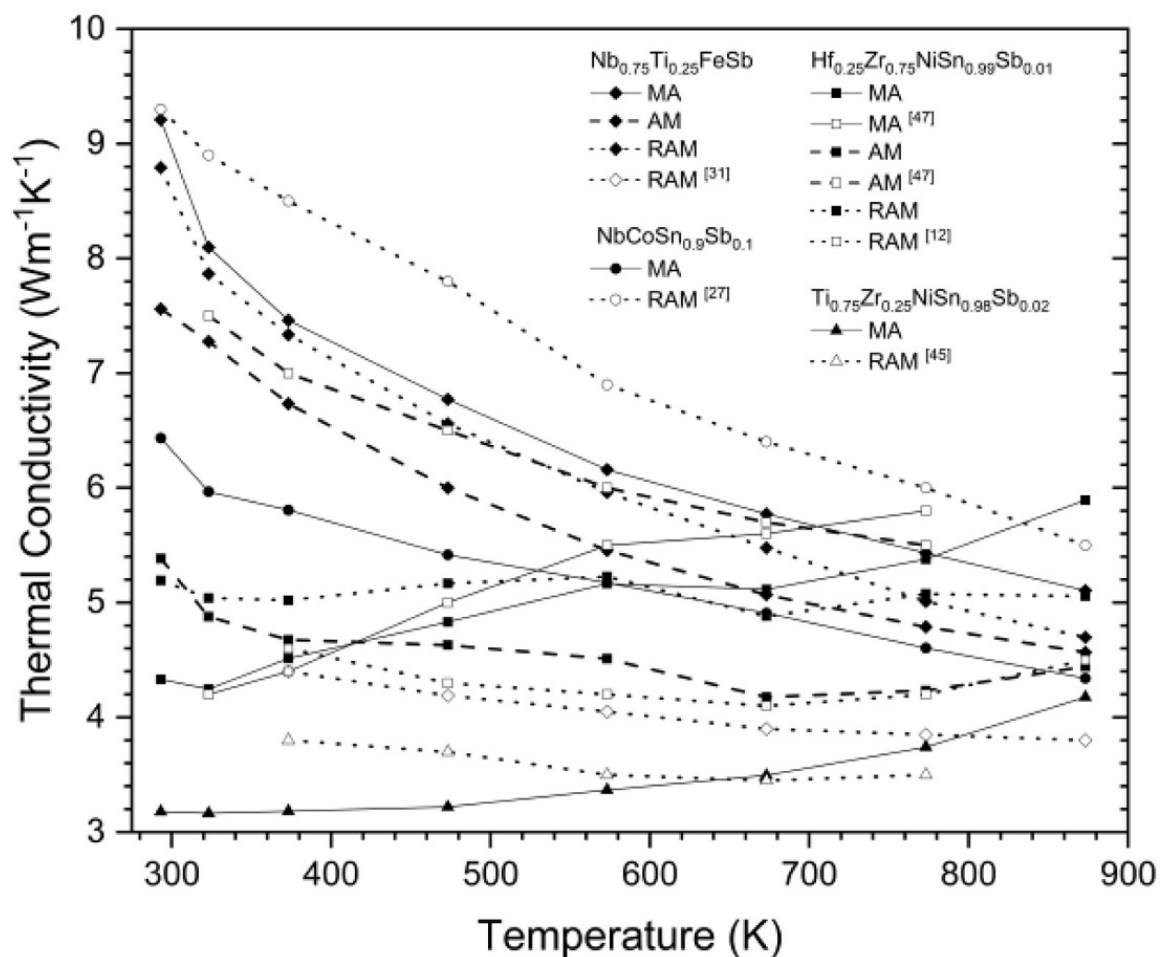
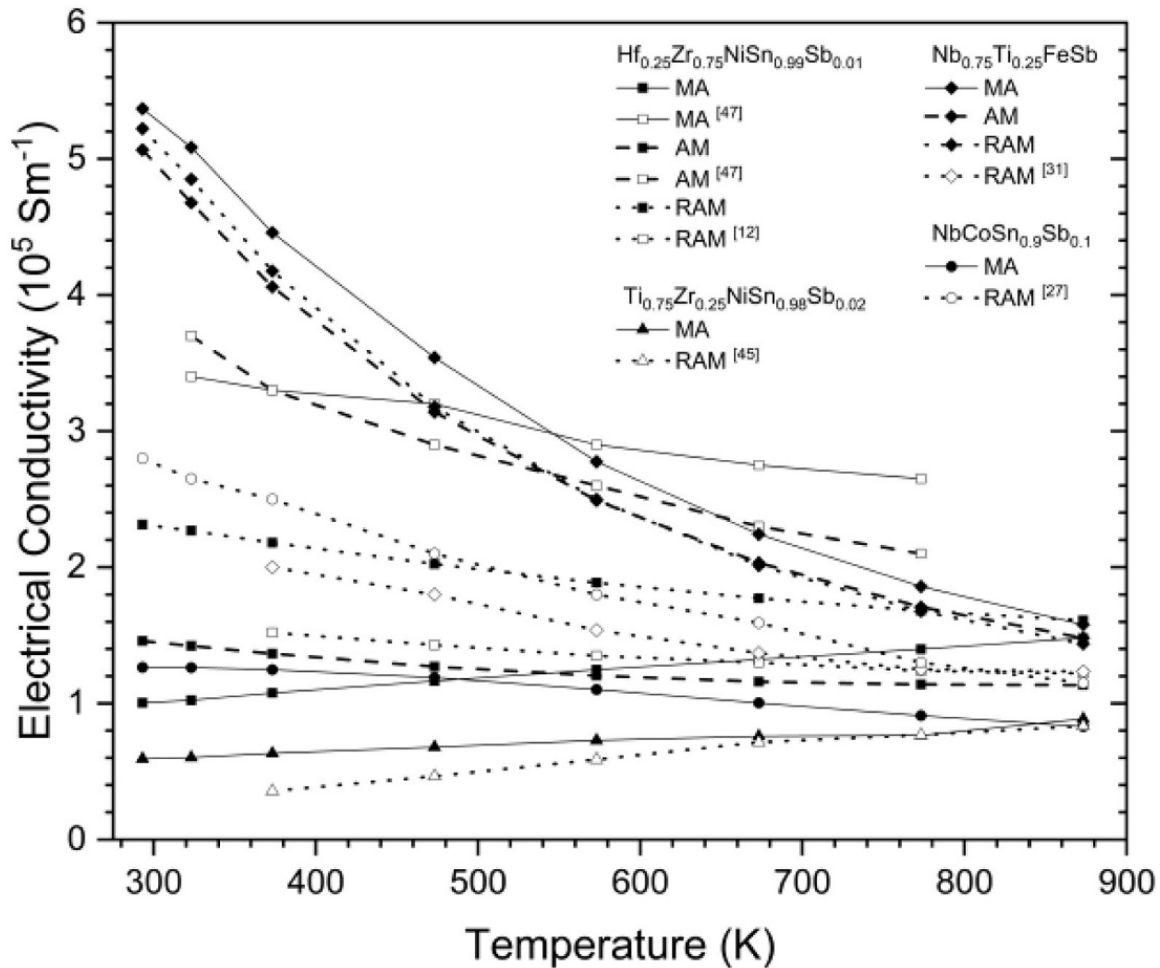


Figure B.11 The thermal conductivity of synthesized half-Heuslers (indicated by symbol shape) made via arc-melting (AM, dashed lines), mechanical alloying (MA, solid lines), and ball mill refined arc-melting method (RAM, dotted lines) along with comparable reference data indicated with open symbols.



**Figure B.12** The electrical conductivity of synthesized half-Heuslers (indicated by symbol shape) made via arc-melting (AM, dashed lines), mechanical alloying (MA, solid lines), and ball mill refined arc-melting method (RAM, dotted lines) along with comparable reference data indicated with open symbols.

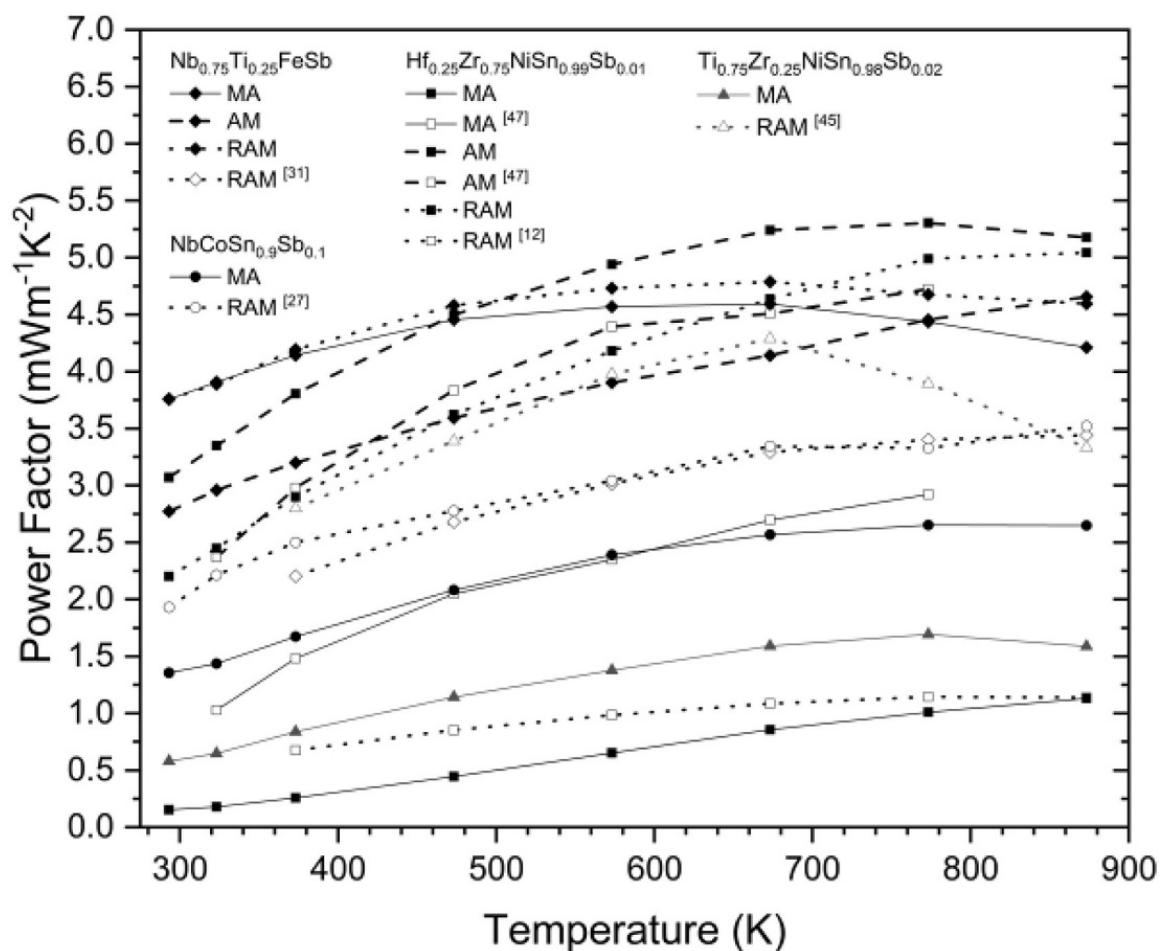


Figure B.13 The calculated power factor of synthesized half-Heuslers (indicated by symbol shape) made via arc-melting (AM, dashed lines), mechanical alloying (MA, solid lines), and ball mill refined arc-melting method (RAM, dotted lines) along with comparable reference data indicated with open symbols.

## Tables

Table B.1 Synthesis and ZT comparison for select half-Heuslers.

Year	Group	Composition	Peak ZT	Temperature (K)	Synthesis Route
2006	Ono et al.	NbCoSn <sub>0.9</sub> Sb <sub>0.1</sub>	0.3	850	arc-melting <sup>52</sup>
2016	He et al.	NbCoSn <sub>0.9</sub> Sb <sub>0.1</sub>	0.6	973	arc-melting <sup>53</sup>
2019	Pedersen et al.	NbCoSn <sub>0.9</sub> Sb <sub>0.1</sub>	0.53	873	HEPBM - This work
2008	Kimura et al.	NbCo <sub>1.05</sub> Sn	0.3	1000	optical floating zone <sup>54</sup>
2018	Ferluccio et al.	NbCoSn <sub>z</sub> Sb <sub>1-z</sub>	0.33	773	solid state reaction <sup>40</sup>
2019	Ferluccio et al.	Nb <sub>0.83</sub> CoSb	0.5	950	solid state reaction <sup>39</sup>
2014	Joshi et al.	Nb <sub>0.6</sub> Ti <sub>0.4</sub> Sb <sub>0.95</sub> Sn <sub>0.05</sub>	1.0	973	arc-melting <sup>31</sup>
2015	Fu et al.	Nb <sub>0.88</sub> Hf <sub>0.12</sub> FeSb	1.5	1200	levitation melting <sup>47</sup>
2019	Pedersen et al.	Nb <sub>0.75</sub> Ti <sub>0.25</sub> FeSb	0.72	873	HEPBM - This work

**Table B.2** Thermoelectric performance of select half-Heuslers produced by mechanical alloying, arc-melting, and ball mill refined arc-melting synthesis routes as compared to literature.

<b>Nominal Composition</b>	<b>Type</b>	<b>Synthesis</b>	<b>Peak ZT</b>	<b>Temperature (K)</b>
Hf <sub>0.25</sub> Zr <sub>0.75</sub> NiSn <sub>0.99</sub> Sb <sub>0.01</sub>	N	AM	1.02	873
Hf <sub>0.25</sub> Zr <sub>0.75</sub> NiSn <sub>0.99</sub> Sb <sub>0.01</sub>	N	MA	0.17	873
Hf <sub>0.25</sub> Zr <sub>0.75</sub> NiSn <sub>0.99</sub> Sb <sub>0.01</sub>	N	RAM <sup>12</sup>	0.98	873
Hf <sub>0.25</sub> Zr <sub>0.75</sub> NiSn <sub>0.975</sub> Sb <sub>0.025</sub>	N	MA <sup>51</sup>	0.38	873
Hf <sub>0.25</sub> Zr <sub>0.75</sub> NiSn <sub>0.975</sub> Sb <sub>0.025</sub>	N	AM <sup>51</sup>	0.62	873
Hf <sub>0.25</sub> Zr <sub>0.75</sub> NiSn <sub>0.99</sub> Sb <sub>0.01</sub>	N	RAM	0.87	873
Ti <sub>0.75</sub> Zr <sub>0.25</sub> NiSn <sub>0.98</sub> Sb <sub>0.02</sub>	N	MA	0.35	773
Ti <sub>0.75</sub> Zr <sub>0.25</sub> NiSn <sub>0.98</sub> Sb <sub>0.02</sub>	N	RAM <sup>41</sup>	0.93	773
NbCoSn <sub>0.9</sub> Sb <sub>0.1</sub>	N	MA	0.53	873
NbCoSn <sub>0.9</sub> Sb <sub>0.1</sub>	N	RAM <sup>53</sup>	0.53	873
Nb <sub>0.75</sub> Ti <sub>0.25</sub> FeSb	P	MA	0.72	873
Nb <sub>0.75</sub> Ti <sub>0.25</sub> FeSb	P	AM	0.89	873
Nb <sub>0.75</sub> Ti <sub>0.25</sub> FeSb	P	RAM	0.85	873
Nb <sub>0.96</sub> Ti <sub>0.04</sub> FeSb	P	RAM <sup>31</sup>	0.80	873